Object-surface interaction in small-body surfaces

by

Onur Çelik

(CELIK Onur)

Dissertation

submitted to the Department of Space and Astronautical Science

in partial fulfillment of the requirements for the degree of

Doctor of Philosophy

The Graduate University for Advanced Studies, SOKENDAI

September 2020

Acknowledgments

"I like things that look like mistakes." – Frances.

This thesis is a culmination of research work in about four years I spent at the Institute of Space and Astronautical Science of Japan Aerospace Exploration Agency (ISAS/JAXA). It was the probably hardest project I undertook in my life. I was lucky to work with exceptional engineers and scientists of JAXA and had a chance to involve in space mission projects. I learnt about the challenges and different approaches to problems in a real-life setting which prepared me for the years ahead. This was thanks to my thesis advisor Prof. Kawakatsu, who accepted me as an inexperienced master's student five years ago. I am grateful for the opportunity he provided for me. The parts of this study (most of Chapter 4) were performed at the University of Colorado Boulder, under the supervision of Prof. Daniel J. Scheeres. I am grateful for his hospitality during my time there and allowing me to realize my dream to work with him. Dr. Koji Wada and Dr. Kazunori Ogawa were two investigators of the DCAM5 project, who generously included me as a science team member and allowed me to work in the mission design analysis of the project, which constitutes most of Chapter 5. I am grateful for that opportunity. I would also like to thank my MSc advisor Dr. Joan-Pau Sanchéz from Cranfield University and internship advisor Dr. Özgür Karatekin from the Royal Observatory of Belgium, for their continuous support in different ways throughout my PhD.

I also took part in several other projects during my PhD research. I felt privileged to be part in the DESTINY$^+$ project as a mission analyst, which provided another item to my research portfolio and another achievement to be proud of. I would like to acknowledge the current and former DESTINY$^+$ team members. Another was the MARAUDERS project, through which I had a chance to devise a mission concept from

scratch with our team. Being in the MARAUDERS project always felt like a Christmas dinner, all friends together with only a few missing.

The Japan experience will always be something I will cherish for the rest of my life. At times it looked like a mistake, both personally and professionally, but otherwise an enlightening one, especially in terms of personal growth. I believe I became a better person and it was only possible with the people who stood by me and shared their friendship at all times. Nicola, Stef, and Ron not only helped me with my research but also supported me through the pains of the PhD process with their wisdom. Ferran and Lucie will always be my “cool people," the ones I know I can always rely on. I am glad to have worked on an evolved version of our friendship with Ferran and glad to have met Lucie. I am sure our year 30 will be a great one. Another person deserving a special mention is Brie, whose presence helped me go through some really difficult times.

One of the things I collected and maintained over these years is friends all across the world. The people from Deep Space Mission Design Lab. (aka Kawakatsu Lab.), Celestial and Spaceflight Mechanics Lab. (aka Scheeres Lab.), and numerous others in Sagamihara/Tokyo and Boulder are part of those, making my experiences all the fun, and I am thankful to them. I always felt the support of my friends from Turkey no matter how little we interact. I am especially glad to have reconnected with Ece and would like to thank for her presence and support. The same goes for Çağrı, who made me feel like home in Morgantown, WV with Emel on the other side of the world. Görkem’s surprise postcards always made my day. Cansu deserves a special mention, whose patience and understanding with me will be hard to match by anyone I know.

Most importantly, my family. Without their continuous unreserved support, I would not be able to succeed at any point in my life. The years showed me day after day how open-minded I grow up, how they shielded me from whatever adversity coming on my way to reach my goal. This work is dedicated to them, Mustafa, Şaziye, and Tuğba Çelik. I hope I can make them proud.

This work is supported by the Japanese Government (Monbukagakusho) Research Scholarship throughout my time in Japan. SOKENDAI Student Dispatch Program provided financial support for my research stay at the University of Colorado Boulder.

Onur Çelik.

Sagamihara, September 18, 2020.

Abstract

The recent observations from the small-body exploration missions have shown that asteroids and comets may have hard rocky surfaces and soft granular surfaces next to each other or mixed in the same region. This previously unknown variety in small-body surfaces poses challenges in understanding and modeling the interaction of natural and artificial objects with small-body surfaces during low-speed impacts. From an engineering perspective, the limited knowledge in the surface interaction makes it difficult to plan and execute spacecraft mission with surface operations. From a scientific perspective, it was recently observed that ejected particles from asteroid surfaces may reimpact and ricochet off the surface. To that end, the surface interaction of natural and artificial objects can be divided into two end-member cases as (1) hard non-penetrable surface and (2) soft granular surface. The models describing the former provides relatively simplified numerically-tractable models. For the latter, on the other hand, the models are very varied and relying heavily on experiments and discrete element method simulations. Even though the Earth-based studies are conducted to understand the interaction between natural and artificial objects with a variety of surfaces, the knowledge is still limited. This is primarily because of the unique environments found around small bodies, which primarily arise from their low-gravity, irregular shape, and surface environment. Therefore, crating a small-body environment on Earth is particularly challenging. For example, performing experiments on drop towers or parabolic flights are expensive and limited in accuracy and test cases. To overcome this, researchers often extrapolate the Earth-based data or rely on simulation studies. While those have shown success on a theoretical level in building an understanding of the surface interaction on small bodies, they still lack a general theoretical framework or experimental validation. In this thesis, this gap is

addressed by investigating two end-member cases of the object-surface interaction. The hard-surface interaction is investigated from an experimental perspective in artificial low-gravity while a theoretical framework is sought for interaction with granular surfaces. In each of these cases, the coefficient of restitution is given a central role. For the granular-surface case, a new analytical expressions are derived via employing the long-established cratering theory. Dependencies of the coefficient of restitution to impact and surface parameters are investigated in both approaches. Finally, implications of object-surface interaction are investigated through a mission-design study.

In the first chapter of the thesis, a rigid body interacting with a hard surface is investigated. The hard surface in this context refers to a type of surface where a rigid-body impactor interacting with a surface without penetrating. Through this, the interaction between the two objects can be approximated as impulsive interaction. Because of that simplified approach, the hard-surface interaction model can offer a numerically-tractable solution by abstracting the interaction with a few coefficients characterizing surface. Thanks to its tractability, large Monte-Carlo-type simulations can be performed to understand overall trends in bouncing motion in small-body surfaces. However, despite their theoretical success, the model lacks an experimental validation under asteroid level gravity at low-speed impacts for nonspherical objects. It is of interest whether, for example, the coefficient of restitution is dependent on the object's impact velocity, impact angle, or impact attitude under asteroid-level conditions or how it can be characterized. Therefore, a set of impact experiments were performed with a cuboid lander assembly under two-dimensional artificial low-gravity created on an air-bearing table. Albeit being on two-dimensions, low-gravity created on an air-bearing table provides an inexpensive, easy, and more controllable environment than those of drop tower or parabolic flights. To that end, the experiments were aimed at representing impact velocities observed on asteroid surfaces thus far, with systematically varied impact and attitude angles. The experimental results are used to investigate trends in post-impact motion and reveal dependencies of the coefficient of restitution to impact angle (in oblique impacts) and attitude angle (in normal impacts). The relationship to the impact angle is found to be more prominent and linearly increasing for the increasing angle. For the attitude-angle dependency, on the other hand, the relationship appears to be more complex, likely due to the rotational effects in post-impact motion. The relationship is found to be non-discernible at least for the

impact velocities considered in the experiments. This study is one of the first examples of the hard-surface impact experiments for non-spherical impactors which is believed to be more representative of realistic lander shapes. The results provide realistic initial coefficient of restitution values for mission planning and trajectory reconstruction for small asteroid landers/hoppers, such as MASCOT or MINERVA-II onboard the Hayabusa2 mission.

The following part of the thesis investigates interaction with granular surfaces in asteroid-level gravity with analytical techniques. The characteristics of this type of interaction are such that the surface would deform plastically upon an impact. The impactor is still assumed to be a rigid body. This type of interaction between an object and a granular surface has been studied in different perspectives from basic physics to planetary cratering. Most works are experimental or simulation-based and often material-specific due to the intrinsic complexity of granular materials. For the low-speed impact phenomena that characterize impacts of lander spacecraft or natural objects on small-body surfaces, the complexity is even higher, as granular behavior is largely unknown in those environments. The currently-available experimental data of object-surface interaction in granular surfaces under low-gravity could only provide phenomenological explanations, while simulation studies are currently restricted to a few case studies. There is a general lack of analytical understanding that is supported by previous observations. To that end, the thesis study handles the object-surface interaction in granular surfaces under low-gravity as a cratering phenomenon. The long-established cratering theory is investigated as a mean to model object-surface interaction in regolith-covered portions of small-bodies for low-velocity impacts. Those crater-scaling laws have been successful in large craters arising from astronomical impacts, which occur at orbital speeds of several km/s in the past. Moreover, it has recently been demonstrated experimentally under Earth gravity that the theory can also capture small craters that occur as a result of low-speed impacts (~m/s). Building on this hypothesis, this research employs discrete-elements method simulations to prove the applicability of the cratering theory in low-speed impacts under low-gravity of small bodies. Then, the analytical expressions of the cratering theory are utilized to derive an analytical coefficient of restitution expression. As a result of the study, a critical impactor-to-target density ratio is identified for bouncing/submerging of an impactor. and an upper-limit coefficient of restitution value is estimated by the

analytical model.

Implications of the object-surface interaction in a small-body surface are discussed in the context of the Deployable CAMera 5 (DCAM5) lander, an optional payload proposed to be deployed to the surface of Phobos during the Martian Moons eXploration (MMX) mission. In the DCAM5 case, the surface interaction becomes especially important as there are regions of Phobos that overflow its Roche lobe. A numerical study in the chaotic three-body problem showed that the escape speeds on Phobos can be as low as 2 m/s, contrary two-body problem estimation of ~9 m/s at minimum. Therefore, the maximum post-impact is restricted to a more realistic minimum of 4 m/s which could only be achieved via the surface interaction as DCAM5 has control capability. The results from the previous two chapters are applied to constrain the maximum impact speed for a chosen surface type. Through the estimated values in both hard and granular surface approaches, upper limits on impact speed and angle are determined to constrain the maximum post-impact speed to guarantee for surface settling. Combined with the deployment studies from MMX's planned quasi-satellite orbits (QSOs), the mission design space is constrained together with the surface interaction element. Reachable regions on the surface with this approach are discussed from the science point of view. The feasibility of the landing trajectories and the reachable regions are demonstrated to be strongly affected by the chosen surface type. While a granular surface allows for all access to the equatorial regions of Phobos, a hard surface restricts the landings to sub-Mars and anti-Mars regions only.

To conclude, the research presented here investigated the limit interaction cases in small-body surfaces from a multifaceted perspective through experiments, simulations, and analytical approaches. Implications of quantifying this interaction are demonstrated in a mission design example. The result found during this study could be used in more accurate operational planning on lander spacecraft and in understanding natural phenomena in small-body surfaces.

Contents

List of Figures

List of Tables

1 Introduction

The last two decades witnessed an ever-increasing interest in small body (asteroid, comet) missions. This interest is threefold. First, small bodies are believed to contain pristine material from the early ages of the solar system, therefore they are essential pieces of the puzzle to understand the formation of the solar system. Second, governments and the space community takes the asteroid impact threat seriously, for which the exploration and test missions could exploit small bodies as test beds for the deflection strategies. Finally, private ventures have a profound interest in prospecting asteroid material for commercial purposes. The exploration missions can, therefore, provide valuable information about the composition of the target body to assess its potential for mining.

There has been a number of successful missions that brought back samples and invaluable remote-sensing information from small bodies, such as NEAR-Shoemaker, Rosetta, Deep Impact, Hayabusa [8, 9, 10]. Following those, several US- or Europe-led missions are also proposed, such as Marco Polo-R, Binary Asteroid in-situ Exploration (BASiX), and Asteroid Impact Mission (AIM) as a part of Asteroid Impact and Deflection

Assessment (AIDA) collaboration [11, 12], albeit without success. The recent HERA proposal follows the footsteps of AIM in testing planetary defense techniques in binary asteroid Didymos [13]. Hayabusa2 and OSIRIS-REx are currently ongoing missions that will bring samples from their targets Ryugu and Bennu, respectively, while the DART mission will test the kinetic impactor technique for asteroid deflection [14, 15, 16].

Further increase in the scientific return of these missions would be achieved by deploying small landers to the surface. Such landers can be employed much more daringly, due to their relatively low cost, simple architecture and low operational risks, as compared to their multi-million dollar mothercraft. They can provide unprecedented information about the surface environment which may not be achievable through conventional remote sensing techniques, by very simple instruments, such as thermometers, accelerometers, or small cameras. For example, the depth of the regolith layer, or the strength of the surface can be measured by accelerometers at the impact(s) of a lander [17, 18]. Similarly, constructed trajectories after an impact may inform scientists about the gravity field of the target body [19] alongside the strength of the surface. Similarly, surface temperature gradients or direct camera measurements can give hints about the particle sizes [19, 17]. This information is not only valuable from the planetary science perspective but can also be used to select landing sites and design surface operations of the mothercraft. An example to that is Target Markers, a small reflective ball, which was deployed from both the Hayabusa and Hayanusa2 spacecraft and successfully guided them to the surface [20]. While the above examples demonstrate the generally agreed usefulness of such landers for in-situ exploration, it also highlights the challenges of these deployments entail in small body environments. Landing in small body dynamical environments significantly differs from landing in a larger gravity well, say, the Moon or Mars, because of the irregular gravity field and shape, littered with rocks and boulders whose distribution is usually unknown a priori. Even landers with active damping mechanisms like Philae can be challenged significantly due to previously unanticipated environment conditions [21]. When one adds errors and uncertainties in the deployment to that, trajectory construction before deployment poses a great challenge for mission planners. Nevertheless, the same microgravity environment makes purely ballistic landing as a viable option, as the low impact speeds may in principle be damped by passive devices on the lander and through interaction with the surface.

On the other side of the medallion, it was observed during the ongoing OSIRIS-REx mission that surface particles are ejected from the surface [22]. The observed materials are m/s and sub-m/s speed levels and a few centimeters across within the observational limitations, hence smaller particles may be expected [22]. Active asteroids like Bennu are known to exist, and a famous example to those is “rock comet" 3200 Phaethon, the speculated parent body of Phaethon-Geminid meteor shower [23]. 3200 Phaethon’s activity is attributed to its highly eccentric orbit, *i.e.* very close perihelion (~0.14 AU) and very far aphelion (~1.27 AU) which causes thermal fracturing and material ejection [23]. In Bennu’s case, various mechanisms are proposed [22], including high-speed micrometeoroid impacts and thermal fracturing. Whatever the mechanism might be, some of the ejected materials have velocities below the escape speed of the asteroid, and considerably large sizes compared to micrometeoroids. Those would fall back to surface after an orbital motion; ejecting material through making new craters or ricochet off the surface, possibly after breaking apart. In fact, the latter was observed on Bennu’s surface [24]. Even though natural phenomena outlined in this paragraph appear to be different from a lander impact, it can be used to characterize surface properties through observations much like instrumented landers. For instance, the observed ricochet event on Bennu allowed researchers to estimate a coefficient of restitution value for the impact point [24].

Be it for a sampler spacecraft, a small ballistic lander or reimpacting ejected particle, understanding surface interaction with small-body surfaces is essential to model impact phenomena in small-body surfaces. Those impacts are primarily characterized by **low-speed impacts**, in this thesis referring to m/s and sub-m/s impact regime where no chemical processes take place, *e.g.* phase changes due to melting, vaporizing, etc. This definition, therefore, excludes astronomical impacts or other high-speed impacts (such as Hayabusa2’s Small Carry-On Impactor experiment) that occur at several km/s that cause drastic chemical and mechanical changes in impacting object. Furthermore, low-speed impacts in small-bodies occur in a variety of surface types. The observations from small-body exploration missions have shown that small-body surfaces have hard rocky regions and soft granular regions next to each other, or even mixed within the same region [25]. Surface interaction in small-bodies this regime can be tackled in different ways, depending on how an impactor or surface is modeled, as shown in the diagram below.

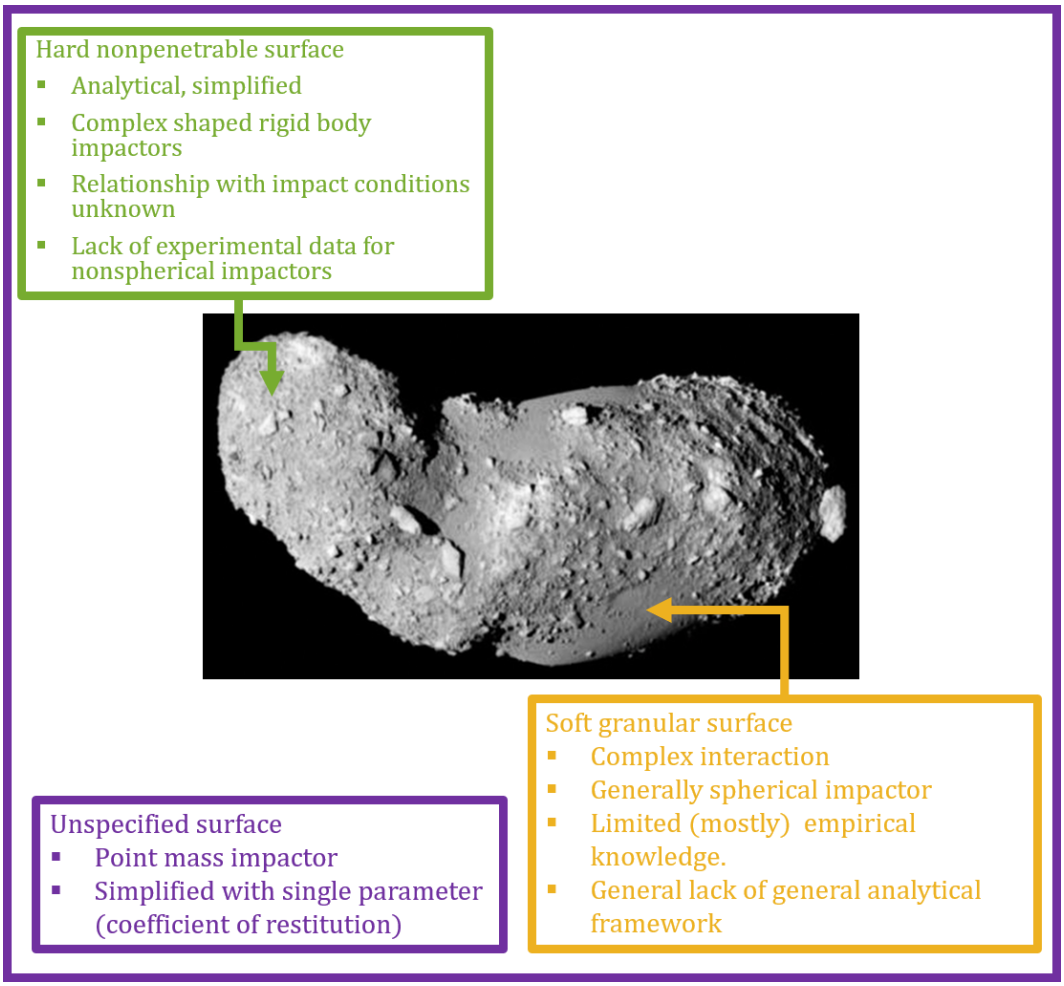

Figure 1.1: Some common surface interaction approaches

The simplest solution to the surface interaction problem is to assume a coefficient of restitution of a point-mass regardless of surface type. In the context of landing in small bodies, this approach was used by Tardivel & Scheeres (2013), Çelik et al. (2018), and Ferrari & Lavagna (2017) in computing ballistic landing trajectories of a massless particle in binary asteroids surfaces with a fixed coefficient of restitution [26, 27, 28]. Similarly, Yu and Baoyin (2014, 2015) studied the dynamical behavior of particles to understand the grain migration in asteroids [29, 30]. They also employed a massless particle approach and a surface with a fixed coefficient of restitution [29, 30]. Zhang et al. (2019) also recently modeled the motion of particles on and near the surface of Bennu [31]. When combined with errors on the deployment, this approach provides a

quick understanding of the possible dynamical behavior and surface dispersion of a particle; however, it fails to account for highly irregular terrain that can change the motion drastically, and the lander properties, e.g. shape or mass.

An improvement to this highly simplified model could be the hard surface approach. The hard surface approach in this case refers to a modeling approach with non-penetrable surface and rigid-body impactor. The hard surface approach allows for an intuitive understanding of the surface motion by modeling abstracting out complexities in interaction with only a few coefficients. Because of that, it is generally possible to derive (semi-)analytical expressions for the force models with different shapes of a lander. It is also remarkably fast, even with the stochasticities included (e.g. rocks and boulders), especially after the computational techniques are implemented [32]. Hence, it enables large scale trajectory estimation and sensitivity studies under uncertainties. Tardivel et al. (2014) employed this approach to analyze the impact statistics of a rigid spherical lander on a hard terrain with normal and frictional forces and rolling resistance with statistically generated rocks [33]. Van wal et al. extended this work to arbitrary shapes and implemented the Stronge impact model [34], and particularly focused the numerical techniques to reduce the computational burden that was caused due to the frequent gravity and surface interaction evaluations [35, 36, 37]. The authors later carried out a large parametric study on spherical pods on small body surfaces and investigated the sensitivities of settling statistics to relevant surface and hardware variations on the coefficients of restitution and friction, rock/boulder distribution, as well as the mass distribution of the lander [38]. The effect of the lander shape on the settling statistics was also discussed by the same authors in more recent work [35]. Van wal et al. put a significant effort into a variety of numerical and computational techniques to increase the speed of simulations, such as signed distance fields or GPU-based computing, for large-scale trajectory construction studies [32]. However, despite the theoretical triumph of the hard surface approach, a few of the assumptions of the hard surface model may be inapplicable for nonspherical impactors under low gravity. For instance, the constant coefficient of restitution assumption is contradictory to experimental observations [34, 39], although those are primarily for spherical objects. When one considers nonspherical shapes, which are more realistic for both lander and natural objects, *there is a general lack of experimental understanding on the post-impact behavior of nonspherical objects under low gravity. Especially it remains unknown*

whether there is any relation between impact velocity, angle and attitude with post-impact properties through interaction coefficients. A few examples to the experiments relevant to the small-body exploration context are Sawai et al. (2001), Biele et al. (2017), and Gautier et al. (2020) [40, 41, 42]. In the former, the authors performed microgravity tests in drop tower and in a vacuum environment to investigate the expected energy damping in the Hayabusa 2 Target Markers [40]. They inferred that there is an optimal number of balls to dissipate energy and identified the possible exchange between rotational and translational motion at touchdown [40]. Gautier et al. (2020) also performed low-speed impact experiments in a microgravity drop tower to simulate CubeSat landing on asteroids [42]. Biele et al. (2017) attempted to determine the structural coefficient of restitution of the MASCOT lander in a laboratory experiment by impacting the lander on a pointy target at different attitude configurations [41].

When one considers “soft" granular portions, the studies are primarily centered around simulations and experiments. Soft surface in this case refers to granular regolith material that is penetrable. The experiments with granular materials are considerably harder to perform for low gravity applications, for granular materials are harder to handle under low-gravity, as well as the cost, accessibility, and limited low-gravity time of reduced-gravity facilities, such as parabolic flights, drop towers and International Space Station. The Discrete (or Distinct) Element Method (DEM) simulations then appear as an alternative to address this issue. The DEM is a general term used for the simulations that handle particle-particle interactions in granular media [43]. The particles are usually considered to be spherical to reduce the computational load, and angularities are included with frictional coefficients. The soft-sphere approaches can also account for particle deformation during the collisions [6]. The DEM simulations for the lander-surface interaction can be thought of as a form of numerical impact experiment in granular media, possibly including a variety of impact conditions and impactors. It can, therefore, be argued that they can provide a more accurate representation of the lander-surface interaction, given that surface is known to be granular. The DEM simulations are recently performed to investigate the behavior of MASCOT in Ryugu’s regolith surface during and after the impact [44, 45]. The studies are motivated from largely unknown properties of Ryugu’s surface, for which the authors investigated the sensitivities of the behavior to grain related parameters, such as particle size, porosity, regolith depth, in addition to usual parameters lander attitude

or spin. The results highlight that effective CoR and CoF are indeed velocity-dependent and other dependencies with regolith properties also exist [44]. In a subsequent study, Thuillet et al. (2018) proposed the impact craters after the touchdown as a way to search for the lander after the first impact [45]. In a more recent study, Cheng et al. (2019) studied the hopping dynamics and granular behavior under a controlled motion of a cuboid probe [46]. Additionally, Jiang et al. (2016) implemented the DEM simulations to investigate the hopping motion a spherical grain, mimicking a spacecraft[47]. It should also be noted that the DEM results not only help to understand lander-surface interaction but also inform scientists for the expected regolith properties as a by-product.

The main drawback of the DEM-based surface interaction simulations is the computational time it requires to simulate a large number of particles, despite using relatively simple force and torque models. Especially if one aims for smaller particle sizes and/or large beds, the simulations often require supercomputers to complete them in a reasonable amount of time. For instance, Maurel et al. performed nearly 500 simulations on supercomputers to reveal trends in MASCOT's bouncing. Moreover, the theory of granular materials is still developing, meaning that only certain patterns are known and there is no agreement on a general force model, despite unification efforts [48]. The complexity of granular behavior is known even to a lesser extent in the low-gravity environments, which often renders studies as mission-specific. *There is therefore a lack of a general analytical framework for surface interaction in soft granular surfaces in small-bodies that could capture the observed behavior in granular surfaces without dealing with the complex details of granular materials at grain scale, hence reducing the number of simulations while obtaining a general understanding.*

The goal of this thesis is to address the lack of experimental and analytical framework in the literature in two end-member approaches to object-surface interaction in small-body surfaces. A fundamental measure of surface interaction, the coefficient of restitution, is given a central role throughout the thesis in quantifying and comparing the interaction models in doing so. Specifically, first, through the impact experiments with a nonspherical impactor performed under artificial low gravity created on an air-bearing table, post-impact motion trends of the impactor are elucidated and the relationship between the coefficient of restitution and impact parameters (i.e., velocity, angle, and attitude) is established for hard surfaces. On the other end, the lack of the

analytical framework in soft surface interaction is addressed via deriving an analytical theory of coefficient of restitution, inspired by the crater scaling laws of astronomical impacts. In order to do so, first, it was proved that low-speed impacts under low gravity obey similar laws as the astronomical impacts. Then, a new analytical expression is proposed for the coefficient of restitution, and its relationship with impact parameters is elucidated. Finally, the derived relationships for hard- and soft-surface impacts are applied to an example initial mission design of a small ballistic lander in the Mars-Phobos environment to ensure settling on the surface, and identify reachable scientifically-interesting regions.

1.1 Thesis outline

In Chapter 2, the models used during the thesis work are introduced. Those include gravity, dynamical and surface interaction models.

In Chapter 3, object-surface interaction in hard surfaces is discussed. First, experimental setup and methods are introduced, and an error analysis is presented. Then, post-impact motion trends and coefficient of restitution and its relation with impact conditions are discussed.

In Chapter 4, object-surface interaction in soft surfaces is discussed. A hypothesis on the applicability of the original cratering theory is developed with a thorough literature study. Then the low-speed validation of the cratering theory of astronomical impacts is done through the results of the DEM impact simulations in sub-m/s velocities under small-body level gravity. Then, a new analytical expression is derived to express energy dissipation inside a crater, alongside the other energy sinks in the interaction process. Finally, the coefficient of restitution is computed in soft surface interaction.

In Chapter 5, the results of the previous two chapters are combined for a initial mission design study of a lander payload to compare how much mission design space would be constrained based on the chosen interaction model. With the Mars-Phobos system and a ballistic lander as an example, first, Phobos surface environment is presented, including the expected coefficient of restitution for hard and soft surface interaction models. Then, a large database ballistic landing trajectories are generated and downselected with the allowable impact velocities and impact angles as a result of the coefficient of restitution results. Finally, reachable scientifically-interesting regions

are presented according to the selected trajectories for each model.

In Chapter 6, the results are summarized, the possible implications of the research are outlined and future directions are presented.

Figure 1.2 below shows the connection between chapters from Chapter 2 to Chapter 6.

1.2 Bibliography disclaimer

This thesis includes portions of text, figures, tables and other material from the following published works of the author:

1. O. Çelik, N. Baresi, R.-L. Ballouz, K. Ogawa, K. Wada, and Y. Kawakatsu, "Ballistic deployment from quasi-satellite orbits around Phobos under realistic dynamical and surface environment constraints," Planetary and Space Science, 178, 2019. doi: 10.1016/j.pss.2019.06.010.

2. O. Çelik, D. J. Scheeres, R.-L. Ballouz, Y. Kawakatsu, "Cratering laws in low-speed impacts," Japan Geosciences Union Meeting, 12-16 July 2020, Chiba, Japan.

3. S. Van wal, O. Çelik, K. Yoshikawa, Y. Tsuda, Y. Kawakatsu, "Experimental validation of hard-surface impacts using air-bearing assembly for small body landers," 32nd International Symposium on Space Science and Technology (ISTS 2019), 17-21 June 2019, Fukui, Japan.

4. O. Çelik, N. Baresi, R.-L. Ballouz, Y. Kawakatsu, "High-fidelity simulations of ballistic small body landers," 68th International Astronautical Congress (IAC 2018), 1-5 October 2018, Bremen, Germany.

5. O. Çelik, N. Baresi, R.-L. Ballouz, S. Van wal, Y. Kawakatsu, "Analytical contact models for regolith covered small body surfaces," 28th JAXA Astrodynamics Symposium, 22-23 July 2018, Sagamihara, Japan.

6. O. Çelik, R.-L. Ballouz, N. Baresi, Y. Kawakatsu, "Deployment and Surface Interaction of Passive Phobos Landers," Japan Geosciences Union Meeting, 20-24 May 2018, Chiba, Japan.

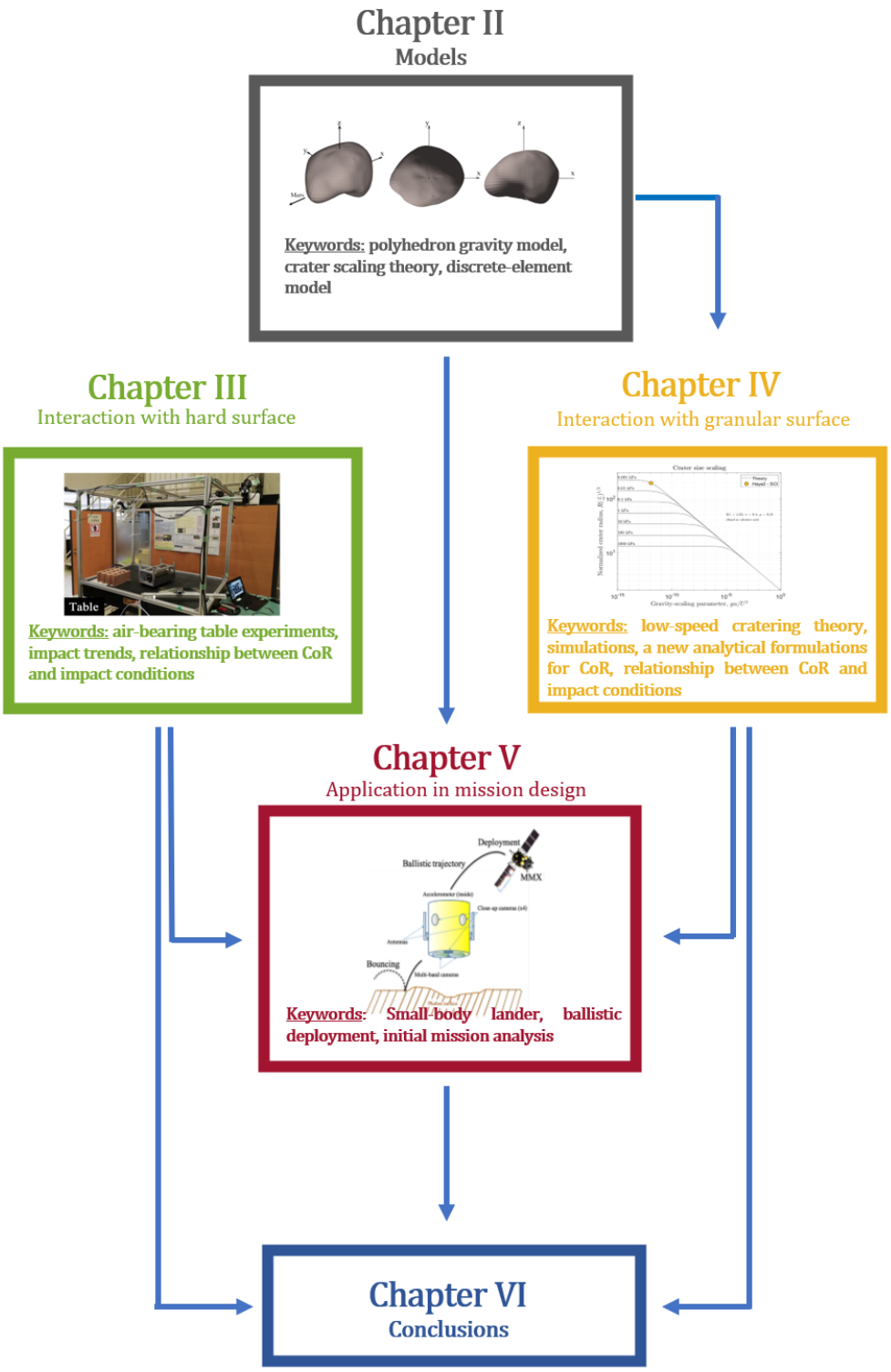

Figure 1.2: Structure and connection between thesis chapters

2 Models

2.1 Introduction

This thesis takes a multifaceted and interdisciplinary approach to object-surface interaction in small bodies. Experimental, simulation and analytical techniques from astrodynamics and planetary science are implemented within the body of the work. This chapter outlines the models that are used in each chapter and throughout the thesis. Specifically, the gravity field of a small body is modeled with the constant density polyhedron model by using a shape model of a target body [49]. The dynamics around a small body is modeled with Hill problem and including the polyhedral gravity of the secondary (in Chap. 5). On the other hand, surface environment in the soft surface interaction (Chap. 4) is modeled with analytical cratering theory [50] and numerical discrete element method [6] with the net surface acceleration calculated from the polyhedron gravity model and Hill problem. Hard surface impact experiments require no model to be presented, for which any other necessary information is provided in Chap. 3.

2.2 Constant density polyhedron gravity model

Small bodies come in all shapes and sizes, hence the point-mass approximation for their gravitational field can be very deceptive, especially for near-surface investigations. The gravity field of an constant density ellipsoid is often a good starting point to investigate the dynamical environment around small bodies [49]. On the other hand, when one considers about the (near-)surface environment, a more sophisticated representation of the gravity field is usually necessary. The constant density ellipsoid approximation outputs as zero when computed at the surface as a mathematical artefact [49]. On the other hand, models with gravity harmonics fails inside the Brillouin sphere of target body [49]. Hence, resolving collisions and simulating the motion in the vicinity of a small body becomes challenging. Therefore, it was deemed appropriate to employ constant density polyhedron gravity which avoids the limitations above-mentioned methods. It can take into account the real shape of the target body and successfully compute the acceleration field near the surface.

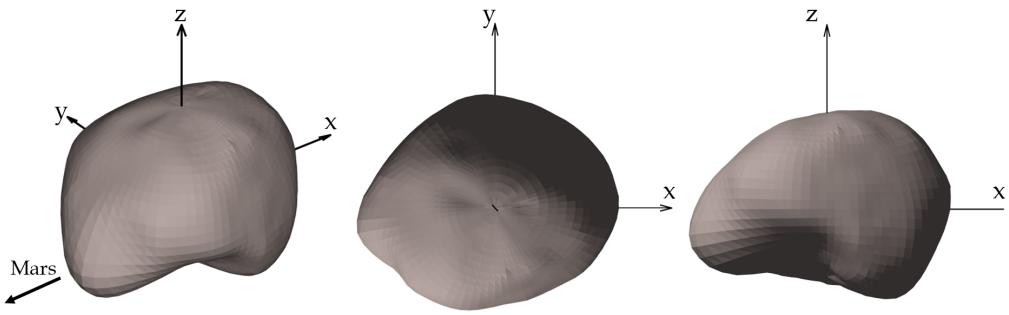

Figure 2.1: Deimos shape model

A polyhedron shape model is composed of triangular facets of shape of interested celestial body. Figure 2.1 illustrates an example shape model of the Martian moon Deimos which is composed of 5040 triangular facets[1]. Each facet is connected to neighbouring facets through shared edges, *i.e.* an edge is shared by two connected

[1]The shape model was downloaded from https://sbn.psi.edu/pds/resource/oshape.html (Accessed on February 21, 2020)

facets, hence $n_e = \frac{3}{2} n_f$, where n_e and n_f are number of edges and facets in a polyhedron shape model, respectively. A *closed* polyhedron would also satisfy following relation:

$$n_v + n_f - n_e = 2 \tag{2.1}$$

Equation 2.1 is known as Euler criterion. n_v denotes number of vertices. Substituting the aforementioned relation into Eq. 2.1 yields following expressions [49]:

$$n_f = 2n_v - 4 \tag{2.2a}$$

$$n_e = 3n_v - 6 \tag{2.2b}$$

Equation 2.2 provides a simple yet powerful way to confirm the consistency of polyhedron shape model of body. Failing to satisfy above relation means that the obtained/constructed shapes contain open regions, duplicate vertices or other kinds of errors. Those kinds of errors in a shape can be corrected by utilizing the freely-available `MeshLab` software[2]. Implementation of these formulae in gravity computations via polyhedron shape models allows pinpointing or eliminating shape-related errors in the computation process.

The fidelity of a shape model highly depends on length of observations made on that particular celestial body and assessed by number of facets and edges generated through those measurements. That is to say, the higher the number is, the more detailed the shape is. However, increasing fidelity on a shape model also increases the computational cost in gravity field calculations as contribution of each facet needs to be accounted in the general gravity-field calculations. Regardless of detail in shape, the gravitational field of a celestial body described with a polyhedron shape can be

[2]It can be downloaded on http://www.meshlab.net/ (Accessed on February 20, 2020.)

computed with the equations in the closed form [51], given as follows [49]:

$$U(\mathbf{r}) = \frac{G\sigma}{2}\left[\sum_{e\in edges} \mathbf{r}_e \cdot \mathbf{E}_e \cdot \mathbf{r}_e L_e - \sum_{f\in faces} \mathbf{r}_f \cdot \mathbf{F}_f \cdot \mathbf{r}_f \omega_f\right] \tag{2.3a}$$

$$\frac{\partial U}{\partial \mathbf{r}} = -G\sigma\left[\sum_{e\in edges} \mathbf{E}_e \cdot \mathbf{r}_e L_e - \sum_{f\in faces} \mathbf{F}_f \cdot \mathbf{r}_f \omega_f\right] \tag{2.3b}$$

$$\frac{\partial^2 U}{\partial \mathbf{r}^2} = G\sigma\left[\sum_{e\in edges} \mathbf{E}_e L_e - \sum_{f\in faces} \mathbf{F}_f \omega_f\right] \tag{2.3c}$$

where Eqs. 2.3 are the expressions for polyhedron gravity potential, gravitational acceleration and its gravity gradient. In the equations $\mathbf{r}_e$ is the distance from any point in the edge e to $\mathbf{r}$ and $\mathbf{r}_f$ denotes the same for face f. G and σ are universal gravitational constant and density of celestial body, respectively. In this thesis, density of the interested body is assumed to be constant but Eqs. 2.3 also allow density variation via assigning different densities to each facet.

The other terms in Eqs. 2.3 are defined as below:

$$\mathbf{E}_e = \hat{\mathbf{n}}_f \hat{\mathbf{n}}_e^f + \hat{\mathbf{n}}_{f'} \hat{\mathbf{n}}_e^{f'} \tag{2.4a}$$

$$\mathbf{F}_f = \hat{\mathbf{n}}_f \hat{\mathbf{n}}_f \tag{2.4b}$$

$$L_e = \ln\left(\frac{r_1^e + r_2^e + e_e}{r_1^e + r_2^e - e_e}\right) \tag{2.4c}$$

$$\omega_f = 2\tan^{-1}\left(\frac{\mathbf{r}_1^f \cdot \tilde{\mathbf{r}}_2^f \cdot \mathbf{r}_3^f}{r_1^f r_2^f r_3^f + r_1^f \mathbf{r}_2^f \cdot \mathbf{r}_3^f + r_2^f \mathbf{r}_3^f \cdot \mathbf{r}_1^f + r_3^f \mathbf{r}_1^f \cdot \mathbf{r}_2^f}\right) \tag{2.4d}$$

the $\hat{(\cdot)}$ notation describes unit vector whereas the $\tilde{(\cdot)}$ notation describes skew-symmetric matrix operator. Then, $\hat{\mathbf{n}}_f$ and $\hat{\mathbf{n}}'_f$ denote the face normals for face f and its neighbour f', r_1^e and r_2^e denote the vertices that are associated with edge e and e_e is the length of the edge, defined as $|r_1^e - r_2^e|$.

Also relevant to this thesis, one can also define Laplacian as:

$$\nabla^2 U = -G\sigma \sum_{f \in faces} \omega_f \tag{2.5}$$

where ω_f is the projected area of f onto the unit sphere whose centre is at $\mathbf{r}$. Hence the value of total projected area is zero outside the body and 4π when inside. Thanks to this property, the Laplacian can be used as an indicator of whether a particle is inside or outside of the body and allow to determine collisions with the target body.

2.3 Dynamical Models

2.3.1 Hill Problem

Motion of a particle in the vicinity of a planetary moon can be described with the equations of the classical restricted three body problem, where a test particle (representing the spacecraft) is assumed to move under the gravitational influence of primary (*e.g.*, planet) and secondary (*e.g.*, moon) without affecting those in return [52]. However, due to the generally small mass ratio of planet-moon systems ($\mu \longrightarrow 0$ where μ is mass ratio), as well as the small particle-moon distance, motion of a particle in the vicinity of a planetary moon can also be described with Hill Problem (HP). Scheeres (2012) provides a list of planet-moon systems where Hill approximation can be applied [49].

As shown in Fig. 2.2, equations of motions of the Hill Problem are defined in a rotating reference frame located at the barycenter of the secondary, where the x-axis is parallel to the line connecting the larger and smaller bodies, the z-axis is parallel to the orbit angular momentum vector of the mutual orbit and the y-axis completes the right-handed triad. In dimensional coordinates, equations of motion of Hill problem take the following form [49]:

$$\ddot{x} = -\frac{1}{\gamma}\left(\frac{\mu_s}{r^3}x - 3\omega^2 x\right) + 2\omega\dot{y} \tag{2.6a}$$

$$\ddot{y} = -\frac{1}{\gamma}\frac{\mu_s}{r^3}y - 2\omega\dot{x} \tag{2.6b}$$

$$\ddot{z} = -\frac{1}{\gamma}\frac{\mu_s}{r^3}z - \omega^2 z \tag{2.6c}$$

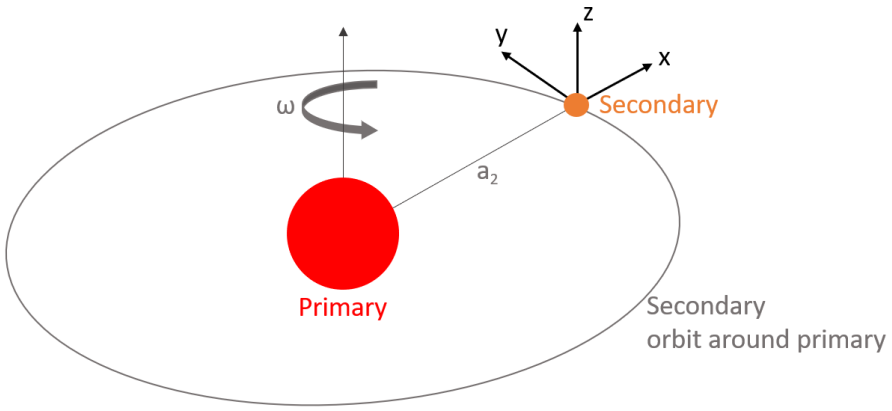

Figure 2.2: Hill problem diagram

The expressions in Eqs. 2.6 describe Elliptical Hill Problem (eHP), *i.e.*, the general form of HP by taking into account the elliptical orbit of secondary its parent body. In Eq. 2.6, ω denotes the angular rate of the orbit of secondary around primary, and μ_s denotes the gravitational constant of secondary and $\gamma = (1 + e\cos\theta)$ where e the eccentricity of moon's orbit and θ denotes orbit true anomaly. It is beneficial to normalize Eqs. 2.6 to generalize its results to more such celestial systems. To do so, one can also define the time and length units of the system as $\tau = \omega t$ and $l = (\frac{m_2}{m_1})^{\frac{1}{3}} a_2$. Normalizing equations of motion of the third body (spacecraft) would yield

$$\ddot{x} = -\frac{1}{\gamma}(\frac{x}{r^3} - 3x) + 2\dot{y} \tag{2.7a}$$

$$\ddot{y} = -\frac{1}{\gamma}\frac{y}{r^3} + 2\dot{x} \tag{2.7b}$$

$$\ddot{z} = -\frac{1}{\gamma}\frac{z}{r^3} - z \tag{2.7c}$$

If secondary's orbital eccentricity is negligible, then one can also assume $e = 0$ and define Circular Hill Problem (cHP) for convenience. This assumption result in $\gamma = 1$ and further simplifies the equations of motion. This final simplification also allows for defining and integral of motion, a useful property in defining admissible regions which will be explored in the next subsections.

Jacobi integral of motion and equilibrium points

One of the useful properties of Circular Hill Problem is that it admits an integral of motion known as the Jacobi integral [49]:

$$C = V(\mathbf{r}) - \frac{1}{2}v^2 \tag{2.8a}$$

$$V(\mathbf{r}) = \frac{1}{2}(3x^2 - z^2) + \frac{1}{r} \tag{2.8b}$$

where v stands for the velocity of the particle in the rotating reference frame, and $V(\mathbf{r})$ stands for effective potential of the system.

The zero velocity surfaces (ZVS) of HP can now be discussed by noting that v^2 is a positive definite quantity. Then, $V(\mathbf{r}) - C \geq 0$, implying that the motion of particles must be forbidden outside of this inequality. Figure 2.3 depicts the ZVS in the Hill Problem.

The ZVS in Fig. 2.3 highlights the existence of three different realms: the primary realm is restricted around primary (to the left of the figure); the secondary realm is restricted around secondary body; and the exterior realm (to the right of figure), which is beyond either of the former regions. There regions are separated by so-called equilibrium points which are stationary in rotating reference frame. In the Hill Problem, there exists two such points along sub-primary and anti-primary direction which are hereby referred to asL_1 and L_2, respectively. They are equivalent of the same points in three-body problem, but the difference is that they are symmetric in the Hill Problem on two sides of the secondary body. They intersect with the ZVS and can be calculated

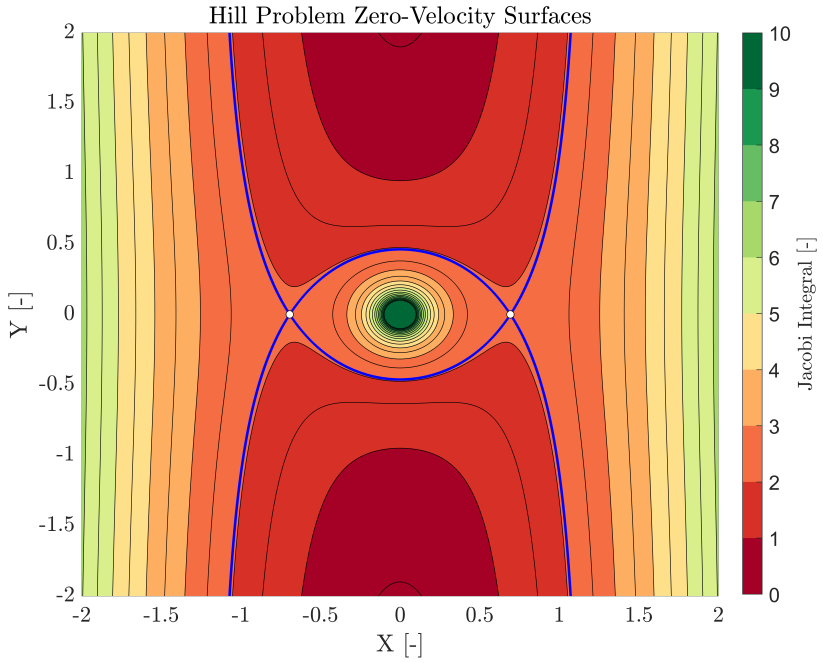

Figure 2.3: Zero Velocity Surfaces in Circular Hill Problem

from Eq. 2.7 analytically in normalized coordinates as

$$\mathbf{L}_{1,2} = \begin{bmatrix} \pm(\frac{1}{3})^{1/3} \\ 0 \\ 0 \end{bmatrix} = \begin{bmatrix} \pm 0.6934 \\ 0 \\ 0 \end{bmatrix} \tag{2.9}$$

The Jacobi integral value for L_1, L_2 is then 2.1634. Because of the location defined for L_1 and L_2 and the definition of rotating reference frame in this thesis, L_1 takes negative and L_2 takes positive sign. The positions of equilibrium points can be dimensionalized by multiplying Eq. 2.9 by $(\frac{m_1}{m_2})^{\frac{1}{3}} a_2$. This means that the position of equilibrium points is linearly-scaled with the distance between primary and secondary.

Hill Problem with polyhedral gravity

In addition to above description of the problem with point masses, this thesis in addition considers higher fidelity gravity model of target secondary bodies where necessary. Fidelity in gravity modelling is improved with polyhedron gravity model.

This is primarily because of the apparent inadequacies of commonly-used spherical harmonics gravity model inside Brillouin sphere of a celestial body [49]. Ellipsoidal gravity model [49], on the other hand, falls short in representing the gravity variations that occurs due to the abrupt changes in the topography, such as large craters.

When implemented in HP, μ/r^3 terms in Eqs. 2.6 are simply replaced with three components of gravity acceleration at a given point, denoted with g_x, g_y, and g_z where appropriate, as follows:

$$\ddot{x} = \frac{1}{\gamma}(g_x - 3x) + 2\dot{y} \tag{2.10a}$$

$$\ddot{y} = \frac{1}{\gamma}g_y + 2\dot{x} \tag{2.10b}$$

$$\ddot{z} = \frac{1}{\gamma}g_z - z \tag{2.10c}$$

The explicit formula to compute g_x, g_y and g_z are provided in Eqs. 2.3. With small eccentricity assumption (*i.e.*, $e = 0$), $1/\gamma = 1$ which defines cHP with polyhedral gravity.

cHP retains its integral of motion. In that case, $1/r$ term in Eq. 2.8 would simply be replaced by moon gravity potential $U_2(\mathbf{r})$ which can be computed through the polyhedron gravity formula given in Eqs. 2.3. Additionally, an important point to note about the equilibrium points is that, due to the irregular gravity induced by the shape model, they would no longer be located on the x-axis of the rotating reference frame and cannot be found in a simple way as described previously. They would need to be found via numerical techniques, such as with Newton method [49].

To demonstrate above statements, let one consider Mars-Deimos system as an example. Mars-Deimos system has a mass ratio of $2.2327{\cdot}10^{-9}$ and Deimos orbital eccentricity is 0.0002, thus it is very well-suited for Circular Hill Problem. Deimos shape model shown in previous section is used in this analysis. As noted, the shape is constructed via 5040 facets. The ZVS of the system is provided in Fig. 2.4.

One can note that now the ZVS is not symmetric after the polyhedron gravity model addition to HP. In Fig. 2.4a, one might notice the slight distortion of the central core towards lower left of the figure. This is due to the irregularity of Deimos' shape and can be seen in the Deimos-superimposed figure on the right (Fig. 2.4b). Due to the irregularity in the gravity field, equilibrium points will also no longer be symmetrical

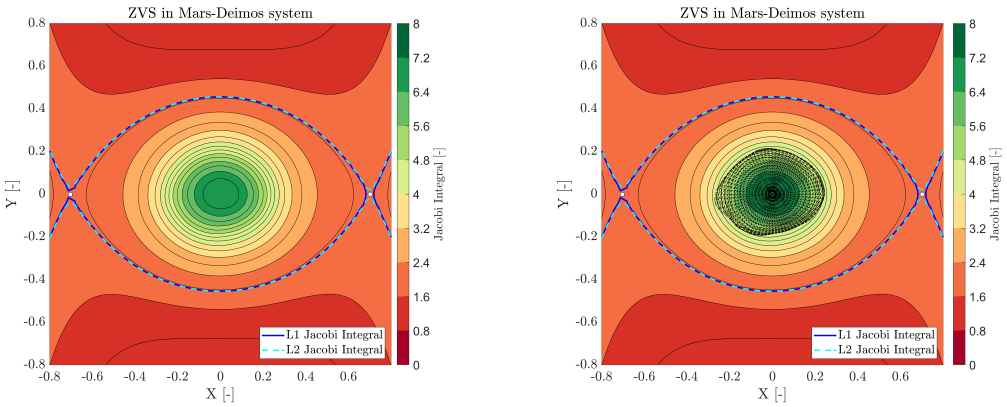

(a) ZVS without Deimos (b) ZVS with Deimos superimposed

Figure 2.4: Zero Velocity Surfaces in Mars-Deimos system

and cannot be computed analytically. Numerical computations yield equilibrium point in non-dimensional coordinates as:

$$\mathbf{L}_1 = \begin{bmatrix} -0.7027 \\ -9.2342 \cdot 10^{-4} \\ -0.0018 \end{bmatrix}, \mathbf{L}_2 = \begin{bmatrix} 0.7016 \\ -5.3689 \cdot 10^{-4} \\ -8.5228 \cdot 10^{-4} \end{bmatrix}$$

And in dimensional coordinates:

$$\mathbf{L}_1 = \begin{bmatrix} -21.7597 \\ -0.0286 \\ -0.0564 \end{bmatrix} \text{km}, \mathbf{L}_2 = \begin{bmatrix} 21.7246 \\ -0.0166 \\ -0.0264 \end{bmatrix} \text{km}$$

L_1 and L_2 now have both y and z coordinate and not symmetric. Jacobi integral values for $L1$ and $L2$ are 2.1826 and 2.1809. $L1$ has a higher Jacobi integral value and therefore first to open up to connect the primary and secondary realms. Decreasing the value of the Jacobi integral will result in opening up the L2 point, thereby connecting all the dynamical realms described above.

Due to the smaller size of Deimos an its relative farther distance from Mars compared to Phobos, the effect of irregular gravity is not as prominent, the analysis above demonstrates its effect. However, as it will be demonstrated in Chap. 5, Mars-Phobos system exhibits more interesting dynamical landscape as a result of this.

2.4 Surface Interaction Models

2.4.1 Cratering theory

Overview and equations

In order to mathematically model the observed scaling behaviour in planetary craters, Housen, Holsapple & Schmidt developed crater-scaling relationships in their seminal papers [53, 50, 54] by making use of Buckingham's π theorem [55]. The assumption of the theory is that a few key parameters can be utilized in a functional relationship, such as in crater volume below:

$$V = f(a, \delta, U, \rho, Y, g) \tag{2.11}$$

Equation 2.11 includes a total of 7 parameters (including V), which are described in the units of mass, length and time. Those parameters will be mentioned in the later parts of the chapter, hence it is given in Table 2.1 with their definitions.

Table 2.1: Glossary of cratering theory

Symbol	Definition
V	Crater volume [m^3]
a	Impactor radius [m]
δ	Impactor density [kg/m^3]
U	Impact velocity [m/s]
ρ	Target density [kg/m^3]
Y	Target strength [Pa]
g	Gravity [m/s^2]

According to π-theorem, those 7 parameters can be reduced to 7 - 3 = 4 dimensionless

parameters by combining them which are provided in Eqs. 2.12.

$$\pi_V = V\frac{\rho}{m} \tag{2.12a}$$
$$\pi_2 = \frac{ga}{U^2} \tag{2.12b}$$
$$\pi_3 = \frac{Y}{\rho U^2} \tag{2.12c}$$
$$\pi_4 = \frac{\rho}{\delta} \tag{2.12d}$$

π_V is defined as “cratering efficiency" with mass of the impactor is defined for a spherical impactor as $m = \delta\frac{4}{3}\pi a^3$. π_2 is so called “gravity-scaling parameter," and a measure of gravity in the crater size. It is originally written as $\pi_2 = g/U^2(m/\delta)^{1/3} = 3.22ga/U^2$, but the constant is generally omitted.

The third equation π_3 is “nondimensional strength" and signifies the strength contribution in the cratering. Finally, π_4 is target-to-impactor density ratio. Combining equations in 2.12 in order to create a functional relation like in Eq. 2.11 would result in as

$$\pi_V = K_V \pi_2^{-\alpha} \pi_3^{-\beta} \pi_4^{-\gamma} \tag{2.13}$$

where K_V, α, β, γ are constants to be determined. Instead, Holsapple & Schmidt (1987) makes use of coupling parameter $C = aU^{\mu}\delta^{\nu}$ and rewrites Eq. 2.11 as

$$V = f(C, \rho, Y, g) \tag{2.14}$$

The dimensional analysis can be performed again to finally reached a crater volume relation as:

$$V = K_1\left[\pi_2\pi_4^{\frac{6\nu-2-\mu}{3\mu}} + \left[K_2\pi_3\pi_4^{\frac{6\nu-2}{\mu}}\right]^{\frac{2+\mu}{\mu}}\right]^{\frac{-3\mu}{2+\mu}} \tag{2.15}$$

Now a few simplications can be made in Eq. 2.15. The extensive experiments on Earth in different materials have all resulted in ν value as ~0.4 [2], hence this value will

be fixed throughout the study. The μ value, which is known to relate to high pressure properties of the target material lies between $1/3 \leq \mu \leq 2/3$, in which the lower and higher ends of the range means impactor momentum or impactor energy drive the crater size, respectively. If K_2 term is assumed to be close to 1, and "effective" strength is defined as $\bar{Y} = K_2 Y$ and substituting the π values in Eq. 2.12 into 2.15 would yield as

$$V = K_1 \left(\frac{m}{\rho}\right) \left[\left(\frac{ga}{U^2}\right) \left(\frac{\rho}{\delta}\right)^{-\frac{1}{3}} + \left(\frac{\bar{Y}}{\rho U^2}\right)^{\frac{2+\mu}{\mu}} \right]^{\frac{-3\mu}{2+\mu}} \tag{2.16}$$

In Eq. 2.16 K_1, μ and $\bar{Y}$ are material-dependent and experimentally-determined constants. Although the expression is given for crater volume, it is often easier to observe or measure crater radius, which can be found with the following expression:

$$R = K_1 \left(\frac{m}{\rho}\right)^{\frac{1}{3}} \left[\left(\frac{ga}{U^2}\right) \left(\frac{\rho}{\delta}\right)^{-\frac{1}{3}} + \left(\frac{\bar{Y}}{\rho U^2}\right)^{\frac{2+\mu}{\mu}} \right]^{\frac{-3\mu}{2+\mu}} \tag{2.17}$$

If a crater is simplified as a paraboloid, then its volume can also be written in terms crater radius as

$$V = \frac{1}{2} \pi R_a R_b d \tag{2.18}$$

where R_a and R_b are major and minor axis dimensions of an ellipsoidal paraboloid, but often it is taken as an mean radius, hence $R_a = R_b$. In equation, d is crater depth. In astronomical impact phenomena of km/s-impacts, d is found to be somewhere between $R/2$ to $2R/3$ [56, 57].

Now that the volume equation is derived, it is possible to discuss physics of the cratering process. If a material is effectively strength-less, *i.e.* if it is easier to break it than to excavate material out of the crater bowl, then crater is considered to be "gravity-dominated" and the second term in the paranthesis in Eq. 2.16 can be ignored. For this reason, cratering in granular materials on Earth is almost always gravity-dominated, because effective strength that granular material exhibits is caused by angle of friction between grains and not as a material structure [2]. Cohesive strength, on the other hand, is too little to overcome Earth gravity. Due to low gravity environment found in small-body environments, the situation might be different,

which will be discussed later.

On the other hand, if it is much harder to break material than to excavate material, then crater is said to be strength-dominated and gravity-related terms are ignored in Eq. 2.16. A transition strength can be defined to separate those two regimes by setting gravity and strength terms equal to each other in Eq. 2.16 [50] as

$$Y_t = \rho U^2 \left[\left(\frac{ga}{U^2}\right) \left(\frac{\rho}{\delta}\right)^{1/3} \right]^{\frac{2}{2+\mu}} \tag{2.19}$$

Strength values higher than Y_t would in principle indicate a crater in strength regime. As noted earlier, due to low-gravity environment found in small-bodies, transition strength can be very low, therefore even little amount of cohesive strength can result in strength-dominated crater. To illustrate this, Eq. 2.16 is plotted with the π_2 values between 10^{-15} and 10^{0} and strength values 0.001-1000 kPa. The K_1 and μ values are used for sand or cohesive soil from Holsapple & Housen [58]. Figure 2.5 shows the crater size results.

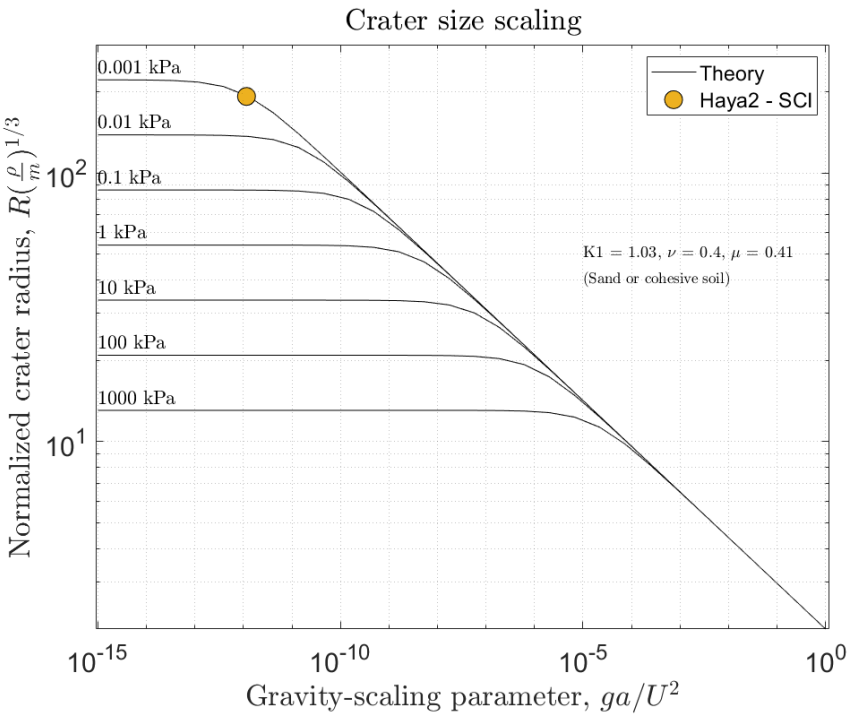

Figure 2.5: Cratering theory estimations with Ryugu parameters [1]

Note the y-axis in Fig. 2.5, which is modified from original π_V expression to provide crater radius, as in Eq. 2.17. As long as a crater is in gravity-regime, and obeys the scaling, it will be on a straight line in the log-log graph. Then, with a right combination of parameters, same normalized crater would be found at different environments. Once there is nonzero strength, cratering process is started to be dominated by that hence the divergence from the straight line. For a given π_2 value and surface parameters, the strength values larger than Y_t will result in craters sizes on this divergent lines. Note that the opposite situation would have happened if the x-axis was nondimensional strength π_3 instead of pi_2.

It is now reasonable to look at this with a practical example of Hayabusa2 Small Carry-on Impactor (SCI) experiment. The SCI experiment was performed in 2019, and thus far the most controlled extraterrestrial cratering experiment with both pre-impact conditions and post-impact observations [1]. The 2-kg impactor of oxygen-free copper impactor was shot into asteroid Ryugu's surface at 2 km/s with an explosive charge. The impact resulted in a crater diameter of 14.5 m ±0.4 m [1]. Given gravity acceleration and bulk density of Ryugu as $\sim 1.25 \cdot 10^{-5} g$ and 1200 kg/m^3 [59], respectively, and the impactor density ~9000 kg/m^3, the scaled crater radius π_R becomes 63.26 while gravity-scaling parameter $\pi_2 = 1.15 \cdot 10^{-12}$. This was also plotted in Fig. 2.5 as an example. With the parameters used in generating Fig. 2.5, the SCI crater is mostly in the gravity-regime within its error bounds, as inferred by Arakawa et al. (2020) [1]. However, the gravity-strength transition occurs at $Y_t = \sim 1$ Pa with the material properties used. It has been previously theorized that small-bodies can have cohesive strength larger than 1 Pa [60]. Therefore, if there is cohesive or some other sort of strength existing in the impact site, then the SCI crater could actually be in some transition region between gravity- and strength-dominated regimes.

Crater formation time, T_g has also been studied during the development of the cratering theory. T_g captures the time from the beginning of impact and at the end of the excavation stage. For craters in the gravity-regime, the expression is given by Schmidt & Housen (1987) as follows [56]:

$$T_g = K_{cr,g} \sqrt{\frac{V^{1/3}}{g}} \tag{2.20}$$

$K_{cr,g}$ value is determined to be 1.6 by Melosh et al. (1989) [57] or 0.8 [56]. As

long as craters are in the gravity regime, K_{cr} would be the same for all craters due to "self-similarity" [61]. However, it should be noted that the timescale of craters under Earth- and low-gravity are very different. For instance, material ejection is observed even after minutes later the SCI experiment [1], as opposed to craters that form within seconds. Therefore a modification to this value will be necessary and discussed later in Chapter 4.

The equivalent crater formation time in strength-regime would be written in short form as[50]:

$$T_s = K_{cr,s} V^{1/3} \sqrt{\frac{\rho}{\bar{Y}}} \tag{2.21}$$

However, Richardson et al. (2007) notes the lack of availability in strength-regime cratering data [61]. The authors also note that even the data available, crater formation times would only be similar for similar experiments [61] cannot be generalized to all strength-regime craters as in gravity-regime counterparts.

The ejecta from a gravity-regime crater would take the following form according to cratering theory [50]:

$$v(r) = C_2 \sqrt{gR} \left(\frac{r}{R} \right)^{-1/\mu} \tag{2.22}$$

and in strength-regime as

$$v(r) = C_3 \sqrt{\frac{\bar{Y}}{\rho}} \left(\frac{r}{R} \right)^{-1/\mu} \tag{2.23}$$

where R crater radius, r denotes material launch position. C_2 and C_3 are constants that relate to crater formation time.

Another aspect of cratering theory is "mass ejected faster than velocity v." In other words, this refers to total amount of mass ejected within radius r. This can also be written in terms of volume, and can be written for gravity-craters as [50]:

$$M(v) = C_5 \rho R^3 \left(\frac{v}{\sqrt{gR}} \right)^{-3\mu} \tag{2.24}$$

similarly for strength-craters as

$$M(v) = C_6 \rho R^3 \left(v \sqrt{\frac{\rho}{\bar{Y}}} \right)^{-3\mu} \tag{2.25}$$

where C_5 and C_6 are experimentally-determined constants.

Using the equations given above, cratering-scaling theory is traditionally represented with a group of power-law scaling relationships, a general form of this is adapted from Housen & Holsapple (2011) in Fig. 2.6.

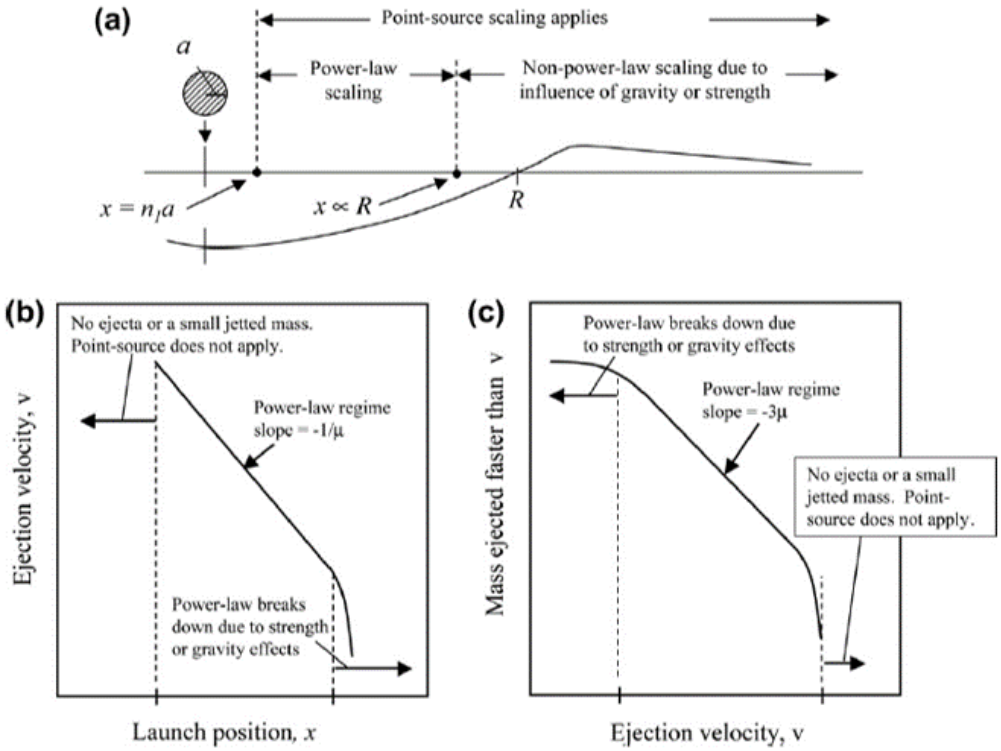

Figure 2.6: Power-law scaling of crater and ejecta (from [2])

Housen & Holsapple (2011) provides an excellent review and discussion on these, their applicability range, and dependencies to different material parameters in the light of the experimental data to date [2]. According to that, the applicability range of the crater-scaling laws is from some close distance from the impact point to near crater rim for power-law scaling. Near an impactor, there is no ejecta or ejecta is in the form of a jetted mass, hence the scaling laws do not apply. Similarly, near a crater rim gravity/strength effects are more prominent hence the scaling also fails.

According to Housen & Holsapple (2011), the range of applicability is within some $n_1 a \leq r \geq n_2 R$ where $n_1 \approx 1.2$ and $n_2 \approx 1$. This range is derived from experiments that are performed with impact velocities, where complex, often phase-changing processes such as melting, vaporizing or breaking occur [57]. According Melosh et al. (1989), up to 50% of initial impact energy could be spent in those processes [57]. However, these may not be true for low-speed impact where the interaction is mainly collisional and frictional and no phase changing processes occur. It will therefore be of interest to investigate these processes on low-speed impacts on small-body surfaces in the light of the crater-scaling laws. A hypothesis will be built on the applicability of the laws to low-speed impacts through the existing experimental data in the literature.

A ballistic model for grain ejection

Richardson et al. (2007) proposed a grain ejection model to estimate the velocity of ejected materials during the impact experiment of Deep Impact on comet Temple-1 [61]. The model combines the basic ideas from Maxwell's Z-model (1977) [62] and crater-scaling theory [50] to provide an ejection model that is consistent with hypervelocity impact experiments of Cintala et al. (1999) [63]. Maxwell's Z-model, which was initially developed for explosion craters and later expanded into Earth and other planetary craters, provides an analytic model to describe grain motion during cratering. It follows experimentally-observed features that (1) cratering excavation flow continues long after the initial impact stresses fade out and (2) this flow can be approximated as incompressible flow along stationary streamlines. Figure 2.7 shows simplified cratering flow with Maxwell Z-model.

Following those, the model possess following features, from Richardson et al. (2007) [61]:

- All particles at a given radial distance r from the impact site will begin motion at the same speed
- For a vertical impact (parallel to the surface normal), all stremline tubes will be axially symmetric with respect to surafce normal.
- All particles in a given streamline will be ejected from the surface with the same velocity

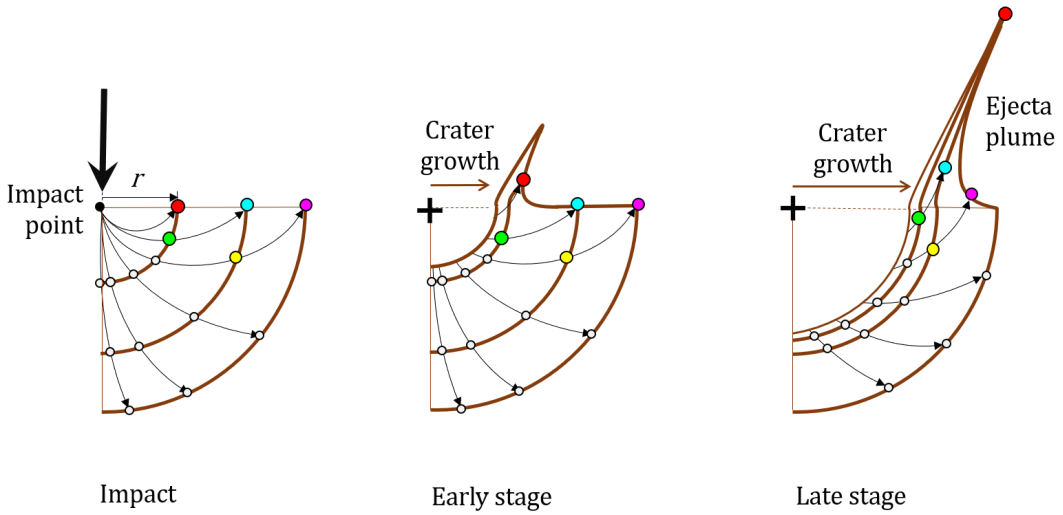

Figure 2.7: Illustration of Maxwell Z-model and simplified crater excavation flow

- As particles move along streamlines, they are slowed down by frictional forces.
- Once the particles in each streamline have moved above the pre-impact surface level, their motion is considered to be ballistic and free of all frictional effects.

More detail on this can be found in Richardson et al. (2007) [61]. With the development of computer technology and modelling codes, Maxwell Z-model lost much of its importance, but still provides “good" initial guesses to simulation and design studies [61].

The velocity expression of this ballistic model combines crater formation time and time-dependent velocity expressions from Housen et al. (1983) [50]. One of the primary assumptions of the model is that the ejection occurs at 45^o with surface local horizontal [61]. In reality, the angle is steeper near impact point and shallower as crater size increases, however current assumption covers a large portion of the ejection process. Furthermore, the expression will be shown to be versatile enough allow a modification if it is deemed necessary.

The ballistic model hereby will be summarized only for gravity-regime craters for relevance to this study as well as for conciseness. Interested reader may refer to Richardson et al. (2007) for more discussion on strength-regime craters [61].

The development of the ballistic ejection model begins with crater formation time T_g:

$$T_g = K_{cr,g}\left(\frac{\pi d}{2}\right)^{1/6}\sqrt{\frac{R_g^{2/3}}{g}} \tag{2.26}$$

This T_g expression is written in terms of crater radius instead of crater volume as provided in Eq. 2.20 with parabolic crater assumption. d denotes crater depth. Note that this T_g expression is essentially the same but written in a more general form than the one provided in Richardson et al. (2007) [61]. The difference arises from the fact that Richardson et al. (2007) assumes a crater depth $2R_g/3$ from high-speed cratering literature, which simplified it to $T_g = K_{cr,g}(\pi/3)^{1/6}\sqrt{R_g/g}$. The expression is now written in a more general form with a circular paraboloid assumption. To simplify the equation one can define a term $C_{T,g}$ as:

$$C_{T,g} = K_{cr,g}(\frac{\pi}{2})^{1/6} \tag{2.27}$$

which brings $C_{T,g} \approx K_{cr,g}$ within experimental accuracy. From Housen et al. (1983), crater radius progression as a function of time is given as [50]:

$$r(t) = C_{pg}R_g(t\sqrt{\frac{g}{R_g}})^{\frac{\mu}{1+\mu}} \tag{2.28}$$

By setting up $t = T_g$ and $r = R_g$, one can arrive a C_{pg} expression as

$$C_{pg} = \left[C_{T,g}d^{-1/6}R_g^{2/3}\right]^{-\frac{\mu}{1+\mu}} \tag{2.29}$$

It is worthwhile to note that $t = T_g$ and $r = R_g$ assumptions imply that power law holds for entire crater growth process because of gravity (or strength) effects, as also noted in the previous subsection. This is not entirely true but true for a large portion of crater growth in high-speed cratering. Rearranging Eq. 2.28 would result in a time as a function of transient crater radius as:

$$t(r) = C_{T,g}R_g^{2/3}d^{-1/6}\sqrt{\frac{R_g}{g}}(\frac{r}{R_g})^{\frac{\mu+1}{\mu}} \tag{2.30}$$

which will later be used in derivation of ejection speed as a function radial distance. Time-derivative of Eq. 2.28 would then yield tangential velocity component of ejecta

as:

$$v_h(t) = C_{pg}(\frac{\mu}{\mu+1})(t\sqrt{gR_g})^{-\frac{1}{\mu+1}} \tag{2.31}$$

with 45^o ejection angle assumption noted earlier, magnitude of ejection velocity as function of time would take the following form

$$v_e(t) = \sqrt{2}C_{T,g}^{-\frac{\mu}{\mu+1}}[d^{-1/6}R_g^{2/3}]^{-\frac{\mu}{\mu+1}}\sqrt{gR_g}(t\sqrt{\frac{g}{R_g}})^{-\frac{1}{1+\mu}} \tag{2.32}$$

Substituting Eq. 2.30 into 2.32 would finally yield as

$$v_e(r) = \frac{\sqrt{2}}{C_{T,g}}[d^{1/6}R_g^{-2/3}](\frac{\mu}{\mu+1})\sqrt{gR_g}(\frac{r}{R_g})^{-\frac{1}{\mu}} \tag{2.33}$$

by defining $C_{vpg} = \frac{\sqrt{2}}{C_{T,g}}[d^{1/6}R_g^{-2/3}](\frac{\mu}{\mu+1})$, Eq. 2.33 can be shortened as

$$v_e(r) = C_{vpg}\sqrt{gR_g}(\frac{r}{R_g})^{-\frac{1}{\mu}} \tag{2.34}$$

Even though Eq. 2.34 provides a velocity expression for material ejection, it does not ensure that crater formation halts at some point, *i.e.*, $v_e(r)$ values become infinitely small while r approaches to infinitely large craters. The velocity expressions implicitly includes frictional effects but do not include gravity (or strength) to stop crater growing. In other to incorporate those effects in the ejection velocity expressions, Bernoulli's energy balance equation is used [61]. With negligible strength assumption, effective ejection velocities would yield as:

$$v_{ej}(r) = [v_e(r)^2 - C_{vpg}^2 gr]^{\frac{1}{2}} \tag{2.35}$$

For the coefficient of restitution expression that will be derived later, Eq. 2.34 will sufficient as it is needed to know the initial velocity of ejected material rather than ejection velocity. However, both $v_e(r)$ and $v_{ej}(r)$ expressions have dependencies on the crater formation time and crater depth, hence those will need to be modified with the data available. The $v_{ej}(r)$ expression will therefore be used to test these modification against simulation/experiment outcome which will be discussed later.

2.4.2 Discrete Element Method (DEM)

Granular systems are comprised of small individual particles of different shapes and often different properties. Depending on the media and forces acting upon them, granular systems may show solid, liquid and gas like behaviour. This varied behaviour is driven by interaction of individual grains in micro-scale. Experimental studies can only measure macroscopic behaviour and hence, microscopic nature of granular system would be explained only in intuitively, but not with the underlying physical process. On the other hand, continuum modelling approach can model granular systems as near-solid, -liquid or -gas with highly-complicated models. With advancement of computer, especially with dedicated workstations and graphical processing unit (GPU) accelerated systems, it is now possible to handle the discontinuous nature of granular material and the micro-scale interaction between them. This approach is commonly known as discrete (or distinct) element method (DEM) and it is widely used in science and engineering problem that involves granular materials such as sands, powders and grains. In general terms, DEM is a numerical simulation technique to simulate and analyze behaviour of particle systems within which all system elements interact with neighbouring particles. The interaction between particles can be in varying complexity depending on the particle system structure and interaction frequency. For example, while more disperse systems can be modelled through event-driven simulations with instantaneous particle impacts, more compact systems are needed to be modelled through lasting contact and evolving force between them [64]. Because of the computational nature of DEM, it can provide *quantitative* information about the microscopic interaction between particle that is normally inaccessible which would allow performing detailed parametric studies and allow design exploration of hardware before testing [64]. The results of the DEM simulations would allow researchers to relate macroscopic granular behaviour to microscopic and mesoscopic scale interactions hence provide a systematic framework to explore interaction between an object and granular surface, as this dissertation aims to tackle.

In an excellent historical review, Thornton dates the earliest particle simulations studies back to 1953 [64]. However, computational models that were commonly used today appeared did not appear until early 1970 [64]. The first papers that lay the foundations of the “soft sphere" approach are attributed to Cundall (1971) and later

Cundall and Strack (1979) where the technique was called as “distinct element method." In this approach, particles are allowed to overlap with each other during contacts that last in finite time [65, 66]. Overlapping particle contacts in normal and tangential directions are enabled with linear spring-damper systems and the force is allowed to evolve incrementally during compression and restitution phases. Thanks to that, compact particle systems with continuing contact during deformation can be modelled.

The DEM approach have also find applications in space and planetary science. The DEM simulations avoid limited non-standard gravity (*i.e.*, lower or higher than the Earth gravity) time and test conditions, as well as noisy data in drop towers, parabolic flights and centrifuges while allowing to perform numerical *experiments* in virtually any planetary environment. Thanks to that, the DEM approach is now a standard technique to derive and test planetary science theories to simulate lander impacts on asteroid surfaces. To name a few, Walsh et al. investigated binary asteroid formation with the “hard sphere" DEM model where contacts are handled as instantaneous collisions as mentioned earlier [67, 68]. Ballouz et al. attempted to explain the existence of red/blue units on Phobos surface with orbital eccentricity driven grain motion through DEM simulations with “soft surface" approach [69]. Sánchez and Scheeres (2014) used the DEM simulations to demonstrate nonzero cohesive strength in asteroid [60]. On a more engineering and technology side, the DEM models are frequently used for modelling locomotion of planetary rovers [70]. In addition, Maurel et al., Thuillet et al. [44, 45] analyzed the natural bouncing motion of the MASCOT lander on regolith-covered asteroid surfaces, whereas Cheng et al. [46] simulated controlled motion of an asteroid hopper. Thuillet et al. (2020) used the DEM simulations for medium level impacts in assessing the performance of the Hayabusa2 sampling mechanism [71]. More recently, the DEM simulations were also used in designing a CubeSat-based centrifuge in the low-earth environment in order to test planetary science theories [72, 73].

In this thesis a parallelized KD-tree gravity code `pkdgrav` is employed in order to simulate the object-surface interaction in small-body surfaces. `pkdgrav` treats particle collisions through a soft-sphere discrete element method (SSDEM) [6]. Through SSDEM implementation, `pkdgrav` handles multi-contact and frictional forces using dissipative and frictional parameters that allow mimicking the behaviour of angular and rough particles that translate, rotate, roll and twist around each other. Furthermore, `pkdgrav` allows assembling simple geometric shapes by using its “wall" functionality

to construct the shape of an object to investigate the interaction in higher fidelity. The code has been tested extensively and calibrated for a variety of materials to realistically represent the actual granular behaviour throughout different studies [74, 29].

3

Interaction with hard surfaces: Experimental investigations

3.1 Introduction

The impulsive models are among the simplest approach to model interaction between an object and surface that the object is interacting with. In its simplest form, the interaction of a spherical object *e.g.* a tennis ball, with a flat surface, *e.g.* a table, is modeled by assuming the spherical object as a point mass, and the surface nondeformable, even though both the object and surface have a certain level of deformability accordingly with their respective material properties. The energy loss to material deformation or some temperature increase would be represented by a term called *the coefficient of restitution* (CoR), which is defined as the ratio of post- and pre-impact velocities and represents the energy loss through the interaction between the object and the surface. Once the interaction ends, a spherical object would bounce back with some reduced velocity, determined by CoR. In an oblique impact case, as there is a tangential

component of the velocity vector, one can also define a tangential CoR. This would allow for an abstraction of the physical process into one or two coefficients without dealing with individual material properties. The point mass assumption also avoids dealing with more complex rigid body effects involving rotational motion. Because of this simplicity, the point mass model would be the easiest method to apply when very little is known about the surface environment in lander mission planning [75].

Being a relatively simple approach, the initial mission design space of a lander can significantly be constrained by defining an admissible impact speed and angle by using the surface coefficient of restitution when combined with natural dynamical environment and deployment conditions. Significance of the surface coefficient of restitution in preliminary mission planning has been successfully demonstrated by Celik et al. (2019) via impact simulations for ballistic deployments on Phobos for a cylindrical lander when interacting with the fully granular surface via simulations [3]. The study revealed an effective coefficient of restitution that is dependent on the impact angle but independent of impact speed. [3]. The same could also be done for impacts on a hard-surface case when the relevant dependencies of CoR have been revealed. Relevant to the topic of this thesis, the experimental studies for low-speed impacts under artificial two-dimensional low-gravity created on a table showed different results for different impactors. For instance, Calsamiglia et al (1999) found disk-type impactors show relatively high CoR with no variation to impact angle [76]. For square impactors, Nishiura & Sakaguchi (2014) observed an inverse linear relation with target properties similar to impact angle [77]. In a full 3D experiments for the MASCOT lander, Biele et al. (2017) observed CoR values that vary between 0.2-0.8 with no visible trend [41]. These experiments show both a lack of robust understanding of the post-impact behavior of a rigid body, especially when it is nonspherical, and in low-speed impacts under low-gravity. For example, it remains unclear whether CoR has any relation with impact velocity, angle, and attitude for nonspherical impactors under conditions relevant to small-body environments.

In this chapter, the experimental data obtained in the low-speed impact experiments under artificial low-gravity, performed by Van wal et al. (2019) [78] is analyzed to investigate trends in the coefficient of restitution. Specifically, the dependency of the coefficient of restitution as a function of impact velocity, angle, and impact attitude is sought under conditions relevant to small-body environments. Through the data

of a total of ~2500 experiment runs, the experiments that will be presented in the following sections provide the abundance of impact data that is lacking for nonspherical impactors at low-speed impacts.

3.2 Methods

3.2.1 Experimental setup

The experiments were performed with a cuboid air-bearing assembly under near-frictionless, two-dimensional artificial low-gravity conditions created on a table. This relatively simple setup provides an inexpensive alternative to microgravity platforms such as parabolic flights and drop towers. It also replaces the complexity of three-dimensional impacts with far more controllable two-dimensional impacts. Controlled and repeatable release of the air-bearing assembly is achieved using a switchable magnet. This lander is accelerated along the inclined table towards a cement block that acts as analog for a hard asteroid surface, as shown in Fig. 3.1.

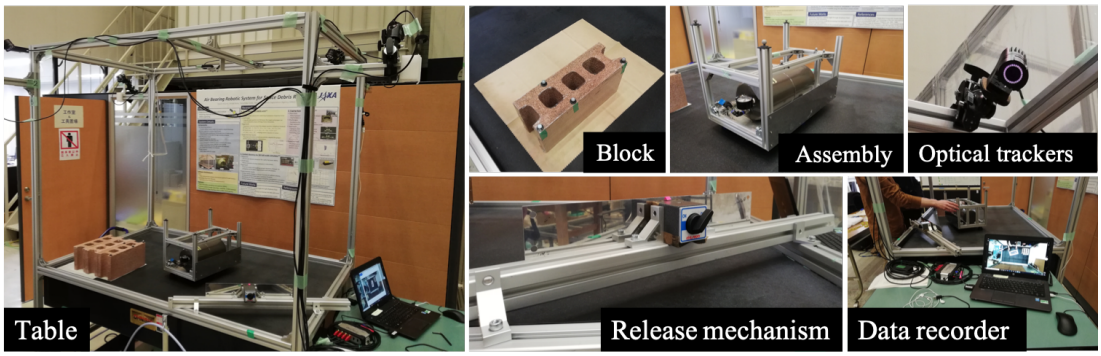

Figure 3.1: Experimental setup.

The following subsections provides a detailed overview of the each element depicted in Fig. 3.1 and the data obtained and how it is handled.

3.2.2 Setup

The experimental setup consists of the following elements, also shown in Fig. 3.1:

- *Smoothed granite table.* The experiments are performed on a smoothed granite block of 1.5 m x 1 m in size. The table can be inclined to provide the necessary acceleration, as will be explained more in detail in the next subsection.

- *Air-bearing assembly.* The air-bearing assembly used as the lander in this study is a rectangular-prism-shaped structure, built with aluminium supporting rods whose base dimensions are 400 mm x 250 mm. The height of the assembly is variable due to the placing of optical tracking markers at non-symmetrical positions. The assembly also includes an air tank and three air bearings through which air is supplied to levitate the assembly and enable a near-frictionless motion on the smoothed table. The mass of the assembly is 6.00 ± 0.01 kg. The mass-normalized moment of inertia value that is obtained from the CAD model is 0.0226 m^2. Note that the CAD model does not include tubes that connect the tank and the air-bearings, and the actual shape of the tank, however this value is very close what was found from the experimental data.

- *Release mechanism.* The release mechanism is based on a switchable magnet. The magnet was mounted on a aluminium alloy bar of same material as the air table structure and the floating assembly. This material is not magnetic, therefore a SUS430 magnetic steel alloy plate of 400 mm x 100 mm in size and 0.5 mm is thickness is mounted in front of the magnet. A matching steel plate was mounted on the assembly, as well. During the experiment runs, one has to switch the magnet from “ON" configuration, where the assembly is attracted to the release mechanism, to “OFF" configuration where the magnetic attraction ceases and the acceleration begins because of table inclination. The switchable-magnet-based release mechanism provides a controllable, albeit limited, and affordable solution to release of the lander. It avoids the uncertainties and complexities of more sophisticated systems, such as spring-based release mechanisms which are prone to show directional errors, or electromagnets which require computerized control to impart desired force.

- *Hard surface.* Generic cement bricks were used to represent hard surface. In general, two or three blocks were used in conjunction to support the impacted brick (depending on the available free space on the table) in order to avoid

vibrations and motion due to momentum imparted during an impact. The bricks are covered with tape to prevent chipped block particles scattering onto the granite table after impact. For the same purpose and to avoid damage to the table, an anti-slip sheet was placed under the blocks.

- *Optical tracking.* The assembly was tracked with the OptiTrack^{TM} Motion Capture System. The system operates with four optical cameras placed in the top corners of the table structure. These synchronized cameras capture 3D position and attitude information of the target by tracking reflective markers relative to a table-fixed reference frame defined within the data recording software. Six markers are mounted on the assembly in an asymmetrical configuration in order to avoid multiple attitude solutions that could be encountered in otherwise symmetrical configurations. Markers were also placed on the impacted block to define a contact plane and surface normal, and to verify that the block does not move during impact.

3.2.3 Reference frames

The tracking markers on the floating assembly and block are used to define various reference frames used in the tracking software and data analysis. A total of four frames is used, with the table frame $\boldsymbol{T}$ as main frame in which the marker positions are expressed. The other three frames appear exclusively in the data analysis process. The four frames are illustrated in Figure 3 and are defined as follows:

- *Table frame* $\boldsymbol{T}$: The origin of this inertial frame is defined at a reference point on the side of the granite table. The z^T and x^T axes span the long and short dimensions of the table, respectively, with the y^T axis completing the orthonormal triad and pointing out of the page. In this frame, the gravitational acceleration along the inclined table acts along the $+z^T$ direction. This frame is shown in red in Fig. 3.2.

- *Mechanical frame* $\boldsymbol{M}$: The origin of this moving, rotating frame is equal to the A_3 marker. The x^M axis points from marker A_3 to marker A_2, while the y^M axis is equal to the table-frame y^T axis. The z^M axis completes the orthonormal triad. This frame is shown in green in Fig. 3.2.

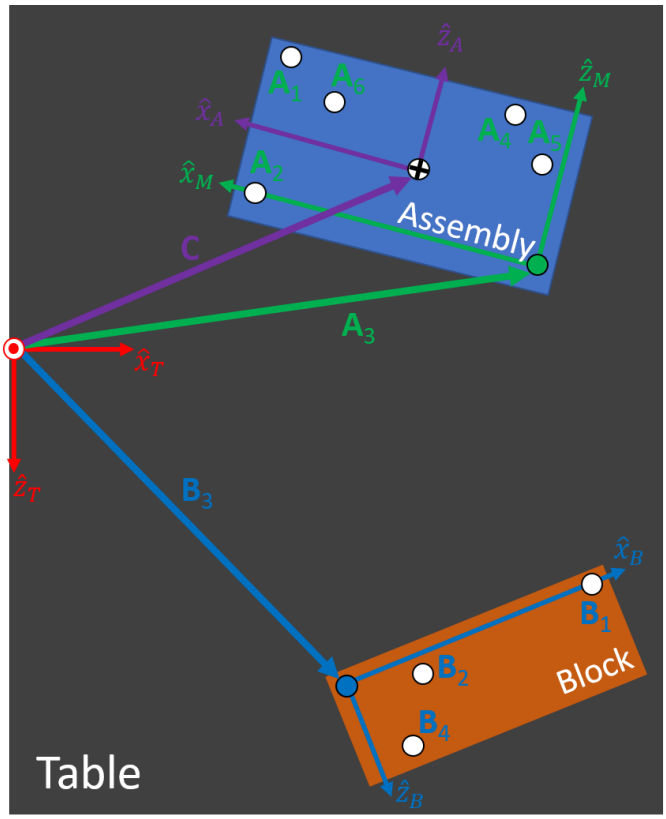

Figure 3.2: Reference frames used in this study

- *Assembly frame* ***A***: The origin of this moving, rotating frame is equal to the assembly center of mass, as defined by the ***C*** vector in Fig. 3.2. The x^A, y^A, and z^A axes are equal to the ***M***-frame axes. This frame is shown in purple in Fig. 3.2.

- *Block frame* ***B***: The origin of this moving, rotating frame is equal to the B_3 marker. The x^B axis points from marker B_3 to marker B_1, while the y^B axis is equal to the table-frame y^T axis. The z^B axis completes the orthonormal triad. This frame is shown in blue in Fig 3.2.

3.2.4 Test cases

Landings observed in small body environments occur at relatively low speeds but with a variety of impact conditions, due to the low-gravity environment. As the most recent example, the surface acceleration of Ryugu, the target of Hayabusa2 spacecraft,

is $a \approx 0.15$ mm/s^2 [59] or $a \approx 1.25 \times 10^{-5}$ Earth g. In this environment, the cover of the MINERVA-II-1A/B hoppers experienced speeds ≈28 cm/s at impact [79]. This is a relatively high impact speed, given that the surface escape speed of Ryugu is about ~36 cm/s. Landing speeds of similar order of magnitude were also observed during the NEAR, Hayabusa, Rosetta, and OSIRIS-REx missions [80, 81, 21]. Therefore, experiments here are aimed to be performed at the impact conditions relevant to small body landings.

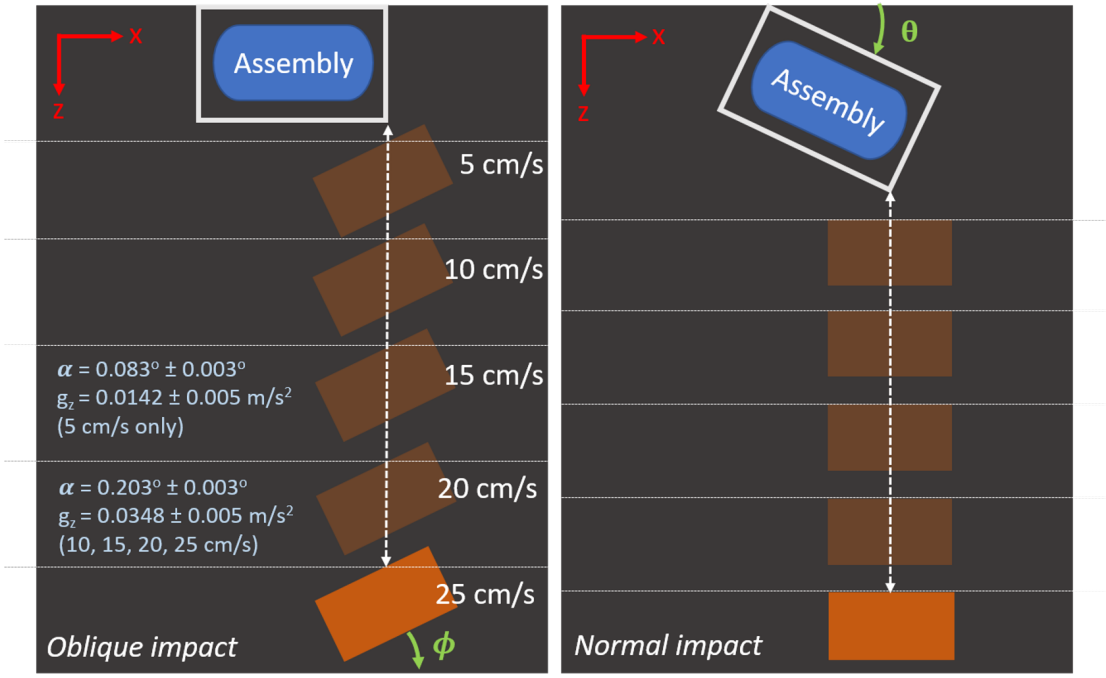

Figure 3.3: Illustration of (*left*) normal and (*right*) tangential impact experiments. The transparent landers illustrate how cross-track velocity deviations affect the impact location.

The experiments performed in this work attempt to address these varying conditions. Two main test cases, as illustrated in Fig. 3.3, are considered. In both cases, the smoothed granite block is inclined to accelerate the air-bearing assembly in z-direction (hereafter, along-track direction) until the impact occurs, as the magnetic release mechanism in principle does not provide any deployment speed. In addition to the table inclination, three other parameters, one distance and two angles, are varied. For a given table inclination, the desired impact speed is achieved by varying the distance of the

Table 3.1: Parameter space covered in the experiments

Parameter	Value	
Inclination [deg]	0.083	0.203
Impact speed [cm/s]	5	10, 15, 20, 25
Impact angle [deg]	20, 40, 60, 75	
Attitude angle [deg]	20, 40, ~60, 75	

impacted block to the air-bearing assembly, d. In the oblique impact case shown on the left figure in Fig. 3.3, the angle of the block with x-axis (hereafter, cross-track direction), α is varied in order to generate impact cases that has a tangential velocity component with respect to the normal direction of the block (or the impacted surface). This is the case where the effect of impact angle was tested for a fixed lander attitude. On the other hand, the effect of lander attitude was tested by varying attitude angle θ for the impact velocity vector parallel to the block normal. The attitude angle θ was varied by moving the release mechanism along-track and cross-track directions as illustrated in Fig. 3.3. The parameter space of the experiments are tabulated in Table 3.1.

Five impact speeds were considered in the experiments: 5, 10, 15, 20, 25 cm/s. These impact speeds are achieved at the measured table inclination values $i = 0.083 \pm 0.003\ ^o$ and $i = 0.203 \pm 0.003\ ^o$. As shown in Fig. 3.4 for a general case of table inclination between 0 to 0.5^o, this provides effective acceleration of $a = 0.0142 \pm 0.005$ m/s^2 and $a = 0.0348 \pm 0.005$ m/s^2 or 1.5 milli-Earth-g and 3 milli-Earth-g, respectively. Former inclination value is only used for the 5 cm/s impact case in order to prolong the acceleration time for better data resolution. The impact speeds in Table 3.1 are controlled by placing the cement blocks at distances where the lander along-track velocity reaches those values. To identify the distances, the assembly was accelerated freely towards the end of the table and the collected data was analyzed.

In the tangential impact case, four impact angles were tested, from nearly normal $\theta = 20\ ^o$ to grazing $\theta = 75\ ^o$ impacts. Initial observations showed that impacts at $\theta = 80\ ^o$ would be hard to distinguish in the data, therefore the highest impact angle was restricted to $\theta = 75\ ^o$. On the other hand, four attitude angles were set for the normal impact. In this case $\phi = 80\ ^o$ was not considered because the release configuration is almost parallel to the along-track direction. It was observed that the release becomes inaccurate at this angle, often resulting in undesired torque at release due the residual

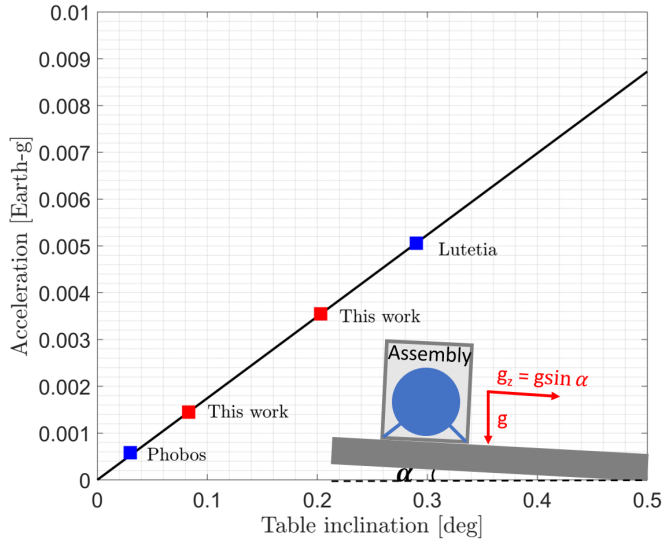

Figure 3.4: Effective acceleration as a function of table inclination.

magnetic attraction. It is important to highlight the special case of $\theta \approx 60\ ^o$ in the normal impact case. An impact at this attitude is a *central impact* where the normal force acts through the center of mass (CoM) and produces no torque on the lander. In such a case, the friction force does not act, hence it allows to measure the coefficient of restitution independently. The impacts at this attitude were tested within a range of values within $\theta = [59, 63]\ ^o$ and a suitable value was selected for each batch of runs.

3.2.5 Center of mass estimation

As the impact models are assessed for rigid bodies, it is important to know the center-of-mass (CoM) of the body. This information was not available a priori for real shape of the mock lander but some reduced CAD drawing. In order to find the CoM location on the lander, a *free rotation* test is performed. In this case, the lander was given a small “kick" on a flat table while air-bearing are open to generate low friction. The initial kick makes the lander move and rotate at the same time. In principle, as a rigid-body rotates around its CoM, this point would follow a parabolic trajectory following Newton’s law. On the other hand, any other point would follow a *epicycle*-like motion due to the existing rotation, as shown in Fig. 3.5.

In Fig. 3.5, rectangular shape represents the lander as seen from top. Red circles

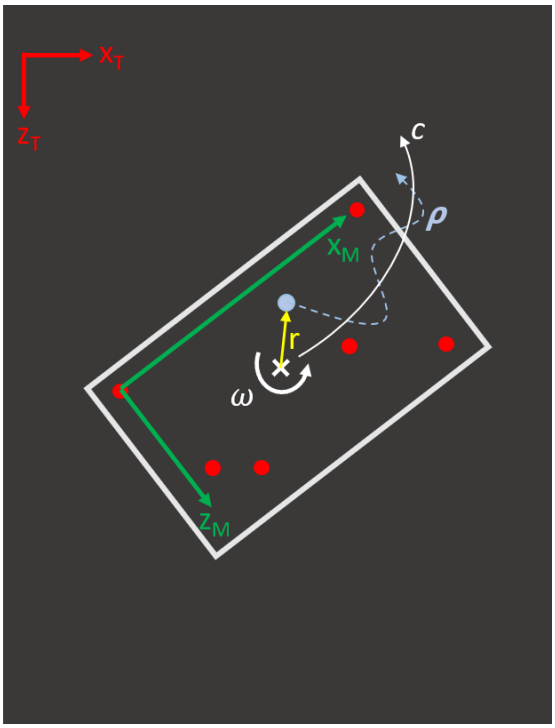

Figure 3.5: Illustration of center-of-mass motion

within the lander are approximate marker location as explained earlier. The lander position information is given in a global reference frame centered somewhere on the table which can be used to build a mechanical reference frame centered on one of the markers to track motion at that mechanical frame. The mechanical frame is also shown in Fig. 3.5, centered on marker 3, with x-axis defined through vector connecting marker 3 to 2, y-axis pointing out-of-table, and z-axis completing the triad. In the table reference frame, the CoM motion can be described with simple *free fall* equations:

$$\mathbf{c}(t) = \mathbf{x}_0 + \mathbf{v}_0 t + \frac{1}{2}\mathbf{a}t^2 \tag{3.1}$$

In Eq. 3.1, $\mathbf{x}_0$ and $\mathbf{v}_0$ denote initial position and velocity of the CoM, and $\mathbf{a}$ is the acceleration. The CoM position is sought primarily according marker 3 where the mechanical frame is centered. A point that at $\mathbf{r}$ distance from this point would exhibit a motion in table frame that can be described as follows:

$$\rho(t) = \mathbf{c}(t) + [TM]\mathbf{r} \tag{3.2}$$

where $[TM]$ is transformation matrix from mechanical to table frame, created from the measurements. If the position measurement of marker 3 is denoted as ρ^*, then the following cost function can be minimized to find the CoM position $\mathbf{r} = [\mathrm{u}, \mathrm{v}]^T$ vector with respect to marker 3 as:

$$rms = \sqrt{\frac{\Delta\rho^T \Delta\rho}{N}} \tag{3.3}$$

where $\Delta\rho = \rho - \rho^*$.

The CoM position that minimizes Fig. 3.3 was found by using MATLAB's built-in unconstrained optimization function `fminunc` with optimality tolerance of 10^{-6}. Note that although $\mathbf{r}$ is defined from the mechanical frame origin marker 3, it can also be defined for other markers. According to the outlined procedure above, $\mathbf{r}$ vectors found in twenty free rotation runs can be found in Fig. 3.6.

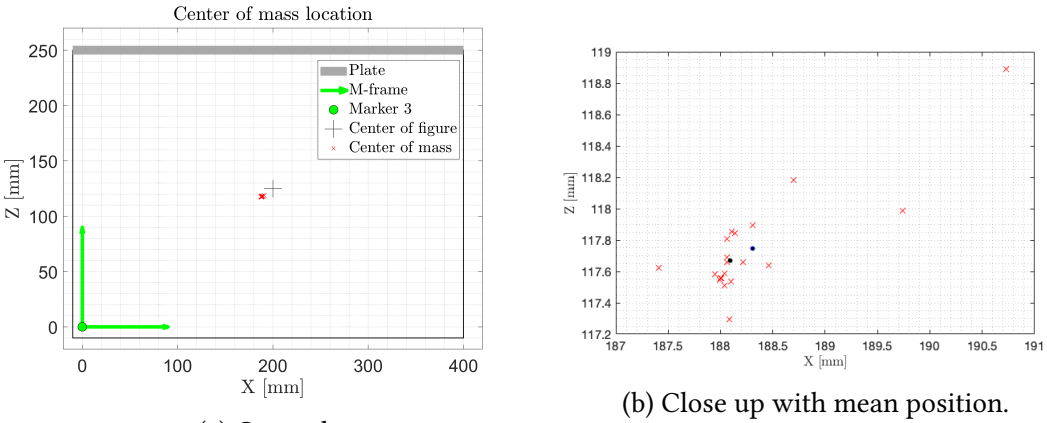

(a) General

(b) Close up with mean position.

Figure 3.6: The center-of-mass position in mechanical frame centered on Marker 3

While the most points are clustered a region, few outliers can be found. After removing outermost outlier, the CoM position in mechanical frame is [188.1, 117.6] ±1 mm and lies roughly 3 mm away from center-of-figure given by the optical tracking software. This information will then be used to analyze rigid-body motion data obtained during the experiments.

3.2.6 Data processing

As mentioned earlier, optical tracking process position information of each placed marker and and additional center-of-figure position for a defined object by selecting markers. The tracking software also provides attitude information of this center-of-figure, but this information is not used during this study and attitude is computed during post-processing from the collected position measurement. Figure 3.7 depicts a typical optical tracking data, acquired during one of the runs.

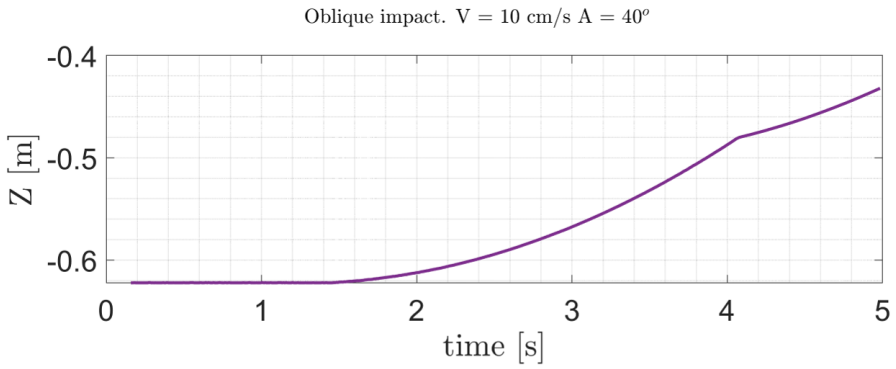

Figure 3.7: Typical raw position data in experiments.

As the motion is restricted to xz-plane, that is to say, as there is no out-of-plane component of the lander motion, y-component of the position only varies in sub-mm level, possibly due to uneven inclination of the table or vibration of the structure. In general, three main phases can be identified from the data: *pre-release*, *pre-impact* and *post-impact*. Most runs have this three main phase, some runs differ. Specifically, some data include pre-release adjustment of the lander assembly, and some include secondary impacts before data recording is terminated. An example of this can be seen in Fig. 3.7. For robust and automated data processing, those parts of the data are excluded from raw data manually.

If friction, air resistance, uneven table inclination and other unmodelled dynamical effects are ignored, the lander assembly is only subject to the *effective* gravitational acceleration along the inclined table. Therefore, the CoM motion performs virtually *free-fall* motion. Looking at the data, this is predominantly true the alongtrack direction (*i.e.*, along z-axis), with some residual motion in the crosstrack direction (*i.e.*, along x-axis), as well. This is also true for post-impact motion. The pre- and post-impact

motions can therefore be found by fitting second order polynomials to measurement data as follows:

$$\begin{aligned} \mathbf{X}^{-}(t) &= \mathbf{X}_0^{-} + \mathbf{V}_0^{-} t + \frac{1}{2}\mathbf{a}_0^{-} t^2 \\ \mathbf{X}^{+}(t) &= \mathbf{X}_0^{+} + \mathbf{V}_0^{+} t + \frac{1}{2}\mathbf{a}_0^{+} t^2 \end{aligned} \tag{3.4}$$

The assembly pre- and post-impact velocity expressions are simply the derivatives of Eqs. 3.4 as

$$\begin{aligned} \mathbf{V}^{-}(t) &= \mathbf{V}_0^{-} + \mathbf{a}_0^{-} t \\ \mathbf{V}^{+}(t) &= \mathbf{V}_0^{+} + \mathbf{a}_0^{+} t \end{aligned} \tag{3.5}$$

In order to determine correctly fit the polynomials to measurement data and find impact timing, the raw data is first filtered. To do that, a second order Savitzky-Golay filter is utilized through MATLAB's `sgolayfilt` function with framelength 31. The Savitzky-Golay filter is a digital filter that is used to smooth the data without distorting signal's general tendency. It works by fitting polynomials to successive subsets of digital signal with linear least squares method [82]. Second order filter is selected because the free-fall motion exhibits second-order polynomial, whereas the framelength value is selected through trial and error among multiple odd values, as the method requires. The velocity values, or derivative of the position data, is *not* obtained via finite differences not to amplify the existing errors, but instead obtained via convolution by using MATLAB's `conv` function. Through which a relatively smooth signal is achieved, as shown in Fig. 3.8.

Figure 3.8 shows three-main parts of the data, pre-impact, impact and post-impact. The manual data-clipping is also shown as exclusion regions. In addition to those, there is a transition region after the release where, due to the residual magnetism and the vibration at the separation, the lander receives an additional *acceleration* that increases the velocity in a shorter time, before it accelerates steadily towards the block. This transition region can be seen in the bottom plot in Fig. 3.8. Because of the existence of the transition region, the pre-impact fitting was started from some initial velocity instead of $\mathrm{V}_0^{-} = 0$. That initial velocity was intuitively selected to be $\mathrm{V}_0^{-} = 0.2 \cdot \mathrm{V}_{exp}$, where V_{exp} is the expected impact speed of the experiment run of interest.

Impact time of a free-falling object under a given gravity acceleration can be computed analytically. The actual acceleration time under non-ideal experiment

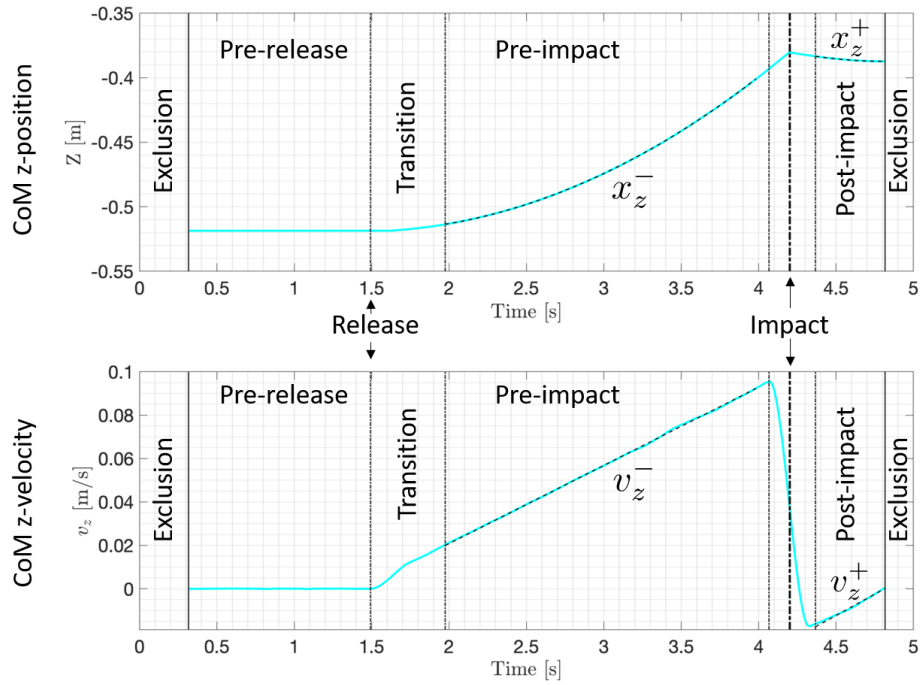

Figure 3.8: Typical processed experiment data.

conditions would be different than the nominal value, but within some bounds that also include the nominal impact time. The bounds are defined within ±20% of the nominal impact time of experiment run. The pre-impact and post-impact fits are performed up from beginning to the lower bound and from upper bound of the impact time to end time, respectively. The impact time can then easily be founded from from the common solution for pre- and post-impact parabolic equations as provided in Eqs. 3.4. The solution would give two roots, one of which must fall into the bounds of impact time. This value could also be verified by finding the common solution of pre- and post-impact linear equations for the velocity data. After the parabolas of pre-impact and post-impact motion are found, the velocity and acceleration can be found as the first and second derivatives of the fitted parabolas. After impact time is found, the cross-track and attitude motions can also be easily fit in a similar fashion. As a side note, the parabolic fits were found with MATLAB's `fit` function, which only outputs coefficients of parabola, among other data of choice. Saving and using only those coefficients for each run and impact time reduce data overhead during

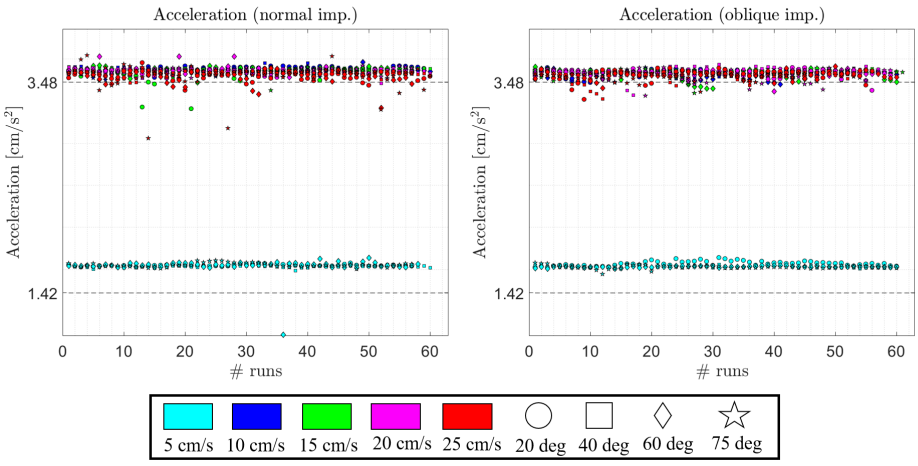

Figure 3.9: Effective acceleration. Left: Normal impacts. Right: Oblique impacts

post-processing significantly. In the following section, the outcome of this fits are going to be presented in the form of pre- and post-impact conditions.

3.3 Error analysis

One of the key aspects of these experiments is low-gravity. As noted in the previous section, the theoretical nominal acceleration is 0.0142 m/s^2 for the 5 cm/s case, and 0.0348 m/s^2 for the other impact velocities from the table inclination. The inclination was set by manually tightening and loosening bolts in the structure holding the table. The inclination were also measured in at least nine different points across the table every day of the campaign. However, uneven inclination, residual magnetism and vibration at the release may cause effective acceleration to deviate from the expected nominal. Figure 3.9 therefore quantifies effective acceleration achieved during the all experimental runs both normal and oblique impact cases.

The reference lines in Fig. 3.9 marks theoretical nominal values respectively. Despite a couple of outlier cases, a consistent acceleration values were achieved in overall in both test cases. It can be seen that there is a bias from the theoretical nominal values on average on both cases, when one removes the outlier cases. The bias is more

prominent in the smaller acceleration value. As also noted in the previous section on data processing, there is a nonnegligible push from the release mechanism due to vibrations which could be factor in this bias. Although unquantified at this point, the region of the table where the 5 cm/s case could have a steeper inclination, which may not be cancelled out as the impact distance is just about ~8 cm. The bias in effective acceleration would naturally decrease the impact time calculated with the theoretical nominal value, whose results are presented in Fig. 3.10.

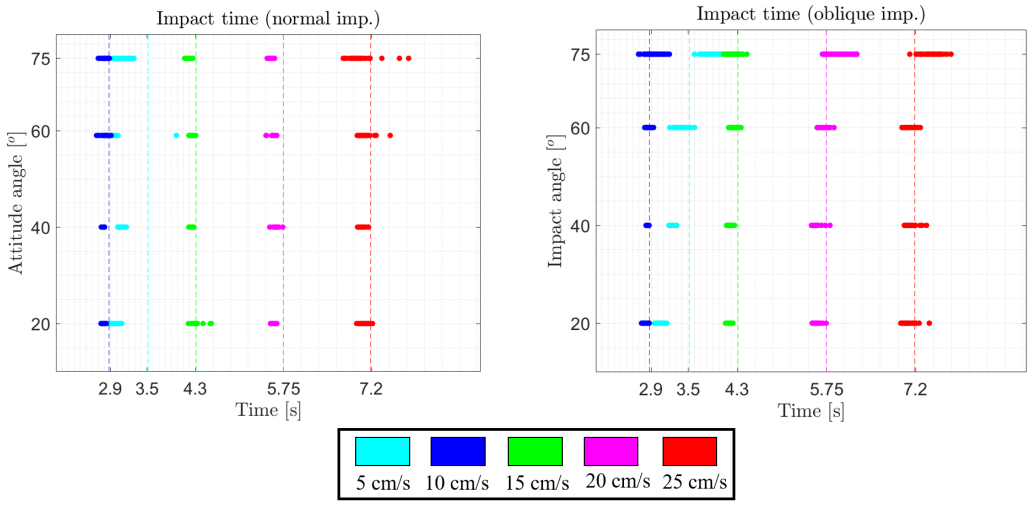

Figure 3.10: Impact time. Left: Normal impacts. Right: Oblique impacts

The vertical lines in Fig. 3.10 mark expected thoretical expected impact times. Note that the 5 cm/s cases have theoretical impact time less than the 10 cm/s case due to lower effective acceleration. In general, the inference from effective acceleration values are correct that the impact occurs earlier than expected. However, there are exceptions to that, especially in the higher impact angle cases in the oblique impacts. There is a visible delay in impact time, and in some cases it occurred in all runs of that particular case. This is primarily caused by the block alignment. As explained earlier, the block angle is set to the impact angle to achieved. At steeper angles, the block movement through the runs is visible especially at higher speeds. This results in impacts occurring at different locations on the block, delaying the impact time in

general. As more impacts occur at these steeper angles, the block angle becomes steeper,as it will be shown later, causing further delays in impact time. The problem is combined with initial attitude and rotation errors induced by the mismatch in the alignment of the steel plates. Regular setting the block to its original position solved the problem to a certain extent but did not diminish it completely. To that end, Fig. 3.11 shows how block attitude varied for oblique impacts in all valid experimental runs.

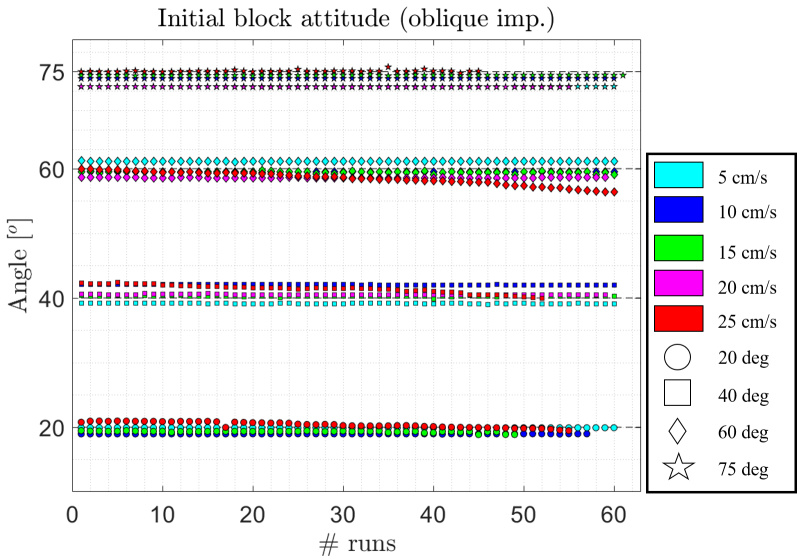

Figure 3.11: Block attitude throughout the experimental run. Oblique impacts.

The block attitude appeared to be achieved within $\pm 3^o$ in oblique impacts, and in general kept steady throughout the experiments, except highest velocity impacts. Indeed one can see clearly that there is a deviation from initial block angle at the 25 cm/s cases. The highest of those is about 3^o at the 60^o case. This deviation is partially the reason in delay in the impact time.

In the normal impacts, on the other hand, the block attitude needs to be at 0^o with respect to table frame. The results of the block attitude in the normal impact case is presented in Fig. 3.12.

The block was kept within $\pm 2^o$. For the most of lower-velocity impacts the values were actually kept within $\pm 1^o$. Similar to the oblique impacts, the largest deviations occur in the highest impact velocities. The manual corrections to the block angle can be observed in the figure as sharp drop in the angle value after continuous increase.

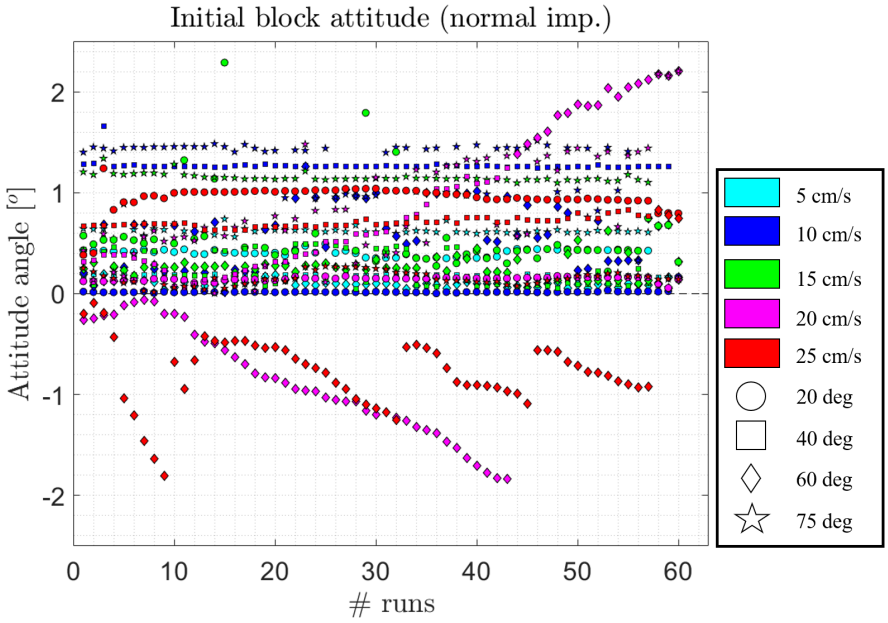

Figure 3.12: Block attitude throughout the experimental runs. Normal impacts.

The deviation in block attitude ultimately means nonzero or 90^o impact angle, which results in small deviations in the post-impact behaviour, as it will be discussed in the next subsection. But before that it is reasonable to discuss angular velocity at impact, as well, whose results are provided in Fig. 3.13.

In general, impact angular speed is controlled within $\pm 2^o$ for both test cases, but slightly better in oblique impacts. Majority of the clustered around around the targeted value. If friction is assumed to be negligible during the acceleration phase, then that could be assumed as the angular speed error at the release. The value is quite small; however, it should be mentioned that 1^o angular speed error over the course of ~7.5 seconds, *i.e.*, the maximum impact time observed in Fig. 3.10, this would result in ~7.5^o attitude error at impact.

3.4 Results

Impact process is assumed to be instantaneous throughout this study. In order to justify this assumption, three different approaches are taken. First, a qualitative analysis is performed by investigating images from videos of experiments. To do that, a 0.1-sec

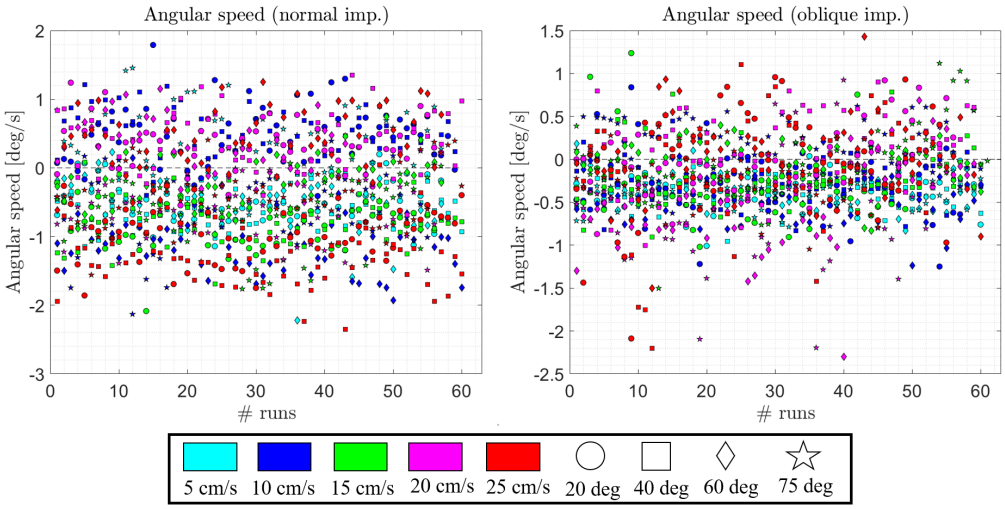

Figure 3.13: Angular speed at impact. Left: Normal impacts. Right: Oblique impacts

snippet is taken from all available videos, approximately before, during, and after impact. It is then decomposed into 4 images (at t = 0, 0.033, 0.066, and 0.1 sec), and then each image is observed to detect contact and separation. An example is shown in Fig. 3.14.

Figure 3.14 requires a careful analysis to identify contact separation and the contact process is more apparent when images are collected into an animated form. Nevertheless, one can see that in between t = 0 sec to t = 0.033 sec, the contact appears to happen. It ceases some time point between t = 0.066 sec to t = 0.1 sec. This suggests a contact duration less than 0.1 sec, and probably some time ~0.5 sec.

To further confirm this impulsive-contact claim, assembly velocity is calculated via finite-difference method from discrete position and time information. The timestep between two measurements, Δt, equals to 0.083 seconds, hence velocity at time point, v_i (i = 1, 2, ..., n), can be found from the raw data as $v_i = \Delta x_i / \Delta t$, where $\Delta x_i = x_{i+1} - x_i$. The finite-difference velocity information from the example run in Fig. 3.7 is presented below in Fig. 3.15.

Even though finite-differencing the position data results in a noisy velocity information, it avoids artifacts of data filters, in which data smoothing may appear as long contact duration as it will be shown later. According to the left panel in Fig. 3.15,

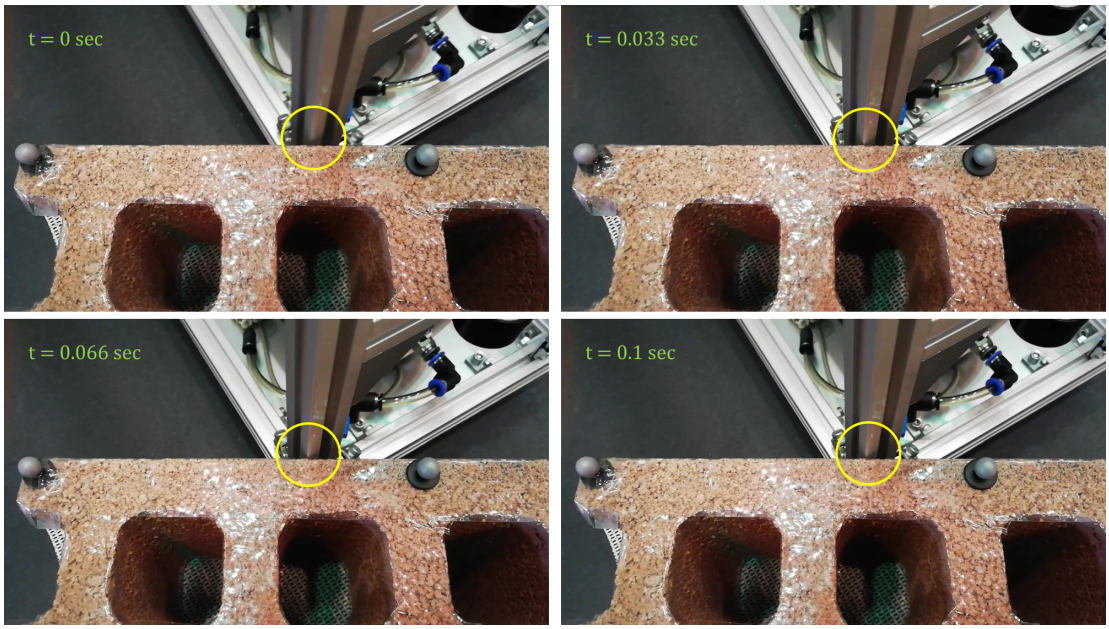

Figure 3.14: Impact process. Impact case unknown.

impact occurs in around 8.73 sec, after which velocity decreases sharply within 0.05 sec to ~10 cm/s and increases again with the along track assembly motion. Therefore, it is believed that contact in this impact experiment occurs within 0.05 sec. For similar impact experiments under Earth gravity, impacting objects with velocities in the range of impact velocities considered here was observed to stay in contact with surfaces between 0.15-0.6 msec for two impacting spheres of same sizes, depending on material and impact velocity [83]. The quantitative results obtained in the impact experiments here suggest a higher contact duration, which may be related to reduced effective acceleration.

A contact process can be approximated as impulsive if the orientation change during the contact is negligible. A simulation of the contact process is performed to demonstrate minimal attitude change during the contact process. An illustration of the simulated system is provided in Fig. 3.16.

In the simulations, a normal force is applied to the contact point with associated friction. The contact point velocities and rotation are computed under the normal and frictional impulse and the torque generated by those. The simulations are performed only for normal impacts at all impact speed and attitude angle values and for a duration

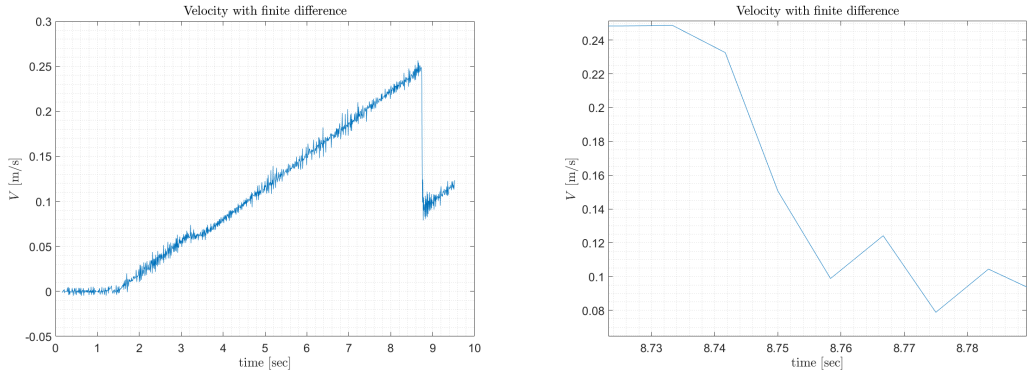

(a) General (b) Zoomed-in.

Figure 3.15: Finite-differenced center-of-mass velocity. Normal impact, V = 25 cm/s, θ = 20^o.

of 0.1 sec. The coefficient of restitution and friction are assumed as 0.3 and 0.45, respectively. One limitation of this model is the magnitude of normal impulse. It is not known how much of the initial impact energy is lost to the surface upon impact, and how much is given back to the impactor. In the absence of this information, it is assumed that the response of the surface is perfectly elastic. This will result in an exaggerated rotation. If, even in this exaggerated rotation behavior, attitude does not change significantly, then it can be safely assumed that the contact is impulsive. Rotation and attitude evolution of the lander assembly is provided in Fig. 3.17.

In the end of the simulations, qualitative rotation behaviour observed in the experiments were confirmed with the simulations. Yet the attitude change is within 1^o and that was only observed in the 20^o-attitude case where the rotation is the highest in experiments. Therefore, it is believed that the impulsive contact approach should be sufficient for the impact case considered. In simulations, a gravity dependence of rotation is identified in the 5 cm/s impact case in which a significantly low rotation is observed compared to the other cases. However, this difference was not exactly observed in the experiments, as it will be shown in the next section. Recall that two gravity levels in this study are on the same order of magnitude; hence, in the presence of other energy sinks in the process, including energy dissipated to the surface or lost to vibration, the gravity effects may be less effective.

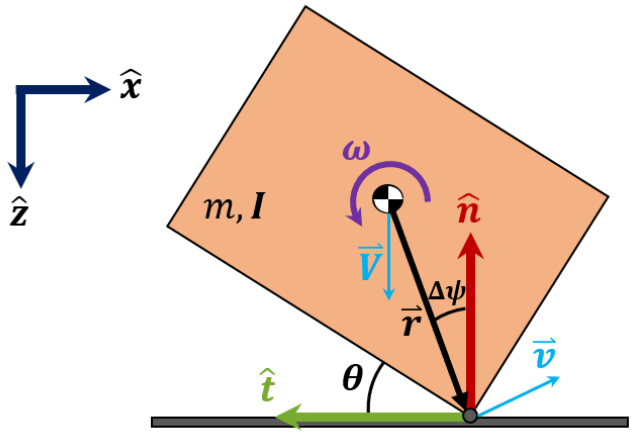

Figure 3.16: Simulated system for contact duration

3.4.1 Pre-impact conditions

Figure 3.18 shows pre-impact speed results in normal impact experiments for both along-track and cross-track motion. As the motion was primarily targeted in z-axis, the targeted pre-impact speeds are of interest which was shown in Fig. 3.18a. It appears that the impact speed was controlled within ±1 cm/s in all target impact speeds. On the other hand, attitude angle θ does not seem to be as accurate. The θ values worsen for impact speeds higher than 10 cm/s. In the 5 and 10 cm/s cases, the attitude error was constrained to be within $\pm 6^o$. As the impact speed increases. the attitude precision worsens. For instance, in the observed worst case of 25 cm/s at 40^o, the attitude angle at the impact is always below 40^o and spans down to 25^o. This is primarily due to the initial attitude errors, residual rotation at the release, as well as the other uncertainties that may not be modelled, which propagate longer for high impact speeds due to the design of the setup. Figure 3.18b on the right depicts the deviation in the cross-track velocity and the lander attitude from from the expected value. It can be seen that the attitude deviation is smaller in low-speed and greater in high-speed impacts. The impact speed, on the other hand, is a lot more precise constrained within ±0.5 cm/s.

The impact conditions in the oblique impact cases are presented in Fig. 3.19. The opposite case of normal impact is seen in along-track results, as shown in Fig. 3.19a. This time the impact angle was very precisely controlled within $\pm 2^o$ across all impact speeds. It is not alwats the case the targeted impact angle was achieved. For instance,

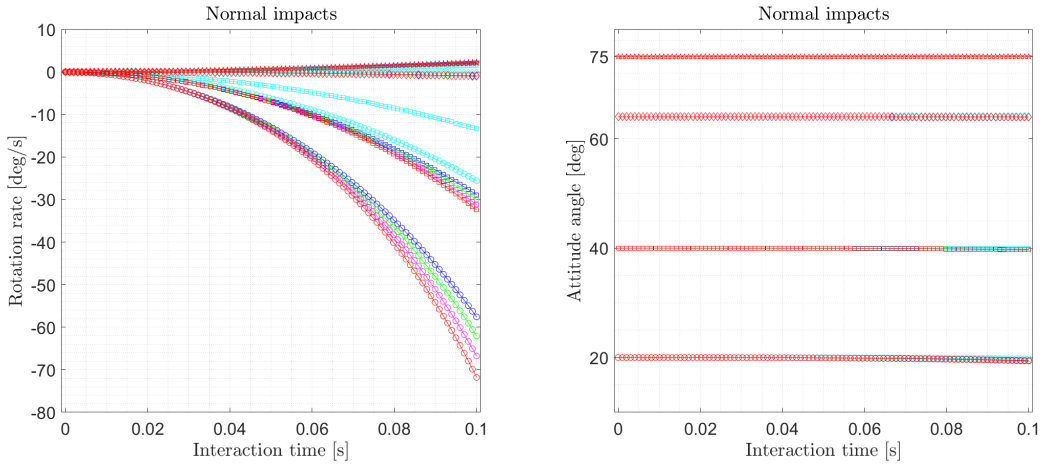

(a) General (b) Zoomed-in.

Figure 3.17: Rotational and attitudinal evolution of lander assembly during contact

at 10 cm/s-40^o impact case the impact angle is well-constrained but around 42^o. The fact that the achieved angle is different than the targeted is not detrimental to the results, as in this case the achieved impact is very well constrained to 42^o. On the other hand, impact speeds also seem to be well-controlled until the highest value, *i.e.* 75^o. Although the deviation is more prominent at the highest impact angle, it appears to start 60^o impact angle and at higher impact speeds. The block orientation at 60^o and 75^o, especially in the latter value, the block is almost parallel to the along-track direction. This causes impacts to be often grazing the surface, which results in variations in the detected impact speed due to the implemented post-processing method. However, the primary reason for the variation is the initial imprecision in cross-track velocity, which propagate longer as the targeted impact speed increases. As a result, the lander impact point differs. That is to say, some runs take longer to impact, which increases the final impact speed. This is somewhat evident at 75^o impact angle at different impact speeds; the variation seems to increase as the impact speed increases.

3.4.2 Post-impact trends

Investigating post-impact velocities thoroughly also sheds light on the post-impact trends on the motion. But before presenting the trends in post-impact motion, it is reasonable to provide a recap of rigid body motion and contact dynamics. First of all,

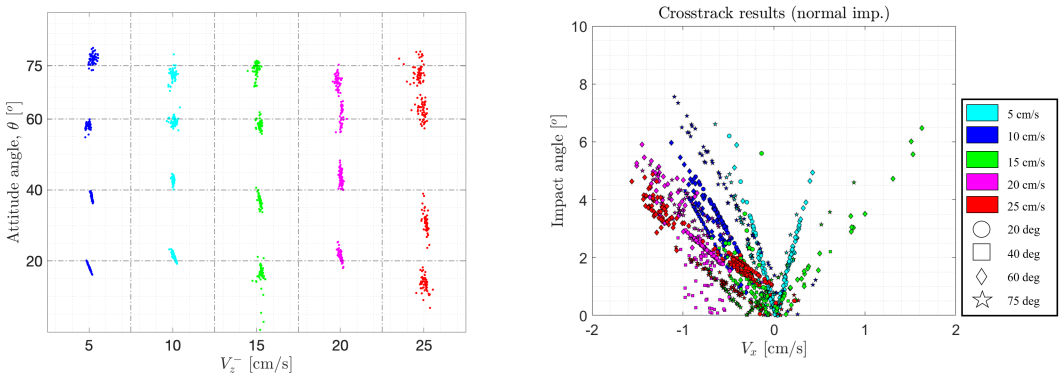

(a) Along-track (b) Cross-track

Figure 3.18: Normal impact pre-impact velocity results

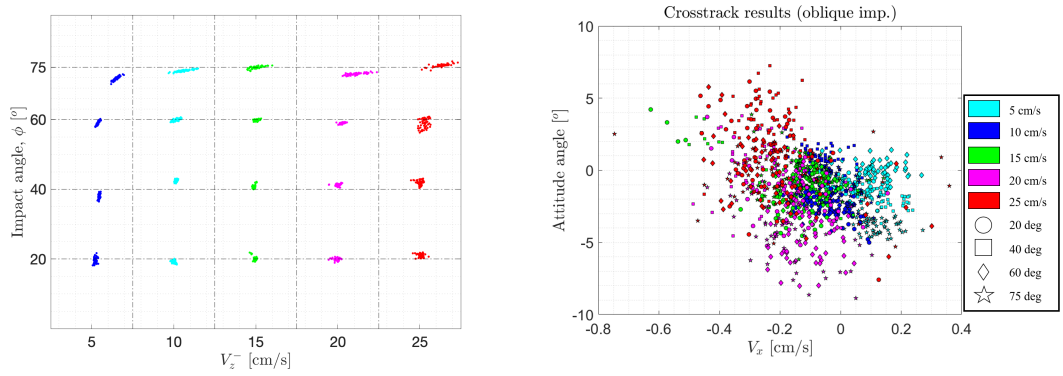

(a) Along-track (b) Cross-track

Figure 3.19: Oblique impact pre-impact velocity results

the center-of-velocity (CoM) velocity of a rigid-body, $\mathbf{V}$ is written as

$$\mathbf{V} = \mathbf{v} + \omega \times \mathbf{r} \tag{3.6}$$

where $\mathbf{v}$ denotes velocity of corner that is impacting, ω denotes angular velocity and $\mathbf{r}$ is position of impacting corner point from the CoM. If pre-impact angular velocity is ignored as targeted in this experiment campaign, the second term in the right hand side would be zero, *i.e.*, $\mathbf{V} = \mathbf{v}$. Angular velocity in post-impact is generated via torques induced by normal and frictional impulses. Frictional impulse would only do work when there is nonzero tangential velocity. And in general, torques are only generated

when the impact is noncentral, as illustrated in Fig. 3.20.

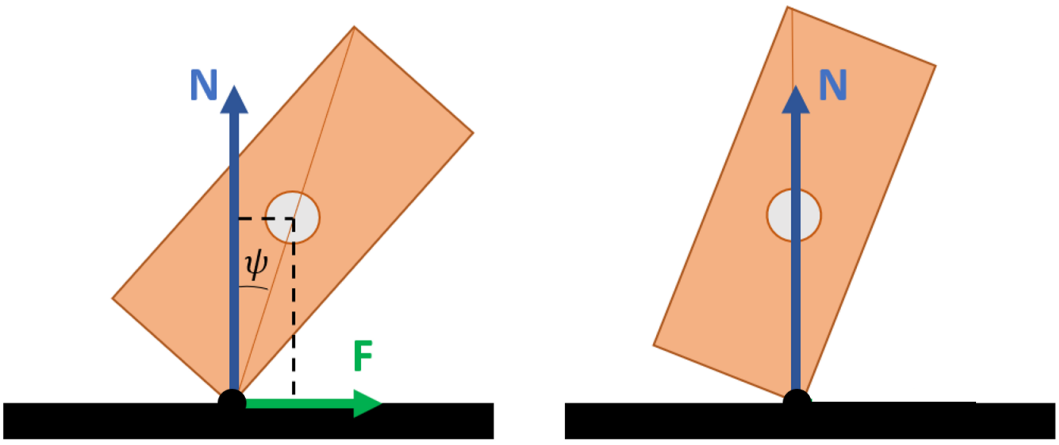

Figure 3.20: Impact configurations. Left: Noncentral impact. Right: Central Impact.

As shown in the illustration in Fig. 3.20, both normal and frictional impulses induce torque. In the normal impact case tested here, initial tangential velocity would be zero, therefore normal impulse would be only source of torque, which would be expressed as $T_N = Nr \sin \Delta\theta$. Once T_N induces rotation around the CoM, nonzero tangential corner velocity would also be introduced where the frictional impulse start acting and induce torque around the CoM as $T_F = \mu Nr \cos \Delta\theta$, where μ coefficient of Coulomb friction. At the end of the impact process lander would continue to its post-impact motion determined this interaction and the surface coefficient of restitution. When impact is noncentral, and tangential corner velocity is nonzero, as in the oblique impact case here, normal and friction impulses are coupled [34]. On the other hand, when impact is central, *i.e.*, lander attitude is arranged such that normal impulse direction coincides with the vector extended from the CoM to impacting corner, a special case occurs. In that case, normal impulse does not generate any torque around the CoM (as $\psi = 0$) and if the tangential velocity component of the impactor corner is zero at the beginning of impact, frictional impulse would never be involved in the process. In such case, lander (or any rigid body) would simply bounce back in the same direction without any rotation. The magnitude of post-impact velocity would then be determined by the surface coefficient of restitution. On the other hand, in the oblique impact case, torque is generated only by frictional impulse.

In the following, first the post-impact trends in the normal impact case will be investigated.

Normal impacts

In normal impacts, ~60^o impact serves as some kind of a divider between two trends observed, hence would first be explained. As noted earlier, the ~60^o case in the normal impacts would ideally occur through the CoM thus would generate no torque around the CoM. In an ideal case, the lander would impact to the block and reflect back with some reduced post-impact velocity. This was observed in most of the cases, at least in observational level, as shown in Fig. 3.21.

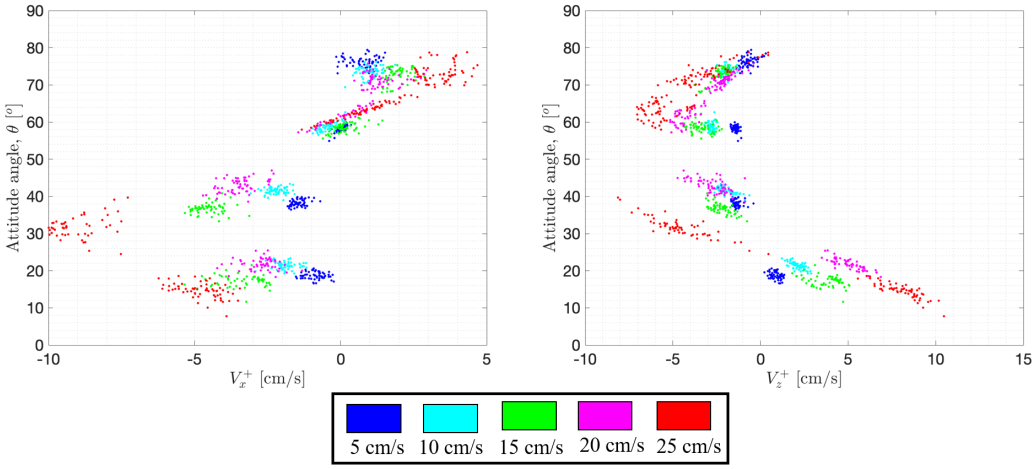

Figure 3.21: Normal impact post-impact velocity results

However, due to the release and impact conditions, some residual cross-track velocity remained or induced after the impact. This can be seen on the left plot of Fig. 3.21 where the non-zero cross-track velocity is clustered around ~60^o. Accordingly, in right panel of Fig. 3.21, one can observe the bounced lander's along-track velocity component on the negative side, as expected. With respect to this, there are two types of behaviour, as illustrated in Fig. 3.22.

If the attitude angle θ is higher than 60^o, *i.e.* the 75^o-case, then the lander tends to gain a positive post-impact cross-track (or +x) velocity. On the other hand, for the impact angle values smaller than 60^o, the lander tends to gain a negative cross-track

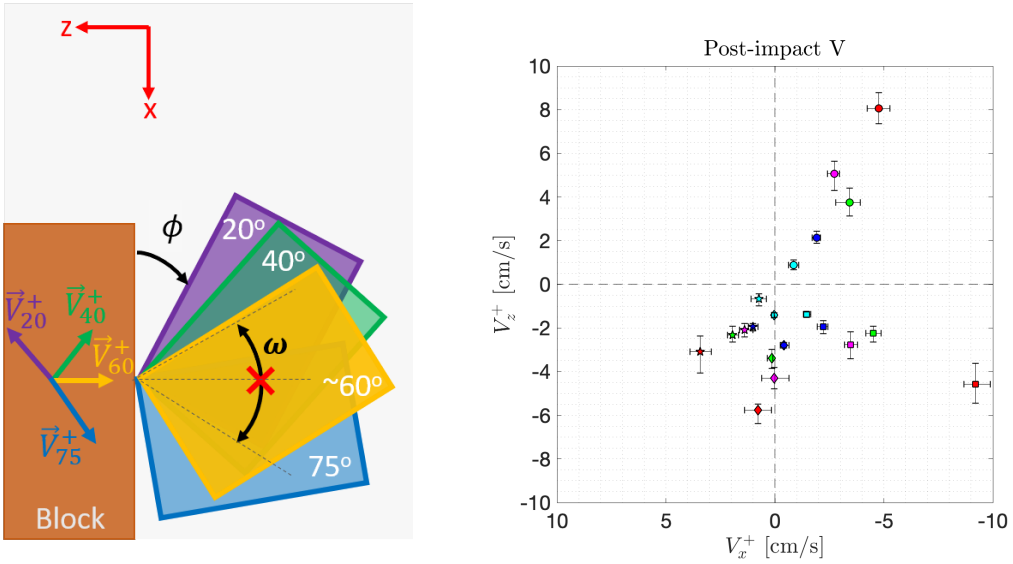

(a) Post-impact motion trends in normal impacts

(b) Post-impact velocity components

Figure 3.22: Normal impact post-impact trends in motion

velocity. This due to the position of the CoM with respect to the surface normal, which affects the the torque the lander receives after the impact. The post-impact angular velocity of the lander could be used to validate this statement, as shown in Fig. 3.23.

To confirm post-impact trends, one can observe Fig. 3.23 alongside Fig. 3.22a. As expected, the central impact case receives nearly no post-impact rotation, except the 25-cm/s case, which is mainly induced by the longer propagation of initial release errors. Lower θ angles result in rotation in one direction, whereas higher attitude angles result in rotation in positive direction, respectively. Furthermore, the post-impact rotation scales linearly with increasing impact speed.

The above results showed primarily the CoM behaviour after the impact. However, as explained, the CoM velocity is a combination of both corner velocity and the CoM rotation. First, post impact trends in impacting corner velocity will be investigated. Recall that corner velocity equals to the CoM velocity prior to the impact as there is practically no rotation. Post-impact angle of the corner velocity, measured from the local tangent, is provided in Fig. 3.24.

The left panel in Fig. 3.24 shows all results whereas right panel only shows average values with their associated errors. According to that, the corner post-impact angle

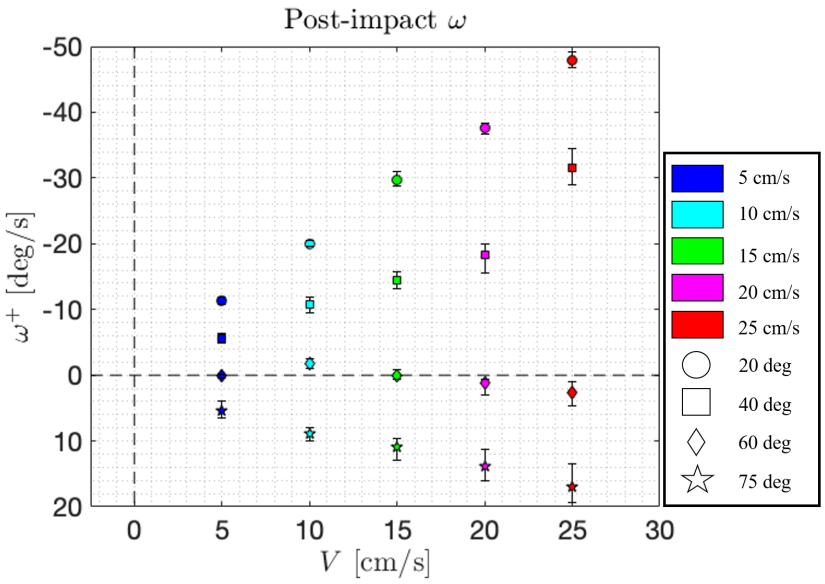

Figure 3.23: Normal impact post-impact angular velocity

shows minimal or no dependency to impact speed and but rather varies with attitude angle, at least for these experiments.

Oblique impact

The oblique impact post-impact results are shown in Fig. 3.25.

They do not seem to be as straightforward to explain the trends systematically as in the normal impact cases. Nevertheless, there appears a generally linearly-increasing trend for along-track velocity component. The cross-track velocity component, on the other hand, increases until 60^o impact angle, then decreases. Figure 3.26 illustrates the generally observed behaviour for mean velocity components with their associated upper and lower boundaries.

Although the motion direction is shown as separated by the impact angle, it does not quite follow this behaviour as shown Fig. 3.26b. Only statement can be made is higher post-impact velocity component for higher targeted impact speed as one may expect. The only clear trend that could be deduced in the oblique impact post-impact results is the angular speed, whose results are presented in Fig. 3.27.

According to Fig. 3.27, the post-impact angular velocity increases linearly with impact speed and decreases with increasing impact angle, for given impact speed.

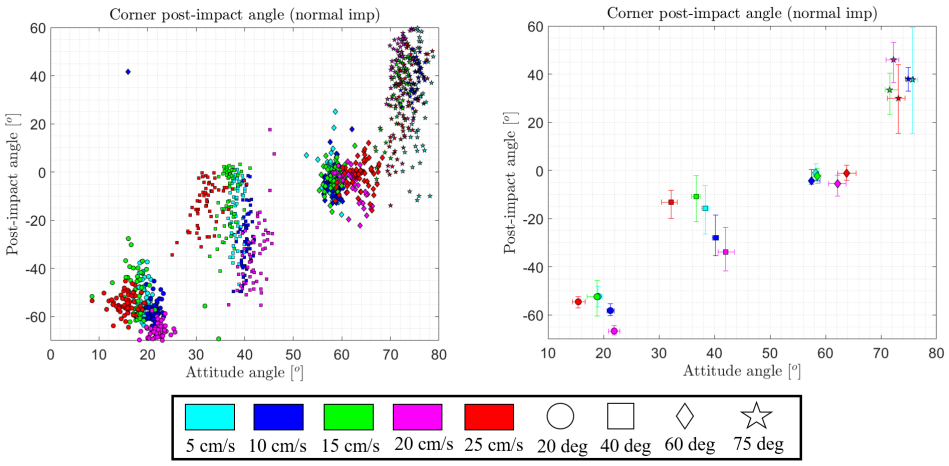

Figure 3.24: Corner post-impact angle as a function of attitude angle

This latter statement is such that the lander gains nearly no torque. This could be explained with the angle between the CoM vector with respect to impact point and the surface normal to that point. It is the highest in the 20^o case hence the highest rotation. Similarly the 40^o and 60^o case separate from the surface normal at decreasing angles, therefore their post-impact rotation is lower. Although the motion direction is shown as separated by the impact angle, it does not quite follow this behaviour as shown Fig. 3.26b. In the 75^o case, the CoM vector is then separated from surface normal with the smallest angle, hence normal impulse induces less torque, similar to the case in normal impact, as shown in Fig. 3.22. Then this suggests a very low coefficient of friction, such that even though moment arm for frictional impulse is gets longer, it cannot induce large torque. Or the torque is somehow balanced by the frictional and normal impulses.

Similar to the normal impact case, corner post impact velocity will be investigated next. The results are presented in Fig. 3.28.

The left panel in Fig. 3.28 shows all results whereas right panel only shows average values with their associated errors. Except the very large variation observed 5 cm/s 60^o case, the other results show that post-impact angle of corner velocity is independent of impact velocity but depends of impact angle, even though the trend is not very strong.

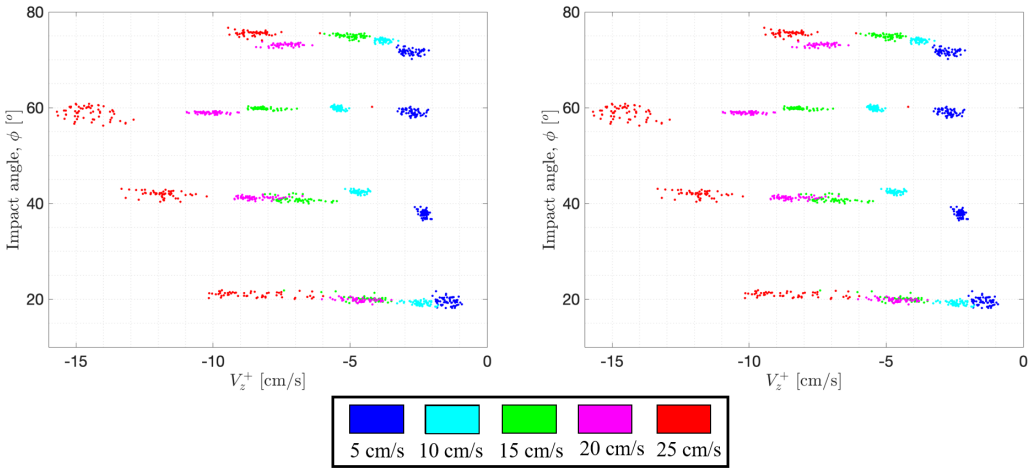

Figure 3.25: Oblique impact post-impact velocity results

3.4.3 Effective coefficient of restitution

Rigid, non-spherical body makes the coefficient of restitution, ϵ, estimation more complex. However, as a first order estimation, one can discuss the trends that appear in the data with more simplified definitions. This would provide a preliminary understanding on dependencies between impact parameters and ϵ. The classical definition of ϵ as the ratios of normal post- and pre-impact velocity is derived for spherical particles and primarily for free-fall kind vertical impacts, therefore it may not be appropriate for the rigid-body lander considered here. In order to account for both along- and cross-track velocities, as well as the rigid-body nature, an $effective$ coefficient of restitution (ϵ_{eff}) can be defined as

$$\epsilon_{eff} = \frac{V^+}{V^-} \tag{3.7}$$

where V^-, V^+ denote the CoM pre- and post-impact velocity magnitudes respectively. ϵ_{eff} can then be computed for normal and oblique impacts. Recall rigid body CoM velocity from Eq. 3.6. Trends in ϵ_{eff} is then a function of both corner velocity magnitude and rigid body rotation. the latter is assumed to be zero initially. With this formulation, the individual terms of the CoM velocity are abstracted out and a rather macro coefficient of restitution is investigated. However, if trends are not visible

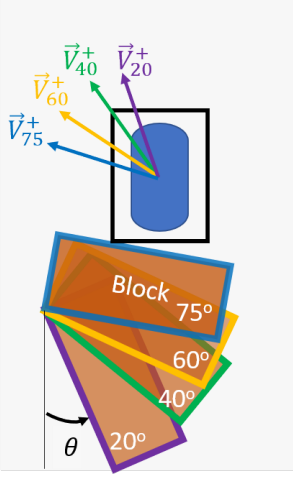

(a) Post-impact motion trends in normal impacts

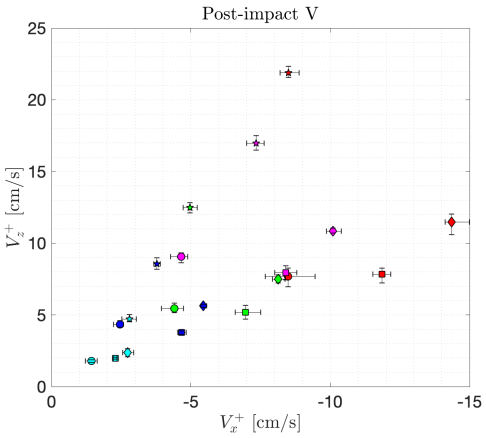

(b) Post-impact velocity components

Figure 3.26: Oblique impact post-impact trends in motion

in ϵ_{eff}, that does not necessarily mean that they do not exist, but may be hidden in corner velocity and in rotational terms. In the following subsections, ϵ_{eff} will first be investigated for the normal impact case against attitude angle, and then for the oblique impact case against impact angle.

Normal impacts

The ϵ_{eff} values in are first computed for each impact velocity with Eq. 3.7 and presented as a function of attitude angle in Fig. 3.29.

Figure 3.29 shows no discernible trend in ϵ_{eff}. There are large errors in the computed values. A very weak trend seems to appear in 10, 15 and 20 cm/s cases and those are not followed by 5 cm/s and 25 cm/s cases, therefore makes the validity of the other cases questionable. Figure 3.30 instead presents the ϵ_{eff} results of all runs together.

A few general conclusions can be drawn from Fig. 3.30. As an an overall behaviour, there is a weak decreasing trend in ϵ_{eff} with attitude angle. The ϵ_{eff} value is bounded between 0.1 and 0.45 during these experiments. As noted earlier, the central impact case can be used to measure the coefficient of restitution independent of friction, the result of which can be considered as the ϵ_{eff} of the block when its interacting with

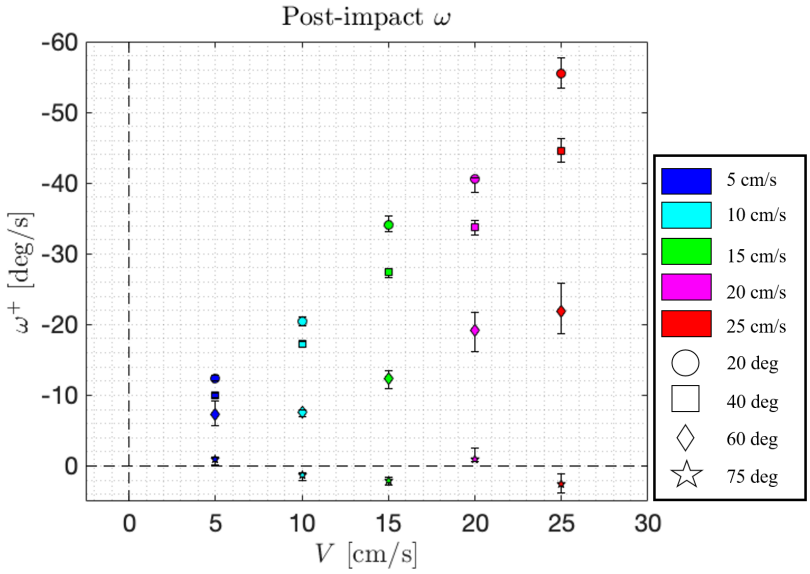

Figure 3.27: Oblique impact post-impact angular velocity

the lander assembly used in the experiments. The value of ϵ_{eff} in the central impact corresponds to 0.2-0.3 within its error bounds.

Although no strong trends were observed in the normal impact case, those could be hidden corner and rotational components of V^+. Given that angular velocity increases with impact velocity and decreasing with attitude angle (for given impact velocity), one expect rotational contribution of V^+ to be linearly scaled with impact velocity or attitude.

Oblique impact

The effective coefficient of restitution is computed in the same way as the normal impact case, this time for the oblique case. the results are presented in Figure 3.31 for each impact velocity.

Recall once again that the oblique impact case tested the effect of impact angle in the post-impact motion. At each impact velocity, there is a clear trend as a function of impact angle. The average value is approximately the same at each impact angle regardless of the impact speed. The nondependency of impact speed may be explained with the linearly-scaled rotational motion as a function of impact speed at each impact angle. As a result, ϵ_{eff} is calculated as the ratio of post- and pre-impact speeds, the

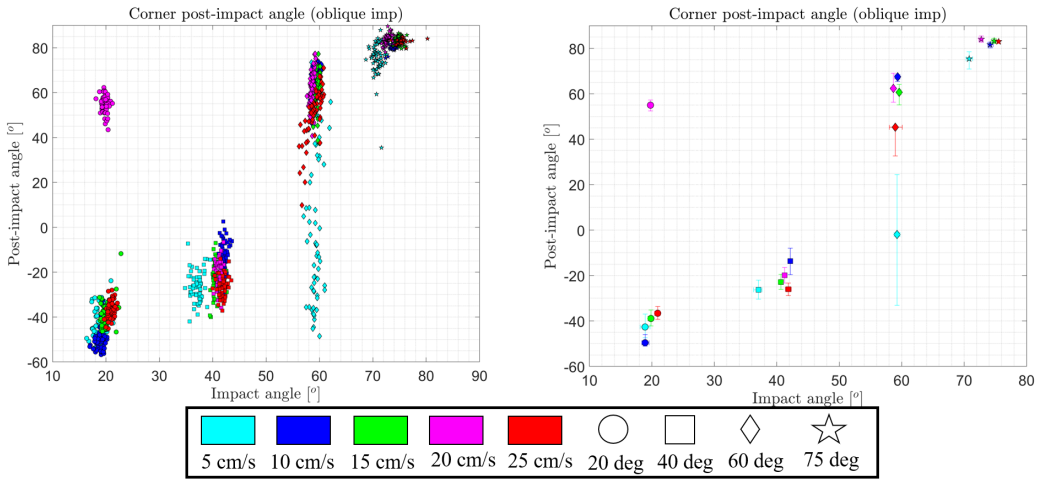

Figure 3.28: Corner post-impact angle as a function of impact angle

impact speed effects vanish as the post-impact rotation is proportional to impact speed. The trend can be seen much better in Fig. 3.32, with all oblique impact runs are combined.

According to the general results presented in Fig. 3.32, the ϵ_{eff} value was found to be always varying within 0.07 between different runs except the two outliers of the 5 cm/s 60^o and 75^o case. The ϵ_{eff} values are between 0.45 to 0.91, with distribution for each increasing impact angle being 0.45-0.52, 0.55-0.6, 0.72-0.78 (excluding the outlier) and 0.84-0.9. The uncertainty bounds in these values within an experiment runs is very low, and virtually nonexistent in some cases, such as the 40^o case in contrast to normal impact experiments. Furthermore, a linear relation can also be defined as ϵ_{eff} = aθ+b, where θ is impact angle, while a and b are coefficients of polynomial. This polynomial relation yields ϵ_{eff} = 0.47θ + 0.29, where θ is in radians. The variation in polynomial coefficients a and b, which are likely to be surface-dependent, is a potential experimental study in the future.

It is also worth discussing these results in the light of the recent MASCOT landing on asteroid Ryugu. In Scholten et al. (2019), the authors extracted the landing trajectory of MASCOT and identified at least four bouncing events [4]. The first impact is estimated to have occurred with 17.04 cm/s [4], similar to the velocities considered in this study. The velocity magnitudes of the landing event that spans about 18 minutes is

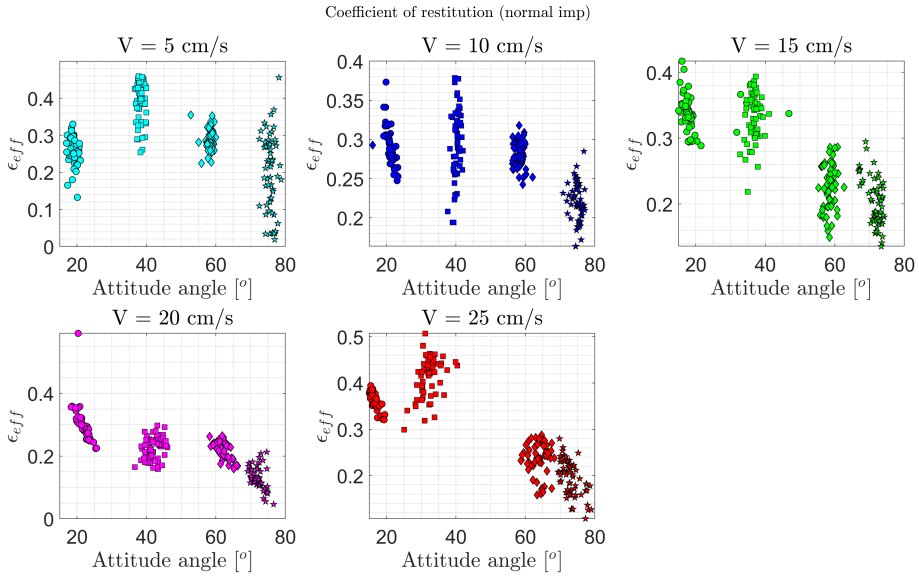

Figure 3.29: Effective coefficient of restitution in normal impacts

summarized in Scholten et al. (2019) [4], allowing to compute the effective coefficient of restitution similar to the one presented in this section. Table 3.2 summarizes the MASCOT impact properties, adapted from Scholten et al. (2019) [4], alongside the estimated effective coefficient of restitution, ϵ_{eff}.

Table 3.2: MASCOT Bouncing events (adapted from [4]) and corresponding ϵ_{eff} from this study.

Bounce #	V^- [cm/s]	V^+ [cm/s]	ϕ^- [deg]	ϕ^+ [deg]	ϵ_{eff} [-]	ϵ_{eff} (This study) [-]
1	17.04	5.31	43.98	68.32	0.31	0.72
2	6.14	3.46	52.74	75.08	0.56	0.74
3	3.80	2.39	64.11	62.25	0.63	0.81
4	2.33	2.28	67.51	42.16	0.97	0.84

Note in Table 3.2 that there is about 7.25 sec of contact between Ryugu's surface which discussed as a multiple-contact event [4]. The other bouncing events appear to occur instantaneously or at least take less than 0.1 sec (not shown in the table) [4]. The calculated ϵ_{eff} results in Table 3.2 are different than estimated values. This is to be expected: The level of gravity, the impacted surface, the impactor shape,

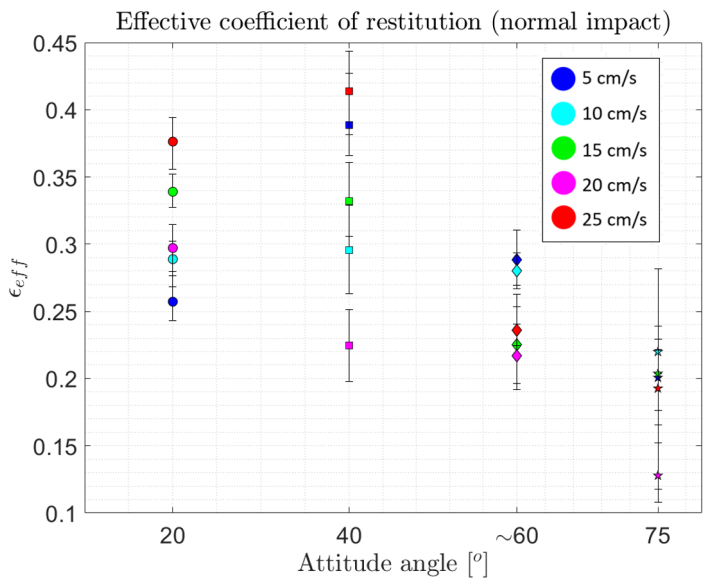

Figure 3.30: Effective coefficient of restitution in normal impacts

mass, inertia and surface material, as well as attitude are all different. Moreover, the MASCOT impact is three-dimensional most likely occurs on the face than the corner and involves multi-contact events unlike the experiments here. However, one general aspect is appeared to be captured. The impact angle of MASCOT, ϕ^-, increased at each bounce. Following the linear relation presented in Fig. 3.32, this would result in increasing ϵ_{eff}. According to Table 3.2, the effective coefficient of restitution of MASCOT increased with impact angle. The slope of this increase may be affected by any of the factors mentioned above, combination of those, or any other factor not mentioned here, but the linear relationship demonstrates the impact-angle dependent effective coefficient of restitution for nonspherical impactors in two different levels of gravity. The instantaneous contact assumption may not be wrong either, as the data shows that the contact duration of MASCOT is very short. The exception to that is the first impact, which seems to occur at a very steep boulder with the post-impact motion is *towards* the surface, resulting in multiple bounces. If it hit the surrounding surface, it would likely to show the same behaviour as the other impacts.

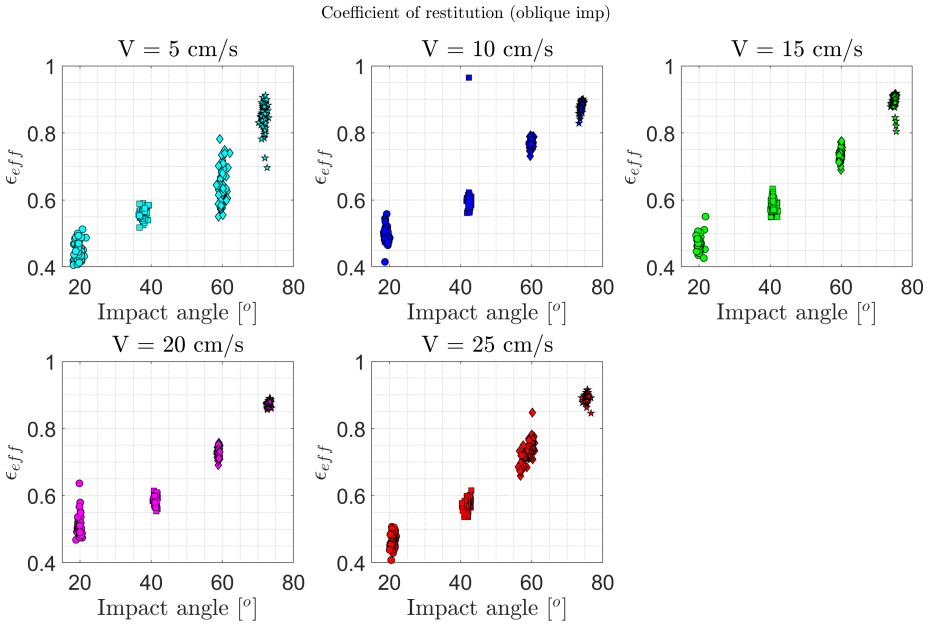

Figure 3.31: Effective coefficient of restitution in oblique impacts

3.4.4 Comparison of experimental results with Brach impact model

One of the aspects of this study is to investigate the applicability of low-speed impact theories in reduced gravity conditions. More specifically, it was aimed at evaluating trends in the data obtained (if any) and discuss the outcome in relation to the controlled impact parameters (*i.e.*, impact speed, angle, attitude). It was also aimed at discussing the trends in the experimental data with the statements of the employed contact model and propose suggestions on the applicability of the model to the contact problem discussed here.

As confirmed by the contact duration simulations, the contact between the lander assembly and the block can be approximated as impulsive. There are multitudes of impulsive contact models in the literature, each handling the contact impulse differently. For instance, Stronge (2000) contact model handles the contact impulse as an independent parameter in place of time and describes the coefficient of restitution as the ratio between work done by normal impulse to total energy. Stronge model was successfully applied in Van wal (2020) to model the hard surface interaction between an object and the surface [35] for lander-surface interaction in small bodies. However,

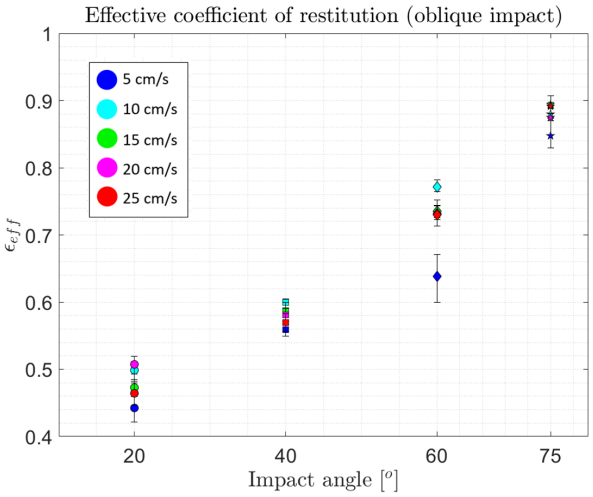

Figure 3.32: Effective coefficient of restitution in oblique impacts

a recent study shows that Stronge model may not be applicable for low-gravity applications, because the obtained coefficient of restitution and friction values do not show any dependence to impact conditions and mostly varies randomly (Van wal, Çelik et al., 2020, under review).

Following this result, another contact model, Brach (1988) impulsive contact model is used to compare the the experiment results with theory. Brach model relies on the coefficient of restitution, defined as the ratios between post- and pre-impact velocities in the normal direction, as well as the coefficient of friction, defined as the ratio between tangential and contact impulses and applies conservation of angular moment to finally derive a set of algebraic equations to output the post-impact velocity and rotation.

Compared to Stronge contact model, Brach model is completely algebraic and provides general solution to a set of equations that are written in a matrix form, albeit being relatively complex. It also considers the fact that contact occurs in an area rather than a point as it is commonly assumed. Brach then introduces a so-called the *angular* coefficient of restitution, denoted as ϵ_m, to describe the moment generated in contact point, which also drives the evolution of angular momentum. ϵ_m appears only in part of Brach's works, such as in Brach (1981) [84], but the author appears to drop this idea in later papers for three-dimensional rigid body impacts [85], or only focused on simplified impact cases of rigid bodies [85]. While this coefficient is theoretically

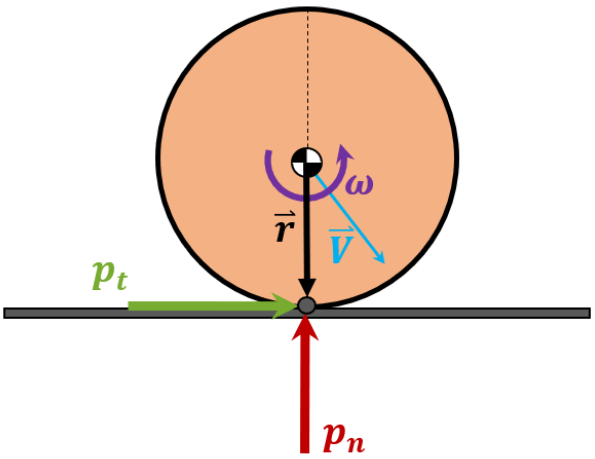

Figure 3.33: Free-body diagram of contact in Brach model

independent of the coefficient of restitution for translational motion, they relate in certain conditions. The model equations are theoretically applicable to nonspherical shapes. For an instantaneous impact case, post-impact motion equations can be written as follows:

$$V_n^+ = -\epsilon_n V_n^- \tag{3.8a}$$

$$V_t^+ = V_t^- - \mu(1+\epsilon_n)V_n^- \tag{3.8b}$$

$$\omega^+ = \mu(1+\epsilon_n)\mathbf{I}^{-1}(\vec{r}\times m\vec{V}^-) \tag{3.8c}$$

where V_n, V_t denote normal and tangential center-of-mass velocity components, ω denotes angular speed, m denotes mass. ϵ_n and μ are the coefficients of restitution and friction. The expressions in Eqs. 3.8 are written in a simplified form, in which no initial rotation is assumed, as it is the case in the experiments. Because the equations are theoretically applicable to all objects, final equation is written in vector form.

Brach model is used to extract trends from the experimental data and discuss the results in concert with the statements of the model, derived from experiments. To do so, both grid-search and least-squares analysis approaches were taken to match the measured rotational and translation motion to find the coefficient of restitution and friction values as a function of impact properties. First, both coefficients were found for

one case (*i.e.*, 5 cm/s) for all attitude/impact angle values depending on the impact case and applied to all other cases to test whether the same set of coefficients can describe the post-impact behavior of other impact cases. Then, the same procedure is applied in all cases to further validate the results. It is clear that the set of equations in Eqs. 3.8 is general and will output a certain number. However, if the experiment results do not agree with the expected trends in the model, or the values derived are unphysical (such as ϵ_n>1), that would suggest that the Brach model (or any other impact model when tested) would be inapplicable for low-gravity applications, despite having no gravity terms in the model equations. In an ideal test, first, the coefficient of restitution and friction would have been estimated prior to the experiments, and would be uses in the theory to extract post-impact velocity and rotation and compare it with the experimental findings. But those coefficients were not available during the experiments and could not be tested. The approach taken here is akin to inferring surface properties from experiments and discussing the results with the inferences of the impact model.

The first results are provided for the normal impact case in Fig. 3.34.

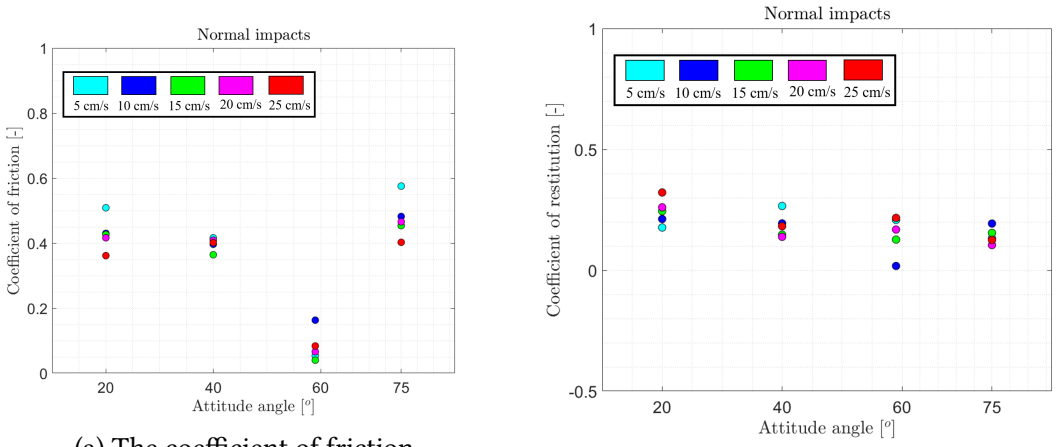

(a) The coefficient of friction

(b) The coefficient of restitution

Figure 3.34: Interaction coefficients as inferred with the Brach model in normal impacts

Both the coefficient of friction and restitution show no apparent dependency to attitude angles. The coefficient of friction values that are closer to zero in Fig. 3.34a are due to the central impact condition, in which, ideally, the coefficient of friction cannot be mathematically defined as it does not involve in the interaction process. However, it is indeed estimated with much lower values, as the perfect central impact

condition cannot be obtained due to the imprecisions during the experiments. The impact velocity dependency is more apparent in the coefficient of friction estimation, although both coefficients show relatively minimal dependency to impact speed. The coefficient of restitution trend in Fig. 3.34b shows some similarity with the effective coefficient of restitution results in Fig. 3.30. The values in both vary between 0.2-0.4 around an average of 0.35 and without a clear trend. The coefficient of restitution value is between 0.4-0.5 with a few outlier cases. Rotational behaviour is then generated with a constant coefficient of friction and restitution assumption by substituting the mean coefficient values into Eq. 3.8. The mean coefficient values are 0.4 for friction and 0.35 for restitution. The result is presented in Fig. 3.35.

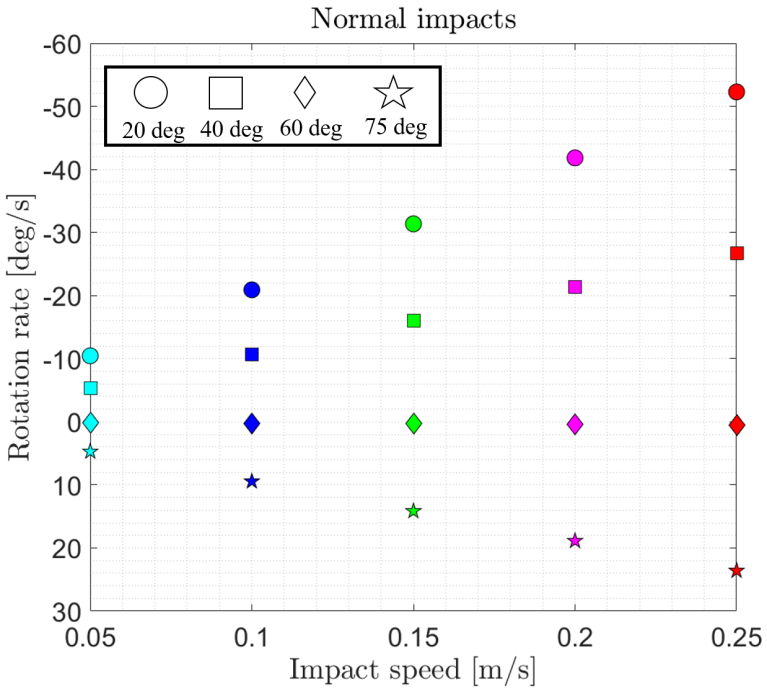

Figure 3.35: Post-impact rotation behaviour as obtained with the Brach model in normal impacts

When compared with the experimental results in Fig. 3.23, it can be stated that the overall rotation behaviour can be captured with a constant coefficient of restitution approximation in normal impacts. At higher impact speeds, rotation rates appear to be overestimated which is due to the lower restitution values compared to the constant mean value selected. The central impact case is also captured with evident

zero rotation. As a result, it can be suggested that, if Brach contact model is employed for object-surface interaction in low-gravity environments, the interaction coefficients can be assumed to be independent of attitude at least in the case of a corner impact or when the interacted small enough. The extent of the latter statement must be confirmed with more experiments.

It is then becomes interesting to test the same constant coefficient assumption for oblique impacts, where the impact angle dependency is tested. The found coefficients in the normal impacts applied to the oblique impact case. This time block attitude is varied and impact velocity at the impact point is calculated. The obtained post-impact rotation is presented in Fig. 3.36.

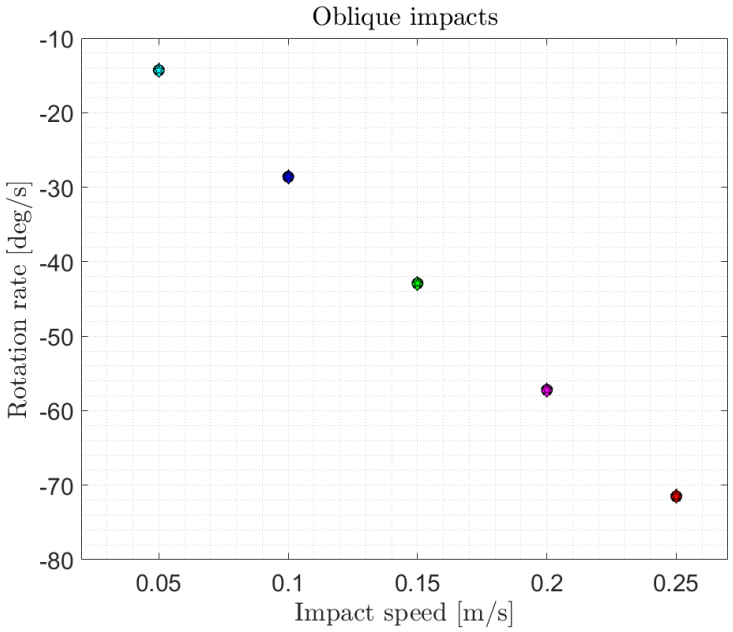

Figure 3.36: Post-impact rotation behaviour as obtained with the Brach model in oblique impacts with the coefficients obtained from normal impacts

When compared with Fig. 3.27 (note the inverted y-axis), it can clearly be seen that the constant coefficient assumption yield constant rotation rate in each case, scaled with the impact speed. This is due to the fixed attitude angle, resulting torque arm being constant. It is clear that this is not the behaviour observed in the experimental data. Therefore, the coefficient of friction must be variable. However, this is against the idea of the coefficient of friction as an intrinsic material property, as commonly

assumed in the impact models. Brach suggests that, instead of the coefficient of friction, the tangential-to-normal impulse ratio is variable and dependent upon impact angle [86]. With this in mind, the fitting procedure is applied to match the rotational and translational with freely chosen pair of coefficient of friction and restitution. The results are provided in Fig. 3.37.

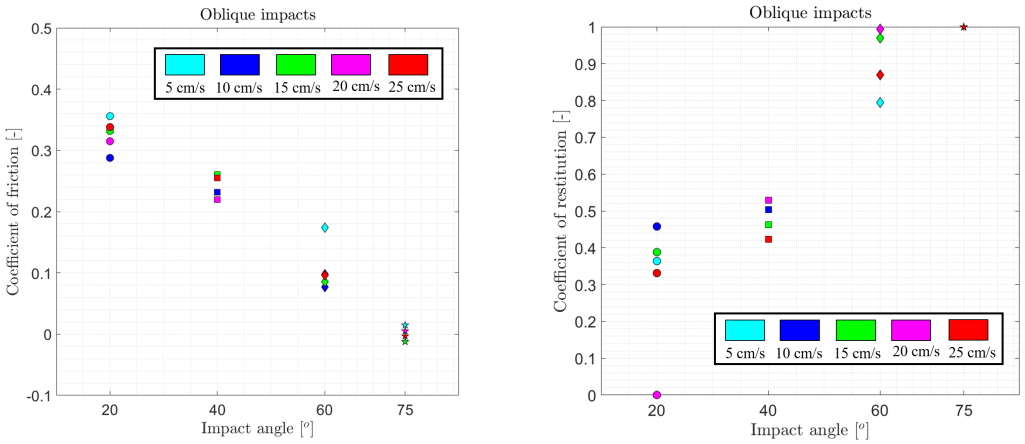

(a) The coefficient of friction

(b) The coefficient of restitution

Figure 3.37: Interaction coefficients as inferred with the Brach model in oblique impacts

According to Fig. 3.37, a clear dependency to impact angle is observable for both coefficients. The coefficient of friction decreases as the impacts becomes shallower, whereas the opposite happens for restitution. In both, the impact speed dependency appear to be minimal. The values for the coefficient of friction vary between nearly 0 to 0.4. The coefficient of restitution values vary between 0.3 to nearly 1, with an outlier case at the 20 cm/s - 20^o impact case. Post-impact rotation behaviour with the coefficients presented in Fig. 3.38.

Figure 3.38 confirms the observed post-impact rotational behaviour in the oblique impact case, except for one outlier case mentioned earlier. Near zero rotation is obtained for the 75^o case and it is confirmed that rotation is proportional to impact speed and inversely proportional to impact angle, *i.e.*, shallower impacts leave the surface with lower rotation rates. Linear scaling of rotation rate with impact speed is likely reason of why the impact-speed dependency is rather minimal in the coefficient values.

All in all, the results suggests that if Brach impact model is employed as the

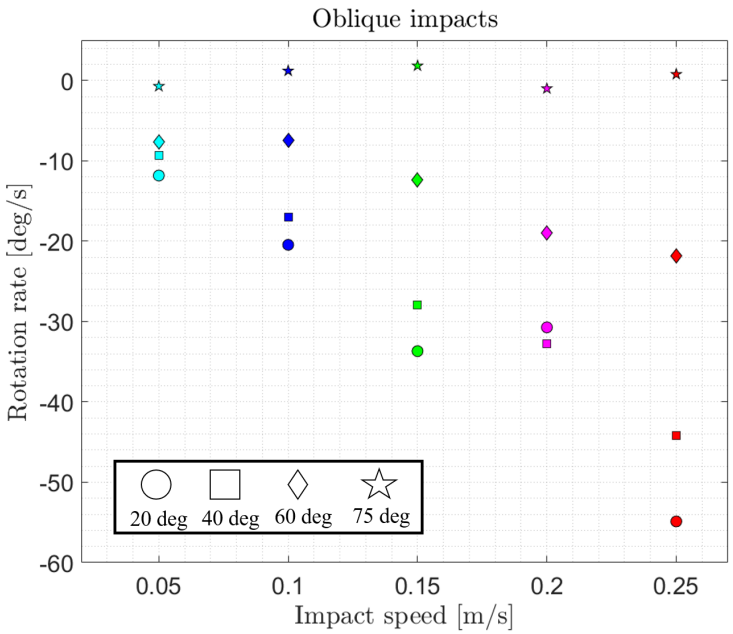

Figure 3.38: Post-impact rotation behaviour as obtained with the Brach model in oblique impacts when the coefficients are freely chosen.

hard-surface interaction model for low-gravity applications, the interaction coefficients are considered to be a linear function of impact angle with friction as decreasing and restitution as increasing with impact angle for given angle convention in this experimental campaign. The coefficients can be assumed as independent of impact speed for given range of impact speeds considered in this study.

3.5 Discussion

This chapter presented the experimental investigations on the post-impact motion of nonspherical impactors/landers when they impact hard nonpenetrable surfaces in artificial low gravity. More specifically, the study investigates the effect of the impact conditions (velocity, angle, attitude) on the post-impact behavior and in the final coefficient of restitution. The artificial two-dimensional milli-gravity environment is created in an air-bearing system. The system comprised of an inclined smooth table, an air-bearing assembly, a switchable-magnet-based release mechanism that is designed and built, a representative hard surface, and an optical tracking system. In that setup,

the normal and oblique impact cases are tested for four angles and four impact speeds relevant to the current landing missions, such as MASCOT or MINERVA. About 2500 data points are generated and the collected data is post-processed to investigate the post-impact conditions as a function of pre-impact conditions with the impulsive contact assumption.

The results demonstrated a successful experiment campaign. A consistent milli-gravity level is achieved for the vast majority of the impact runs. The release mechanism allowed for precise control of impact speed, angle, and attitude. Imprecisions are mostly resulted from residual magnetism due to manual control of release and the block movement as a result of impacts. The imprecisions are more pronounced in the highest impact speed cases, as they travel longer in the table to accelerate. All in all, the impact speed was controlled within ±1 cm/s, the impact angle was controlled within $\pm 2^o$ and the attitude is controlled within $\pm 6^o$.

In normal impacts, where the effect of the impactor attitude is tested, the post-impact direction is observed to be dependent on impact attitude. The magnitude of this vector linearly scales with the impact speed and its direction is determined by the impact attitude. The torque acting on the impactor due to the surface friction is the driver for this, which increases with the offset angle, ψ between the surface normal and the line connecting impact point to the center of mass increases. The magnitude of this torque linearly scales with impact speed at each attitude angle.

In oblique impacts, where the effect of the impact angle is tested, the post-impact direction is more complicated. Post-impact speed is linearly scaled with impact speed, but the direction of it is not very clear. Post-impact angular motion is, on the other hand, has a linearly-increasing trend with impact speed. The angular velocity magnitude increases with ψ.

An effective coefficient of restitution, ϵ_{eff}, in this study is defined as the ratio of post- and pre-impact velocity magnitude. ϵ_{eff} did not show a distinguishable trend in normal impacts. On the other hand, ϵ_{eff} is found to be linearly-dependent on impact angle with only minor dependence on impact velocity in oblique impacts. It is believed that the reason fot this is the linearly-scaling post-impact speed and with impact-speed, which, when their ratios are computed, render impact speed effects to disappear. The linear relationship between the impact angle and ϵ_{eff} is also confirmed with the recent MASCOT landing data. Although the results presented here are for a specific impactor

shape, the general conclusions drawn throughout the chapter should hold for other impactor shapes, as well. Thus, the findings in this study would then help reconstruct lander trajectories and build confidence in the operational planning of small body landers/rover deployments in the future.

The apparent non-dependence of ϵ_{eff} to impactor attitude may not be conclusive, however. The data is analyzed with idealized conditions. Moreover, although the impacts are aimed at to be in the impactor's edge, it is in fact a curvature that would affect the impactor's departure conditions from the surface. Other effects, such as surface and/or impactor deformation upon impact, are ignored in this study, which may affect the post-impact motion. Deformation is not expected to be too high in the impactor, as the impact energy and the gravity are low. Similarly, the air-bearing assembly in this study is not a closed structure but rather a "skeleton," built with aluminum rods. It is observed that the assembly is visibly vibrated at the release and the impact, thus it is believed that this and other unmodeled aspects need to be investigated further before concluding the non-dependence of ϵ_{eff} to attitude angle.

Finally, the results are compared against an impulsive contact model developed by Brach [86]. The coefficient of friction and restitution are found to be impact attitude and impact speed but linear function of impact angle. However, it is likely that the Couloumb coefficient of friction, as assumed as an intrinsic property of an impacted surface, is constant but the ratio of tangential and normal impulses vary with relative tangential velocity, as stated in Brach [86].

Some recommendations can now be made for object-surface interaction applications in small-bodies. Even though the results here demonstrated non-dependence to impact attitude, that does not mean that impact attitude does not affect energy damping upon impact. Impacting on one face or other will indeed affect the amount of energy damping due to increasing (or decreasing) interaction surface. But it appears that impact attitude is not affecting the properties of interaction at a given point. On the other hand, impact speed appears to be scaling the post-impact behaviour linearly for tested range of impact speeds. The tested impact speeds are likely to be linear elastic region of impactor material, therefore no significant energy loss due to deformations occurs despite increasing impact speed. As a result, the effect of impact speed manifest itself in post-impact velocity and rotation magnitude but vanishes for given impact or attitude angle in each case. Therefore, for small-body applications, if impact speeds

confirmed to be within linear regime of the impacting material, dependency to impact speed may be ignored during simulations, as well. Impact angle appears to be the dominant driver in estimation of the interaction coefficients. In this experimental campaign, the coefficients were shown to be a linear function of impact angle. This relation probably holds different materials with which the interaction can be assumed impulsive. However, the slope of the linear function must be a function of interacted material. Therefore, it is necessary to confirm the linear relation with experiments prior to simulations. During space missions, a straightforward derivation of those parameters will likely to be very challenging, but a combination of pre- and post-impact speed and impact angle data can be used to derive the coefficients by assuming those independent of attitude.

4

Interaction with granular surfaces: Analytic investigations

4.1 Introduction

An object's interaction with a soft granular surface is a complex phenomenon because of the very nature of granular materials. Granular materials exhibit both solid- and liquid-like behavior. Any realistic interaction situation would deform granular materials plastically as the impact-generated stress would be well above elastic limits of the material. In high-speed (~km/s) impacts, drastic changes happen to both impactors and impacted surfaces: Impact energy breaks, melts and vaporizes impactors, the target, and the impactor material are mixed and jetted, and rest of the material would be excavated from the initial cavity to eventually form a crater. In low-speed impacts, the impact process is a lot more benign. Before explaining those details, it is worth defining the range of speed that could be considered as low speed. The speed of sound in granular material is an indicator that is commonly used to define hypervelocity. In

this work, as the targets that considered are small bodies, a more practical approach is taken and speed ranges relevant to space missions and some of the natural low-speed impact phenomena are considered. That can be generally below the escape speed of a target body, which, in this case, would be below meter-per-second level. This may not be very definitive as bodies like Phobos have escape speeds around or greater than meter-per-second [3]. In that case, the approach is adaptive, *i.e.*, the outcome of the impact is the driver of the low-/high-speed impact definition. The primary division between a high- and low-speed impact arises from the impact outcome. While high-speed impacts result in a complex crater formation, low-speed impacts generate much less fanfare. First and foremost, impactors, for the most part, survive the impact as one piece. Some material is pushed aside and excavated, while others compressed with down with the crushing of pores, some energy would turn into temperature and impactor and particle rotation but likely not much else happens. In the end, despite their largely different outcomes, the commonality between high- and low-speed impacts is that the impact energy is dissipated multiple ways and plastic deformation occurs to make a cavity in the interacted surface that is called a crater. One can then argue that the interaction between an object and a soft granular surface is a cratering process. The energy spent in this process can then be analyzed to estimate the remaining energy which could be considered as the coefficient of restitution. However, questions remain on the energy sinks during a cratering process. While material ejection is a straightforward example of an energy sink, it is also not known how the ejecta velocity profile looks like in low-speed impacts in low-gravity environments.

One way to investigate craters in different granular environments is crater scaling laws. Starting with large scale impact phenomena, the pioneers of the cratering field focused on analytical models derived from empirical studies with buried explosives or high-speed impacts in the absence of large computational simulations. Dimensional analysis with Π-theorem [55] was proposed to characterize crater and ejecta properties in the form of power-law scaling, and as a function of impact, impactor and macro surface properties (gravity, strength, density), avoiding granular level complexity [53, 54, 50, 56]. The empirical studies in the last half-decade in the Earth-based conditions have repeatedly shown trends and similarities in the model parameters, making crater scaling laws the household tool to evaluate craters in planetary bodies

[2, 58, 25, 1]. Low-speed cratering, on the other hand, has recently gained momentum in planetary science and granular mechanics. Repeated impact experiments under Earth-gravity, reduced gravity in parabolic flights, and fluidized beds, as well as in inclined planes have all confirmed that power-law scaling laws can be derived for *crater sizes* [87, 88, 89, 90]. Even though the potential of using crater scaling laws is demonstrated by these works for *crater sizes*, there is still a gap in the literature as to the applicability of those laws under small body level gravity. Thus far, a limited number of low-speed impact experiments in asteroid-level conditions are performed, but yielded mostly phenomenological explanations in terms of impact cratering, summarized in Ref. [91]. Moreover, even if it is assumed that the scaling laws can be extrapolated for small body conditions, it remains unknown whether ejecta profiles obtained in the Earth-based conditions would hold for small bodies. For instance, an ejecta model that is developed to explain the crater ejecta made by the Deep Impact spacecraft's impact on Tempel-1 is based on the Earth-based experimental parameters [61], and it is unknown whether that could be applicable to low-speed impacts. Once those are identified, one can then begin estimating energy sinks in cratering process. Those can be used to estimate remaining energy of an impactor, if any. Hence, in this chapter, object-surface interaction in granular surfaces is tackled from a cratering perspective. The coefficient of restitution is defined as the residual energy after energy dissipation during cratering. Before that, first, the study validates the low-speed crater scaling laws. Unlike other studies, the study will exploit opportunities provided by the discrete element method to simulate impacts in small body conditions. Because each particle's and the impactor's dynamical state is tracked throughout a simulation, measurement challenges in ejecta velocity and ejected mass can be overcome, quantitative analyses can be performed to finally derive appropriate analytical scaling laws smilar to high-speed impacts (refer to Chap. 2 for the scaling law equations). Then, the most dominant energy sinks are identified, and analytical expressions are derived for each to calculate the relative contributions of the identified energy sinks, hence the residual energy. The obtained coefficient of restitution results are compared with the simulation results and the limitations of the model will be discussed in the end.

4.2 Hypothesis on the applicability of the cratering theory in low-speed impacts

There has been efforts to test different aspects the scaling laws by researchers. Because of that, the available data is varied and do not include all aspects of the laws, *i.e.*, crater size, ejection speed, and ejected mass at the same time. Among those, the crater size is easiest to measure and rather abundant data is available for it. This is because its static nature, *i.e.*, once the crater is fully formed it does not change its shape significantly before measurements are taken unless it is disturbed in some way. On the other hand, grain ejection speed and total ejected mass are harder to measure, mostly due t small experiment chambers and limitations in measurement, *e.g.* frame rate of a camera. The latter is harder to overcome; the high-speed imaging technology was limited in the past and is still relatively expensive today.

Among the works specifically focusing on astronomical craters in relatively low speed experiments, Tsujido et al. (2015) investigated the effect of projectile density on the crater sizes and grain ejection velocities [88]. Their impact velocity is between 105 and 215 m/s, i.e. an order of magnitude lower than those of the earlier studies [2, 92, 54], which presents an opportunity to compare Tsujido et al. (2015) results with earlier studies. Yamamoto et al. (2006) performed impact experiments to investigate transient crater growth via low-velocity impact experiment. [93]. The “low" velocity is a relative term here, as the highest impact velocity Yamamoto et al. (2006) used is 329 m/s – higher than the highest velocity at Tsujido et al. (2015) [93, 88]. However, their lowest impact velocity is 11 m/s, which is indeed relatively low. This value is two orders of magnitude lower than that of earlier impact experiments. The final crater sizes were also given in the study [93], allowing to compare it with the scaling laws. More recently, Hayashi & Sumita (2017) and Takizawa & Katsuragi (2020) tested cratering on inclined granular surface with very low impact velocities [94, 90]. Particularly, the Hayashi & Sumita (2017) study tested this for velocities in a narrow range of 4.5-5.4 m/s and showed cratering process at low-speed and inclined surfaces [94]. The Takizawa & Katsuragi study has only a single data point at 1 m/s with lowest values after this being ~7 m/s (also single data point) and ~15 m/s [90]. The authors also studied the cratering process in inclined surfaces at lower speeds by incorporating impact angle and slope angle of the surface in scaling laws[90].

In addition to presented studies under Earth gravity (or $1g$), there are also few experimental studies that were performed under artificial low gravity. In an earlier study, Gault & Wedekind (1977) performed experiments in an artificial microgravity created in the laboratory and shot spheres in a granular bed at ~6.6 km/s [92]. They investigated the crater sizes and their growth as a function of impact energy for gravity levels between $0.073g$ and $1g$ [92]. In an extensive parabolic flight experiments, Cintala et al. (1989) collected crater diameter and growth time data for 65 impact under $0.05g$ to $0.5g$ with impact velocities between ~65–130 m/s [95]. This paper presents an excellent opportunity to test the scaling theory under low-gravity.

Cratering is also experimented in other celestial bodies. Three spacecraft were observed to make craters on small-body surfaces thus far. Two of which, the Deep Impact (DI) experiment in 2005 on comet Tempel-1 [96] and the Hayabusa2 (Haya2) Small Carry-on Impactor (SCI) experiment [1] in 2019 on asteroid Ryugu were deliberately targeted to make craters to measure material strength (DI and Haya2), to estimate age (Haya2) and to expose fresh materials for sampling (Haya2) [96, 1]. The DI experiments was performed by impacting ~400-kg-spacecraft impacting on the comet at ~10.2 km/s [96]. The Haya2 experiment, on the other hand, carried a dedicated deployable impactor system, which consists of solid explosive charge to accelerate the impactor to 2 km/s [97]. On the other hand, Philae lander onboard Rosetta mission was deployed onto comet 67P/Churyumov-Gerasimenko to perform the first comet landing [21]. The Philae operations did not go according to plan due to the system failures and largely-unknown surface environment of the comet prior to launch; however, researcher were able to capture its first bounce and observed the crater it made [21]. As the Philae's impact speed was on the order of 1 m/s and under low-gravity conditions, this presents and opportunity to test the scaling theory for low-speed impacts.

In addition to dedicated planetary cratering literature, there are also studies that focus on granular media and grain ejection dynamics. Among those, Deboeuf et al. (2009) derived a model for dynamics of grain ejection from the experiments [98]. In the study, the impact speeds were kept between 1-4 m/s and the pictures of apparent corona of the ejected grains were analyzed to extract ejection speeds and ejecta mass as a function of impact energy [98]. A scaling law different than Housen & Holsapple was also derived [98]. Boudet et al. (2006) investigated the cratering dynamics in shallow sand layers in low-speed impacts [99]. The impact speeds were on the order of 2-3 m/s

[99]. Information about both crater radius and grain ejection speed for one experiment was given [99]. Table 4.1 summarizes the previous studies that were reviewed here.

Table 4.1: A list of previous studies on cratering. Acronyms: L - Laboratory, SC - Spacecraft, S - Simulations

#	Ref.	Name	Type	Gravity [Earth-g]	Velocity range [m/s]	Measurement
1	[92]	Gault & Wederkind (1977)	L	0.073-1	6640	Crater size
2	[54]	Schmidt (1980)	L	1	1750-6410	Crater size
3	[95]	Cintala et al. (1989)	L	0.16-0.5	65-130	Crater size
4	[99]	Boudet et al. (2006)	L	1	2.65	Crater size, ejection speed
5	[93]	Yamamoto et al. (2006)	L	1	11-329	Crater size
6	[98]	Deboeuf et al. (2009)	L	1	1-4	Crater size, ejection speed
7	[2]	Housen & Holsapple (2011)	L	1	Various	Crater size, ejection speed, ejected mass
8	[88]	Tsujido et al. (2015)	L	1	106-215	Crater size
9	[90]	Takizawa & Katsuragi (2020)	L	1	1-97	Crater size
10	[61, 100]	Richardson & Melosh (2007, 2013) (Deep Impact)	SC	3.46e-5	10200	Crater size, ejection speed, ejected mass
11	[21]	Biele et al. (2015) (Philae)	SC	1.63e-5	1	Crater size
12	[1]	Arakawa et al. (2020) (Hayabusa2 - SCI)	SC	1.25e-5	2000	Crater size

One can see in Table 4.1 that impact velocities are quite varied; the difference

between the highest and the lowest is four orders of magnitude. This then allows to test the cratering laws at various impact velocities. All the studies reported in Table 4.1 includes data regarding crater sizes, therefore that will be the first to be investigated. Note that, the data in #10 includes highly-elliptical craters due to the oblique nature of the impacts, hence include two scales for a crater, major and minor axis radius. In that case, their average is used. Also note that neither Boudet et al. (2006) nor Deboeuf et al. (2009) measured or provided dedicated crater sizes in their studies as in the other planetary cratering studies noted earlier, therefore crater sizes (in both studies) and ejection velocity profile (Boudet et al. (2006) only) were computed indirectly from the given data in the respective papers. The results of crater radius provided in Fig. 4.1. The theory line in Fig. 4.1 is calculated with the equations given in

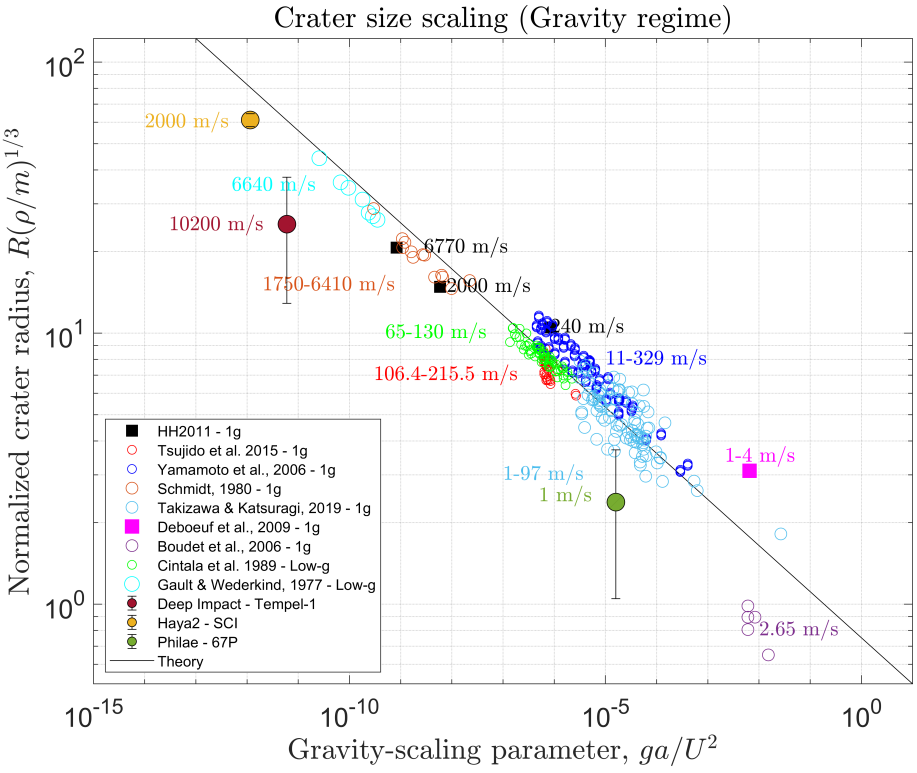

Figure 4.1: Normalized gravity-regime crater sizes from different experiments

previous section for Takizawa & Katsuragi (2020) impactor properties. The x-axis of Fig. 4.1 is π_2 or gravity-scaling parameter and y-axis is normalized crater radius which can be denoted with π_4, as given Eqs. 2.12. According to the figure, there is a strong

correlation in the experimental results in terms of π-scaling. Major outliers in Fig. 4.1 are two indirectly-computed crater radii (by the author of this thesis) from Boudet et al. (2006) and Deboeuf et al. (2009) and two spacecraft craters of DI and Philae. The DI crater has been stated to be a strength crater rather than gravity hence the deviation from the date is to be expected [61, 100]. In the case of the Philae crater, even though the observed crater radius is about 1 m, the error in observation is more than half of the observed crater and about 0.56 m [21]. If it is higher than the stated value in Biele et al. [21], it may be place in the clustered data in Fig. 4.1. The reason for the other two data points is likely to be due to the calculation errors as there is no direct data available for those. On the other hand, for the rest of the data there seems to be an agreements across impact regimes that the cratering theory may be working all those cases. Especially the agreement of two low-gravity data at two different impact velocities (Gault & Wederkind (1977) and Cintala et al (1989)) indicates that the cratering theory may not only be valid under Earth-gravity but also valid under low-gravity. Given the fact that the recent SCI experiment on Ryugu following given scaling laws further reinforces this statement. The agreement of these result with even lower velocity impacts under Earth gravity, is a further indication that the cratering theory may be valid for low-speed impacts as well. Now it is worth noting that the underlying physical processes might be different. It is known that impact at high-speeds (*i.e.* km/s) involves complex processes, such as phase changes in materials and mixing of impactor and surface materials through melting and vaporizing [57]. This does not occur in low-speed cratering; material is merely pushed around and interaction is mainly through friction and momentum exchange. Nevertheless, the results show an agreement in crater sizes at different impact regimes.

Before discussing the other aspects of the cratering theory, the crater radius discussion will be further extended. In the original paper that the fundamentals of the crater-scaling theory are laid out, Housen, Schmidt & Holsapple (1983) discuss crater-scaling in terms of impactor momentum and impactor energy, depending on the value of μ and ν [50]. Given that ν value is very-well constrained to ~0.4 [2], the μ value is expected to be between μ = 1/3 and μ = 2/3 where the values are the limits of momentum- and energy-scaling respectively. In various experiments with dry granular materials the μ value is found to be ~0.41, indicating impactor-momentum dominance in cratering. This is also true for experimental studies investigated here.

The similar stated μ values were found in Schmidt (1980), Yamamoto et al. (2006), Tsujido et al. (2015) and Takizawa & Katsuragi (2020) [54, 93, 88, 90]. The spacecraft craters presented in Fig. 4.1 will be tested against this to (1) further test the theory in low-gravity and (2) verify the driver parameter in the cratering process of those spacecraft craters. The results of this analysis is shown in Fig. 4.2.

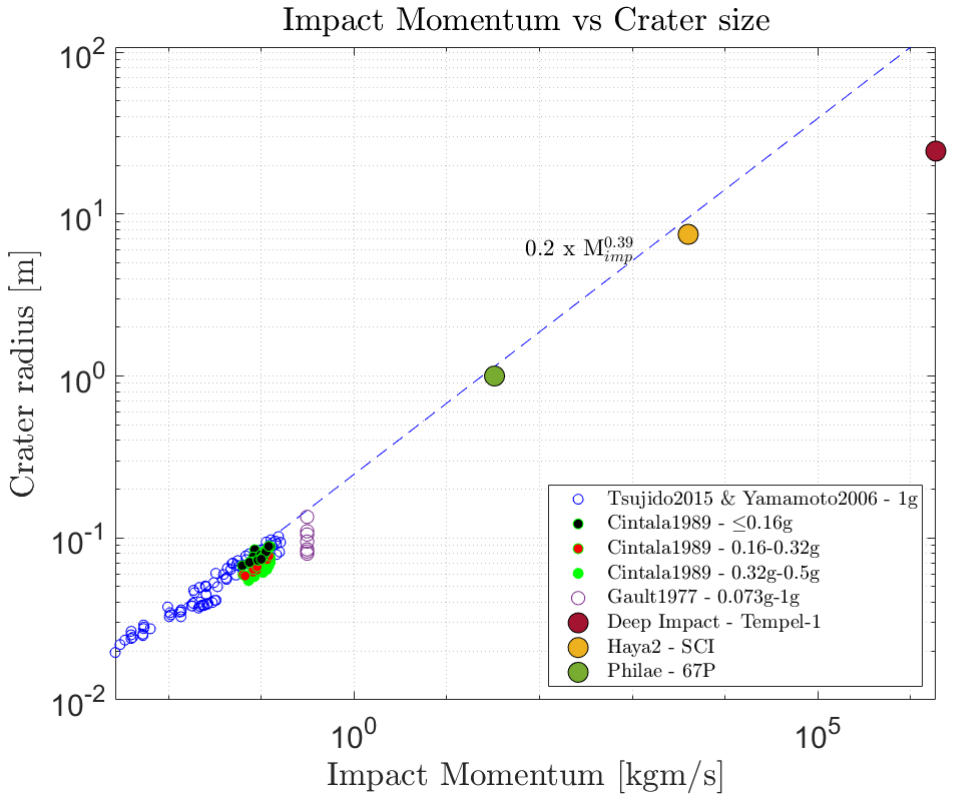

Figure 4.2: Relation between impact momentum and crater size

When generating Fig. 4.2, the crater radii results from the studies in Table 4.1 are used. From the impactor and impact velocity data, impact momentum of each experiment run is computed. Those momentum values were then used to fit an exponential function similar to those presented in the previous studies. Similarly, spacecraft impact momentums were computed by assuming spacecraft as sphere. For example, Philae is a ~97-kg spacecraft with three landing footpads. In that case, the impact momentum of Philae footpads assumed equal in each. The DI spacecraft also was assumed as 1 m radius spherical ball of ~370 kg similar Holsapple & Housen [58].

The SCI has well-defined properties obtained from Ref. [97, 1] hence it is easier to compute its impact momentum. According to the results in Fig. 4.2, impact momentum is scaled with a power of 0.39. The Philae and the SCI craters exhibit near-perfect agreement with this result. However, the DI crater shows a divergence from this result. The exact reason of this is unknown, but that might be due to the strength-regime characteristics of the crater.

From the available data, one can also discuss about ejection speed results. This data is only available in Housen & Holsapple (2011) [2], Tsujido et al. (2015) and for one experimental run in Boudet et al. (2006). Those were all shown in Fig. 4.3.

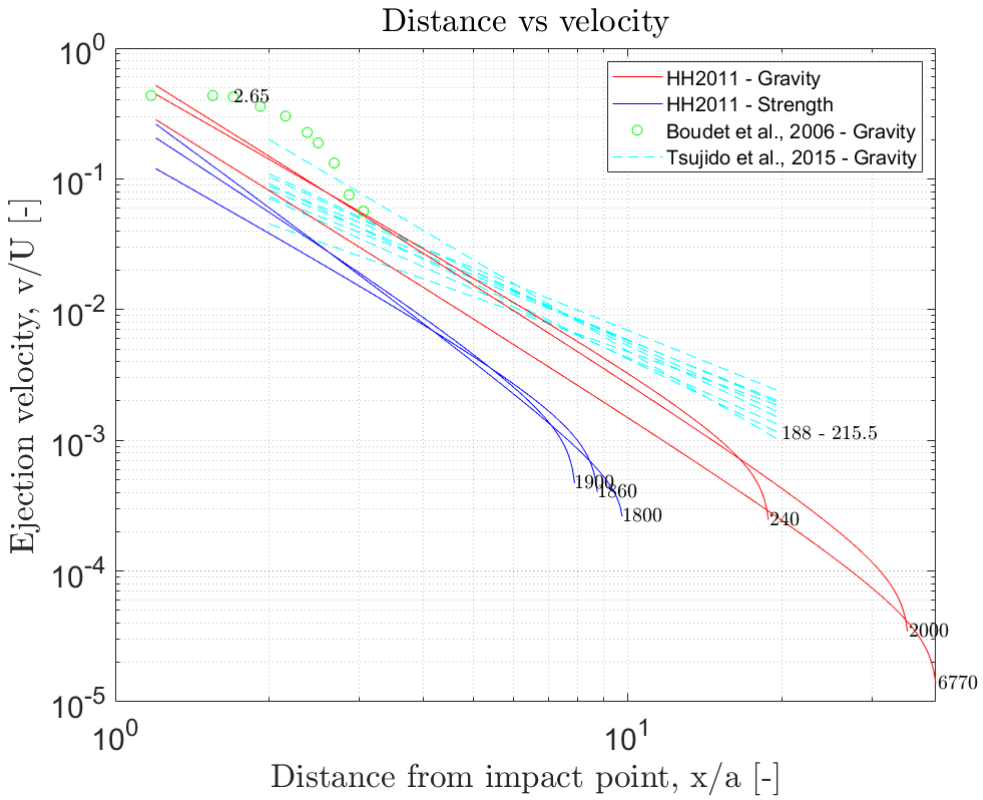

Figure 4.3: Ejection velocity profile in different experiments

Because of the lack of availability in the data, this time strength regime crater ejection velocity results from Housen & Holsapple (2011) were also presented. Note that, in the original convention, the x-axis would show the normalized distance in $(\frac{x}{a})(\frac{\rho}{\delta})$ form. In such case, the Housen & Holsapple results collapse into a single line

[2]. But in this case only x/a is used as normalized radial distance as the data is given in that form in Tsujido et al. (2015) [88]. Again the data in Boudet et al. (2006) was adapted to its form presented in Fig. 4.3. The numbers in the line figures denote impact velocities of those experiments. The results show a weaker agreement than that of crater radii shown in Fig. 4.1. However, an agreement can be confirmed for distances closer to impactor. The parts of data where disagreement occurs may be explained by effect of impact speed, gravity/strength dominance near crater rims which alters the ejection profile, or difficulty in measurement as well as the potential calculation errors (for the Boudet et al. (2006) case only).

The final aspect of the cratering results is "mass ejected with velocity higher than velocity $v(x)$" as defined by Housen & Holsapple [2]. In other words, this is the total mass ejected within a certain radius of crater. However, there is no data available on that at different impact regimes to test this aspect of the theory at this time.

All in all, this section aims to built a hypothesis through the previous studies that there is a compelling evidence that the crater-scaling theory may be working low-speed impacts under low-gravity, at least gravity-scaled craters. The crater radius results show a strong evidence that the theory's predicted crater sizes are valid across different impact regimes. Given the fact that the crater-scaling theory is tested for its different aspects over these years, the theory should also be valid for ejection speeds and ejected mass aspects, even though the data is limited or practically non-existent in the conventional sense that the theory was first posed. In order to test the hypothesis built here and to overcome measurement limitations and make more accurate tests of the theory under the regime of interest, the discrete element method (DEM) simulations will be utilized.

4.3 DEM Simulations

A full study of the applicability of the crater scaling laws to lower-speed impacts is currently a gap in the experimental literature. This is because performing impacts at below-m/s speeds is difficult on Earth in terms of data resolution due to high gravitational acceleration. On the other hand, currently available low-speed impact data under low-gravity only provides phenomenological explanations due to these challenges in measurements [91]. To overcome these limitations and bridge the

aforementioned gap in literature, this study instead makes use of discrete-element method (DEM) granular mechanics simulations in order to test the crater scaling laws quantitatively. The DEM simulations avoid limited low-gravity time and test conditions, as well as vibration-caused noisy data in drop towers and parabolic flights while allowing to perform virtual “experiments" in any small-body environment.

The DEM code employed in the study is called `pkdgrav`, a state-of-the-art parallelized granular mechanics code, which treats particle collisions through a soft-sphere discrete element method (SSDEM)[6]. Through SSDEM implementation, `pkdgrav` handles multi-contact and frictional forces using dissipative and frictional parameters that allow mimicking the behavior of angular and rough particles. The code has been tested extensively and calibrated for a variety of materials to represent granular behaviour realistically throughout different studies [74, 101, 102].

Impact simulations of a spherical impactor in the study are performed in local vertical at speeds between 1 cm/s and 0.5 m/s in a regolith bed under 1e-5g that is created in the simulation environment. The selected level of gravity covers the currently-visited asteroids Ryugu and Bennu, as well as previously-visited comets 67P and Tempel-1 and asteroid Itokawa. The selected velocity range also covers frequently-encountered impact velocities on small-body surfaces. Recall from the previous section that the cover of MINERVA-II landers impacted on Ryugu’s surface at ~28 cm/s [79], whereas Philae impacted on 67P’s surface at 1 m/s [21]. MASCOT landing on Ryugu is estimated to occur at ~17 cm/s from onboard measurements [4].

The DEM simulations were initiated with equal-sized 38000 particles of 1 cm radius and 1600 kg/m^3. The particle size is selected to be equal to eliminate particle size effects in the simulations. On the other hand, the particle density is selected arbitrarily without targeting a specific asteroid material, although the selected value is stated for Phobos material in the past [103]. A selected 35% packing fraction results in 1400 kg/m^3 bulk density material. The simulated free-fall motion of these particles fills a 0.55 m radius cylindrical container up to 0.28 m. Spherical impactor is dimensioned to be a minimum of 5 cm in radius in order to minimize coupling effects in momentum and energy exchange, as suggested by Housen & Holsapple [2]. Similarly, the maximum radius of impactor can be up 11 cm in order to eliminate container effects [104]. Throughout experiments, density of the impactor is varied to observe the difference in interaction. Specifically, the impactor density δ is varied from one-tenth to about twice

the bulk density of the impacted material, ρ. An illustration of the initial simulation set-up is presented in Fig. 4.4.

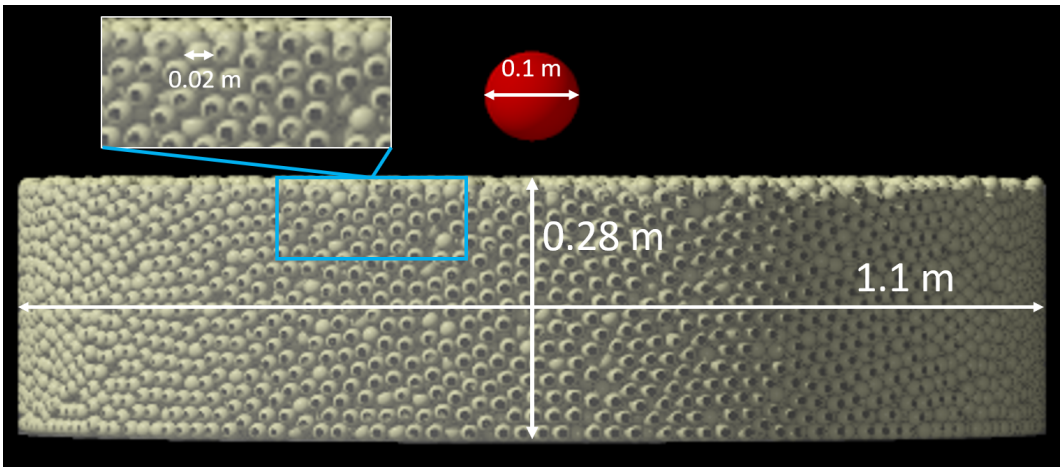

Figure 4.4: Initial simulation setup

As noted earlier, pkdgrav models the interaction between particles with a set of contact parameters. The SSDEM implementation of pkdgrav requires spring coefficient that is determined primarily by expected velocities of the grains [6]. This is not known, except the case of free-fall, hence it was set to be impact velocity. In addition to that, user is required to provide the normal and tangential coefficients of restitution (ϵ_n, ϵ_t, respectively), as well as the coefficients of Coulomb, rolling and twisting frictions (μ_s, μ_r and μ_t, respectively). Instead of arbitrarily appointing these numbers, this study makes use of previously-calibrated values . pkdgrav was previously tested in impact experiments with glass-beads material [101] and in simple avalanche experiments with similar-sized gravel materials [102] and subsequent simulations were performed to reproduce the apparent experimental behaviour. The values are reported in Yu et al. (2014) [102] and Ballouz et al. (2015) [5] and also summarized in Table 4.2.

At the time the reporting of those parameter values in Table 4.2, pkdgrav did not have twisting friction functionality [105], hence it is assumed 0 in the simulations here. The initial simulations are performed with the glass bead parameters. It was previously reported by Housen & Holsapple (2011) that low friction between glass bead particles results in amplified behaviour, especially in ejection velocities [2]. This will be addressed later in the chapter. Table 4.3 summarizes the covered parameter space.

Table 4.2: Summary of SSDEM material parameters [5]. k_n value is calculated from Schwartz et al. (2012) [6]

Parameters	Glass beads (GB)	Gravel (GR)
ϵ_n	0.95	1.31
ϵ_t	1.0	3.0
μ_s	0.43	0.55
μ_r	0.1	0.55
k_n	75.25 kg/s^2	

Table 4.3: Covered parameter space during simulations

Parameter	Value
a [m]	0.05
δ [kg/m^3]	100, 260, 520, 1040, 1910
U [m/s]	0.1, 0.05, 0.1, 0.5
ρ [kg/m^3]	1400
ρ_p [kg/m^3]	1600
r_p [m]	0.01
ϕ [%]	35
g [m/s^2]	$9.81 \cdot 10^{-5}$

Among previously undefined parameters in Table 4.3, r_p and ρ_p are particle radius and density of the granular system, respectively. ϕ denotes porosity and g denotes gravity acceleration.

A total of 27 simulation were performed during this study. As each particle's state is recorded during the simulations, the collected data are post-processed to compute not only crater size but also velocity field and ejected mass during the process. This would then yield a complete test of the theory under given conditions which is typically not available in experimental studies. In the following subsection, simulation outcomes will be discussed in more detail.

4.3.1 Qualitative cratering results in low-speed impacts

The overall simulation outcomes are shown in Fig. 4.5. A large portion of simulated impacts resulted in penetrating the surface before stopping. This includes all 1 cm/s-impacts, most of 5 cm/s-impacts, and half of 10 and 50 cm/s-impacts. Bouncing

behaviour is observed when impactor density is less than or equal the quarter of surface density. While this transition was clear for impact speeds ≥10 cm/s, it is less clear in 5 cm/s and non-existent in 1 cm/s impacts. This might be due to the already extremely low energy in these two cases, where all or most of energy is absorbed upon impact.

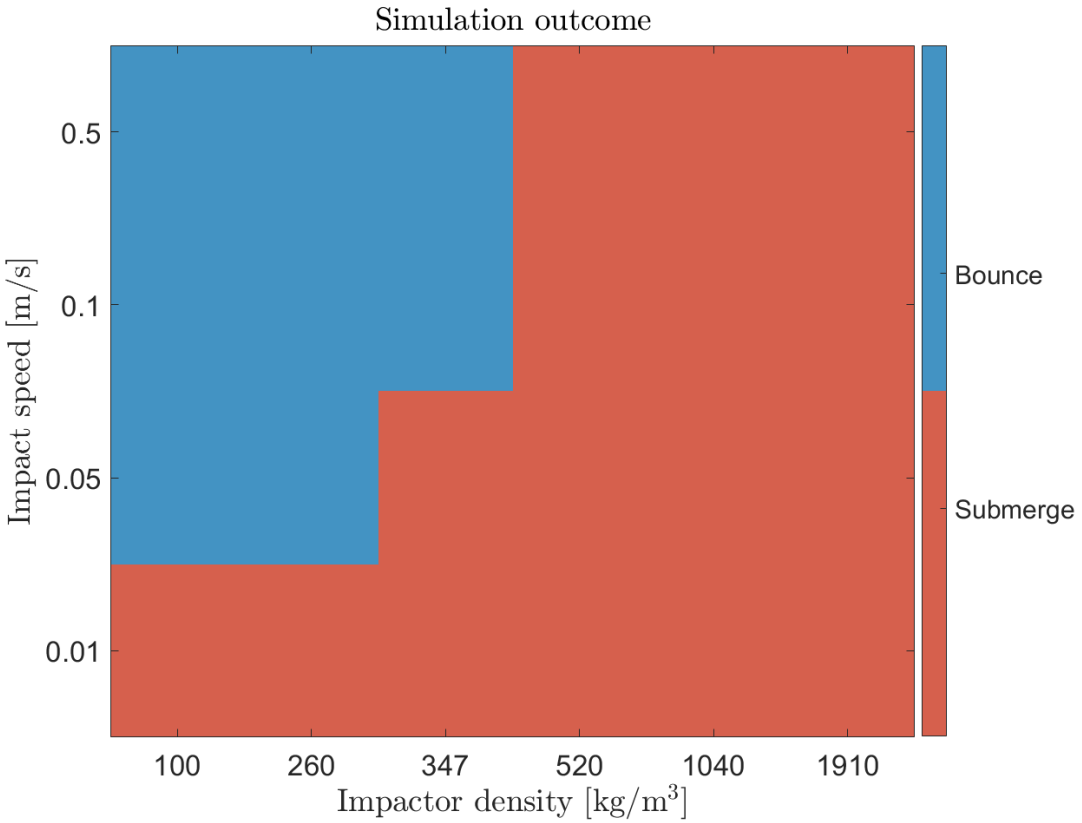

Figure 4.5: Simulation outcomes

In all penetration cases, it was observed that penetration depth is proportional to impact speed, *i.e.*, higher speed penetrates deeper than lower speed for given density. This observation is in line with the experiments performed under Earth gravity or reduced gravity created in laboratory environments, at similar or slightly higher speed impacts [106]. It was also observed that even at relatively low 10 cm/s impact speed, the impactor appears to penetrate through the bottom of the virtual container. On the other end of the velocity spectrum, impactors with 1 cm/s-velocity never fully penetrates but rather creates a depression whose depth is higher at higher densities.

Bouncing to submerging transition appears to begin at about impactor-to-target density ratio δ/ρ ~0.4 where impactor does not penetrate fully, but does not bounce either; rather it slides along transient crater wall as crater is growing. The final crater has an asymmetrical shape in this transition case because of impactor's stopping in crater wall. This behaviour seems to occur when δ/ρ ~0.25-0.4 for the selected granular material properties for $U \geq$10 cm/s. For U ~5 cm/s, lower end of this ratio is reduced to ~0.2. As mentioned earlier, bouncing behaviour was never observed for 1 cm/s-case.

The observed craters can be categorized into two, as"fully-formed" and "partially-formed" craters. An illustration of those with associated formation process is shown in Fig. 4.6.

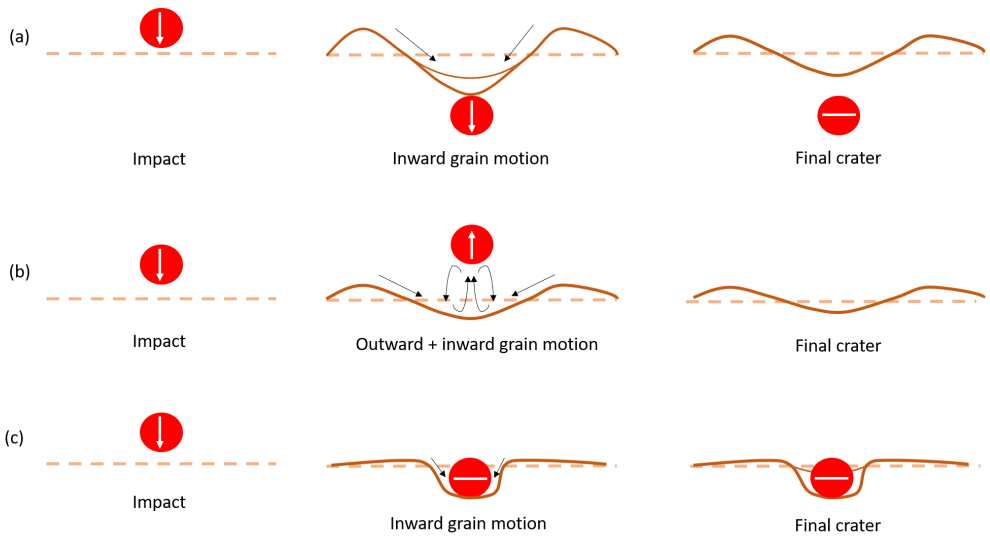

Figure 4.6: The observed crater formation process in the simulation outcomes. (a) Fully-formed craters after impactor-submerge, (b) Fully-formed craters after impactor-bounce. (c) Partially-formed craters. Direction of arrows denote direction of motion. straight horizontal lines denote stationary impactor

"Partially-formed crater" refers to craters where impactor does not submerge or bounce but floats on surface. That situation results merely pushing material to sides and below. Crater depth in this case is the depth impactor penetrates, which would likely to be different than the expected value from crater-scaling theory. This will be discussed

later. This is observed only in 1 cm/s-case for the simulations performed here with selected granular material parameters. Fully-formed craters are more closer to craters that were observed in high-speed impacts. They have parabolic nearly-symmetrical crater shape with elevated rims on the side and distinctive depth. They occur similarly in both full-submerge and bounce cases, albeit with slight difference in the process. In the former, after full submerge occurs, a granular follows occurs from initial transit crater walls towards crater bottom to fill the void created by penetrating impactor. In the latter, there is no full penetration but a bounce after interacting with the first few layers of granular material. There is also smaller scale granular follow from transient crater rim towards bottom but there is also an upwards material ejection from crater bottom. initiated by impactor. Because there is only an interaction between impactor and the first few layers of granular bed, crater depth tends to be higher than their fully-submerged counterparts. In the following subsection, a more quantitative analysis will be presented on crater sizes.

4.3.2 Crater size

Procedure to detect crater size

Crater size will be the first quantitative aspect to discuss. In a laboratory-setting, crater radius (or diameter) is usually the easiest property of a crater to be measured. Because of usually-large impactor-grain radius ratio, the final crater figure appears like a plastically-deformed solid material even though it is in a delicate state and can be disturbed with any contact with it. In the DEM simualtions here, because of the selected particle radius (*i.e.*, 1 cm), the final crater figure is a lot more discontinuous. In that case, one needs to be more careful in correctly estimating radius while being applicable to range of crater morphologies presented in previous subsection. An algorithm is therefore developed to address this and tested in different craters. That was presented in Alg. 4.1 and applied in determining crater radius and depth.

In short, Alg. 4.1 selects particles on top few layers of final crater and finds a circle that fits the best to closest particles to impact points, representing the crater rim. One of the primary issues with this approach is that best-fitting circle shifts towards regions where more particles are found due to the inherent nature of the least-squares method. However, a crater in this case is defined by empty regions

Algorithm 4.1 Crater radius detection algorithm

procedure CRATER RADIUS AND DEPTH(Initial granular state, Final granular state)
    Select grains within container dimensions and selected height
    Calculate radial, angular positions of particles, R_p, θ
                                                ▷ First, find crater radius
    Find highest particle's height, h_{max}
    if $h_{max} > 0$ **then**
        Select all particles from 1 cm below the initial height, h_0, to h_{max}
        Divide circular region defined by cylinder radius to 3, 6, 9 portions, n_r
        for n_r = 3, 6, 9 **do**
            for j = 1:n_r **do**
                Find total number of particles in each region, n_p
                if $n_p \geq 5$ **then**
                    Sort particles in ascending order of R_p
                    Select first five particles
                else if $n_p < 5$ **then**
                    Select all found particles
                end if
                Apply a least squares algorithm `fitcircle`(R_p) to find crater radius $R_{cr}^{n_r}$
            end for
        end for
        R_{cr} = mean($R_{cr}^{n_r}$)
    else
        Warning: "Crater is either larger than the container dimensions or not formed at all. Check output"
    end if
                                                ▷ Second, find crater depth
    Find particles with $R_p \leq 2r_p$ & $h_p < 0$
    Sort selected particles in descending h_p order
    Select max(h_p) as crater depth d_cr
end procedure

rather than populated regions, therefore a careful selection of particles is necessary. Similarly, selected number of particles also affect final calculated crater. If more particle is selected, then crater size will naturally be overestimated and if, on the other hand, too few particles are selected, then the crater radius will underestimated. Moreover, a blind selection of closest N particles would not work either, because it would only result in a shifted circles towards particles in most densely-populated part of final crater, as a crater is often not perfectly symmetrical.

In order to overcome these difficulties, circular region defined by container radius is divided into portion and closest N particles are selected within that portion, so a proportionate particle selection can be ensured. Furthermore, in order to avoid over- or underestimation of crater radii, that circular regions is scanned and divided into larger or smaller portions and a mean crater radius is calculated. In each portion, $N = 5$ particles are selected after an analysis of between number of portions and particles selected as provided in Fig. 4.7.

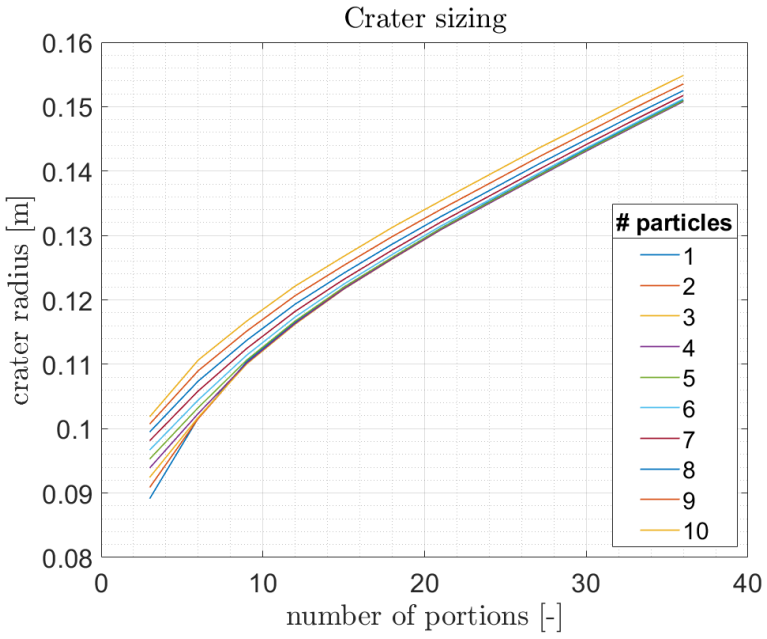

Figure 4.7: Crater sizing algorithm parameter selection

According to the results of Fig. 4.7, there is a parabolic increase in the beginning when there are small number of portions and grows linearly after ~10 portions. It also appears that estimated crater radius is largely the same for up to same particles except

when number of portions is small. Therefore five particles are selected at each portion in order to increase fidelity in the least-square results. Also, three different number portions of 3, 6, and 9 (scanning 120^o, 60^o and 45^o) are selected to mitigate over- or underestimation. An example result from this algorithm can be seen in Fig. 4.8.

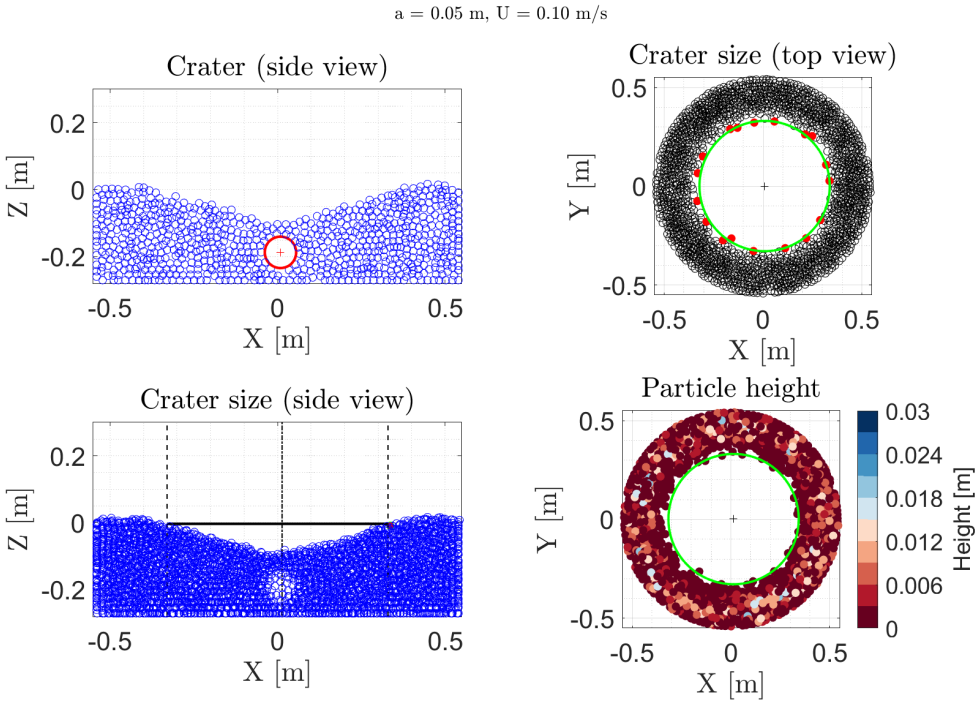

Figure 4.8: An example result from crater-size detection algorithm. The example impact case is U = 10 cm/s, δ = 1910 kg/m^3.

As one can see in Fig. 4.8, the finally-detected crater represent the observational crater well (left figures), and the selected particles (red dots in top-right figure) are evenly distributed to represent a crater rim. Particle heights are also close to 0 (bottom-right), and calculated from this point, therefore appropriate for comparison to experimental data. All in all, the applied algorithm appears to be robust while simple and versatile enough to modify when necessary, *e.g.* when there are emptier regions or the shape is more elliptical.

Results

The results of all simulation runs are tabulated in Table. 4.4.

Table 4.4: Tabulated simulation conditions and outcomes. All simulations under 9.80665e-5 m/s^2 (0.00001g). Radius of all impactors is 0.05 m. S: Submerge. B: Bounce.

#	U [m/s]	δ [m^3]	ρ [m^3]	DEM ParSet	R_{cr} [m]	d_{cr} [m]	π_2	π_R	Out
1	0.1	1910	1400	GB	0.329	0.103	4.903e-4	4.089	S
2	0.05	1910	1400	GB	0.240	0.081	1.961e-3	2.984	S
3	0.01	1910	1400	GB	0.093	0.084	4.903e-2	1.153	S
4	0.1	100	1400	GB	0.152	0.048	4.903e-4	1.890	B
5	0.05	100	1400	GB	0.106	0.031	1.961e-3	1.318	B
6	0.5	100	1400	GB	0.294	0.086	1.961e-5	3.645	B
7	0.1	1040	1400	GB	0.326	0.073	4.903e-4	4.040	S
8	0.05	1040	1400	GB	0.238	0.052	1.961e-3	2.956	S
9	0.01	1040	1400	GB	0.089	0.074	4.903e-2	1.111	S
10	0.1	520	1400	GB	0.280	0.066	4.903e-4	3.478	S
11	0.05	520	1400	GB	0.192	0.077	1.961e-3	2.386	S
12	0.01	520	1400	GB	0.075	0.047	4.903e-2	0.935	B
13	0.1	260	1400	GB	0.226	0.053	4.903e-4	2.800	B
14	0.5	260	1400	GB	0.380	0.107	1.961e-5	4.715	B
15	0.05	260	1400	GB	0.168	0.041	1.961e-3	2.087	B
16	0.1	1910	1400	GR	0.282	0.129	4.903e-4	3.501	S
17	0.1	346.7	1400	GB	0.259	0.066	4.903e-4	3.220	B
18	0.01	100	1400	GB	0.046	0.015	4.903e-2	1.375	B
19	0.01	260	1400	GB	0.065	0.032	4.903e-2	1.419	B
20	0.05	346.7	1400	GB	0.182	0.048	2.000e-3	3.604	S
21	0.01	346.7	1400	GB	0.072	0.043	4.903e-2	1.424	S
22	0.50	520	1400	GB	0.516	0.134	1.961e-5	8.901	S
23	0.50	346.7	1400	GB	0.527	0.097	1.961e-5	10.413	B
24	0.05	260	1400	GR	0.123	0.097	1.961e-5	10.413	B
25	0.10	260	1400	GR	0.158	0.052	4.903e-4	3.429	B
26	0.10	530	2118	GB	0.211	0.072	4.903e-4	4.153	B
27	0.10	706	2118	GB	0.187	0.099	4.903e-4	3.345	S

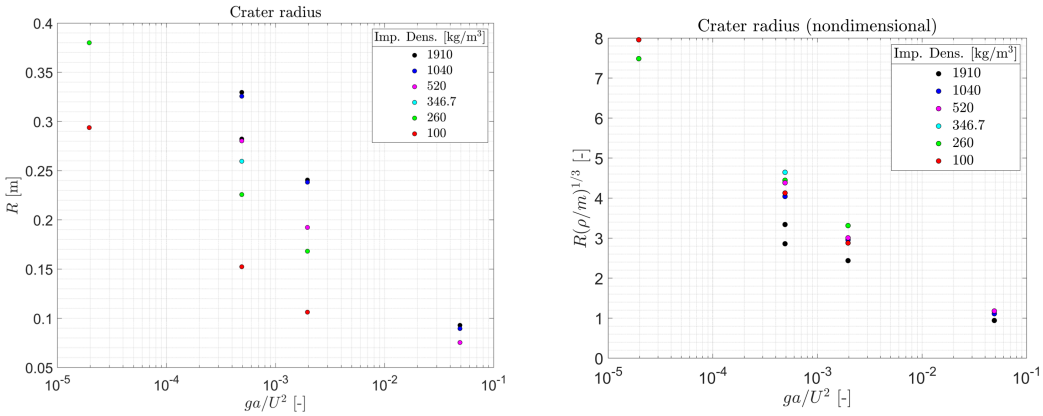

(a) Dimensional

(b) Nondimensional

Figure 4.9: Crater radius as a function of gravity-scaling parameter

In Table 4.4, a new π-scaling parameter, nondimensional crater radius is introduced and can be defined as follows:

$$\pi_R = R_{cr}\left(\frac{\rho}{m}\right)^{\frac{1}{3}} \tag{4.1}$$

As it is often easier to measure crater radius then crater volume itself, π_R will be used to compare the previous experimental studies. Figure 4.9 shows dimensional and nondimensional crater radius as a function of π_2 or gravity-scaling parameter.

Note in Figure 4.9 that x-axis is in log-scale whereas y-axis is in linear-scale. A distinctive feature is present: Lower the π_2 values are (higher impact speed), larger the crater is, irrespective of submerging or bouncing, for a given δ. Among different δ values, higher δ values result in larger craters. Even though this statement is true for all δ values that are tested, the crater size in two highest δ cases are very close to each other, regardless of impact velocity and their different depth. The reason is not known at this point, but that could be pointing out a impactor-to-target density ratio above which density effects are negligible. At lower densities impactor does not have enough weight to overcome the shear strength that is applied by the granular system through the frictional interaction between grains. It happens such that at the lower end of δ values the impacts actually result in bounce of the impactor away from the surface. When, the results are investigated in π_R-π_2 space, as provided in Fig. 4.9b, one can notice clustering of all $\delta < \rho$ cases together, irrespective of their bouncing or submerging situation. Those δ values represent cases that are 0.07%-0.75% of target

density ρ. At this range, crater radius seems to have minimal dependence to impactor density. The only diverging case is $\delta = 1910$ kg/m^3, *i.e.*, $\approx 2\rho$. A few more data points are necessary to state in a robust way that density dependency exists or not, but it does not seem to be the case when $\delta < \rho$. The impactor density dependency is still an open issue in cratering theory, and thus far only Tsujido et al. (2015) tackled the problem extensively and few other studies mentioned in Housen & Holsapple (2011) [88, 2].

Furthermore, as a test case, one simulation was run with gravel properties presented in Table 4.2 and with $\delta = 1910$ kg/m^3 (equivalent to 1 kg impactor) with $U = 10$ cm/s. This resulted in a smaller crater, in fact the crater is nearly in the size of a crater made by an impactor of quarter the density at the same impact velocity. This provides a glimpse of the effect of more frictional grain properties in cratering in low-speed, which will be discussed later.

In order to quantitatively assess the cratering law in low-speed impact regime under low-gravity, one can write following relation from π-scaling relations provided in Sec. 2.4.1:

$$R_{cr}\left(\frac{\rho}{m}\right)^{\frac{1}{3}} = K_1\left(\frac{ga}{U^2}\right)^{-\frac{\mu}{2+\mu}}\left(\frac{\rho}{\delta}\right)^{\frac{6\nu-2-\mu}{3(2+\mu)}} \tag{4.2}$$

In π-scaling terms, the equation would take the following form:

$$\pi_R = K_1\pi_2^{-\alpha}\pi_4^{-\gamma} \tag{4.3}$$

As stated earlier, the density effects will be assumed to be negligible until more data available. Then the π_R relation would take the following form:

$$\pi_R = K_1\pi_2^{-\alpha} \tag{4.4}$$

where $K_1 \approx K_1\pi_4^{-\gamma}$. From Eq. 4.2, following equality can be found:

$$\alpha = \frac{\mu}{\mu+2} \Rightarrow \mu = \frac{2\alpha}{1-\alpha}$$

where μ is a material-dependent exponents usually related to high-pressure properties of target. μ is usually found ~0.4 for dry sand found ~0.55 for water in gravity-regime cratering. The values in between are also found. μ value drives whether impactor momentum or impactor energy drive the crater radius. Therefore this value is going to be calculated to decide the cratering regime that low-speed craters under low-gravity

Table 4.5: μ values of different data sets. δ = 1910 - GR (single data point with gravel DEM properties) were omitted in all data sets.

	μ	R^2	Remark
Set#1	0.55	0.96	All data
Set#2	0.50	0.92	All but partially-formed craters data
Set#3	0.51	0.98	Only $\delta < \rho$ data
Set#4	0.46	0.96	$\delta < \rho$ data without partially-formed craters

are. In cratering experiments thus far, the procedure to find μ usually follows similar steps except specific aspects of cratering process that are targeted in studies. This is because impact speeds are usually high, impactors are small in size and no partial cratering occurs, hence experiments are similar. Even bouncing results are limited to few recent studies, *e.g.*, Ref. [90, 107]. However, in the simulations here, there are at least three different ways of cratering occurs, as described in the previous subsection. Therefore, multiple μ values will be computed on order to achieve a fair comparison with the literature.

First of all, a single case of impact with gravel DEM properties will be removed from the dataset such that all data constitute same material properties. Second, partially-formed craters (*i.e.*, all 1 cm/s impacts) will be removed from the dataset to compare only fully-formed craters. Third, only data from $\delta < \rho$ cases will be utilized (including partially-formed craters). Finally, third set will be utilized without partially formed craters. The power law fit will be found with MATLAB's `fit` function. The μ value of each dataset is provided in Table 4.5.

The use of all crater data available results in a μ value of 0.55 - scaling exponent similar to water. It is also higher than half between momentum or energy scaling, showing more of a impactor energy dependence. While a granular media in low gravity can behave differently than on Earth, this scaling result might actually be pointing out a density-dependence on crater size. Tsujido et al. (2015) found similar a μ value from impact experiments at relatively low speeds (~100-200 m/s) and varying δ between 1100 and 11000 kg/m^3 [88]. In the simulations here, δ is varied by a factor of ~20, hence the results here is likely to be following the findings of Tsujido et al. (2015) [88]. Of course, the data in Set#1 also includes data from partially-formed craters, which may not be entirely appropriate to include in the analysis to compare due to their

non-traditional nature. The μ value decreases to 0.5 when partially-formed craters were excluded. The μ value found in this case is in the mid-point between momentum and energy scaling, but ultimately it could still be density effects that is involved in this case, as there is a divergence in the high-δ case. The best fit for the μ value is achieved in Set#3, again greater than 0.5. While the density effects are minimal in this data set, the inclusion of partially-formed craters in the data could artificially be increasing the μ exponent. Set#4 is the only data set that is free of any of the aforementioned affects, *i.e.*, the density effects are minimal and all craters are fully-formed with both bouncing and submerging cases. It is therefore believed Set#4 represents the best of scaling in these simulations. A μ value of 0.46 is recovered in this case. This value is higher than generally-accepted ~0.4 for sand or cohesive soil [58] but still in the momentum-scaling regime. Previously Cintala et al (1989) found μ as 0.444 at relatively low-speed (65-130 m/s) under reduced gravity [95]. Given that the gravity acceleration in these simulations are actually lower than those of Cintala et al. (1989), decreasing gravity may be responsible for this. On the other hand, it was stated in Housen & Holsapple that low friction between particles generally results in larger craters with increased ejecta velocities [2]. This is indeed the case in these simulations, in which glass beads parameters exhibit angle-of-repose of about 20^o, on the contrary to ~40^o gravel parameters [102], similar to those of real materials. It is expected that the gravel properties would result in smaller craters (as shown in a single case in Table 4.4), which would eventually drive μ values to lower.

One can also investigate crater radius result from impact energy perspective, as shown in Fig. 4.10.

There appears to be a crater radius is correlated with impact energy. If the relation is described as a power law, the crater size would scale with ~ $E^{0.198}$, where E is impact energy. A similar scaling exponent has also been calculated in low-speed impact experiments of Takizawa & Katsuragi (2020) and other works therein under Earth-gravity [90]. From the reported literature in Table 4.1, the energy-scaling is investigated in Yamamoto et al. (2006) and Cintala et al. (1989) for relatively low-speed cratering experiments under Earth- and low-gravity, respectively [93, 95] and the scaling exponent of ~0.19 is recovered. Therefore, it can be stated that energy-scaling results also hold for low-speed impacts under low-gravity, and may be universal, as stated in Takizawa & Katsuragi (2020) [90].

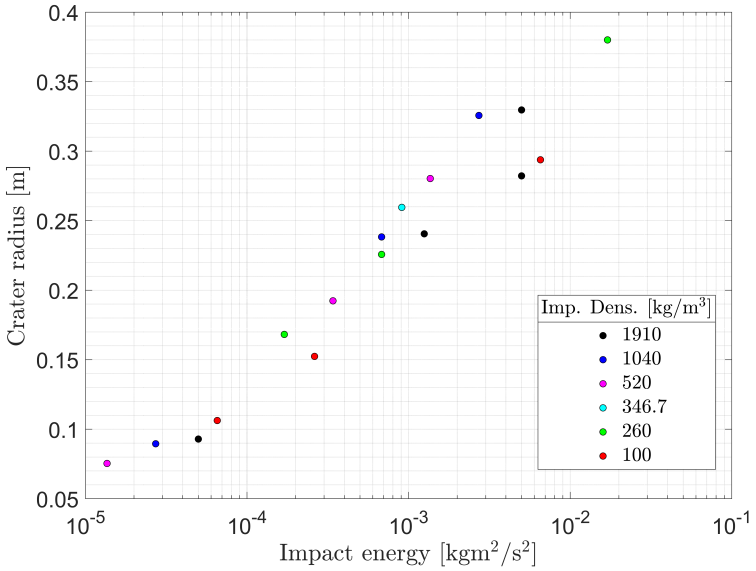

Figure 4.10: Crater radius as a function of impact energy

More discussion can be made on the crater size dependency on impact momentum, with the data provided in Fig. 4.11.

Compared to the energy dependency, the momentum dependency shows more of the effect of the density. However, the power-law momentum dependency is hinted in the small density values. At the lowest three density values, the power law dependency is around $\sim M^{0.36}$. For highest three density values, for which the data is more scattered, but the power law exponent is ~0.35. These values are slightly lower than the value ~0.39 computed from Yamamoto et al. (2006), Tsujido et al. (2015) and Cintala et al. (1989) but within same range of values.

It is also important to investigate crater depth in relation to crater radius. This relation is analyzed for both dimensional and nondimensional crater radius π_R. For the latter a nondimensional crater depth is defined as follows:

$$\pi_d = d_{cr}\left(\frac{\rho}{m}\right)^{\frac{1}{3}} \tag{4.5}$$

The results of crater depth analysis are presented in Fig. 4.12.

As noted earlier, the depth values of partially-formed craters are determined by the impactor's size, as impactor floats inside crater. Therefore radius-to-depth ratio

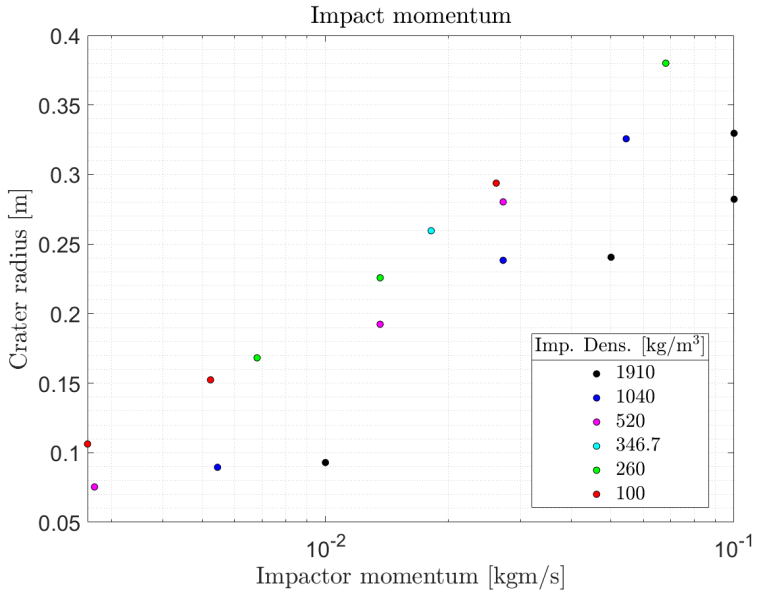

Figure 4.11: Crater radius as a function of impact momentum

reaches nearly to the side of crater and diverging from general trend almost completely. Those data are boxed in both figures. The rest, on the other hand, show a linear trend with d_{cr}/R_{cr} values varying between 0.2-0.4. Although the data appear to be scattered, one could notice individual linear trends in each density values. Trend lines that were placed follow d_{cr}/R_{cr} ~0.3 in both figures. Comparing with other works in the literature, Yamamoto et al. (2006) found d_{cr}/R_{cr} ~0.22-0.28 for impacts at 11-329 m/s impacts [93]. On the other hand, Tsujido et al. (2015) reported d_{cr}/R_{cr} ~ 0.67-0.8 at ~200 m/s impacts [88]. Tsujido et al values are even higher than those achieved in astronomical impact craters, stated in Melosh (1989) as $d_{cr}/R_{cr} \sim R_{cr}/2 - 2R_{cr}/3$ [57]. However, Tsujido et al. craters are at least an order of magnitude smaller than the craters here, and astronomical craters mentioned in Melosh (1989) are orders of magnitude larger, whereas Yamamoto et al. (2006) crater data is similar to the simulation outcomes here with a number of low-speed impact data hence it is believed to be more comparable to the DEM results. Hence given this comparison, it could be concluded that crater depths are likely to be between 0.2-0.4.

Before finalizing the cratering results, it is worth noting the effect of impactor size in the results. As mentioned earlier in this chapter that the impactor-to-particle size is taken to be 5, *i.e.*, the lower boundary where the impactor size does not affect

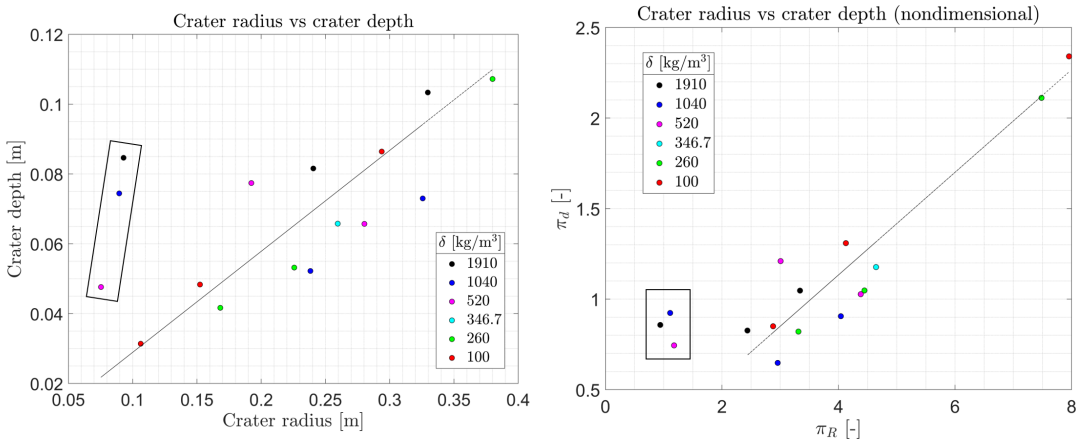

(a) Dimensional

(b) Nondimensional

Figure 4.12: Crater radius-depth relation

cratering results for high-speed impacts [2]. In order to quantify the effect of the impactor size, three more simulations were performed with impactor radius 1, 3 and 10 cm with impactor density, ρ = 1910 kg/m^3. The smallest these impactors has the same radius as the individual grains, thus that simulation can also be seen as impact of a grain to a granular bed. All impact speeds are 10 cm/s. With the scaling laws derived earlier, the crater radii estimated for these impacts would be 9.3 cm, 22.4 cm, 58.7 cm. Note that the last estimated value is larger than the simulation container size. The simulation results showed a crater that exceeded the container size, so it is likely that the scaling law estimation of the crater radius holds for 10-cm-radius impactor. For the smallest two impactors, Figure 4.13 shows the craters that were formed in the end.

The smallest impactor only creates a depression in the surface, which would be recognized when seen from the top. The amount of ejected material is limited a few particles with a small velocities and fell back to the immediate surrounding of the crater. This result matches a recent work Bogdan et al. (2020) of low-speed grain impact to a granular bed [108]. The authors showed that such an at sub-m/s speed would eject less than 10 grains, which the results here confirms [108]. The computed crater size in this impact size 8.5 cm. This value is within ~20% of the analytically-estimated value, 9.3 cm. For 3-cm-radius impactor, the computed crater size is 22.7 cm, within 2% of the analytically-estimated value. In Housen & Holsapple (2011), it is noted that for grain size effects to vanish, the impactor has to be 5 to 10 times larger than the

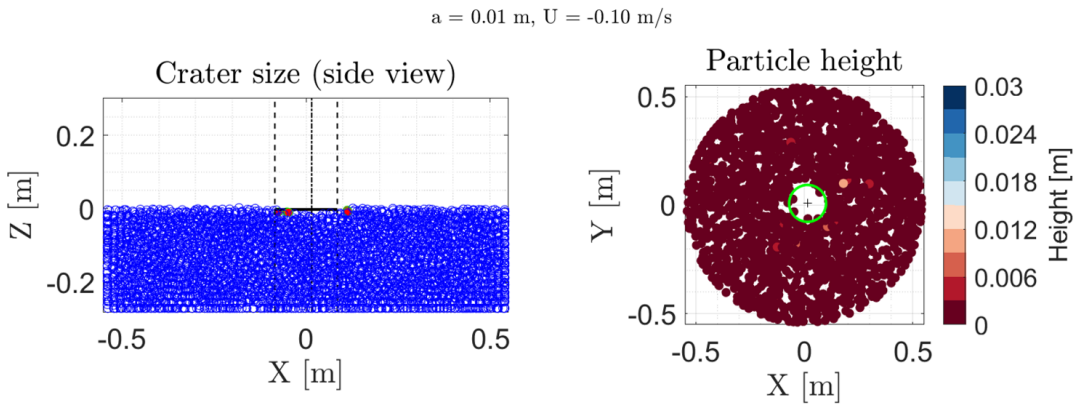

(a) a = 1 cm, U = 10 cm/s

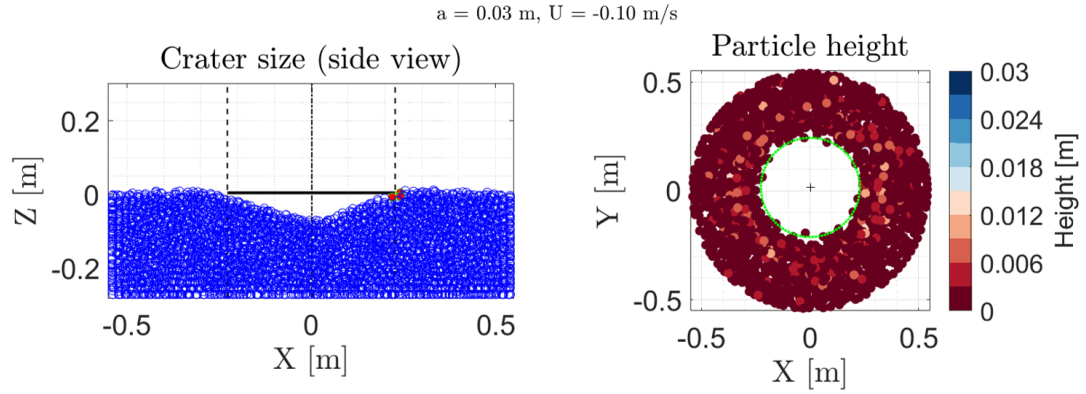

(b) a = 3 cm, U = 10 cm/s

Figure 4.13: Craters formed with smaller impactors.

grains, for $U \geq 1$ km/s [2]. Given the good match obtained between the analytical estimations and simulations results, it can be speculated that this value may be lower in low-velocity impacts in low gravity, *i.e.*, potentially ≤ 3. Even for the smallest impactor, 20% divergence from the analytical results may be a result of the crater-size detection algorithm, as the crater appears to be slightly elliptical. A more in-depth parametric study would demonstrate the particle/impactor size effects more clearly.

Big Picture

After investigating different quantitative aspects of low-speed cratering low-gravity, it is now reasonable to observe the simulation results in the general picture. For that

π-scaling results from simulations are added to Fig. 4.1 in order to compare the results here to the experimental results, as shown in Fig. 4.14.

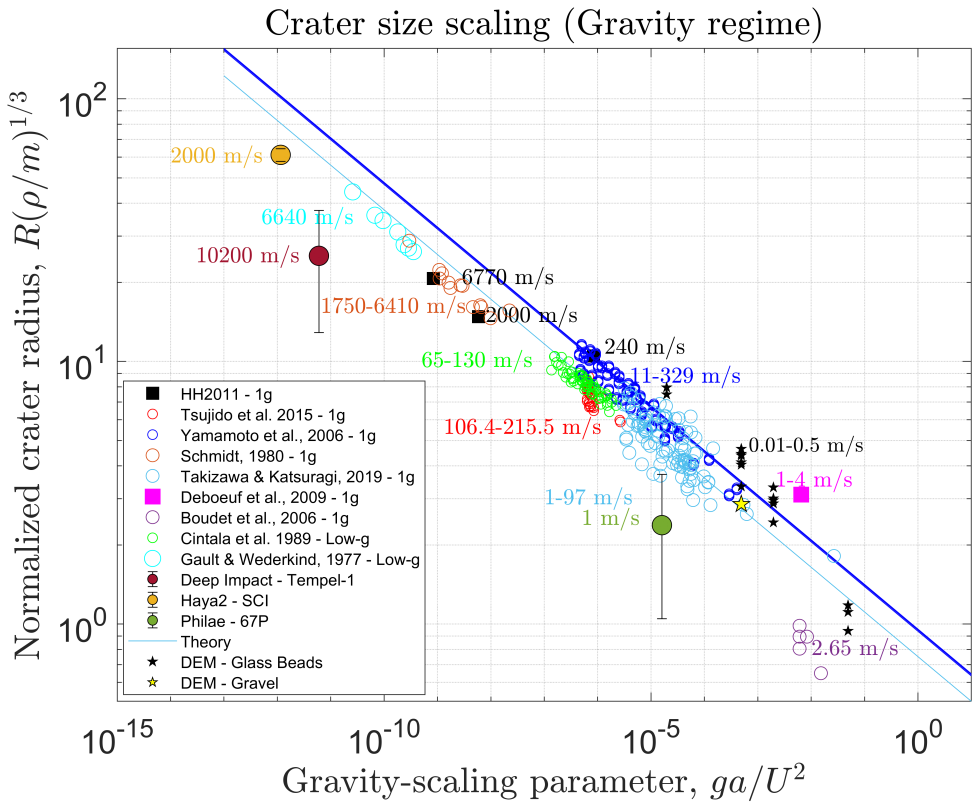

Figure 4.14: Previous experimental studies with the simulation study here. Y-axis is logarithmic.

The theory lines are generated with impact and target parameters of Yamamoto et al. (2006) and Takizawa & Katsuragi (2020) and with generic parameters $K_1 = 1.03$, $\nu = 0.4$ and $\mu = 0.41$ from Holsapple & Housen [58]. The most of the simulation results appear to be slightly outside of the bounds. This is to be expected, however: As noted earlier, low angle-of-friction of the selected DEM parameters result in larger craters [2], which eventually increase the normalized crater value. The example impact case with the gravel DEM parameters (yellow star) exemplifies this; it is placed nearly in the central line between two theory lines. It is also expected that other parameters would follow a similar behaviour and π_R values would decrease with more realistic granular parameters. A close-up comparison of the DEM data and impact experiments with

U <km/s would provide a better comparison wit similar experiment as presented in Fig. 4.15.

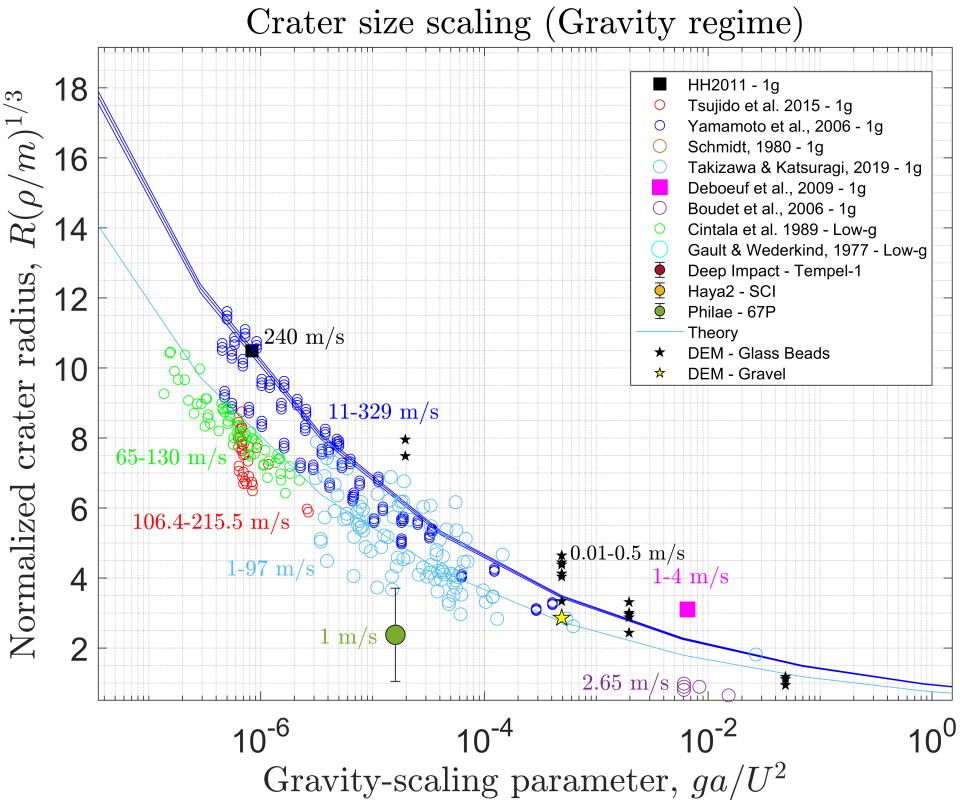

Figure 4.15: A closer look to previous experimental studies together with simulation study here. y-axis is linear.

The largest error as compared to the theory line defined by Yamamoto et al. (2006) is about 32% at most and it is likely to decrease with more realistic granular parameters in the DEM simulations.

All in all, the original results presented here provides a strong case in favor of the applicability of the crater-scaling theories for low-speed impacts under low-gravity. It is clear that more data is necessary to constrain the parameters , particularly μ and ν in order to build a robust cratering theory for impact in this regime. However, the interpretation from an example simulation hints the agreement between experimental *lower*-speed impact data and simulations.

4.3.3 Ejecta profile

Results

The velocity and and angle of the ejected materials are discussed in this section. Ejection in this case is defined to be departing the initially-defined top level of the container or $(x, y) = (0, 0)$ in the container reference frame. At the end of a simulation, the ejected particles from the container is collected and analyzed. Because of high data load otherwise, `pkdgrav` outputs the particle states after certain number of time steps passed. In the simulations here, this was selected to be 2500 steps, *i.e.*, approximately at every ~1.8 seconds, with the integration time step of ~0.7 ms. Because of this discrete data collection, first one needs to determine the particles that left the surface in between each time step or data output. After this, the particle states are collected. It is possible that between two consecutive data output, some of the particles launched from the container level and are in mid-flight. This is effectively all particles as it is not possible precisely control the output time step to synchronize with the ejection time. The states of those mid-flight particles are integrated backwards in time analytically in order to find the states of the particles at ejection. Once the ejection states are determined, it is straightforward to calculate a particle's ejection velocity and angle, as well as, its ejection time. Finally, a mean ejection velocity profile is created by dividing radial distance into 15 portions. It is worth noting that once particles are ejected, they are assumed to be *not* interacting with each other. This assumption is not verified yet with the simulation results directly but should hold for most of the particles. The results of an impact case is shown in Fig. 4.16 below.

The behaviour shown in Fig. 4.16 is largely general, albeit with differences in ejection radius as a result of impact energy. According to Fig. 4.16, the ejection velocity is decreasing with the distance from impact point as expected. The highest velocity ejecta are in the immediate surrounding of the impactor, although velocities are varying. In the specific case here, the highest ejecta velocity is about 8.5 cm/s, although it appears to be a single case. Other high-velocity ejecta have velocities 3.5 cm/s or lower. Most lowest velocity ejecta leave the surface in the outermost regions. Those and other low-velocity ejecta near the crater rim are mostly pushed-up grains during the evolution of crater and not launched from the surface. This is illustrated in Fig. 4.17.

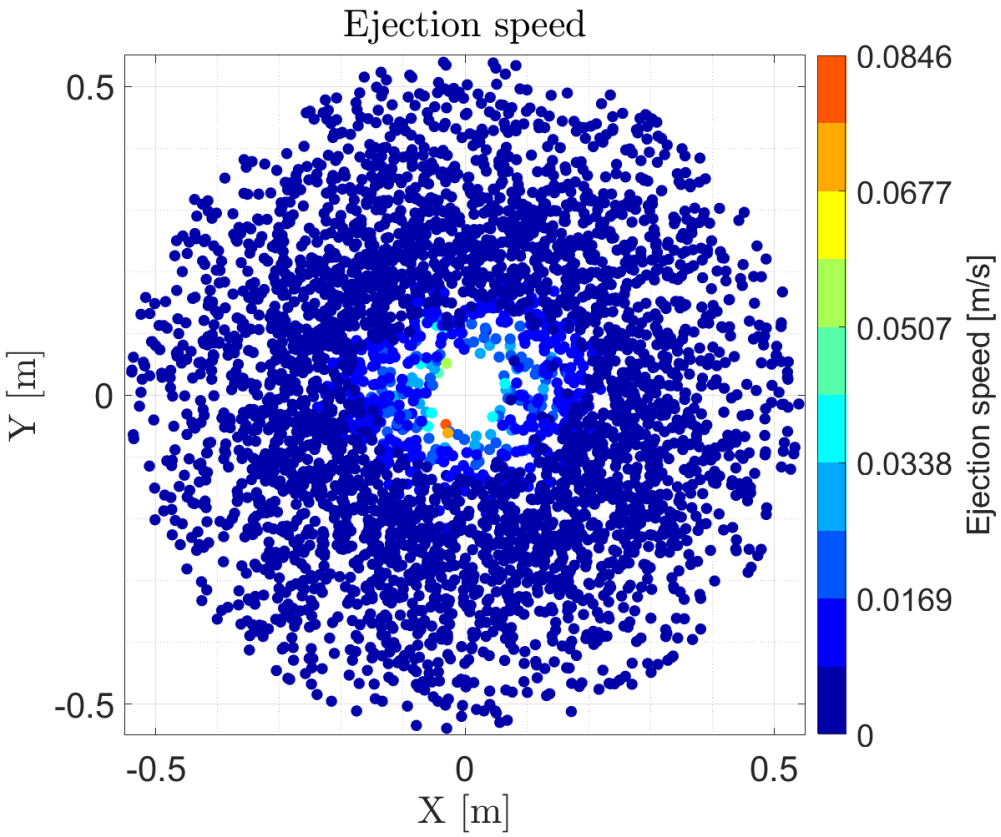

Figure 4.16: Ejecta profile (top view). Impact case: U: 10 cm/s, δ: 1910 kg/m^3 (Impact #1 in Table 4.4)

The ejection process largely ends within the initial transient crater dimensions, however, some grains are pushed above the container level as a result of a some sort of chain reaction initiated upon impact. Some of the initially ejected material also land back within the container dimensions, initiating further upwards motion of the particles. Because of this, the ejection angle of particles in those regions are rather randomized, *i.e.*, both very shallow and steep angles are observed, as shown in Fig. 4.17b. On the other hand, within the initial crater radius, ejection angle follow decreasing trend with the outward particle position,. That is to, very steep angles become shallower with increasing radial distance. This is a similar trend observed in high-speed cratering, as well. One can see mean properties of ejection velocity and angle more clearly in Fig. 4.18.

The profile shown in Fig. 4.17 is now clearer. An exponential decrease in mean

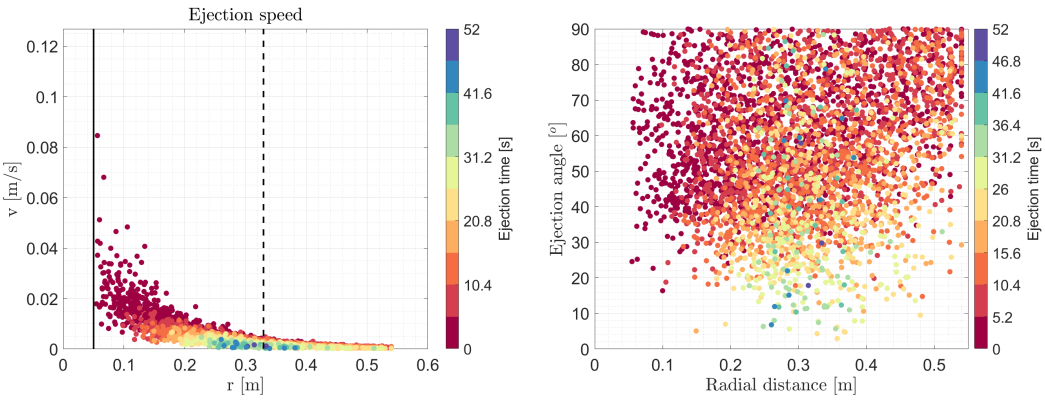

(a) Velocity (b) Angle

Figure 4.17: Ejecta velocity and angle. Impact case: U: 10 cm/s, δ: 1910 kg/m^3 (Impact #1 in Table 4.4)

velocity can be found in Fig. 4.18a. Note that even though the highest velocity in this specific case is about 4.25 cm/s the average within the given range is about 1.13 cm/s at highest. Then the exponential decrease continues slightly below 5 mm/s at the crater rim and down to 1 mm/s or lower as the radial distance approaches to the maximum ejection distance found, which is about the container radius in this case. The ejection angles, presented in the histogram in Fig. 4.18b, show that most particles depart surface with angles between 40^o and 60^o with average around 50^o. However, there's a considerable amount of ejection occur with angles greater than 60^o. Those are primarily the particles *jetted* immediately next to the impact point in the beginning or cratering or *pushed − up* as a result of a chain reaction afar from the impact point at later stages of cratering, from the interpretation of Fig. 4.17b.

Now one can look at the result of all impact simulations. Recall the nondimensional velocity expression in Eq. 2.22. The mean velocity calculated here is normalized in the form presented in Eq. 2.22. Note that the ejecta velocity results of the partially-formed craters are not included in this analysis. That is because those craters do not exhibit a distinguishable ejecta blanket. In that case, the derived μ value is 0.5, as presented in Table 4.5. Figure 4.19 then shows the ejecta velocity results of all impact simulations.

Notice in Fig. 4.19 that x-axis in log scale whereas y-axis is in linear scale. According to the original cratering theory and ejecta model presented by Housen & Holsapple (2011) (Fig. 2.6) that the ejecta model is valid between $1.2a$ and crater size R, [2].

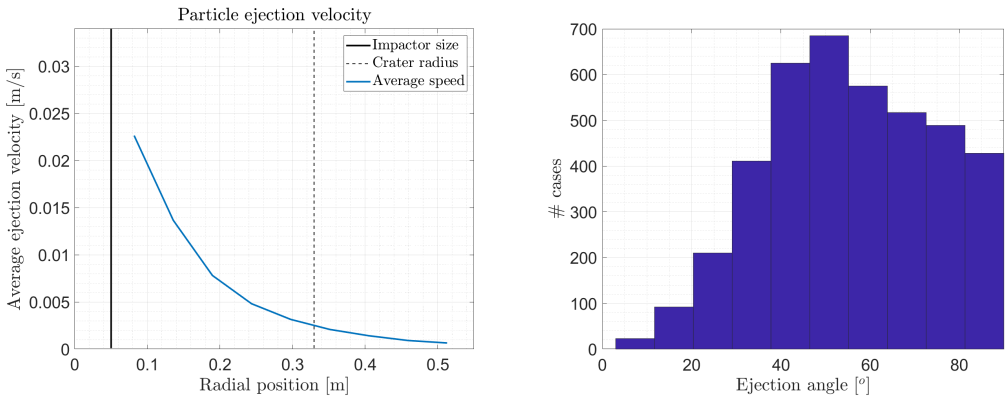

(a) Velocity (b) Angle

Figure 4.18: Average ejecta velocity and angle. Impact case: U: 10 cm/s, δ: 1910 kg/m^3 (Impact #1 in Table 4.4)

Outside this range the theory fails due to small ejected mass or gravity/strength effects. That region is marked approximately for the simulations here between impactor radius and crater radius. Within this range, the power law scaling appears to be valid. Beyond this range, the power-law scaling fails as in the expectations of general scaling theory. Unlike in the case of high-speed impacts, in low-speed impacts discussed here, the failure of the power-law of scaling is also caused by irregularity in velocity of ejected material *inside* crater. This occurs when an impactor bounces off ground instead of penetrating. On the other end, the failure occurs in part due to rather stochastic velocity of the $pushed - up$ material afar the impact point.

The angle of ejection, on the other hand, has no determined value or range, but generally assumed to be constant around 45^o, although observed to be decreasing radially outward from the impact point [50, 61]. It is shown earlier in Fig. 4.17 and 4.18b that ejection angle is certainly not constant but varying. In order to investigate the ejection angle more generally, Fig. 4.20 is generated.

According to Fig. 4.20, majority of the ejection angle is between 40^o and 60^o in all simulations. The angle is lower for lower speed impacts and increasing with impact speed. At the highest impact speed case, the mean angle value is placed between 55-60^o, respectively. It should be noted that higher ejection angles may not necessarily be a result of increasing impact speed, but also low angle of friction (~20^o) of the material used here, as noted in Housen & Holsapple (2011) [2]. The effect of material

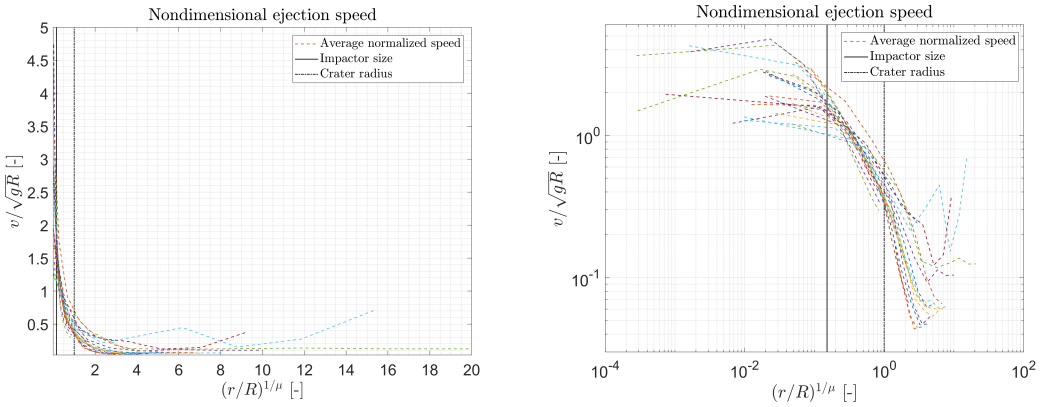

(a) Linear scale

(b) Log-Log scale

Figure 4.19: Average ejecta velocity profile of all simulations

properties in the outcome of ejecta profile will be considered as future study.

All in all, the ejecta velocity results suggest that the ejecta model developed by Housen & Holsapple (2011) for high-speed impacts [2] may be valid for low-speed impacts as well. In the following, this theory will be discussed more in detail in comparison with the ballistic ejecta model proposed by Richardson et al. (2007) [61].

Comparison with analytical ejecta model

Analytical ejecta model by Richardson et al. (2007), uses the ideas from Maxwell's Z-model, as discussed earlier. The model is consistent with the cratering theory mathematically and its results agrees with the experiments. The crater formation time plays an important role in the derivation of equations. Recall two equations:

$$T_g = C_{T,g}\sqrt{\frac{R_g}{g}} \tag{4.6}$$

Eq. 4.6 is an approximate form of the equation where $T_g = K_{cr,g}\sqrt{\frac{V_g^3}{g}}$, where C_{T_g} is found to be $K_{cr,g} \approx C_{T_g}$ within the experimental accuracy, with the crater depth assumption as $2R_g/3$, following Melosh (1989) in high-speed cratering [61, 57]. Note from earlier subsections that$K_{cr,g}$ is between 0.8-0.9 [56, 57]. However this approximation may not be true for craters in low-speed crater under low-gravity. The cratering process takes longer under low gravity than under Earth-gravity. As shown earlier in this chapter,

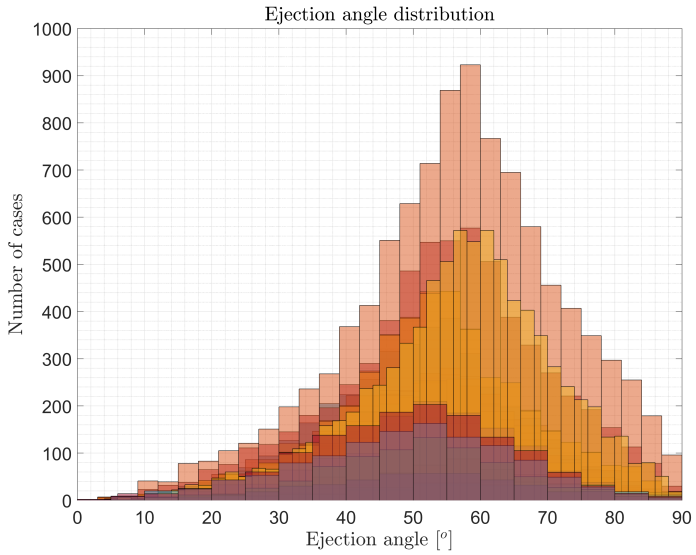

Figure 4.20: Ejection angle profile of all simulations

the depth of low-speed craters, at least in the case here, are between 0.2-0.4 for the most cases. In order to find the exact value for $K_{cr,g}$, the equation $T_g = K_{cr,g}\sqrt{\frac{V_g^3}{g}}$ can be written in its full form, by assuming a paraboloid crater volume for V_g^3:

$$T_g = K_{cr,g}\left(\frac{\pi d}{2}\right)^{1/3}\sqrt{\frac{R_g^{2/3}}{g}} \tag{4.7}$$

where d denotes crater depth. Crater formation time is then needed to calculate $K_{cr,g}$. At this stage of the analysis, the crater time is assumed to be the time the *last* particle is launched from the surface. Albeit looking rather arbitrary, this is a substantial amount of time, as the last particle ejected is generally some particle that is pushed up through the very end of cratering, where downhill material movement inside transient crater rims almost ends. Figure 4.21 below shows the values of $K_{cr,g}$ as function of π_2 and time of last ejected grain, t_f.

Similar to the presentation in Schmidt et al. (1987), t_f is presented in Fig. 4.21b is given as a function of $\sqrt{V^{1/3}/g}$ but in a general form given in Eq. 4.7. Two outlier cases where t_f is very late in the simulations, for which ejection is *not* as a result of natural cratering process but particle mobilized by reimpact of already ejected particles. Those

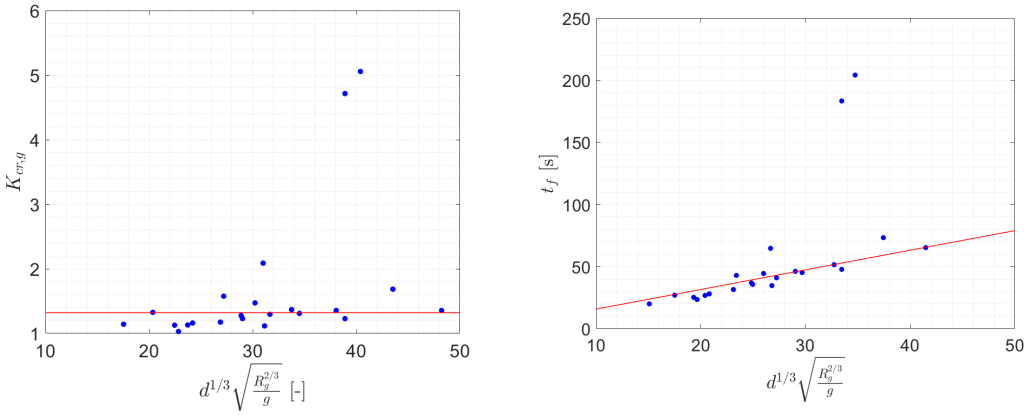

(a) $K_{cr,g}$ (b) Time

Figure 4.21: $K_{cr,g}$ as a function of last ejection time and gravity-scaling parameter, π_2

are not removed from the analysis and shown for consistency, but included neither in the slope calculation in Fig. 4.21b nor in the mean value $K_{cr,g}$, shown as the straight line in Fig. 4.21a. Near linear dependency of t_f can be confirmed from Fig. 4.21b. The fitted slope is 1.58 with values between 1.4 and 1.7. Mean value of $K_{cr,g}$ is found to be 1.32.

The $K_{cr,g}$ value of 1.58 is twice the value found in Schmidt et al. (1987) [56], but very but very close to the value 1.6, as stated in Melosh (1989) based on Schmidt et al. (1987) [56]. The method to find $K_{cr,g}$ value is the same as Schmidt et al. (1987), therefore it is believed $K_{cr,g}$ computed here is nearly twice that of Schmidt et al. (1987). This is believed to be as a result of long crater formation time under low gravity. However, a conclusive statement on that requires a more concrete definition of crater formation time.

With $K_{cr,g}$ at hand, the ejection velocity results presented in previous subsection can be compared with the analytical ejecta model of Richardson et al. (2007) [61]. Ejection velocity expression in Eq. 2.35 is going to be used, where μ = 0.5 and $K_{cr,g}$ = 1.32, 1.4, 1.7 are the values selected. Figure 4.22 shows the result of this comparison.

Because of the intrinsic nature of the analytical ejecta model, the velocity approaches to 0 at crater radius. In the region between impactor radius to crater radius, the analytical ejecta model, with the derived coefficients, matches reasonably well with the simulation results. The model cannot capture the ejection outside the crater; however, it should be noted that ejection velocity outside crater is usually below cm/s

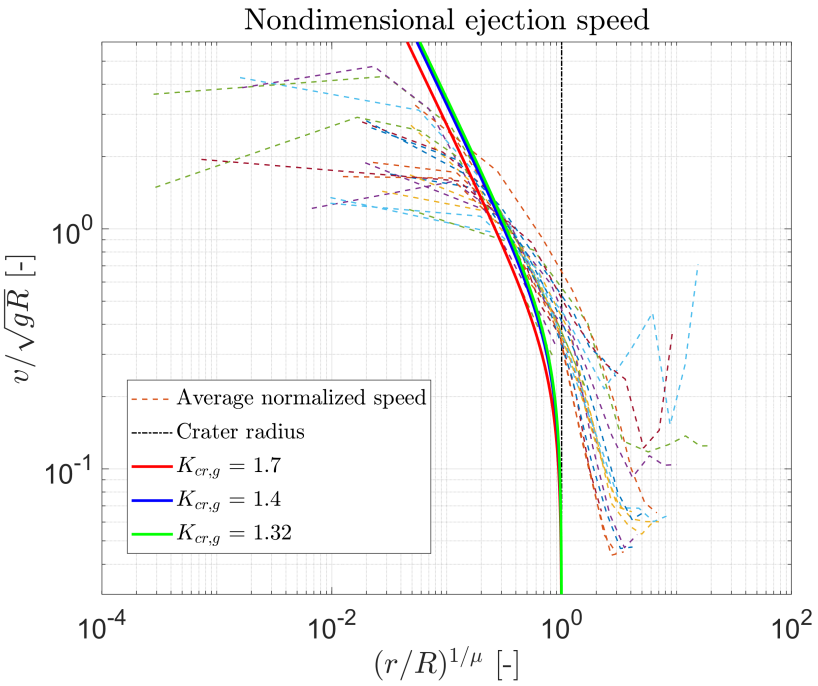

Figure 4.22: Comparison of analytical velocity estimation with simulation results

level, except a few higher-velocity impacts. The reasonable match between analytical model with the simulation results also suggest that crater formation time arguments explained earlier should be largely correct.

4.3.4 Ejected Mass

Following the definition of Housen & Holsapple (1983) [50], *ejected mass with velocity higher than* v (hereafter, ejected mass) will be presented in this subsection. In other words, that refers to cumulative or total mass of particles whose velocity higher than some given velocity v. Because of the intrinsic position dependence of v, the ejected mass is largely representative of the mass as a function of distance, even though it is not directly a function. However, as shown in previous sections, ejection velocity, especially in later stages of crater formation, is not always vary as a function of distance.

Ejected mass is calculated by collecting particles that are faster than average velocities presented in the previous subsection. Total mass of the collected particles

and their corresponding threshold ejection velocity are then recorded. Results of this, as dimensional and nondimensional mass as defined in Eq. 2.24 is provided in Fig. 4.23.

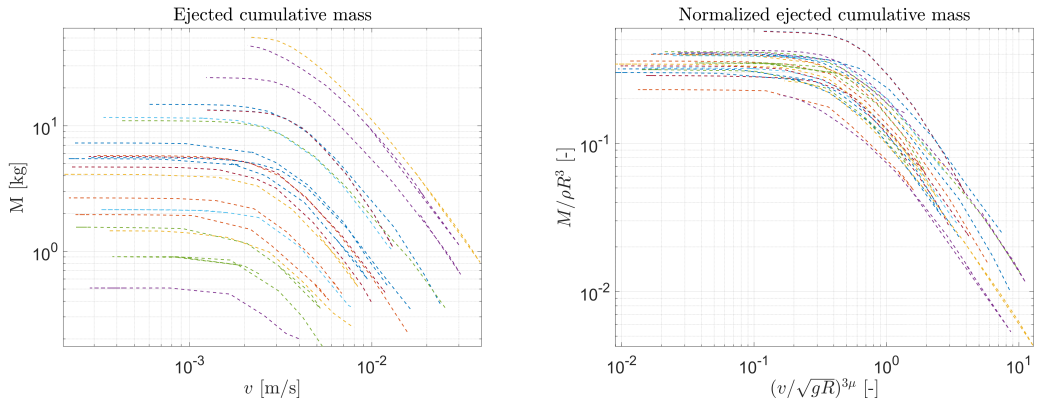

(a) Dimensional (b) Nondimensional

Figure 4.23: Ejected mass as a function of average ejecta velocity

Again, $\mu = 0.5$ for nondimensional mass profile. Ejected mass generally follows the expected mass profile [2]. Power-law scaling fails when close to impactor and impact point, due to little or no mass ejected, as stated by Housen & Holsapple (2011), and seen as constant line in Fig. 4.23. Between the end of constant region to crater size, ejected mass profile follows the power-law scaling. Housen & Holsapple (2011) states that power-law scaling would fail near crater rim due to gravity or strength effects. This was not observed here. Ejection velocity results also appear to follow a power-law scaling until crater size (see Fig. 4.22). That might mean that gravity/strength effects may not be as strong in low-speed impacts under low gravity near crater rim as it does in high-speed impacts under higher gravity levels. Moreover, noncollapse of nondimensional ejected mass values into a single line suggest impactor density dependency which will be investigated further in the future.

4.3.5 Discussion

All in all, it was shown that scaling laws also exist for low-speed impact similar to astronomical impacts. Through the results presented in the previous subsections, the long-established observations of impact experiments were validated, similarities and differences were highlighted. Some of the scaling coefficients are found to be different

which could be resulted from low-speed and low-gravity nature of the cratering, and material properties assigned in DEM simulations. More conclusive results can be presented once more simulations with different material properties and at different impact regimes are performed. The success of the results in validating cratering theory for low-speed impacts also demonstrate the level of maturity that discrete element method has reached in simulating real astronomical phenomena in small-bodies.

In the next section, the results of this section are going to be used to propose a novel approach to calculate the coefficient of restitution in granular small body surfaces.

4.4 The coefficient of restitution

The idea behind defining a coefficient of restitution in this work arises from basic observational object-surface interaction in granular systems, *i.e.*, impacts deforms surface plastically to some degree, regardless of impactor's size, shape, density and impact conditions among the other properties. Surface deformation is essentially called *crater*. Cratering theory outlined in the previous section thrives to characterize and connect shapes and sizes of craters to target and impactor properties. The power of cratering theory is that it avoids the complexity of granular behaviour in grain scale, for which there are numerous independent force models from different schools of thought, and focus on macro behaviour. Even though it has grain-scale origins, the coefficient of restitution can also be characterized with macro behaviour. Then, the coefficient of restitution can be formulated as remaining energy after some (or all) of initial impact energy spent on interaction, *i.e.* primarily on cratering, compression of empty volume due to porosity, and some sort of frictional interaction during penetration. A simplified illustration in Fig. 4.24 shows the idea behind the coefficient of restitution in this thesis.

In short, the adopted approach handles CoR in granular systems as an energy exchange process, in which some or all initial impact energy is spent during the cratering process in accordance with the cratering theory and remaining energy is utilized in the post-impact motion. Accordingly, a coefficient of restitution, ϵ,

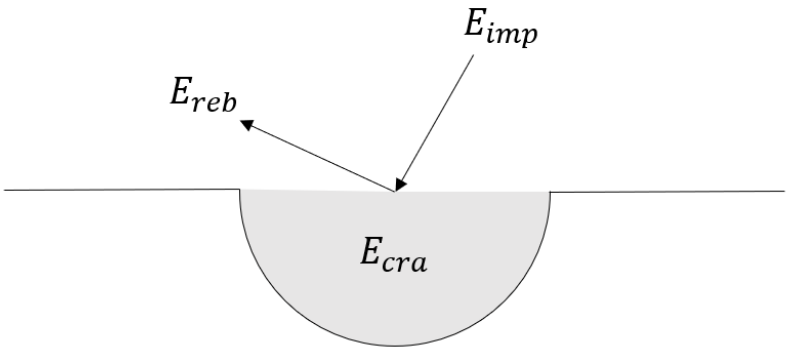

Figure 4.24: The idea behind the coefficient of restitution in granular systems.

expression can be defined as follows:

$$\epsilon = \sqrt{\frac{E_{reb}}{E_{imp}}} \tag{4.8}$$

where $E_{reb} = E_{imp} - E_{cra}$. Here, E_{reb}, E_{imp}, and E_{cra} denote rebound, impact, and energy spent in cratering, respectively. E_{cra} itself can be broken down into several elements:

$$E_{cra} = E_{mob} + E_{vol} + E_{temp} + E_{misc} \tag{4.9}$$

where each element is defined as below:

- E_{mob}: Energy spent on material mobility, which constitutes both ejecta and displaced material inside crater.
- E_{vol}: Empty volume that is compressed as impactor penetrates to surface
- E_{temp}: Temperature increase due to frictional interaction between impactor and surface
- E_{misc}: This includes the aspects of the interaction that are not modelled fully analytical, *e.g.*, energy spent on mobilized particle rotation, impactor rotation, etc.

The actual interaction process in granular systems is extremely complex and there is currently no concrete consensus on what model works the best, despite

the unification efforts [48, 109]. That is to say, for example, E_{mob} can only describe material mobility *within* a crater because of the intrinsic nature of cratering theory. In reality, some material is also mobilized outside final crater dimensions as shown in the previous section. Because of this there will always be some level of disagreement between experiment/simulation results and analytical results. Similarly, rotational aspect of material mobility and impactor is also not counted in the theory but some limits on those will be given in the next subsections. Note that even though Fig. 4.24 depicts an oblique impact for generalization, the current work is limited to local vertical impacts only. The study will be expanded to oblique impacts in the future. There is, however, no loss-of-generality in the general equations and they should describe the oblique impacts in the same way.

E_{reb} can then be written by substituting Eq. 4.9 as:

$$E_{reb} = E_{imp} - E_{mob} + E_{vol} + E_{temp} + E_{other} \tag{4.10}$$

dividing both sides with E_{imp} and defining ϵ' as some coefficient of energy dissipation for each item, $\epsilon' = \sqrt{E_{sink}/E_{imp}}$, Eq. 4.8 would can be written as:

$$\epsilon = 1 - \epsilon'_{mob} - \epsilon'_{vol} - \epsilon'_{temp} - \epsilon'_{other} \tag{4.11}$$

If the impactor's material coefficient of restitution is different than 1, then only a portion of ϵ would be retained for bounce as

$$\epsilon_{final} = \epsilon_{imp} \cdot \epsilon \tag{4.12}$$

where each ϵ' denotes coefficient of energy dissipation for their corresponding energy sink, given as subscript. In the following subsections, all those energy sinks will be quantified before finally arriving a coefficient of restitution.

4.4.1 Energy sinks

This section will present a quantitative analysis on energy sinks in the low-speed cratering process. This study identifies five energy sinks, quantified with coefficient of energy dissipation, ϵ' that are illustrated in Fig. 4.25.

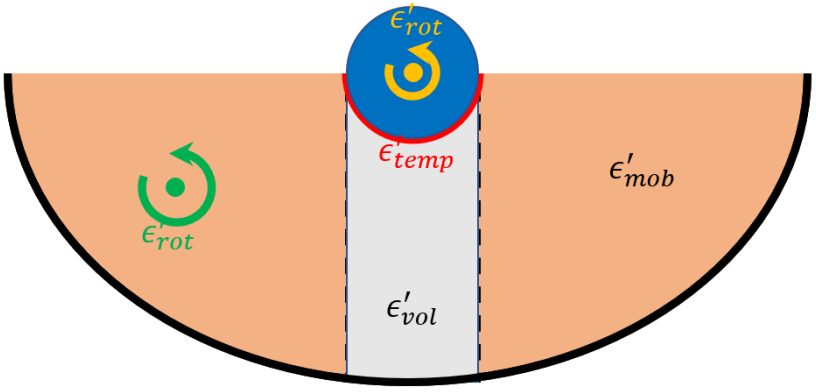

Figure 4.25: Illustration of energy sinks

The largest energy sink the material mobility, ϵ'_{mob}. This includes ejected and pushed aside material inside the crater cavity. It will be calculated from an analytical formulation that will be derived in the following subsections. The other analytically computed energy sinks are volume compression and temperature increase, ϵ'_{vol} and ϵ'_{temp}. There is no analytical way to quantify impactor and particle rotation (ϵ_{rot}), thus they will be extracted from the simulations to put quantitative bounds on them.

Material mobility

The energy spent on material mobility during the interaction is expressed from the cratering theory perspective. According to this, crater radius and its depth can be calculated from equations of cratering theory with coefficients found from the results of the simulations. The velocity field can be expressed with the analytical model presented in the previous subsections with its appropriate coefficients as defined in the previous section. Combining those two, one can then consider the energy of a mass element within the crater dimensions, as shown in Figure 4.26, and express as:

$$\mathrm{d}E = \frac{1}{2}\mathrm{d}m v(d)^2 \tag{4.13}$$

Recall from Fig. 4.26 that the material velocity is higher when radial distance is closer to the impact point. The mass element shown on the left panel is at distance d from the impact point in crater with radius R and depth l. For a volume $\mathrm{d}V$, mass

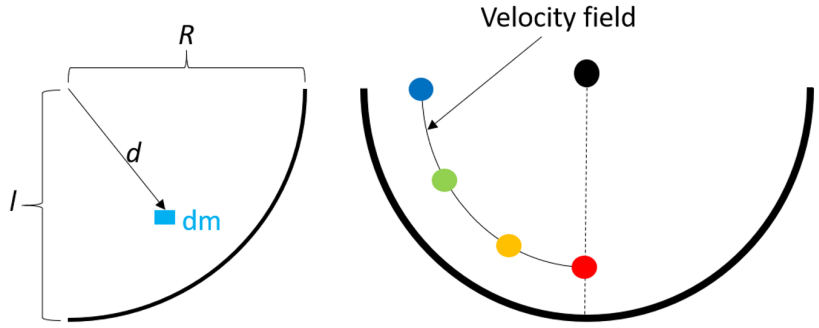

Figure 4.26: Illustration of velocity field in a crater and energy element integrated over a crater volume

element can be described as:

$$\mathrm{d}m = \rho \mathrm{d}V \tag{4.14}$$

where ρ is target material density. Substituting dm into Eq. 4.13 would yield

$$\mathrm{d}E = \frac{1}{2}\rho v(d)^2 \mathrm{d}V \tag{4.15}$$

Integrating Eq. 4.15 then results in energy spent within a volume defined by crater dimensions. After substituting crater radius and velocity expressions into Eq. 4.15, the equation can best be represented in cylindrical coordinates for a parabolic crater, as

$$E_{mob} = \frac{1}{2}\rho g C_{vpg}^2 R_g^{\frac{2+\mu}{\mu}} \int_0^l \int_0^{2\pi} \int_a^{R_g} (r^2 + (l-z)^2)^{-\frac{1}{\mu}} r \, \mathrm{d}r\mathrm{d}\theta\mathrm{d}z \tag{4.16}$$

Because of the exponent $-1/\mu$ the integral cannot be solved analytically. A solution can be found for specific values of μ. ϵ'_{mob} can then be expressed as

$$\epsilon'_{mob} = \sqrt{\frac{E_{mob}}{E_{imp}}} \tag{4.17}$$

where ϵ'_{mob} denotes the coefficient of energy dissipation for material mobility, E_{mob} is energy lost to material mobility and E_{imp} is impact energy. Figure 4.27 shows velocity and ϵ'_{mob} inside a crater calculated with the derived equations above.

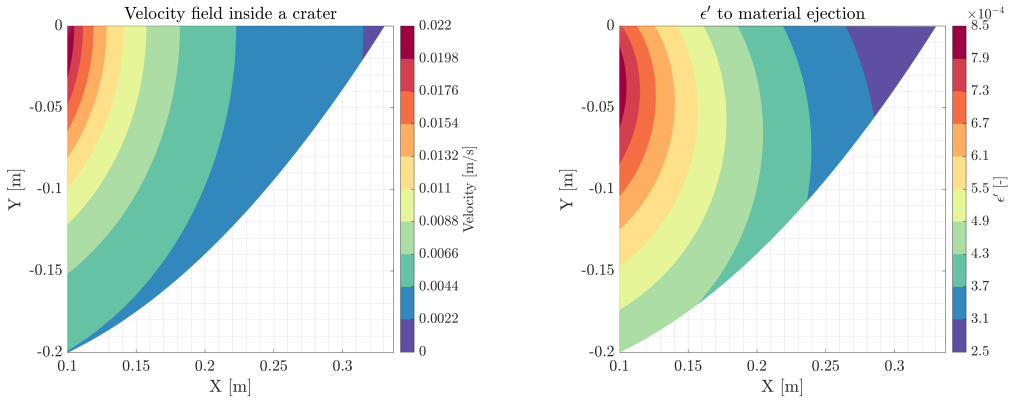

(a) Velocity field

(b) ϵ'_{mob}

Figure 4.27: Velocity field and ϵ'_{mob} inside a crater.

The velocity field in Fig. 4.27a demonstrates that particles that are approximately radial distance from the impact point has the same velocity. ϵ'_{mob} in Fig. 4.27b shows slightly more complex energy field, although follows the general trend, *i.e.*, less energy expenditure when away from the impact point. ϵ'_{mob} for the whole crater is ~0.56, hence material mobility is expected to constitute the highest amount of energy dissipation during cratering.

Volume compression

Volume compression refers to energy spent on crushing pores as impactor penetrates into the granular bed. Volume compression is considered similar to a piston (*i.e.*, impactor) compressing empty space available in its penetration path due to porosity. More specifically, the compressed volume is assumed to be the volume enclosed by impactor radius along the crater depth. This is a simplified definition of actually more complex situation, in which impactor penetrates either deeper or shallower than actual crater depth. In the former, empty space above impactor is filled by inward moving particle from transient crater wall. In the latter, impactor penetrates only a few layers of grain which initiates a chain of impacts that compresses volume. In either case, this simplified approach is believed to represent some mean energy expenditure in overall. Then, the volume compressed by impactor can be written as the volume of a paraboloid portion which is enclosed by impactor radius as:

$$V = \pi \int_0^d (a - f(y))^2 \, dy \tag{4.18}$$

where a impactor radius and $x = f(y) = \sqrt{\frac{R_g^2 y}{d}}$. Solving the integral yields volume as:

$$V = \pi \left[a^2 d - \frac{4}{3} a R_g d + \frac{R_g^2 d}{2} \right] \tag{4.19}$$

Compressed volume would then be equal $V_{comp} = \phi V$, where ϕ is porosity. Then, the energy spent on volume compression can be written as:

$$E_{vol} = \frac{F}{A} V_{comp} \tag{4.20}$$

where F denotes force and equals to $F = mg$, A is the compressing area and equals to area of a half sphere, $A = 2\pi a^2$. In all of the above equations, crater radius and depth can be found from cratering theory, and through which the compressed volume can be computed. Finally, the amount of initial impact energy spent on volume compression, According to this procedure, ϵ'_{vol} is calculated for a range of impact speeds U and impactor density δ and crater depth between $0.2R_g$-$0.45R_g$ (accordingly with cratering results) for other fixed simulation parameters in Fig. 4.28.

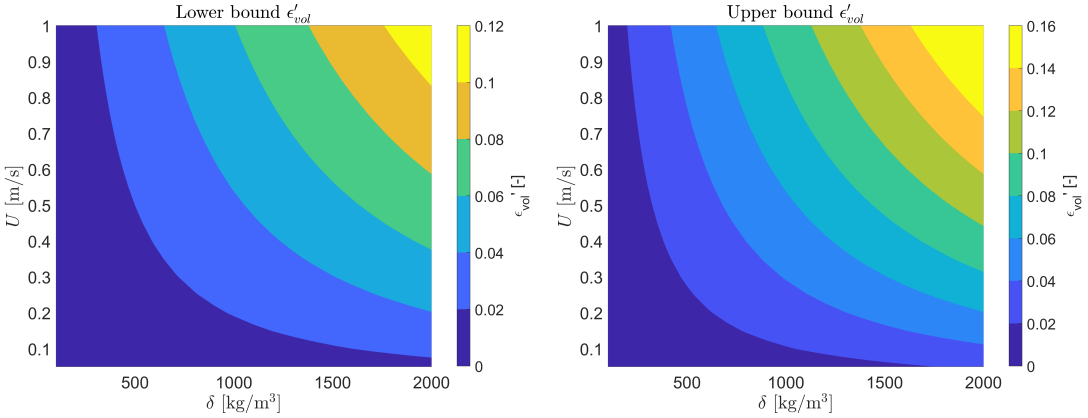

(a) Lower bound for ϵ'_{vol}

(b) Upper bound for ϵ'_{vol}

Figure 4.28: Upper and lower bounds of ϵ'_{vol}

The effect of volume compressing appears to constitute up about 2.6% of total

Table 4.6: Specific heat values of different metals [7]

Material	c_p [J/gK]	δ [g/cm^3]
Aluminum	0.902	2.70
Bismuth	0.123	9.78
Copper	0.386	8.96
Brass	0.380	8.73
Gold	0.126	19.32
Lead	0.128	11.32
Silver	0.233	10.49
Tungsten	0.134	19.3
Zinc	0.387	7.14
Mercury	0.14	13.56

energy (ϵ'_{vol} ≈0.16) and this would only occur in the highest values of U and δ. In the lower impact speed, the ϵ'_{vol} value is almost always below 0.1. As a result, relative contribution of volume compression should be considered in final energy budget, but its contribution may be ignored if its contribution is negligible when other sources of errors are larger than that.

Temperature

Temperature and subsequent phase changing events melting and vaporizing in astronomical impacts constitute of significant portion of initial impact energy. According to Melosh (1989), that equals up to 50% of initial impact energy [57]. However, complicated processes such as melting and vaporizing do not occur in low-speed impacts, hence it is expected that its contribution would be minuscule in general cratering process. To quantify this, a simple approach will be taken. Energy spent on temperature change can be expressed as follows:

$$E_{temp} = mc_p\Delta T \tag{4.21}$$

where m is impactor mass, c_p is specific hear and ΔT is temperature change. For an impactor of 5 cm radius with impact speed 10 cm/s, and a few common metals whose density and specific heat presented in Table 4.6, the temperature change as a result of spending *all* impact energy is given in Fig. 4.29.

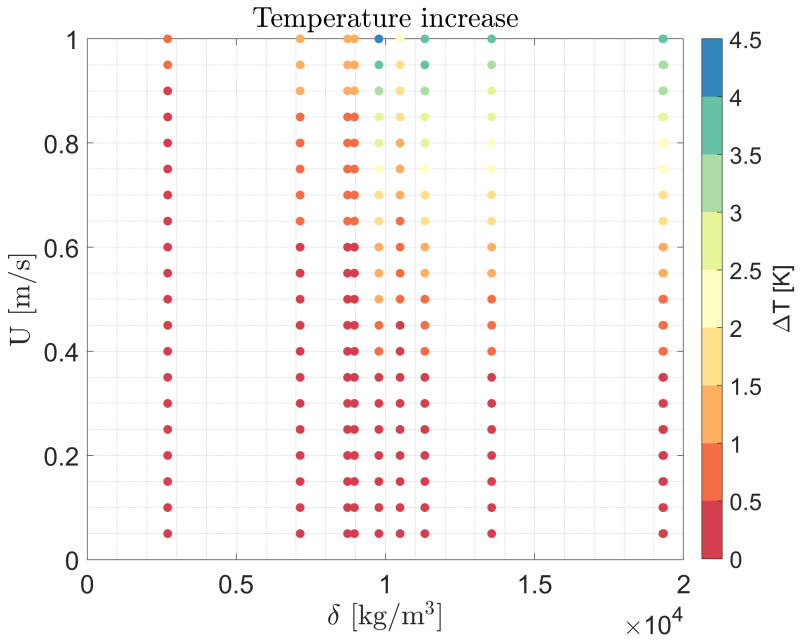

Figure 4.29: Temperature increase with impact energy for given materials

According to Fig. 4.29, the temperature change ΔT cannot be higher than ~5 K, even if all impact energy turns into heat. All impact energy is certainly not available, therefore ΔT should be considerably less than the upper bound value of ~5 K. It is believed that the contribution of impact energy into heat should be minuscule and likely to be included in the energy sink through material mobility.

Impactor rotation

Other energy sinks include energy turn into rotation for both impactor and mobilized material. The latter is a lot harder to quantify because it is possible that some interchange happens between translation and rotation as material moves within the bed. In order to quantify rotational sources, an empirical approach is taken. The outcomes of the simulations presented in the previous section is used to calculate rotational energy of a solid spherical impactor and solid spherical particles. Recall rotational energy formula as:

$$E_{rot} = \frac{1}{2} I \omega^2 \tag{4.22}$$

where I and ω denote moment of inertia and rotational velocity respectively. Figure

4.30 shows initial translational energy that turns into rotation in the form of coefficient of energy dissipation, ϵ'_{rot}.

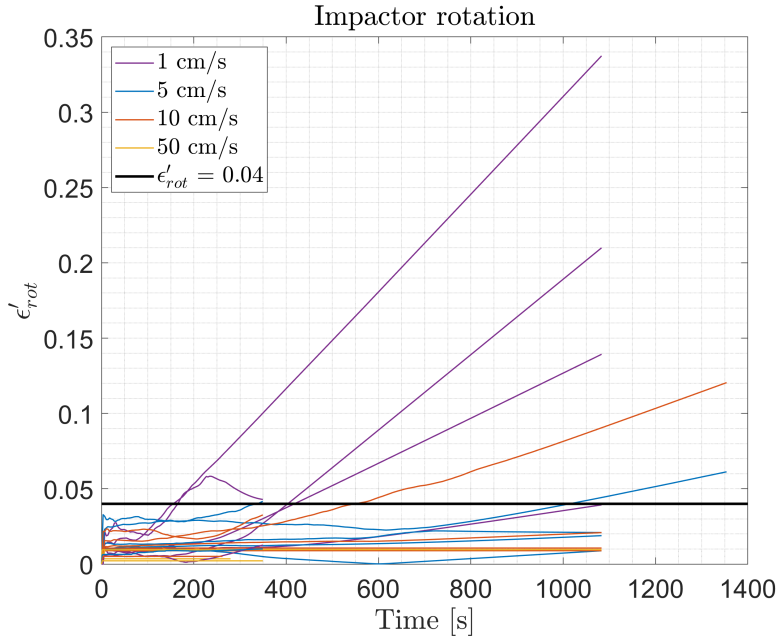

Figure 4.30: Rotational energy of impactor presented as ϵ'_{rot}

According to Fig. 4.30, in most impact cases ϵ'_{rot} ≤0.04, *i.e.* only a minuscule amount of impact energy turns into rotation. Three of five cases above this value are 1 cm/s case, where there is no bounce or significant submerge occurs and craters are partially formed. ϵ'_{rot} for the other two are 0.12 and 0.06 and occur for two submerge cases. For bouncing impactors, the $\epsilon_{rot'}$ values are on the order of 0.02. Note that, however, for more frictional materials and in oblique impacts, it is anticipated that more of impact translational energy would turn into rotation.

Particle rotation

Particle rotation is among the most difficult energy sinks to quantify in a cratering process. Even though the simulation outputs provide the particle rotation, it is difficult to know whether the rotation is originated with the impact itself or the interaction between grains and the container walls, that continue even the impactor comes to a halt. Nevertheless, the rotation is attempted to be quantified in this study. For that, it was

assumed that rotation of particles are initiated by their interaction with the impactor *only* if they are *ejected* and their original position is in the final crater size. This is because, if a particle is still within the container dimensions, it is significantly more difficult to distinguish impact-originated rotation from particle-particle interaction originated rotation of particles. That is to say, once a particle is ejected, with the assumption that they are not interacting afterwards, its rotation will remain the same as there is no additional external torque applied to that. This happens relatively quickly for the majority of particles, whereas particles inside the container dimensions continue interacting with each other even after the impactor stops. It is worth noting that the current choice of quantification of the particle rotation may result in underestimation. But it certainly avoids overestimation or even unphysical results where the total amount of particle rotational energy exceeds impact energy.
According to that, after the crater size is detected from the simulation output, rotation of the ejected particles which are originally in the crater cavity are extracted from the same simulation output, and their rotational energy is calculated with Eq. 4.22. The results are presented in Fig. 4.31.

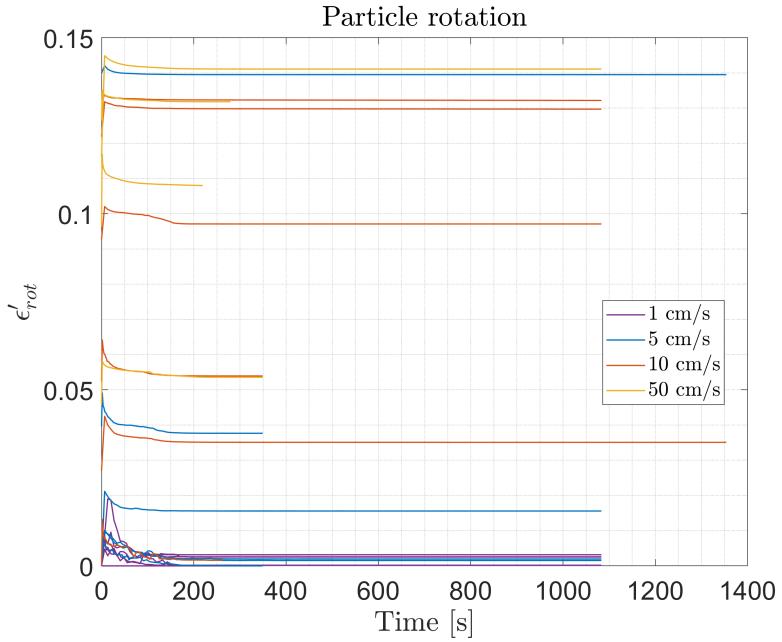

Figure 4.31: Rotational energy of particles presented as ϵ'_{rot}

As soon as the impact occurs, particle rotational energy jumps from zero to some

peak value, before settling down some constant value as the particles depart from the surface. The constant value is the total rotational energy of the departed particles, and the peak value is their original total rotation before they surface and depart. The highest $\epsilon_r ot'$ value is about 0.15, corresponding to about 2.25% of the impact energy. This peak value value will be considered in the remaining analysis.

4.4.2 Results

After various energy sinks were identified and their contribution to energy dissipation process is quantified, it is now possible to estimate the coefficient of restitution and compare with simulation results. As material mobility is discussed to be the largest source of energy dissipation, it will first be discussed. The coefficient of restitution value ϵ is first computed by assuming no contribution from the other energy sinks discussed before, but only only contribution from material mobility, *i.e.*, ϵ = 1 - ϵ'_{mob}. The crater sizes are estimated with equation of cratering theory and crater depth is assumed to be ranging from lower bound value of $0.2R_{cr}$ to upper bound value of $0.45R_{cr}$ in accordance with the simulation results. These lower and upper bound values would correspond to upper and lower bound of ϵ, respectively, as more material is excavated from a deeper crater or vice versa. Figure 4.32 shows the results of this analysis for a range of impact speed U between 0.05 and 1 m/s, and impactor density δ between 100-2000 kg/m^3, as used in the simulations.

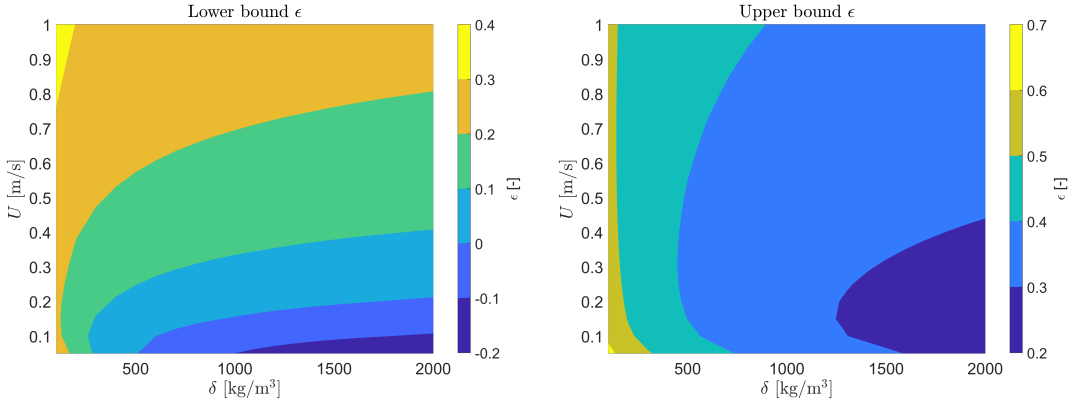

(a) Lower bound (b) Upper bound

Figure 4.32: Upper and lower bounds of ϵ = 1-ϵ'_{mob}

As it can be seen in Fig. 4.32a, some ϵ values are negative, stating that the required energy to excavate material is more than the impact energy in the given scenario. Those impacts would then result in penetration, as one would expect. the highest value of the lower bound ϵ is found ~0.4 at the highest impact speed and lowest density. On the other hand, the upper bound ϵ values increase up to 0.7 at the highest but observed in the lowest velocity and density, contrary to lower bound results. This could be a result of the higher impact energy of 1 m/s case that can be spent on penetration, while for the impactor mass, the 10 cm/s case cannot penetrate to surface as much. Moreover, the lowest values of ϵ for shallower craters are on the order of 0.2. ϵ 0 means bounce off the surface even though that is not what is observed in the simulations. It is then possible that other energy sinks, as well as impactor's coefficient of restitution take part in further energy dissipation. Before discussing those, Fig. 4.33 is generated to compare purely analytical estimations to simulated craters in calculating ϵ.

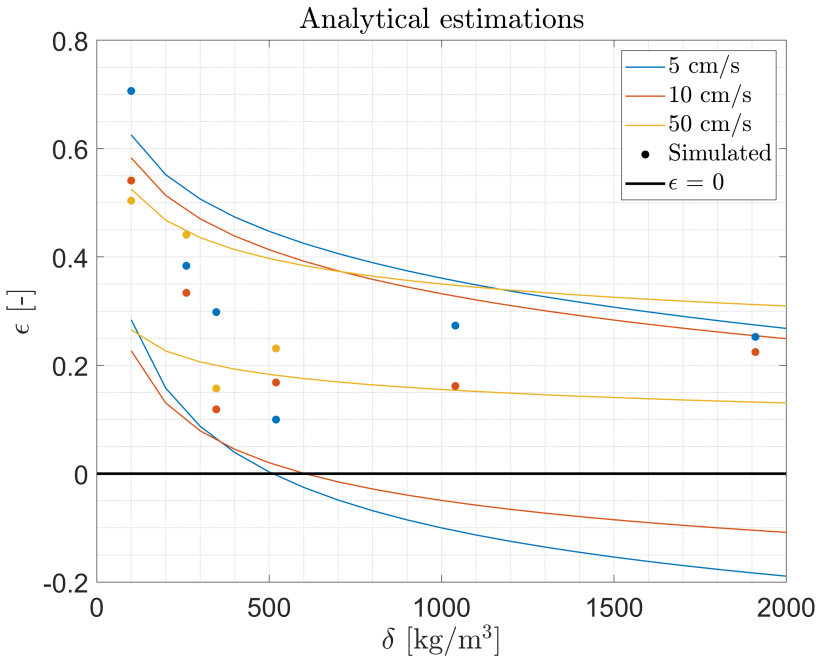

Figure 4.33: Comparison ϵ = 1-ϵ'_{mob} with actual cratering results

Note that the results of partially-formed craters as a result of 1 cm/s impacts are not included in the analysis. Lines are analytical upper and lower bound ϵ = 1 - ϵ_{mob} estimations for U = 0.05, 0.1, 0.5 m/s impact for δ = 100-2000 kg/m^3. Dots are the ϵ

values calculated from actual crater sizes from simulations. The simulated values are generally within the upper and lower bound ϵ values, except two cases. The first one is U = 0.05 m/s δ = 100 kg/m^3, for which the analytical crater size estimation is higher than the actual simulated value, hence more energy is spent on excavation. The second case if U = 0.5 m/s with δ = 346.7 kg/m^3. In this case, the estimated crater is smaller than the simulated one. The error is ~10% and ~25%, respectively. The errors are due to analytical crater size estimation but which have roots on crater size estimation procedure or some other simulation artefact which eventually resulting in these errors. Furthermore, the fact that these outliers are in the cases where impactors bounce off the surface could be indicating that improved cratering laws are necessary when impactor bounces off the surface.

As noted earlier, the other energy sinks must be also playing a role as ϵ 0 values are observed for impacts that resulted in penetration. Among the ones mentioned in the previous subsection, volume compression and impactor rotation will be added to the results. For the latter, a constant value of ϵ'_{rot} = 0.04 will be assumed in accordance with the results presented in Fig. 4.30. During the simulations, the impactor was also given a constant coefficient of restitution value of ϵ_{imp} = 0.6, similar to MASCOT [44]. This means that only 1 of the final ϵ would be retained on the impactor. ϵ, with the contribution of all those energy dissipation mechanisms are presented in Figure 4.34.

ϵ estimation is decreased significantly especially with impact the coefficient of restitution. The maximum value is now less than 0.4. In cases where ϵ = 0, the maximum estimated value is on the order of 0.2 for 50 cm/s case, and around 0.15 for 5, 10 cm/s cases. In general, the values are captured within the estimated analytical estimations. With these results presented, the ϵ output of simulations can now be discussed. *epsilon* is computed with following formula:

$$\epsilon_{sim} = \frac{v^+}{v^-} \tag{4.23}$$

where v^+, v^- are post- and pre-impact velocity magnitudes. Equation 4.23 is essentially the same expression as Eq. 4.11 as initial and final energy are considered only in terms of translation. ϵ_{sim} values are then presented in Table 4.7 for impactor that bounced back.

Table 4.7 presents not only the results of simulations with glass bead (GB)DEM

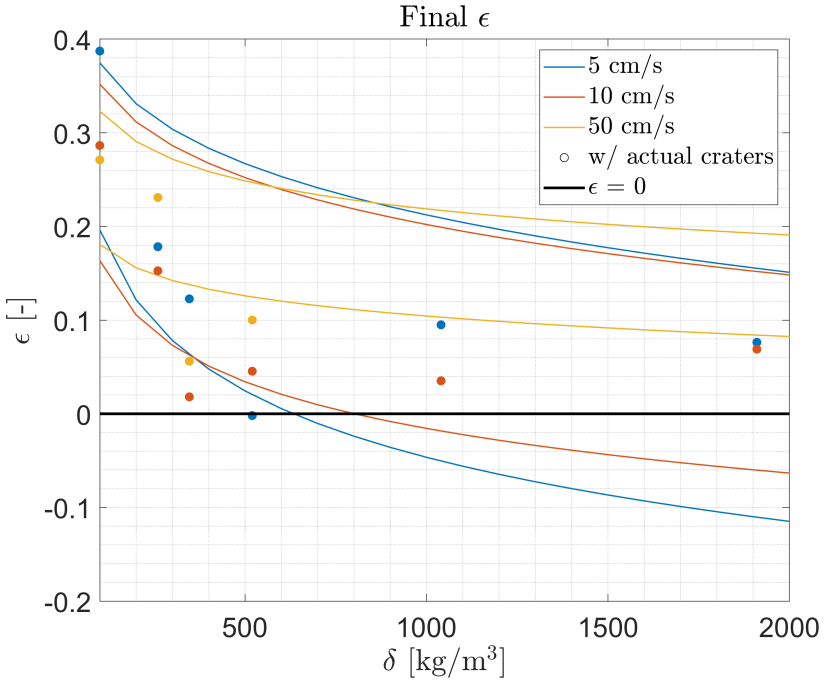

Figure 4.34: ϵ after all energy dissipation mechanisms added

parameter set but also two results from the gravel (GR) set and one other results with higher target and impactor density. This latter was a test to the density ratio for bouncing/sinking transition, *i.e.* $\delta/\rho \approx 1/4$, observed in the other simulations. It seems to hold for higher ρ value, at least in this case. The simulations with gravel DEM parameters were also tests observe the impactor behaviour when surface parameters are different. In that case, switching to gravel parameters nearly doubled the coefficient of restitution value. It is believed that this is due to the high friction between grains, which would increase the strength of granular system.

For glass bead simulation results, the highest ϵ_{sim} value is 0.173 and computed for the lowest density impactor with 10 cm/s impact. The lowest values are observed at the submerge/bounce transition value of δ = 346.7 kg/m^3. For a better comparison, the results in Table 4.7 are plotted in Fig. 4.35 with upper and lower bound ϵ values calculated with the analytical theory.

The agreement between simulation and analytical results vary. In general, ϵ_{sim} results are closer to the lower bound of ϵ with the analytical theory. There is a especially a good agreement in all 5 cm/s cases with the lower bound of the analytical theory. All

Table 4.7: Computed ϵ values from simulation outcomes

#	U [m/s]	δ [kg/m^3]	ρ [kg/m^3]	DEM ParSet	R_{cr} [m]	ϵ
4	0.1	100	1400	GB	0.152	0.173
5	0.05	100	1400	GB	0.106	0.113
6	0.5	100	1400	GB	0.294	0.156
13	0.1	260	1400	GB	0.226	0.106
14	0.5	260	1400	GB	0.380	0.071
15	0.05	260	1400	GB	0.168	0.088
18	0.1	346.7	1400	GB	0.259	0.065
21	0.05	346.7	1400	GB	0.182	0.050
24	0.50	346.7	1400	GB	0.527	0.041
25	0.05	260	1400	GR	0.123	0.160
26	0.10	260	1400	GR	0.158	0.206
27	0.10	530	2118.5	GB	0.211	0.106

5 cm/s and 10 cm/s cases have good agreement again with the lower bound. One of the 50cm/s cases is out of bounds and otherwise the results show a good agreement. Moreover, for three example cases where different material properties are tested, the ϵ envelop defined by the analytical theory appears capture the simulation results.

A couple reasons can be listed to explain the discrepancy between these results and analytical estimations. First of all, the particle rotation is only accounted in a limited way to the overall energy budget, as it is a lot harder to quantify as the exchange between translation and rotation is somewhat elusive in granular scale. Second, the drag force experienced by the impactor is assumed to be included in the cratering process, which may have higher than expected contribution. Futhermore, impactor's departure from surface is not instantaneous, and some rolling and sliding occur, which would further decrease its departure energy. Finally, impactor's bounce from surface is not the same incoming direction, and its departure path often coincides with ejected high-velocity material, dissipating further energy. Nevertheless, the approach presented here constrains the expected coefficient of restitution on a granular small-body surface significantly. It provides a reasonable level of agreement with the simulations of different target properties and promising results for further improvement of the employed approach.

The simulations were only performed for a single-sized impactor thus far. It is

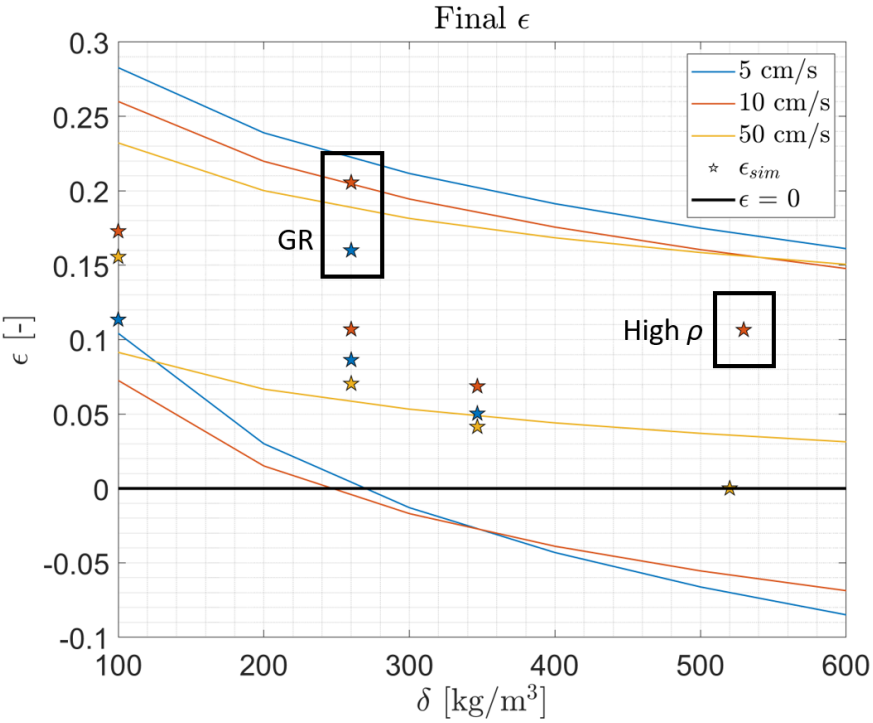

Figure 4.35: ϵ_{sim} with analytical estimations

reasonable to assess its estimation capability for different sized impactors. For this step, the bouncing case of δ = 260 kg/m^3, U = 10 cm/s is selected for impactor radius 3 and 1 cm, *i.e.*, smaller than the original impactor radius of 5 cm. The theoretical estimations with μ = 0.5, K_1 = 0.87, and the simulation results are provided in Table 4.8.

The estimated crater size for 3-cm-radius impactor is close to the simulation results with crater depth is between the range that is found at the end of the simulations. This results in estimated coefficient to be 0.141, while the simulated value is 0.183. For the same density and the impact speed, 5-cm-radius impactor's interaction with the surface resulted in a coefficient of restitution value of 0.106. The increase in the value can be explained with the interacted area with the other particles, which is larger for 5-cm-radius impactor, therefore more energy is lost to the collisions with other particles. In fact, a simulated case with the same density and impact pair but a = 10 cm resulted in no-bounce. However, even though this qualitative inference is also captured quantitatively, there is a discrepancy between analytical estimations and simulation results.

Table 4.8: Estimated and simulated results of the bouncing case with smaller impactor size

	Estimation		Simulation	
Impactor radius [cm]	3	1	3	1
Crater radius [cm]	13.8	5.73	14.8	3.3
Crater depth [cm]	2.8-6.1	1.2-2.5	4.3	0.2
ϵ [-]	0.141	0	0.183	0.023
ϵ @ a = 5 cm	0.08-0.22		0.106	

In 1-cm-radius impactor case, the failure of the crater-scaling theory becomes more apparent. The estimated crater is nearly twice the radius of the simulated and 5-10 times of the estimated depth. Consequently, the estimated coefficient of restitution value is in fact less than 0, which is unphysical, hence presented as 0 in Table 4.8. Nevertheless, the simulation result shows a very small effective coefficient of restitution, which is in agreement with the estimated result. For this small impactor, the interaction is different than that of 3-cm and 5-cm ones. Because the impactor radius equals to the particle radius, impactor may penetrate deeper depending on impact location, potentially losing more energy. A bounce may not even occur in the end. Discontinuous nature of a granular assembly brings an added complexity in the estimation of coefficient of restitution in this case.

4.5 Discussion

This chapter presented an analytical theory on the coefficient of restitution on regolith-covered portions of small-bodies. The theory approaches to the problem as cratering and its associated energy dissipation through material mobility, as well as a series of other energy dissipation mechanisms. For the cratering part, the long-established crater scaling laws are used. Even though past experimental results, primarily under Earth gravity, suggest that theory may apply to low-speed impacts under low-gravity, it is not fully validated for different aspects of the laws including ejecta properties. Therefore, the first half of the chapter is dedicated to testing the applicability to the theory to low-speed impact under low-gravity. After a series DEM simulations under small-body level gravity and subsequent post-processing of the data, basic observation

of the theory is verified in the given impact regime and proven that the same set of equations can be used for low-speed impacts. A previously-proposed analytical ejecta model is modified for low-gravity applications.

In the second half of the chapter, the coefficient of restitution is computed by quantifying energy sinks during the impact process. Utilizing the equations of the crater-scaling theory and analytical ejection model, an integral that defines the energy field of ejecta inside a crater is derived. This constitutes the largest portion of energy dissipation. Other energy sinks, such as volume compression within a crater and impactor's post-impact rotation, are also quantified. Upper and lower bound estimations are made with analytical theory and compared against the simulated results. The limits of the presented theory is discussed and demonstrated with different impactor sizes. The results offer a promising level of agreement for these preliminary studies to the problem for further improvements.

The results presented in this chapter are not only offering new insights into the restitution process in low-speed impacts in granular systems but also provide new insights into the low-speed cratering process under low-gravity in granular systems. The results could provide equally useful inputs into the initial mission analysis of lander missions and the cratering process in small-bodies.

5 Object-surface interaction in lander mission design

5.1 Introduction

Japan Aerospace Exploration Agency (JAXA) is currently planning a Phobos sample return mission to be launched in 2024 [110]. The primary objective of the Martian Moons eXploration mission (MMX) is to address the issue of the origins of Phobos and Deimos, which are believed to be either captured asteroids or products of a giant impact with Mars [111, 112]. Prior to the sampling, proximity operations of MMX are envisaged to be performed from quasi-satellite orbits (QSO) (or distant retrograde orbits) around Phobos [113, 114]. These orbits are stable and at relatively high-altitude with respect to the surface of the Martian moon [115].

In order to support the landing site selection of MMX and to obtain ground-truth observations from the scientifically interesting sites on the surface of Phobos, a number of so-called Deployable CAMera 5 (DCAM5) payloads have been proposed to be

deployed from QSOs [17]. DCAM5s are equipped with both cameras and accelerometers to image the regolith surface in multiple bands and measure surface strength, respectively [17]. Small deployables like DCAM5 could be used to explore regions that are operationally risky for a mothercraft, particularly in terms of geophysical conditions of the site, as well as illumination and temperature conditions. Small landers can provide previously unexpected information of a small-body surface, as it was recently been demonstrated by MINERVA rovers and MASCOT lander [4, 116]. In the case of DCAM5, depth of the regolith layer, the strength of Phobos surface, particle size, and the gravity field information can be obtained from the images and the data transmitted to the MMX spacecraft while in orbit at a safe distance [17, 19, 21]. However, questions remain on how to effectively deploy small probes onto Phobos and guarantee their settlement on its surface.

Following this, the feasibility of the DCAM5 deployments from QSOs around Phobos is investigated within the context of the MMX mission. In particular, a multifaceted approach is proposed to combine the investigation of the dynamical and surface environment of Phobos, with the mission requirements and the orbit constraints of MMX to ensure settlement on the surface. To that end, previous numerical studies on the escape speeds across Phobos are expanded by taking its shape model into account to put upper bounds on post-impact speeds. In parallel, the surface environment is investigated through two end-member approaches to surface interaction, *i.e.*, hard and soft surface approaches, presented in the previous two chapters. The data from the hard surface impact experiments and the analytical methodology for the soft surface interaction are used to estimate the surface effective coefficient of restitution, a key parameter for the estimation of the energy damping as a function of impact conditions. By combining this coefficient of restitution estimations with the high-fidelity escape speed computations, the solution space of ballistic landings on Phobos is constrained while 1) ensuring settlement on Phobos' surface; 2) providing preliminary insights on the surface environment; 3) demonstrating the implications of the choice of surface type in the feasibility of landings as well as reachable regions on the surface.

This chapter is structured as follows: In Sec. 5.2, the DCAM5 payload is introduced along with mission and science requirements that would later drive our analysis. In Sec. 5.3 the dynamical and surface environments of Phobos are presented to further constraint our design domain. Properties of QSOs and the results of a preliminary

deployment speed estimation are provided in Sec. 5.4. The grid search of ballistic landings from QSOs, the optimal deployment conditions, and the reachable, scientifically interesting regions of Phobos are discussed more in detail in Sec. 5.5. Conclusions are presented in the last section.

5.2 Deployable CAMera 5 (DCAM5)

DCAM5 is the fifth member of the DCAM series, building upon the flight heritage achieved onboard IKAROS (DCAM1 and DCAM2) and Hayabusa2 (DCAM3) [117, 97]. DCAM5 is a sub-kilogram class lander in the approximate size of a beverage can. The main objectives of this small mission are to 1) enhance the scientific return of MMX by revealing the surface structure of Phobos and 2) assist MMX landing operations via close-up imaging and measurement of surface mechanical properties. In order to achieve these goals, DCAM5 is equipped with several instruments including multi-band cameras and close-up imagers that will capture the regolith size distribution of Phobos regardless of the final orientation after settlement [17]. The third instrument onboard DCAM5 is a triaxial accelerometer that would help scientist understand properties like the disruptive strength, penetration resistance, and porosity of the Martian moon during impacts with the surface. DCAM5 and its mission are illustrated in Fig. 5.1.

The deployment conditions of DCAM5 are constrained by the orbital path of the MMX spacecraft which will be investigated in more detail in Sec. 5. The deployment mechanism has the capability to give the canister a rotation of 100^o/sec around DCAM5's lowest moment of inertia, parallel to its deployment vector. Due to high angular momentum, DCAM5 orientation is fixed with respect to an inertial frame. During descent and landing, the orientation of DCAM5 with respect to Phobos surface is critical for its imaging conditions. As a results, the so-called camera angle, i.e. the angle between the camera axis and the surface normal at touchdown, is constrained to be no greater than 60^o. In addition, the impact speed and angle are constrained to a maximum of 15 m/s and 45^o due to the structural limitations. A summary of the mission requirements used in this research is provided in Table 5.1. Finally, the battery of DCAM5 lasts for about 3 hours, of which a maximum of 2 hours is dedicated for descent and 1 hour for the surface operations. The lifetime of DCAM5 can be fully extended up to 6 hours by providing cycles of operations.

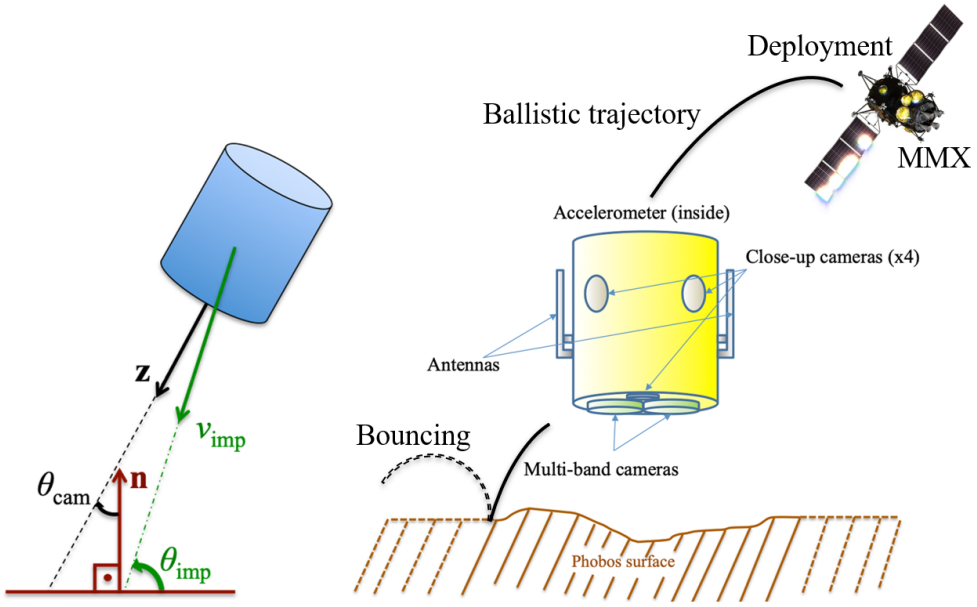

Figure 5.1: Illustration of Deployable CAMera 5 (DCAM5) payload and its components. Left: Impact and camera angles at touchdown. Right: Illustration of the mission and lander components.

The list of requirements provided in Table 5.1, as well as the ballistic nature of the landing operations suggest that a feasibility study on the landing trajectories of DCAM5 must incorporate an accurate model of dynamical and surface environment of Phobos. The results of these investigations are presented in the next sections.

5.3 Dynamical and surface environment of Phobos

Several authors have previously investigated the dynamical and surface properties of Phobos, including Dobrovolskis and Burns (1980), Davis et al. (1981), Zamaro and Biggs (2015, 2016) and Scheeres et al. (2018) [118, 119, 120, 121, 122]. In these papers, the authors have discussed various aspects of the Martian moon system, including escape speeds, gravity slopes, and possible trajectories that space missions can utilize for remote sensing and in-situ operations. The results presented in the below subsections extend these analyses by adding key information for the deployment

Table 5.1: DCAM5 mission requirements relevant to this research

#	Requirement
1	Impact speed shall be less than 15 m/s
2	Descent shall take no longer than 2 hours
3	Impact angle with the local tangent plane shall be greater than 45^o
4	Camera angle with the local normal vector shall be less than 60^o

of DCAM5. In particular, previous escape speed studies in the chaotic three-body system of Mars-Phobos are extended by using an image-derived shape model. In addition, due to the small mass ratio ($\mu \approx 10^{-8}$) and particle distance with respect to Phobos surface, the Mars-Phobos system is approximated with Hill's approximation of R3BP whose equations are provided in Chap. 2. In this analysis the eccentricity of Phobos is neglected, and the Circular Hill Problem (hereafter Hill Problem) is employed, as the eccentricity effects would not have enough time to build up due to the short time scale of the landings. The properties of the Mars-Phobos system used in this research is provided in Table 5.2.

Table 5.2: The Mars-Phobos system properties used in this work. Mass ratio is calculated from the formula given

Property	**Value**
Mass of Mars, m_1 [kg]	6.42×10^{23} [123]
Mass of Phobos, m_2 [kg]	1.07×10^{16} [123]
Mass ratio, $\mu = \frac{m_2}{m_1+m_2}$ [-]	1.67×10^{-8}
Density of Phobos, ρ_2 [kg/m^3]	1872 [124]
Semi-major axis of Phobos orbit, a_2 [km]	9377.2 [123]
Orbit period of Phobos, T [h]	7.66 [123]
Mean motion of Phobos, n [rad/s]	2.28×10^{-4} [123]

In the next subsection, surface dynamical environment around Phobos will be presented under this irregular gravity field and the dynamical properties provided in Table 5.2.

5.3.1 Surface dynamical environment of Phobos

Due to the employed shape model and irregular gravity field induced by it, as well the presence of Mars in close proximity, dynamical and surface environment around Phobos are not trivial as one would found near a spherical or ellipsoidal shape body far away from its parent body. In the next subchapters, these aspects of Phobos and Mars-Phobos system will be investigated in the context of landing problem.

Phobos shape and related properties

The shape model of Phobos in this work is approximated via the Gaskell shape model, derived from Phobos 1 and Phobos 2 missions and consists of 1230 vertices and 2456 facets [125]. Note that the shape model is not most updated and there exist higher resolution models [126, 127]. However, the Gaskell shape model of 2011 is sufficient for the preliminary mission design scenario targeted here. The Phobos shape model and barycentric distances can be seen in Fig. 5.2.

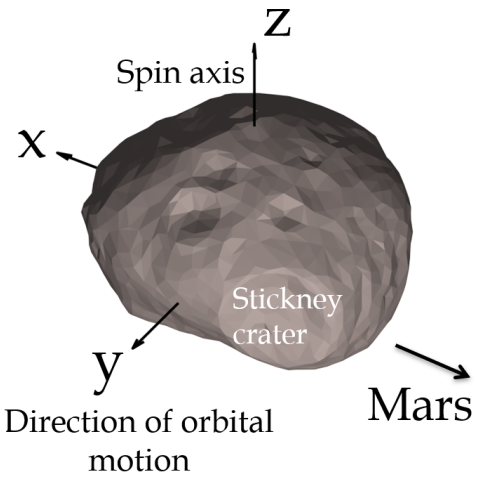

(a) The Gaskell Phobos shape model

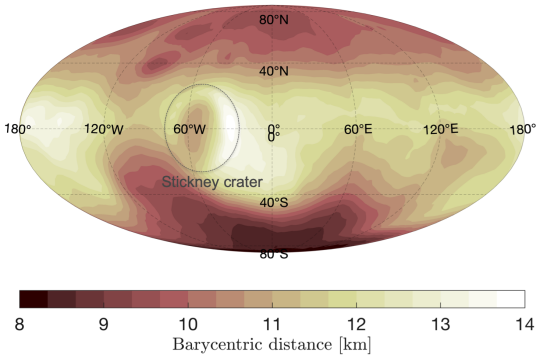

(b) Barycentric distance

Figure 5.2: Shape model and barycentric distance map Phobos. 0^o longitude in the right figure aligns with sub-Mars point.

The reference frame is centered on Phobos in Fig. 5.2a follows the widely used right-hand notation of Hill Problem. Barycentric distances in Fig. 5.2b shows the

surface features in distance form. For example, Stickney crater is marked with a circle in Fig. 5.2b and its rim near sub-Mars points is the highest peak of Phobos and around 14 km from barycentre. The dip of Phobos in this shape model is the south pole (where +z direction defines the north pole) and around 8 km from barycentre. These features are important in showing potential highs and lows and would not be available on spherical and ellipsoidal models of a target body. Gravitational acceleration on Phobos surface can then be computed at each facet of Phobos, as shown in Fig. 5.3.

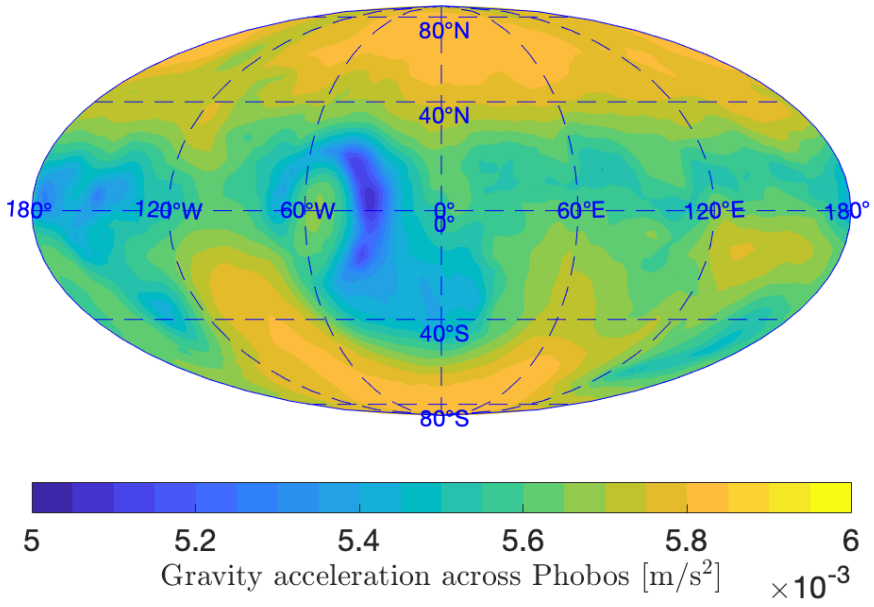

Figure 5.3: Gravity acceleration on the surface of Phobos

Accordingly with the shape shown in Fig. 5.2, the peaks and lows of Phobos exhibit the lowest and highest gravity acceleration, respectively. The range is between 5-6 · 10^{-3} m/s^2. However, the actual acceleration experienced by Phobos is different than gravitational acceleration presented in Fig. 5.3, because of the presence of Mars and the Phobos' orbit around it which induces centripetal and Coriolis accelerations. The acceleration experienced on the surface would therefore be a combination a vector sum of those and would appear as the acceleration term in Hill's problem. Figure 5.4 shows

the magnitude of net surface acceleration on Phobos surface.

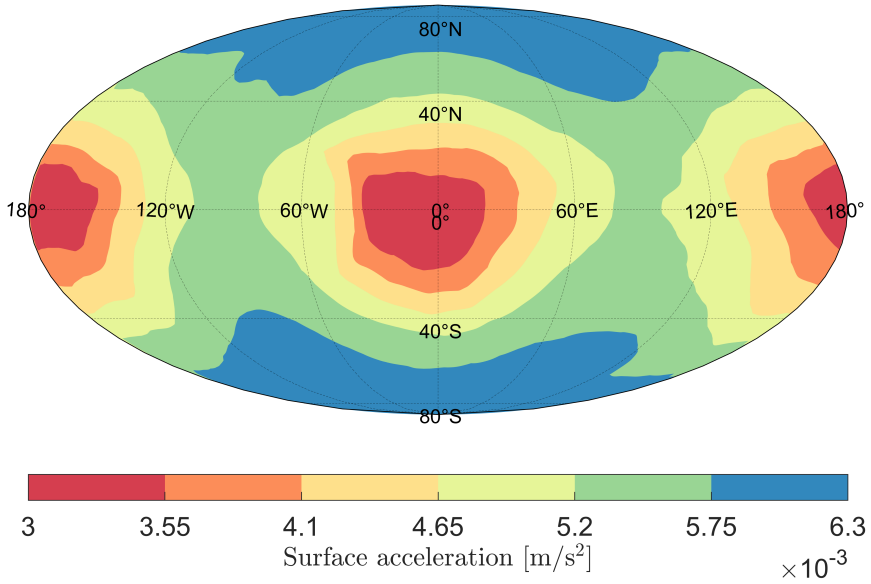

Figure 5.4: Surface acceleration on the surface of Phobos

The magnitude range of gravitational accelerations observed in 5.3 has now stretched in both lower and higher ends. The lowest values decrease to $3{\cdot}10^{-3}$ m/s^2 where the higher values increase to around $6.3{\cdot}10^{-3}$ m/s^2. While this change may not seem very high, in the chaotic small-body environments such small changes could lead up to escape, and thus drives mission-critical operational decisions. The exact description of the dynamical environment should therefore be take into account.

Another investigated aspect is surface slopes, *i.e.*, the direction of gravity vector with respect to surface normal. It is defined as the angle between surface (facet) normal and surface acceleration vector as below:

$$\phi = \pi - \arccos \frac{\hat{n}_u \cdot \mathbf{a}}{|\hat{n}_u \cdot \mathbf{a}|} \tag{5.1}$$

In Eq. 5.1, $\hat{n}_u$ denotes facet normal and **a** denotes surface acceleration at that facet. Surface slope on a small body defines the same concept as climbing uphill on an inclined surface, *e.g.* a mountain, where gravity points downwards to Earth's center whereas the surface normal points somewhere outwards, an angle between which and gravity vector would be less than 180^o due to the inclination. Hence, 180^o defines a 0^o slope. It is therefore an important parameter in defining the landing conditions and often one of the deciding parameters in selecting a landing site as footpads of a spacecraft can withstand certain inclinations. This opens up the possibility to explore high-slope and potentially regions of a small-body with ballistic landers. The results of slope calculations are given in Fig. 5.5.

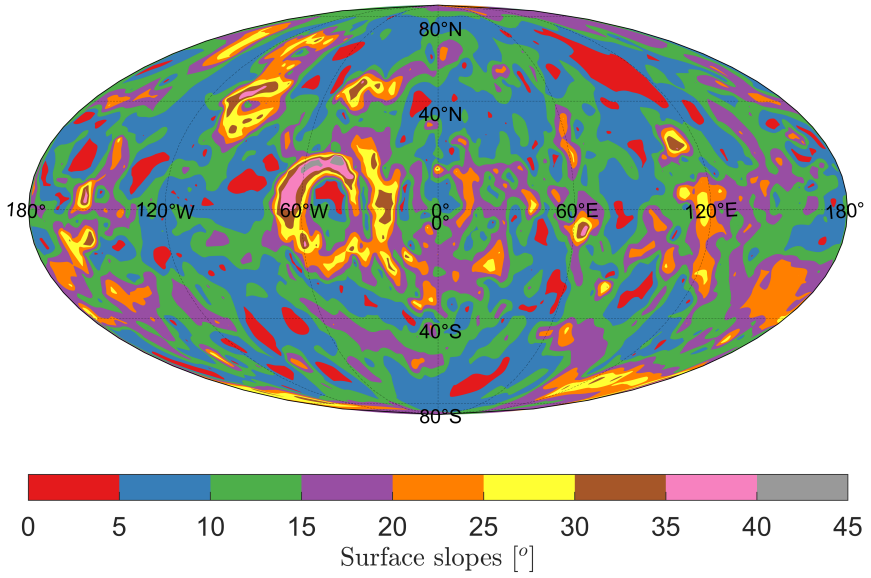

Figure 5.5: Surface slopes of Phobos

On Phobos surface, the slopes are lower than 20^o on average. The values as high as 48^o is observed. Although there are 0^o slope regions the equatorial region, where possible MMX and DCAM5 landings would occur, the majority of the slope values are

between 5^o and 20^o with the exceptions in the bottom of Stickney crater and small regions around 80^oE longitude and anti-Mars point. Following this, static friction coefficient in each facet can be computed with a simple “block-on-a-slope" approach to compute the minimum friction coefficient that is required to keep a particle on that facet with the formula as follows:

$$\mu_f = \tan \phi \tag{5.2}$$

where ϕ is the slope angle. According to Eq. 5.2, the computed μ_f values are presented across Phobos surface in Fig. 5.6.

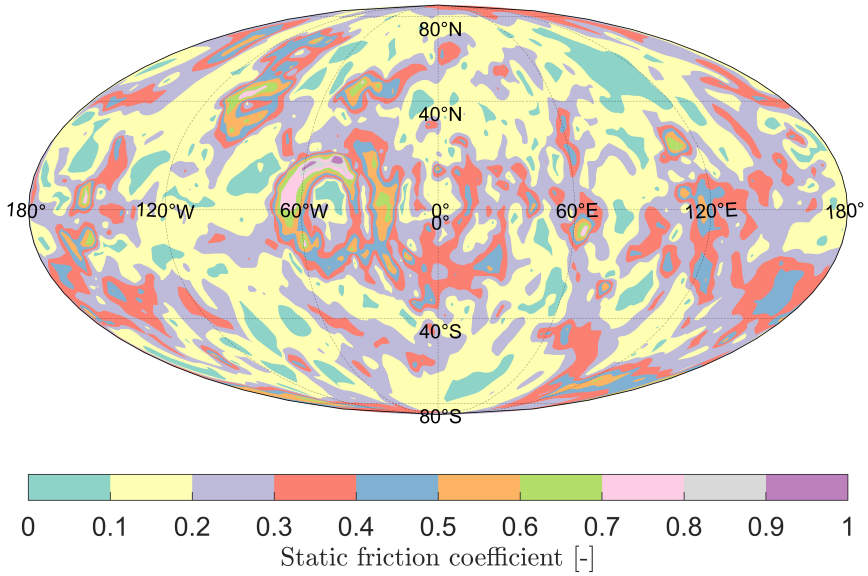

Figure 5.6: Static friction on the surface of Phobos

Majority of Phobos surface exhibit μ_f values less than 0.5 with exception the rim of Stickney crater and mid-latitude regions on the northern hemisphere where values 0.7 and higher are observed.

Finally, tilt angle, a geometrical property of a small-body surface relevant to landing problem is defined. Tilt angles can be used to express the orientation of a facet with respect to the body-fixed frame of a celestial body. It is the angle between the unit vectors of a facet normal and the position vector of a facet barycentre from the centre of mass. It can mathematically be defined as follows:

$$\gamma = \arccos \hat{\mathbf{n}}_u \cdot \hat{\mathbf{r}} \tag{5.3}$$

where $\hat{\mathbf{n}}_u$ denotes the unit vector of facet normal and $\hat{\mathbf{r}}$ denotes the unit position vector from the centre of mass of the body. Note that tilt angle is a geometric quantity and different than dynamical slopes, where the angle between unit vectors of the facet normal and the local acceleration is computed.

If a celestial body is spherical, γ would have always been zero, as the unit radius vector would be parallel to the unit normal vector of a facet. Tilt angles can then be thought of a deviation from this idealized case. Calculation of this deviation would give a preliminary understanding of what would be impact angle at landing. As an example, if a landing occurs at local vertical (i.e. 90^o) on a particular facet and γ is computed to be 20^o for the same facet, then the actual landing would likely to occur at 70^o in the real shape model. Tilt angle values across the surface of Phobos is shown in Fig. 5.7.

As one might expect, the highest tilt angles appear in the crater walls. The values go up to 60^o in the wall of Stickney crater and in the north and south poles of Phobos. In other regions the values are mostly 30^o or less. While high tilt angles imply a challenge for the mothercraft, it also creates an opportunity for DCAM5 type landers, as they can be used much more daringly.

Dynamical properties of Mars-Phobos system

Following the discussion above, first zero velocity surfaces (ZVS) and equilibrium points of the Mars-Phobos system are generated, as shown in Fig. 5.8.

The exact location of the equilibrium points denoted with L1 and L2 in Fig. 5.8 can also be computed via Newton method as:

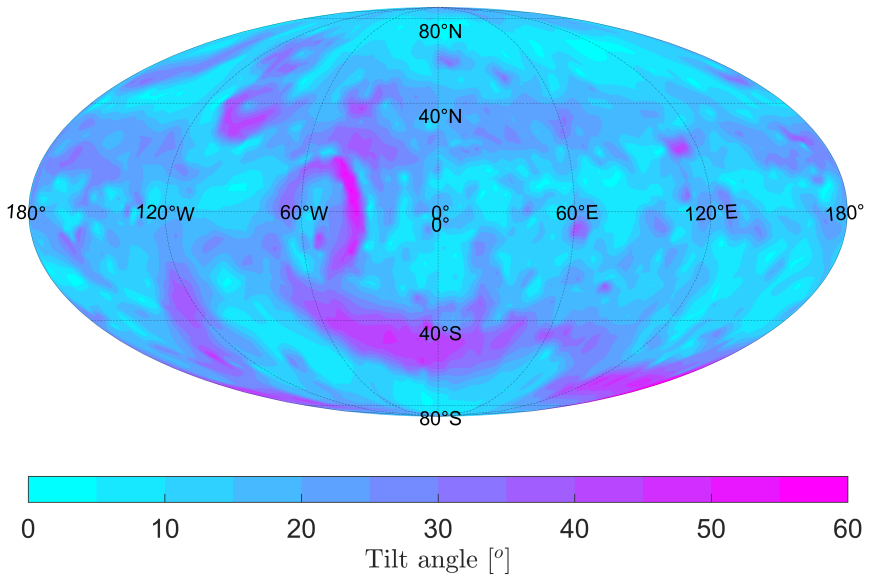

Figure 5.7: Tilt angles on Phobos surface

$$\mathbf{r}_{L_1} = \begin{bmatrix} -17.2989 \\ 0.3945 \\ -0.2581 \end{bmatrix} \text{km}, \mathbf{r}_{L_2} = \begin{bmatrix} 17.2955 \\ 0.4526 \\ -0.0325 \end{bmatrix} \text{km}$$

Note the y and z components of $\mathbf{r}_{L_1}$ and $\mathbf{r}_{L_2}$ are different from zero due to the irregular gravity field of the Martian moon induced by its shape. The Jacobi Integral values of the equilibrium points are $C_{L_1} = 2.2283$ and $C_{L_2} = 2.2251$, respectively and correspond to the blue and red contours in Fig. 5.8.

The unique feature of Mars-Phobos system is revealed by the structure of its ZVS. For the majority of the planetary moons of the solar system, ZVS enclose the entire body at L1 energy level, i.e. there is no connection between primary and secondary. Due to Phobos' size and proximity to Mars, the leading and trailing sides of Phobos "overflow" its *Roche Lobe*, i.e. the enclosing (red) curve defined by Jacobi Integral

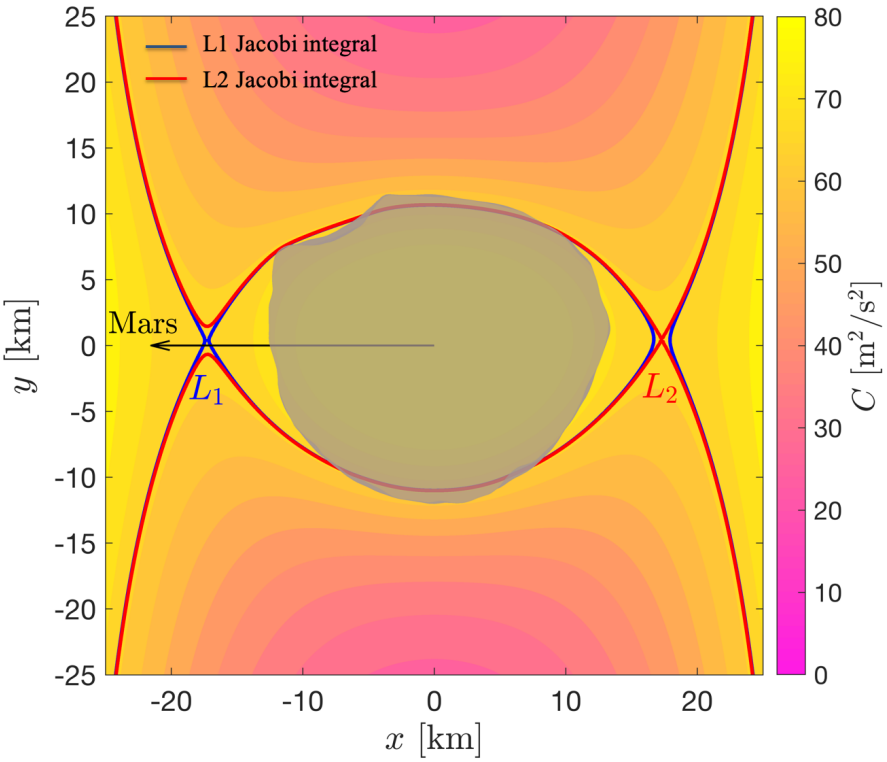

Figure 5.8: Zero-velocity surfaces around Phobos. Blue and red lines show zero-velocity surfaces at Jacobi integral values corresponding to that of L1 and L2 points, respectively.

value of the L1 point. Because of this overflow, particles resting on those regions are *energetically unbound* to Phobos, *i.e.*, they already have enough energy to depart the surface. For the other regions where one can define “guaranteed return speed" with respect to one of the equilibrium points for a particle whose position is below that of the equilibrium points [49]:

$$v_{L_i} = \sqrt{2(C - C_{L_i})} \tag{5.4}$$

where v_{L_i} and C_{L_i} $(i = 1,2)$ are guaranteed return speed and Jacobi Integral value of the respective equilibrium point. If a particle’s speed is lower than or equal to guaranteed return speed, then it would eventually return to the surface. On the other hand, if the speed is greater than the L_1 guaranteed return speed, motion around Phobos cannot be guaranteed. As for particles in the regions of Phobos that is overflowing ZVS, Jacobi integral value is higher than that of L1, hence this value is 0. Guaranteed return speeds across Phobos surface for L1 point can be found in Fig. 5.9. It appears from Fig. 5.9

that, in addition to leading and trailing sides, particles in north pole of Phobos are also energetically unbound to Phobos. The highest value is computed to be 4 m/s and in sub- and anti-Mars regions, respectively.

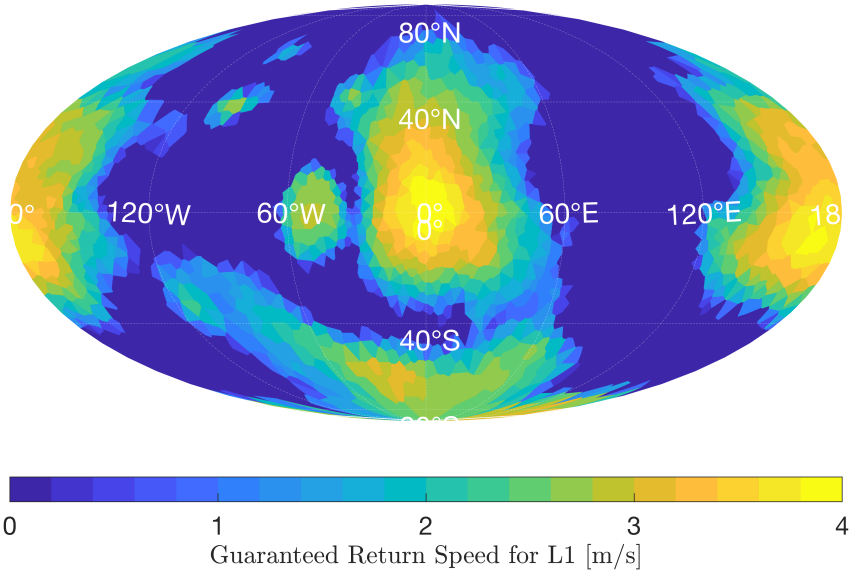

Figure 5.9: Guaranteed return speed across the surface of Phobos for L1 point.

An important point to note is that guaranteed return speed is only a “necessary" but not sufficient condition for escape. In other words, velocities larger than v_{L_1} do not necessarily imply that a particle will depart from the surface of Phobos. The sufficient condition for escape requires a more detailed analysis on the local acceleration vector in this highly nonlinear dynamical regime. A brief numerical analysis about particle motion in these locations is provided by Scheeres et al. (2019) [122]. Moreover, trapping a particle’s motion in the enclosing region around it to ensure surface settling was discussed by Tardivel et al. (2013) [128]. However those conditions in Tardivel et al. (2013) are not applicable to this study, as Phobos overflows its Roche Lobe. Therefore an investigation on the actual escape conditions from the surface is provided in the next section.

5.3.2 Surface escape speed

There is no analytic expression for the escape speed of particles resting on the surface of secondary body in three-body systems. To compensate this lack of knowledge, surface escape speeds from the surface of Phobos are computed with a Monte Carlo simulation. 10000 particles are ejected from each polyhedron facet across the surface of the Martian moon while varying the direction and magnitude of the escape speed. An illustration of this analysis is provided in Fig. 5.10. This analysis extends the similar escape studies in Dobrovolskis and Burns (1980) and Davis et al. (1981) in CR3BP, where Phobos gravity is modelled as an ellipsoid [118, 119]. Differently from those, the real shape of Phobos is taken into account in this thesis in order to provide deeper insights into escape and re-impact conditions on Phobos surface.

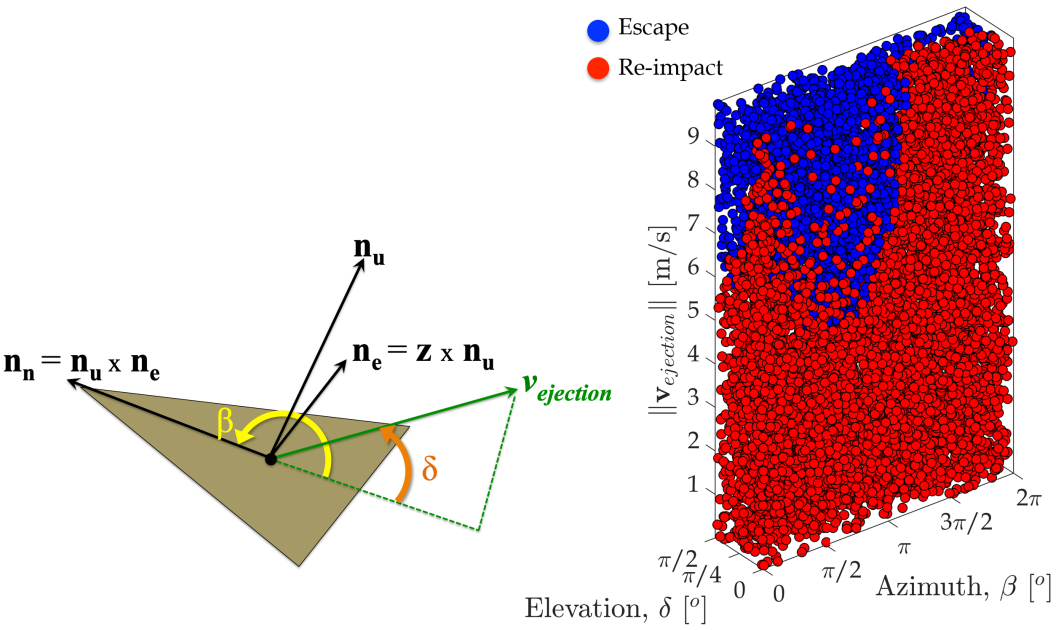

Figure 5.10: An illustration of the escape speed computation on a facet and an example of the simulation outcomes. Right figure is by the courtesy of Dr. Nicola Baresi.

The directions of motion are sampled from spherical coordinates with uniform distributions between $[0,\ 2\,\pi]$ and $[0,\ \pi/2]$ in azimuth and elevation, respectively. The initial velocity varies between 0 and 10 m/s, prompting a numerical integration that follows each of the particles from the barycentre of each facet till either escape or reimpact against Phobos' surface within one orbital period of the Martian moon (i.e.,

twice the battery lifetime of DCAM5). The lowest escape speed computed among all cases is determined as the escape speed of that facet. The results are depicted in Fig. 5.11.

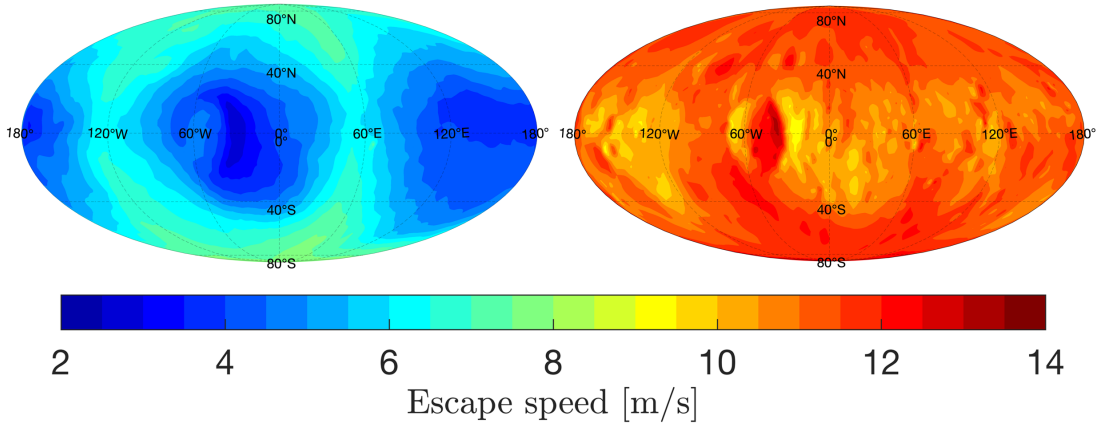

Figure 5.11: Escape speeds on Phobos. Left: Escape speeds in three-body dynamics assumption. Right: Escape speed with two-body dynamics assumption.

Figure 5.11 reveals that escape from the surface of Phobos is possible with speeds as low as 2 m/s. The stark contrast between escape speeds with two-body and and three-body dynamics approximations becomes apparent when one compares the results between those. The minimum escape speed computed with the two-body dynamics approximation results in ~9 m/s, i.e. greater than four times that of the three-body dynamics approximation. Even the maximum escape speed computed with three-body approximation is lower, i.e. about 8 m/s at the poles of Phobos.

Of course, it is possible that longer propagation times might result in new impacts against Phobos, thereby lowering the escape speed from particular facets. However, if one considers the battery life of the lander (~3 hours) as well as the total duration allocated for the mission (~3-6 hours), it is unlikely that these trajectories would be of interest for the mission at hand. That is to say, the mission would be lost already if the lander did not impact back to the surface within one orbital period of Phobos, which is why post-impact speeds are needed to be constrained. In this study, the upper limit for the post-impact speed is taken as a slightly higher value than the minimum of 2 m/s found. This is because that 2 m/s value is very localized, and escape speed values for most of equatorial region is below 4 m/s.

5.3.3 Surface coefficient of restitution

Since the post-impact (~4 m/s) is significantly lower than the maximum allowed impact speed (15 m/s), it becomes essential to surface coefficient of restitution Phobos and understand how much energy can be dissipated during the impact events. In the previous two chapters, this thesis investigated two end-members of surface interaction, namely hard and soft surface models. In this chapter, those will be used to estimate the surface coefficient of restitution and put an upper bound impact speed to constrain the post-impact speed. In both surface models, the coefficient of restitution is dependent upon many parameters, including impact velocity and attitude, impactor shape, as well as surface properties. For that reason, an effective coefficient of restitution is defined for a equal comparison, as:

$$\epsilon = \frac{v^+}{v^-} \tag{5.5}$$

where ϵ is the effective coefficient of restitution, v^- and v^+ are pre- and post-impact velocity magnitudes of the lander, respectively. Unlike the classical definition of ratios of normal velocity components, this definition allows us to make a direct comparison with the escape speeds presented earlier, regardless of the direction of motion. It is worth noting that different definitions of ϵ also exist, see Ref. [129, 44]. The coefficient of restitution values that will be presented in the next subchapters are calculated with Eq. 5.5.

Hard surface

The hard surface impact experiments are used to derive the coefficient of restitution relationships in this subsection. Recall that two different experiment cases were tested at two milli-g levels of gravity with impact speeds between 5 and 25 cm/s. For the purpose of the analysis presented in this section, only oblique impact results are considered. That is because, no attitude effects are simulated in the study, and it is reasonable to assume that nearly all impacts in small body environments are oblique. Moreover, the gravity levels considered in the hard surface experiments are in the same order of magnitudes of surface acceleration experienced on the surface of Phobos, as shown in Fig. 5.4, therefore it is believed that results are applicable to this case. Finally, even though impact velocities considered in this study are at least an order of

magnitude lower than the upper limit of impact velocity that was set for the lander, the fact that there is only a weak impact velocity dependence is observed in the ϵ values in the hard surface impact experiments suggest that the results are valid for a wider range of impact speeds. Figure 5.12 shows the coefficient of restitution values from the hard surface impact experiments.

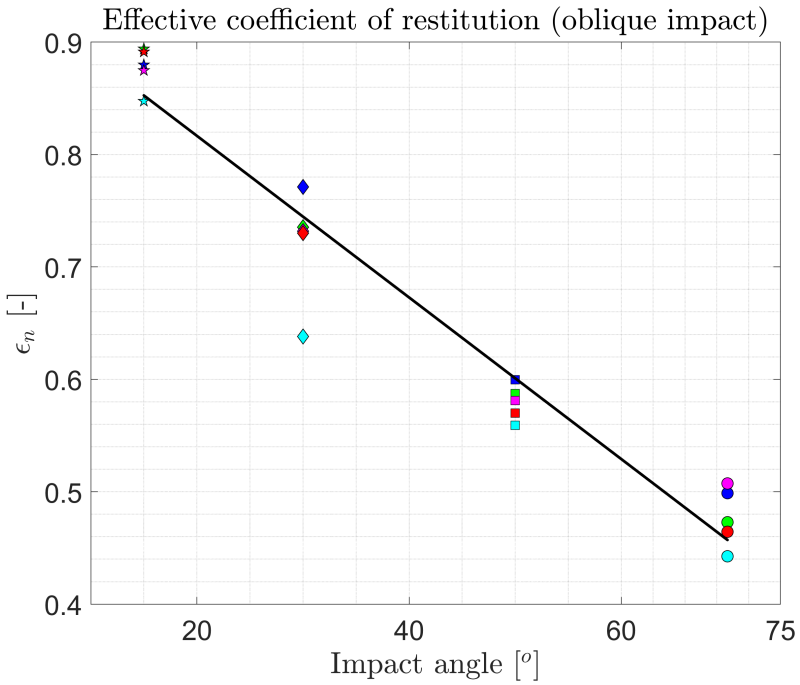

Figure 5.12: The effective coefficient of restitution extracted from oblique impact experiments presented in Chap. 3

Note that the trend line of the figure is different than the one presented in the experiment chapter. This is because here impact angle is measured from local tangent of the impacted surface. According to this, it can stated that there is linearly decreasing trend of ϵ with increasing impact angle. Nevertheless, the ϵ value is relatively high, at especially shallower angles. The minimum value in Fig. 5.12 at 70^o impact angle is ~0.45. The trendline corresponds to -0.41θ+0.96, where θ is impact angle in degrees. If it is assumed that the trend is valid for all impact angles, then the minimum ϵ value would be 0.31 for a vertical impact.

For maximum allowed post-impact speed 4 m/s and structural allowed 15 m/s, as well as the minimum allowed post-impact angles, following constraints can be

imposed to impact speed when the surface is hard: If the impact angle is 45^o, ϵ = 0.67, therefore max. allowable impact speed is ~6 m/s. If the impact angle is 60^o, then ϵ = 0.53, allowing a higher impact speed of ~7.6 m/s. These are then going to be taken as basis when downselecting trajectories with the hard surface assumption.

Soft surface

The second surface type that is considered in this study is soft granular surface, which was studied in the previous chapter. The surface is assumed to be fully granular in this as opposed to a hard surface that is nonpenetrable. An analytical expression is derived for the coefficient of restitution from cratering theory. The derived analytical model is general, *i.e.*, therefore can be applied across different gravity levels and impact speeds. Here, impact speeds between 1-30 m/s are used for a *spherical* lander of 0.05 m radius and 1 kg, equals to impactor δ = 1200 kg/m^3. Phobos surface density is currently unknown, but the reported value ρ = 1600 kg/m^3 with porosity of ~35% is used [103]. According to the analysis presented in the previous chapter, the δ/ρ ratio should result in impactor's submerge. However, the existence of tangential component of motion will enable a bounce, as demonstrated in Çelik et al. (2019) [3]. The power-law coefficients in the analytical formulation are as the same as those used in the previous chapter, as μ = 0.5 and K_1 = 0.87.

As the analytical approach is currently only available for vertical impacts, the tangential coefficient of restitution must be incorporated in the analysis. An empirical approach will be taken for that purpose. The DEM impact simulations data from Çelik et al. (2019) will be used to extract the tangential coefficient of restitution.

In short, Çelik et al. (2019) implemented impact simulations with a state-of-the-art contact dynamics code, `pkdgrav`, is used to simulate the impacts of DCAM5 with the regolith-covered Phobos surface [3]. Details of `pkdgrav` are provided in Chap. 2. Figure 5.13 presents four snapshots from one of the impact simulations carried out for that study [3].

The impacts are initiated 1 m above the representative Phobos surface with landing speeds between 2.5 - 13 m/s. Impact angles are varied from 20^o to 90^o (i.e., in local vertical). A single attitude configuration is considered, in which the bottom of DCAM5 impacts the surface first, i.e. the camera angle is assumed 0^o throughout the simulations.

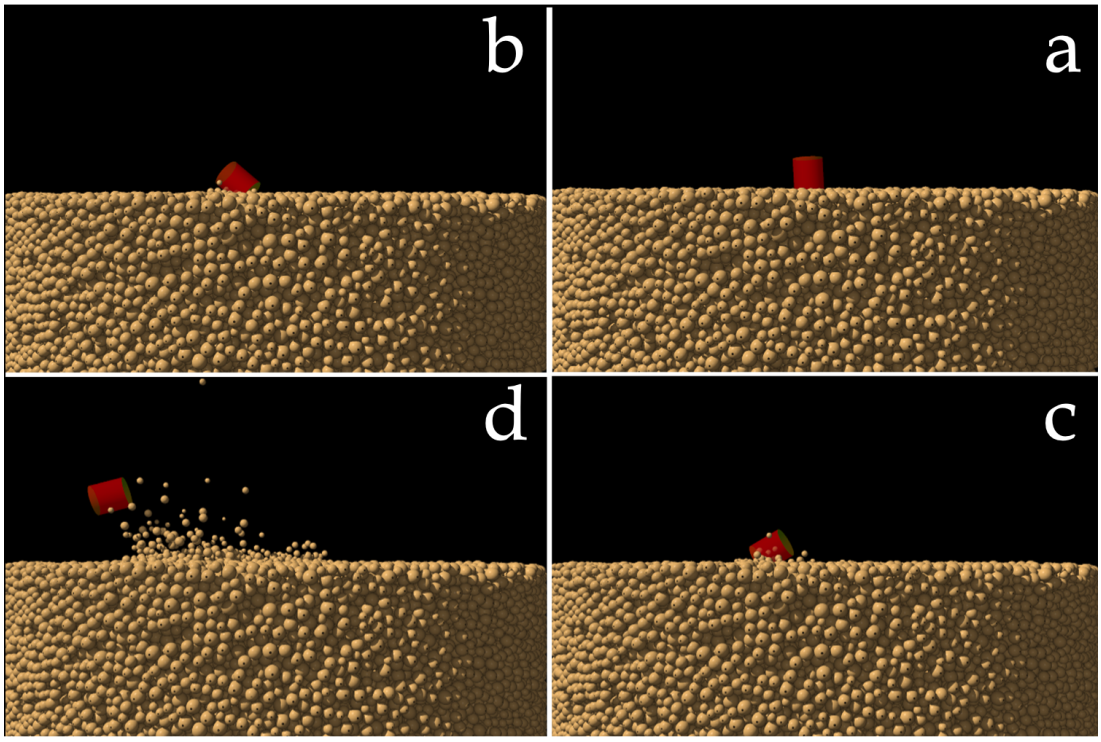

Figure 5.13: Numerical impact simulations. Subfigures a-d from top right corner to lower left corner show respectively the first contact, continued interaction with surface deformation and separation from surface [3].

DCAM5 structure is given a normal coefficient of restitution value of 0.6, similar to the MASCOT lander [44], to account for its structural damping. Table 5.3 summarizes the surface properties simulated in `pkdgrav`.

The tangential coefficient of restitution can then be calculated as:

$$\epsilon_t = \frac{v_t^+}{v_t^-} \tag{5.6}$$

where ϵ_t is the tangential coefficient of restitution, v_t^- and v_t^+ are pre- and post-impact tangential velocity magnitudes of DCAM5, respectively. Figure 5.14 (right) shows the results of the ϵ_t analysis, alongside the analytical estimations on the left.

For normal impacts, the analytical approach results in ϵ values that are asymptotic, *i.e.*, it starts increasing with the increasing velocity, before approaching to some constant value. That is because initially impactor's energy is very low at low speeds,

Table 5.3: Phobos regolith properties used in the simulations [3]

Property	Value used in this work
Grain size	0.6 – 1.3 cm
Size dist.	truncated Gaussian
Shape	Spherical
Internal friction angle	30.7^o
Cohesion	N/A
Macroscopic porosity	~35%

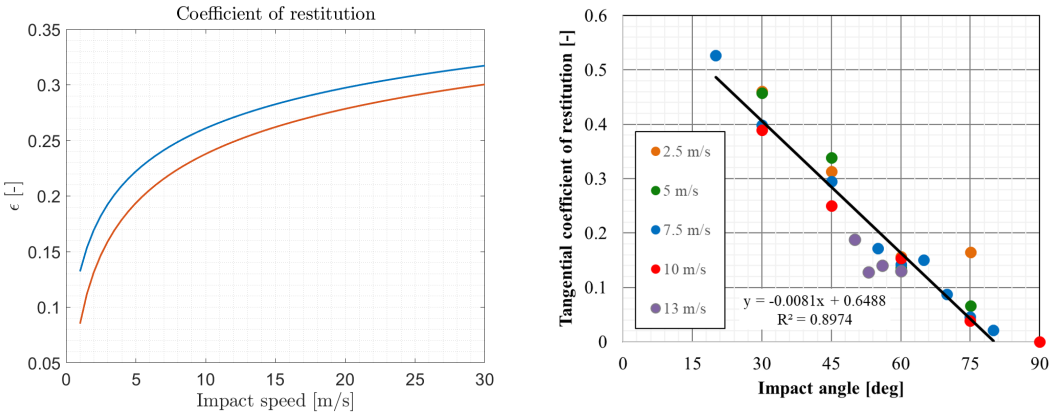

(a) Normal

(b) Tangential

Figure 5.14: The coefficient of restitution values with the soft surface approach. As the analytical model currently only available for normal impacts, tangential component of the coefficient of restitution is used empirically from DEM simulations.

resulting in more energy to spent for cratering, hence less for bouncing. As the impact speed increases, less of energy is spent for cratering, increasing the coefficient of restitution. On the other hand, for ϵ_t, the relationship is more straightforward: ϵ_t decreases linearly with increasing. The impact speed dependence appears to be weak. In order to constrain the impact speed from the information in Fig. 5.14, following expression is used:

$$v^+ = \epsilon v^- \cos\theta_{imp} + \epsilon_t v^- \sin\theta_{imp} \tag{5.7}$$

where v^-, v_+ are pre- and post-impact speed (*i.e.*, 4 m/s), ϵ and ϵ_t values extracted coefficient of restitution values from Fig. 5.14 with impact angle, θ_{imp}. In the light of these and escape speed results, an upper bounds on impact angles and maximum

impact speeds can now be placed. Since θ_{imp} $\geq 45^o$, ϵ_t is ~0.3. This, and the fact that escape from the surface is possible with velocity as low as 4 m/s imply that maximum acceptable impact speed is on the order of 10 m/s. Higher impact speeds may be accepted if and only if their corresponding impact angles are higher than 60^o (corresponding to $\epsilon_t \approx 0.15$). Based on these values, the feasibility of ballistic landings can now be determined. Ballistic landings of DCAM5 will be considered successful if θ_{imp} $\geq 45^o$ when $10 < v_{imp} \leq 10$ m/s and θ_{imp} $\geq 60^o$ when v_{imp} ≤ 15 m/s.

In addition to these constraints, the final constraint will be derived in the next section to constrain the deployment speeds before exploring the feasibility of ballistic landings from QSOs.

5.4 Mission-driven constraints on deployment and landing

This section deals with MMX-driven constraints on the deployment. First, the selected mission orbits are introduced and then a estimation on the upper limit of deployment speeds is made.

5.4.1 Quasi-satellite orbits (QSOs)

For the deployment analysis presented in this paper, three different sizes of QSOs are selected. These are the 30 x 50 km (blue), 24 x 35 km (green) and 22 x 31 km (red) size QSOs, as provided in Fig. 5.15. The largest size is the current baseline of and the second is also considered for MMX close proximity operations. All of these QSOs are currently under investigations by the MMX team for the proximity operations around Phobos [115].

A relevant and important point to this research is that QSOs are highly energetic orbits. The Jacobi integral values of the QSOs presented are -0.79417, -0.47008 and -0.37064 respectively. Hence, in the QSO energy regimes, zero-velocity curves disappear around Phobos, making the analysis in Sec. 5.3 quite critical for ensuring the surface settlement of DCAM5. Moreover, because of high relative speed (~8-15.5 m/s) in the QSOs, it is likely that high deployment speeds would be required to divert the lander's

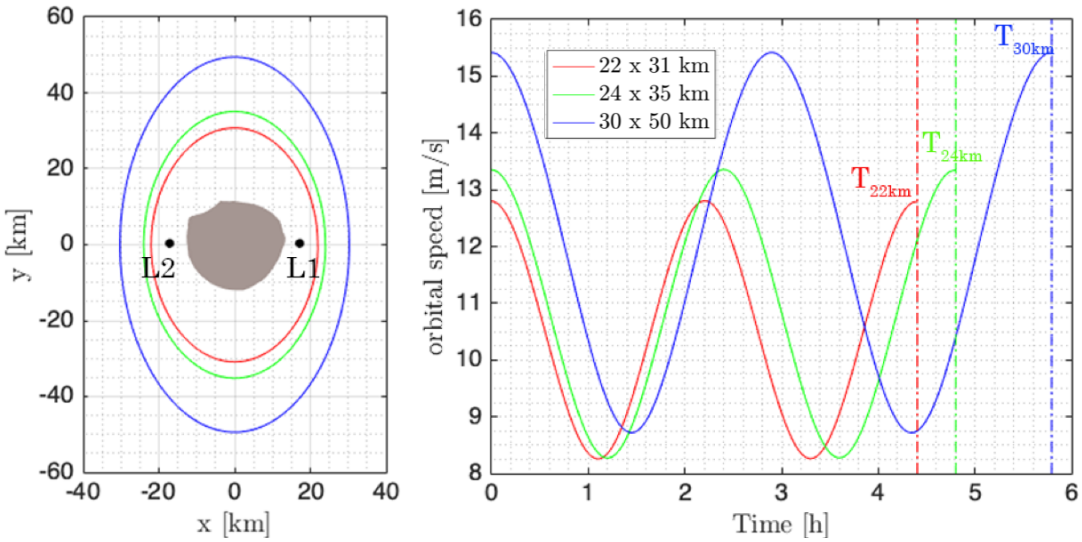

Figure 5.15: Low altitude QSOs around Phobos. Left: QSOs considered in this paper. Right: Their orbital speeds and periods. The periods are shown with vertical dashed lines for each size of QSO.

motion from a QSO to the surface. In order to quantify the order of magnitude of these deployment speeds, a computational procedure will be applied. Its details and outcomes are presented in the next subsection.

5.4.2 Estimation of deployment speeds

Before performing large scale deployment simulations, it is reasonable to have an order of magnitude understanding to constrain deployment speeds. To do that, a two-step procedure is applied. First, minimum landing speeds for a local vertical landing (i.e., $\theta_{imp} = 90^o$) are computed with the bisection algorithm presented in [75] for ballistic landing problems in small body environments. The algorithm propagates trajectories backwards in time from a landing site. Landing speeds are constrained within some upper and lower boundaries to find a minimum landing speed that satisfies predefined criteria for a ballistic landing trajectory. In this study, intersecting the QSOs is employed as the criterion to satisfy. Upper and lower boundaries of the bisection method are defined with two distinct criteria, depending on whether the region is overflowing Phobos or not:

$$[v_{low}, v_{up}] = \begin{cases} [v_{L1}, 2v_{L_1}] & \text{if } v_{L_1} > 0 \\ [0, 2v^{2B}_{esc,min}] & \text{if } v_{L_1} = 0 \end{cases}$$

where v_{low} and v_{up} denote lower and upper bound estimation of landing speeds, respectively and v_{L_1} is the L1 return speed. $v^{2B}_{esc,min}$ is the minimum escape speed computed on Phobos surface with classical two-body dynamics approximation, i.e. ~9 m/s. Once the minimum landing speeds (v_{min}) are computed, Monte Carlo simulations are initiated from each landing point to compute the minimum deployment speeds. Two distinct cases are defined for Monte Carlo samples:

$$[v^{MC}_{low}, v^{MC}_{up}] = \begin{cases} [v_{min}, 2v_{L_1}] & \text{if } v_{L_1} > 0 \\ [v_{min}, 2v^{2B}_{esc,min}] & \text{if } v_{L_1} = 0 \end{cases}$$

where v^{MC}_{low} and v^{MC}_{up} denote the minimum and maximum values of uniform distribution. Then, 1000 trajectories with randomly assigned landing speeds are propagated backwards until the point in time where they intersect the QSO distance. At the crossing point, deployment speeds are computed with a simple formula:

$$\Delta v = |\mathbf{v}_{QSO} - \mathbf{v}_{imp}| \tag{5.8}$$

where v_{QSO} and $v_{landing}$ are velocity magnitudes of QSO and the velocity of landing trajectory at the intersection point, respectively. This two-step procedure is performed for landing locations in equatorial region of Phobos and results are presented in Fig. 5.16 for the 22 x 31 km QSO case.

Figure 5.16 shows impact speeds, deployment speeds and landing times altogether. A clear, linear trend for high-speed landings are visible for increasing deployment speeds. This high Jacobi-constant trajectories are also reaching the surface within an hour of deployment. However, we are more interested in lower impact speeds to increase the likelihood of staying on the surface, and lower deployment speeds for a simpler deployer design. This part of the solution space appears to be more chaotic, due to the highly unstable dynamics near the equilibrium points. Trajectories in this region take longer to the surface, sometimes even longer than the lifetime of DCAM5. However, no landings occur below 3 m/s. As for deployments speeds, the minimum is

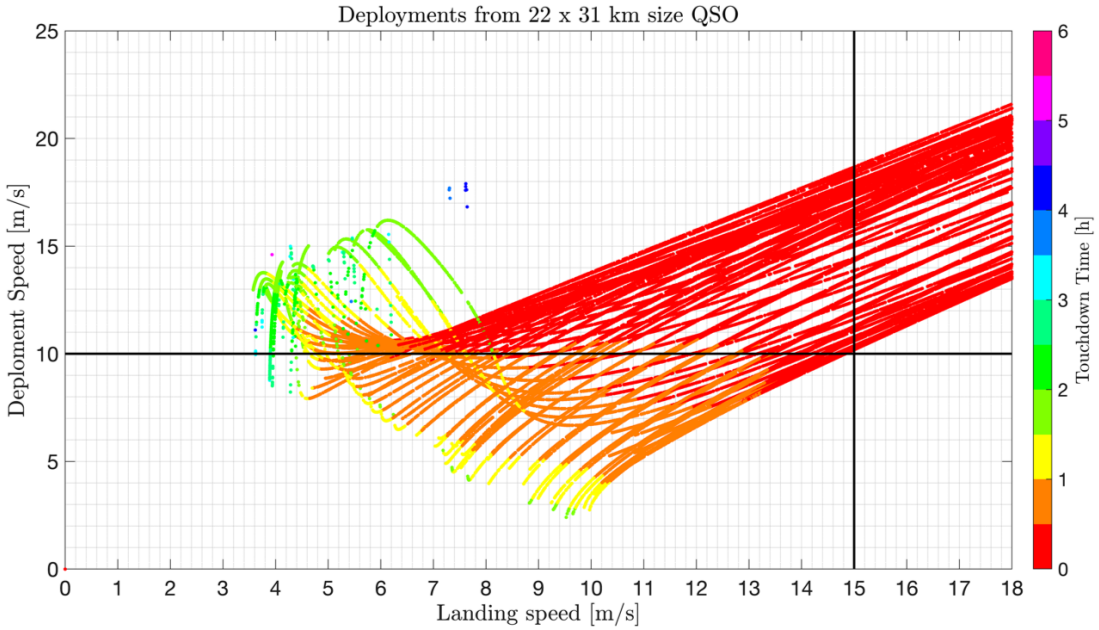

Figure 5.16: Landing speeds and corresponding deployment speed for deployments from 22 x 31 km size QSO. The colour code shows touchdown duration. Maximum allowable landing speed and deployment speed is marked with black lines.

found to be 2.4 m/s and translates to impact speed of 10 m/s on the surface.

Of course, this analysis considers a very specific landing geometry and does not take into account the direction of deployment. But what is more important is that there is no landing possible with sub-m/s deployment speeds, contrary to what is frequently encountered in ballistic landings in small body environments [21, 75, 130]. Slightly different landing conditions, which are most likely to be observed, may result in lower deployment speeds. As a result, the grid search algorithm presented in the next section is constrained to provide 1-10 m/s deployment speeds. This limits the impact speeds to $\leq$~15 m/s in agreement with in the DCAM5 requirements (Sec. 5.2).

5.5 Ballistic landings on Phobos

Before explaining the computational procedure, it is worth summarising the requirements derived in the previous sections. The analyses of the presented in the previous

sections have reduced the design space of DCAM5 ballistic landings as below:

1. The velocity magnitude after the first impact shall be ≤4 m/s (Sec. 5.3.2).
2. The impact angle (θ_{imp}) shall be (Sec. 5.3.3)
   (a) θ_{imp} ≥45^o for impact speed v_{imp} ≤ 10 m/s
   (b) θ_{imp} ≥60^o for 10 m/s ≤ v_{imp} ≤15 m/s.
3. Deployment speed (Δv) shall be between 1 and 10 m/s. (Sec. 5.4.2)

Even though DCAM5 is given a 100^o/s rotation as mentioned earlier, the current study does not include this in the current analysis for the sake of comparability between two surface model, of which one does not currently include rotation in its formulation. Interested reader may refer to Çelik et al. (2019) for an analysis on the effect of spacecraft attitude [3]. Ballistic deployments from the QSOs are computed using a grid-search technique that explore the different combinations of the parameters shown in Fig. 5.17.

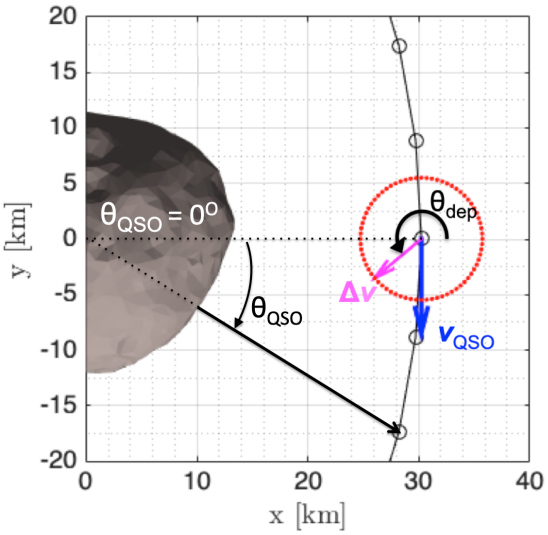

Figure 5.17: Grid search technique applied to ballistic deployments from QSO. θ_{QSO} defines the deployment position on a given QSO. For a given θ_{QSO}, the deployment speed Δv is added to the QSO velocity vector $\mathbf{v}_{QSO}$ at varying deployment angles, θ_{dep}.

First, each QSO is discretized into 37 deployment points which are ~10^o apart from each other. Then, the deployment directions are established in the counterclockwise

direction with an hour angle where 0^o overlaps with x-axis of the rotating reference frame. 72 deployments from a single deployment point are initialized with 5^o separation. The deployment speed is varied between 1-10 m/s. Note that all deployments are planar, i.e. no out-of-plane velocity component is given. A total of 2592 trajectories are propagated together for each deployment speed and QSO size. If a trajectory reaches the surface, the feasibility of a landing is assessed in terms of impact speed (v_{imp}), impact angle (θ_{imp}), and time-of-flight from deployment to landing. All landings longer than 2 hours are marked as infeasible without further checking on the other impact properties. If a trajectory takes less than 2 hours, impact conditions are assessed according to surface type with following criteria:

- *Soft surface.* If $\theta_{imp} \geq 60^o$, then v_{imp} up to 15 m/s is allowed. If $\theta_{imp} \leq 60^o$, then the maximum v_{imp} accepted as feasible is 10 m/s.
- *Hard surface.* If $\theta_{imp} \geq 60^o$, then v_{imp} up to 7.6 m/s is allowed. If $\theta_{imp} \leq 60^o$, then the maximum v_{imp} accepted as feasible is 6 m/s.

In the end of all simulations, the number of feasible cases is calculated in an attempt to identify optimal deployment speeds for each QSO size. The results are presented in Fig. 5.18.

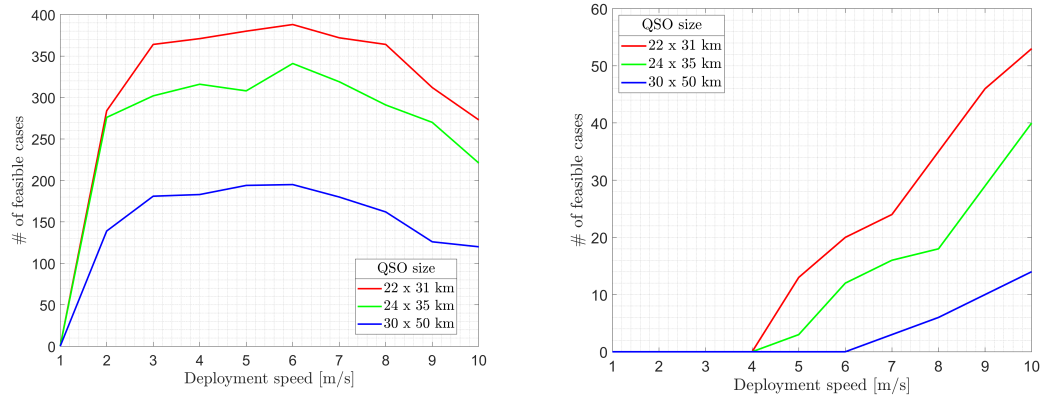

(a) Soft surface.

(b) Hard surface.

Figure 5.18: Optimal deployment speed for each QSO altitude to maximize feasible cases

As expected, the majority of feasible trajectories are encountered in the lowest altitude QSO. An apparent optimal deployment speed exists that maximizes the number of feasible cases when the surface is purely soft, which occurs at 6 m/s at all QSO altitudes. The total number of feasible cases is nearly 400 for the smallest QSO, and ~350 and ~200 for the largest two, respectively. Moreover, there is a wide range of deployment speeds between 2 m/s to 8 m/s where the number of feasible cases vary within only a narrow range, which could be consider for a deployment mechanism design, if, for example, 6 m/s is deemed too high.

When the surface is hard, however, an increasing trend of feasible cases is seen, starting from 5 m/s deployment speed for the two smallest QSOs and from 7 m/s for the largest QSO. Thus, the highest number of feasible cases only appear at 10 m/s. The result for the hard surface case suggests that an optimal point like in the soft surface case may exists for higher deployment speeds. The number of feasible cases is considerably low compared to soft surface case, and 55, 40, and 15 from the smallest to the largest QSOs, respectively. Given the high energy of motion on the QSOs, this is not a surprising result, as the hard surface approach demands a significant speed reduction at impact for feasibility.

It is worth noting that, in Çelik et al. (2019), the authors implemented DEM simulations *with* the attitude dynamics simulations [3]. As a result, a significant reduction in the number of feasible cases is found with a number between the hard and soft surface approaches. While a clear optimal point for each QSO is found, the deployment speeds were observed to be increasing with decreasing QSO size.

Figure 5.19 shows the impact conditions of DCAM5 deployments from each QSO sizes and with the deployment speeds that correspond to the highest cases of feasibility.

Points in Fig. 5.19 are darkened whenever they do not meet the feasibility criteria 1–3 as provided in the beginning of the section. The figures reveal that all kinds of landing configurations are possible, from surface-grazing impacts to near-vertical impacts. In the feasible region, the minimum impact speed is always higher than 6 m/s with the soft surface approach. This value decreases down to 4 m/s with the hard surface approach, albeit with significantly less feasible cases.

It is also of interest to find out reachable landing sites with the surface constraints on the mission. First, reachable regions with the soft surface approach can be seen in

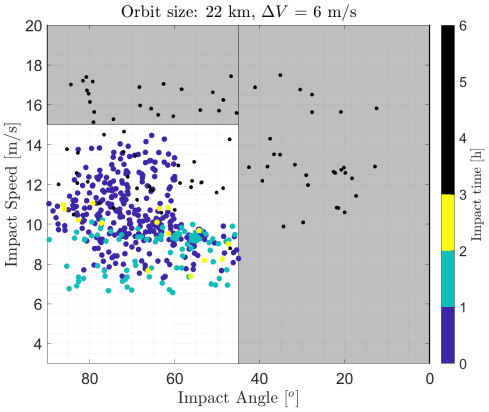

(a) QSO: 22 x 31 km, ΔV = 6 m/s, Soft

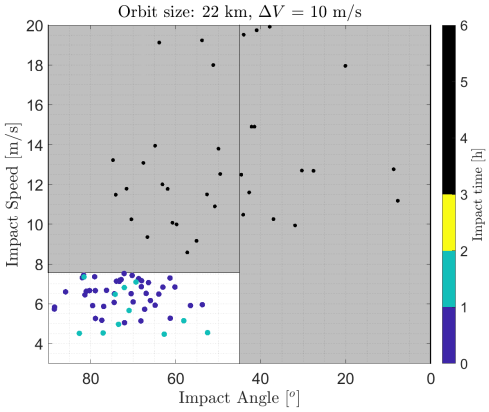

(b) QSO: 22 x 31 km, ΔV = 10 m/s, Hard

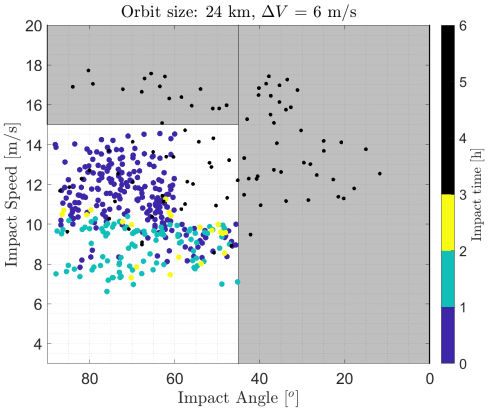

(c) QSO: 24 x 35 km, ΔV = 6 m/s, Soft

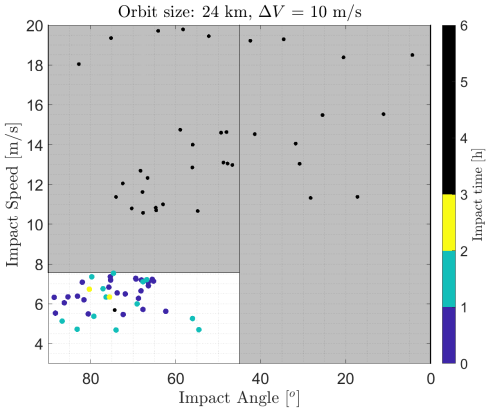

(d) QSO: 22 x 31 km, ΔV = 10 m/s, Hard

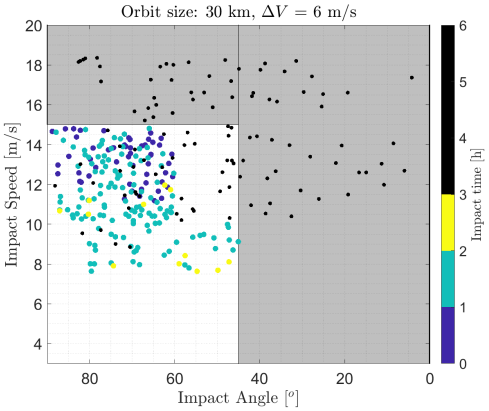

(e) QSO: 30 x 50 km, ΔV = 6.0 m/s, Soft

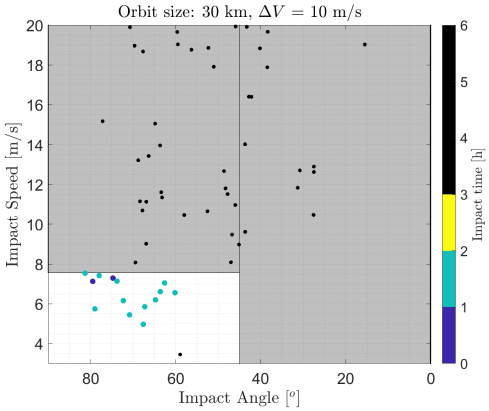

(f) QSO: 22 x 31 km, ΔV = 10 m/s, Hard

Figure 5.19: Impact speeds, impact angles and ToF results of all impacts from the optimal separation cases at each QSO altitude considered for deployment. The shaded areas show infeasible deployments. Black dots show impacts take longer than 3 hours.

Fig. 5.20, where per mille of all deployed trajectories (i.e. 2592) for each QSO altitude is shown, as a function of their impact location.

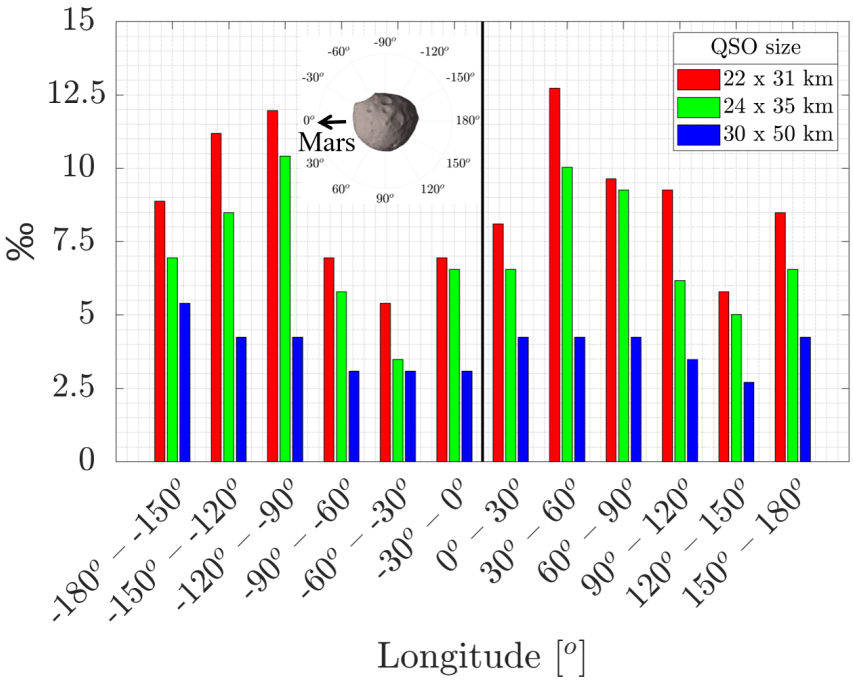

Figure 5.20: Landing dispersion with the soft surface approach across Phobos surface as per mille of 2592 trajectories deployed from each QSO altitude. Red, green and blue bar plots represent the deployments from 22 x 31 km, 24 x 35 km and 30 x 50 km QSOs, respectively. Black line in the middle denotes the sub-Mars longitude.

In general, everywhere on the equatorial region of Phobos appear to be reachable from each QSOs considered. The largest QSO provides the lowest reachability, whereas the smallest provides the highest as inferred from the overall feasibility results. The variation in reachability between regions is highly variable for the lowest, and the mid-size QSO, however. The scientifically-interesting regions, *e.g.*, Stickney crater(-30^o to -60^o), red/blue geological unit (0^o to -30^o), or sub- and anti-Mars points are reachable from all QSOs considered in this study. A potentially interesting result is that the highest reachability is achieved for longitudes between 30^o to 60^o and from the smallest QSO.

When one considers the Phobos surface as entirely hard and rocky, the reachability is extremely limited. While still the smallest QSO provides the highest reachability, its

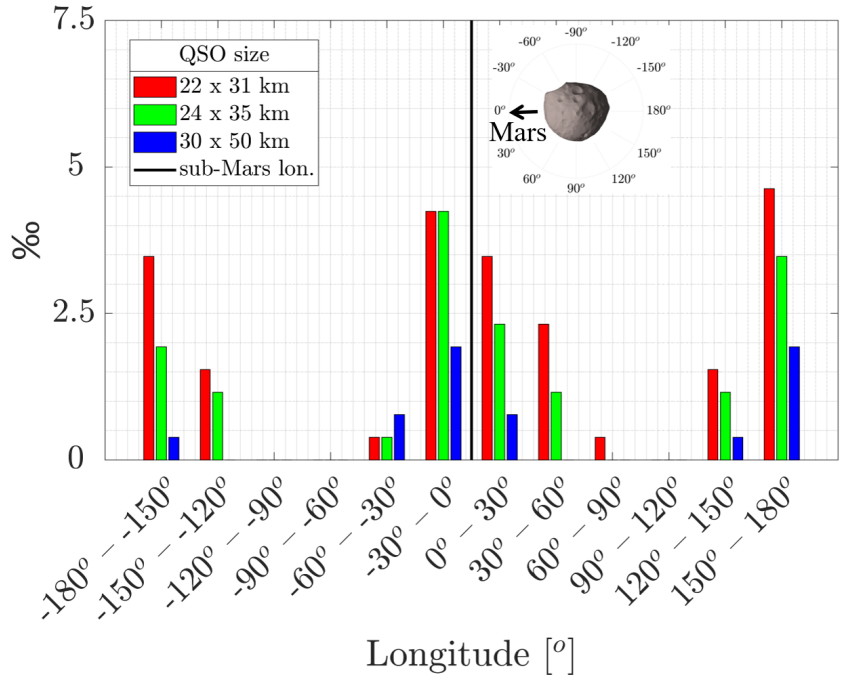

Figure 5.21: Landing dispersion with the hard surface approach across Phobos surface as per mille of 2592 trajectories deployed from each QSO altitude. Red, green and blue bar plots represent the deployments from 22 x 31 km, 24 x 35 km and 30 x 50 km QSOs, respectively. Polar plot in the upper right shows the longitude portions of Phobos that are also shown in the x-axis. Black line in the middle denotes the sub-Mars longitude.

dominance vanishes. For example, two smallest QSOs provide equal rechability to red/blue geological units, or the largest QSO provides more opportunities to Stickney than the other two. Leading an trailing sides, where the soft surface approach enables abundant opportunities to land in, are nearly non-reachable with the hard surface approach. This is likely due to the high speeds that impacts to those regions experience, which are ruled out in the hard surface case. The highest reachability in this case is seen in the sub- and anti-Mars points. That results opens a potentially interesting discussion. In Çelik et al. (2019), where the authors also included the attitude dynamics simulations and the real shape of the lander found out that there are very limited opportunities in the sub- and anti-Mars directions, *i.e.*, regions where Phobos is enclosed by its Roche lobe, or no reachability to Stickney crater from the largest QSO, an opposite result [3]. This comparison of the results above and in Çelik et al.

(2019) suggest that the final attitude is likely to be infeasible with the DCAM5 attitude requirements. When imaging is a crucial part of a mission like in the DCAM5's case, it is therefore important to support simplified analytical calculations with higher fidelity approaches to ensure the feasibility of the mission.

5.6 Discussion

This chapter presented a feasibility study of ballistic landings of DCAM5, a small deployable camera payload proposed for the Martian Moons eXploration (MMX) sample return mission from Phobos.

The dynamical environment in the vicinity of Phobos was first investigated through velocity surfaces (ZVS) and escape speeds. It was shown that particles in the leading or trailing sides of Phobos are energetically unbound to their parent body. For this reason, a numerical study was performed to estimate escape speeds by taking the chaotic dynamics and shape model of Phobos into account. The results of this analysis show that escape from Phobos is possible with speeds as low as ~2 m/s with most of the equatorial region being less than 4 m/s. Then, two different end-member surface approaches are used through analytical formulations and experimental data to constrain the maximum allowable impact speed to ensure post-impact speed to be less than or equal to 4 m/s. For the soft granular surface approach, the impact speeds are constrained to be a maximum of 15 m/s, whereas for the hard surface approach it is found to be about half of that value.

Based on this and DCAM5 requirements, the feasibility of ballistic landings from quasi-satellite orbits (QSOs) is investigated. A parametric study was implemented to find optimal deployment conditions that would ensure settlement in Phobos' surface. Optimal deployment speeds from the 22 x 31, 24 x 35, and 30 x 50 km were also found to be 6.0 m/s when the surface is assumed to be granular. No optimal point is found with the hard surface approach within the deployment speed range considered in this study, and the highest feasibility is found with deployments at 10 m/s. It was also shown that the chosen surface type affects the reachability significantly. While this is expected from the lower feasibility with the hard surface approach, it was shown that the smallest QSO does not necessarily mean higher reachability in the hard surface case. In fact, for example, it was found that for landings in Stickney

crater, the largest QSO provides better accessibility compared to the smallest two. A comparison with Çelik et al. (2019), where a higher fidelity approach is employed with DEM simulations of the actual lander shape and attitude simulation suggest that when the lander attitude is one of the drivers of a mission, more sophisticated approaches (*e.g.*, simulations) may be necessary to support rapid analysis done with the simplified models to down select trajectories that comply attitude requirements, as well.

6

Conclusions and future work

The object-surface interaction problem in the context of this thesis is primarily characterized by impacts that occur in m/s or lower level velocities in the low-gravity environment of a small-body. Those impacts not only characterize humanmade spacecraft but also natural activity in small bodies, as the recent observations revealed. Current approaches to model object-surface interaction in small bodies with rigid-bodies, in general, can be divided into two as (1) hard nonpenetrable surfaces and (2) soft, granular, and penetrable surfaces. When the small-body surface is unknown apriori, the relative simplicity of the former led to fast simulations with nonspherical probe shapes, whereas the latter led to limited higher-fidelity results with slow simulations or experiments, with their respective assumptions of surface structure. However, the lack of experimental evidence on the assumptions of the hard-surface approach for nonspherical impactors in small-body level gravity remains to be filled. Specifically, the relationship between impact conditions (velocity, angle, attitude) and post-impact motion needs to be elucidated. On the other hand, current approaches to simulate soft surface interaction appears to struggle in its granular level complexity and

lacking a level of an analytical framework that could overcome some of its complexity and computational limitations. As a result, the initial mission design of surface probes and natural particle motion could also benefit from these improvements.

Therefore, the interaction between an object and a small-body surface is investigated from a multifaceted perspective in this thesis through experiments, simulations, and analytical techniques, with applications to the mission design of a small-body lander. In all of those, the coefficient of restitution is given a central role in the analyses as a common measure of surface interaction. Experiments are performed for hard-surface impacts, whereas analytical studies are performed for granular-surface impacts. Finally, a mission design application is performed to compare how a surface interaction implementation constrains initial mission design space and reachable regions on the surface of Phobos for deployments from quasi-satellite orbits.

In the following subsection, the general results of the research will be presented for each chapter of the thesis in an itemized form.

Hard surface interaction

Hard surface experiments were performed on an air-bearing table setup with a nonspherical impactor. Following results are achieved:

- With around 2500 experimental runs covering five impact velocities, four impact, and attitude angles, and two different impact cases (normal and oblique) under effective milli-g acceleration, the air-bearing experiment setup is proven as a more accessible and controllable alternative to more expensive and limited parabolic, suborbital and orbital flights, and drop towers.
- The achieved precision in velocity is ±1 cm/s at most (lower on average), and $\pm 5^o$ in attitude and impact angles on average. These errors are primarily due to precision at release and block movement.
- Through an image-based qualitative, as well as simulation and data analysis based quantitative analyses, it was confirmed that contact duration is short and can be approximated as impulsive.
- The effective coefficient of restitution, when defined as the ratio of post- and pre-impact velocity magnitudes, is found to be a linear function of impact

angle in oblique impacts, and independent of impact velocity. There are no distinguishable trends found with attitude angle and impact velocity in normal impacts. In the central impact case, the coefficient of restitution is measured between 0.2-0.3.

- When compared with Brach's low-speed contact model, the coefficient of restitution and friction are found to be attitude and velocity independent but linearly dependent on impact angle.

Granular surface interaction

In this chapter, an object's interaction on a granular soft surface on a small-body is investigated. This type of interaction is essentially a cratering process initiated upon impact with the surface. The coefficient of restitution on a granular surface is defined with residual energy after initial impact energy is dissipated in various ways. The analytical derivations of the cratering process are inspired by the long-established crater scaling theory of astronomical impacts. Current experiments are limited to crater size detection only and mostly under Earth-gravity. Full validation of the theory including ejecta properties for low-speed impacts is performed with discrete-element simulations in small-body level gravity. Following results are obtained:

- It was proven that similar scaling laws exist for low-speed impacts under small-body gravity. Fundamental observations of the original theory are confirmed, and necessary power-law coefficients are determined for the scaling laws.

- Analytical ballistic ejection model is modified with new results and validated for low-speed impacts.

- It was found during the numerical impact experiments that bouncing of an impactor from the surface occurs only when the impactor density is lower than or equal to a quarter of surface density. In the same gravity level, this observation is confirmed in multiple density levels.

- From energy dissipation arguments, a coefficient of restitution expression is proposed. The expression includes energy spent to material mobility, volume

compression, impactor and particle rotation, and impactor's material properties in the form of impactor coefficient of restitution.

- An new analytical integral is proposed to model the energy field inside a crater by utilizing the tools of the crater-scaling theory and ballistic ejection model. The analytical crater size estimations are made for a given impactor size, impactor, and target density and impact speed, which are inputted to the ballistic ejecta model. The final expression is not analytically solvable; its numerical solution yields energy dissipated to material mobility.

- Contribution of other energy sinks is calculated with either other analytical expressions or estimated more empirically. More specifically, the compressed volume is calculated analytically while energy spent on impactor rotation is found from the simulation results, as there is no direct way of calculating that in a granular system without overly simplifying assumptions.

- Final coefficient of restitution results are compared to the simulation results. It was observed that the simulated coefficient of restitution values corresponds to the lower bound of analytical estimations, suggesting that other energy sinks that are currently not captured in the model. Nevertheless, the model demonstrates the promise of this preliminary attempt.

- When the impactor size is changed, the the developed theory still yields reasonable estimations of the coefficient of restitution.

- As a side result, it was demonstrated during this study that discrete-element method simulations can certainly be used in lieu of experiments when they are not possible or feasible to do, provided that they are calibrated with real materials.

- Also as a byproduct of the research, a computational procedure is proposed to detect crater size and ejecta properties in the post-processing of the DEM impact simulations.

Surface interaction in mission design

A small-body lander is considered as a mission design application. Small-body landers possess little or no control capability hence surface interaction is the only way to dissipate energy to settle on the surface. Therefore, surface interaction is an indispensable element of the initial mission design of small-body landers. In this section, the proposed optional payload of the Martian Moons eXploration (MMX) mission, Deployable CAMera 5 (DCAM5) is considered as the case study. Because of the peculiar dynamical environment around Phobos, both high-fidelity three-body dynamics, surface environment, and mission constraints of MMX and DCAM5 are combined to guarantee to settle on Phobos surface after the first impact. Following results are obtained:

- Previous escape speed analysis with the ellipsoidal gravity model is extended to a more accurate constant density polyhedron model with a shape model of Phobos. It was found that in chaotic three-body dynamics escape from the surface is possible with velocities as low as 2 m/s, contrary to analytical two-body problem estimations of 9 m/s. This highlights the importance of implementing high-fidelity dynamics when necessary and increases the importance of surface interaction to dissipate enough energy to ensure a post-impact velocity below this value.

- Using both escape speed and the coefficient of restitution results from both hard and granular surface impacts, as well as mission constraints, allowable impact speed and its angle is constrained to ensure that the post-impact speed to stay always below a selected maximum post-impact speed. In this study, this was selected to be 4 m/s.

- Systematically generated landing trajectories are downselected based on the derived feasibility conditions. It was shown that there is an optimal deployment speed that enables maximum feasibility when the surface is granular, but this is not ensured within the deployment speed range for hard surface impacts.

- Finally, scientifically-interesting reachable regions are identified. When the surface is granular, nearly everywhere in the equatorial region of Phobos is

reachable. When the surface is hard only sub-Mars and anti-Mars regions are feasibly reachable.

6.1 Implications of the research

The research has direct implications in surface probe design for future small-body exploration missions. Some of those are demonstrated in a preliminary mission analysis of a small-body lander. As surface interaction is a crucial element of a surface probe design, the relationship elucidated between impact angle and the coefficient of restitution in both hard and soft surfaces can be implemented in simulating the bouncing motion and in the operational planning. The impact experiment results may also inform the trajectory reconstruction of surface probes when measurements and/or observations are available. In return, measurements and observations could be used to validate experimental observations. Moreover, the analytical and experimental results presented here may facilitate the unification of the two seemingly different camps of surface interaction approaches for a "mixed surface." This would include a hard surface underneath a granular layer, in which partial energy dissipation in the granular layer can be computed analytically, while the empirical relations found in the hard-surface experiments can be used to compute post-impact conditions. Furthermore, ejecta results shown in low-speed cratering would provide useful inputs of landing and sampling of large spacecraft to estimate the ejection velocity and its angle upon touchdown in protecting the sensitive equipment and scientific instruments.

On the other hand, the demonstrated existence of low-speed cratering laws opens new ways to interpret natural phenomena on small-bodies. For instance, small craters on asteroids may be an indication of larger low-speed particles instead of micrometeoroids at extremely high speeds. These low-speed particles would also be an indicator of ejection events. Related to this argument, potentially ejected but unobserved mass can be estimated via analytical crater size estimations.

Other subfields of space science and engineering could also find applications through this research. An example of that is on-orbit rendezvous and docking, potential with debris capturing or on-orbit servicing. In this application, relative velocities between objects are also low and their interaction can be characterized as low-speed impacts. Similarly, processes like ring formation around planets also occur through

collision at low relative speeds, hence some of the results shown in the hard surface impacts may be useful

6.2 Future directions

The research results presented in this thesis offer new insights and approaches to the surface interaction problem in small-body surfaces. These insights are required to be further improved to consolidate the offered insights. Specifically, although the relationship between impact conditions and the post-impact motion is elucidated in the hard surface experiments, it still lacks the connection between material properties of post-impact response. This would not only be relevant to understanding the physical nature of the interaction but would also inform mission designers to relate their measurements to surface properties. Similarly, validation of common compliant contact models, such as the spring-damper model, can be tested under low-gravity experimental data.

In granular surface interaction, an immediate improvement is to extend the model into oblique impacts. There is considerably less amount of studies on oblique impact cratering, hence research towards this direction is necessary not only from surface interaction perspective but also low-speed impact cratering, as well. Similarly, dependencies of the cratering process to, for example, material type, strength, or even impactor shape or rotation may be further investigated. A mixed surface interaction approach would also be impactful to combine the strengths of hard- and granular-surface approaches towards a more realistic surface. Applications of this to space mission design or planetary science problems would always be an active research area.

Bibliography

[1] M. Arakawa, T. Saiki, K. Wada, K. Ogawa, T. Kadono, K. Shirai, H. Sawada, K. Ishibashi, R. Honda, N. Sakatani, Y. Iijima, C. Okamoto, H. Yano, Y. Takagi, M. Hayakawa, P. Michel, M. Jutzi, Y. Shimaki, S. Kimura, Y. Mimasu, T. Toda, H. Imamura, S. Nakazawa, H. Hayakawa, S. Sugita, T. Morota, S. Kameda, E. Tatsumi, Y. Cho, K. Yoshioka, Y. Yokota, M. Matsuoka, M. Yamada, T. Kouyama, C. Honda, Y. Tsuda, S. Watanabe, M. Yoshikawa, S. Tanaka, F. Terui, S. Kikuchi, T. Yamaguchi, N. Ogawa, G. Ono, K. Yoshikawa, T. Takahashi, Y. Takei, A. Fujii, H. Takeuchi, Y. Yamamoto, T. Okada, C. Hirose, S. Hosoda, O. Mori, T. Shimada, S. Soldini, R. Tsukizaki, T. Iwata, M. Ozaki, M. Abe, N. Namiki, K. Kitazato, S. Tachibana, H. Ikeda, N. Hirata, N. Hirata, R. Noguchi, and A. Miura, "An artificial impact on the asteroid 162173 Ryugu formed a crater in the gravity-dominated regime," *Science*, vol. 1701, no. March, 2020.

[2] K. R. Housen and K. A. Holsapple, "Ejecta from impact craters," *Icarus*, vol. 211, no. 1, pp. 856–875, 2011.

[3] O. Çelik, N. Baresi, R.-L. Ballouz, K. Ogawa, K. Wada, and Y. Kawakatsu, "Ballistic deployment from quasi-satellite orbits around phobos under realistic dynamical and surface environment constraints," *Planetary and Space Science*, vol. 178, no. 104693, 2019.

[4] F. Scholten, F. Preusker, S. Elgner, K.-D. Matz, R. Jaumann, J. Biele, D. Hercik, H.-U. Auster, M. Hamm, M. Grott, C. Grimm, T.-M. Ho, A. Koncz, N. Schmitz, F. Trauthan, S. Kameda, S. Sugita, R. Honda, T. Morota, E. Tatsumi, Y. Cho, K. Yoshioka, H. Sawada, Y. Yokota, N. Sakatani, M. Hayakawa, M. Matsuoka,

M. Yamada, T. Kouyama, H. Suzuki, C. Honda, and K. Ogawa, "The descent and bouncing path of the Hayabusa2 lander MASCOT at asteroid (162173) Ryugu," *Astronomy & Astrophysics*, vol. 632, p. L3, 2019.

[5] R. L. Ballouz, D. C. Richardson, P. Michel, S. R. Schwartz, and Y. Yu, "Numerical simulations of collisional disruption of rotating gravitational aggregates: Dependence on material properties," *Planetary and Space Science*, vol. 107, no. 1, pp. 29–35, 2015.

[6] S. R. Schwartz, D. C. Richardson, and P. Michel, "An implementation of the soft-sphere discrete element method in a high-performance parallel gravity tree-code," *Granular Matter*, vol. 14, no. 3, pp. 363–380, 2012.

[7] P. A. Tipler and G. Mosca, *Physics for scientists and engineers.* Macmillan, 2007.

[8] L. Prockter, S. Murchie, A. Cheng, S. Krimigis, R. Farquhar, A. Santo, and J. Trombka, "The NEAR shoemaker mission to asteroid 433 eros," *Acta Astronautica*, vol. 51, no. 1-9, pp. 491–500, 2002.

[9] W. H. Blume, "Deep Impact mission design," *Space Science Reviews*, vol. 117, no. 1-2, pp. 23–42, 2005.

[10] J. Kawaguchi, A. Fujiwara, and T. Uesugi, "Hayabusa-Its technology and science accomplishment summary and Hayabusa-2," *Acta Astronautica*, vol. 62, no. 10-11, pp. 639–647, 2008.

[11] R. C. Anderson, D. Scheeres, S. Chesley, and the BASiX Science Team, "A Mission Concept to Explore a Binary Near Earth Asteroid System," in *Proceedings of the 45^{th} Lunar and Planetary Science Conference*, (The Woodlands, Texas), March 2014. March 17–21, Paper number 1777.

[12] A. F. Cheng, J. Atchison, B. Kantsiper, A. S. Rivkin, A. Stickle, C. Reed, and S. Ulamec, "Asteroid Impact and Deflection Assessment mission," *Acta Astronautica*, vol. 115, no. October–November, pp. 262–269, 2015.

[13] P. Michel, M. Kueppers, H. Sierks, I. Carnelli, A. F. Cheng, K. Mellab, M. Granvik, A. Kestilä, T. Kohout, K. Muinonen, A. Näsilä, A. Penttila, T. Tikka, P. Tortora,

V. Ciarletti, A. Hérique, N. Murdoch, E. Asphaug, A. Rivkin, O. Barnouin, A. C. Bagatin, P. Pravec, D. C. Richardson, S. R. Schwartz, K. Tsiganis, S. Ulamec, and O. Karatekin, "European component of the AIDA mission to a binary asteroid: Characterization and interpretation of the impact of the DART mission," *Advances in Space Research*, Dec 2017.

[14] Y. Tsuda, M. Yoshikawa, M. Abe, H. Minamino, and S. Nakazawa, "System design of the hayabusa 2-asteroid sample return mission to 1999 JU3," *Acta Astronautica*, vol. 91, pp. 356–362, 2013.

[15] E. Beshore, D. Lauretta, W. Boynton, C. Shinohara, B. Sutter, D. Everett, J. Gal-Edd, R. Mink, M. Moreau, and J. Dworkin, "The OSIRIS-REx asteroid sample return mission," *IEEE Aerospace Conference Proceedings*, vol. June, no. 520, 2015.

[16] A. F. Cheng, P. Michel, M. Jutzi, A. S. Rivkin, A. Stickle, O. Barnouin, C. Ernst, J. Atchison, P. Pravec, and D. C. Richardson, "Asteroid Impact & Deflection Assessment mission: Kinetic impactor," *Planetary and Space Science*, vol. 121, pp. 27–35, 2016.

[17] K. Wada, H. Sawada, K. Ogawa, K. Shirai, N. Sakatani, K. Ishibashi, R. Honda, M. Yasui, and M. Arakawa, "Deployable Camera system 5 (DCAM5) proposed for Martian Moon Exploration mission (MMX)," in *Japan Geosciences Union Meeting*, (Chiba, Japan), 2016.

[18] L. Riu, R. L. Ballouz, S. Van wal, O. Çelik, N. Baresi, R. Boden, and S. Crites, "MARAUDERS: A mission concept to probe volatile distribution and properties at the lunar poles with miniature impactors," *Planetary and Space Science*, vol. 189, no. 104969, 2020.

[19] T. Yoshimitsu, S. Sasaki, M. Yanagisawa, and T. Kubota, "Scientific Capability of MINERVA Rover in Hayabusa Asteroid Mission," in *Lunar and Planetary Science*, no. XXXV, pp. 2–3, 2004.

[20] T. Kubota, S. Sawai, T. Hashimoto, and J. Kawaguchi, "Collision dynamics of a visual target marker for small-body exploration," *Advanced Robotics*, vol. 21, no. 14, pp. 1635–1651, 2007.

[21] J. Biele, S. Ulamec, M. Maibaum, R. Roll, L. Witte, E. Jurado, P. Munoz, W. Arnold, H.-U. Auster, C. Casas, C. Faber, C. Fantinati, F. Finke, H.-H. Fischer, K. Geurts, C. Guttler, P. Heinisch, A. Herique, S. Hviid, G. Kargl, M. Knapmeyer, J. Knollenberg, W. Kofman, N. Komle, E. Kuhrt, V. Lommatsch, S. Mottola, R. Pardo de Santayana, E. Remetean, F. Scholten, K. J. Seidensticker, H. Sierks, and T. Spohn, "The landing(s) of Philae and inferences about comet surface mechanical properties," *Science*, vol. 349, no. 6247, pp. 1–6, 2015.

[22] D. Lauretta, C. Hergenrother, S. Chesley, J. Leonard, J. Pelgrift, C. Adam, M. Al Asad, P. Antreasian, R.-L. Ballouz, K. Becker, *et al.*, "Episodes of particle ejection from the surface of the active asteroid (101955) bennu," *Science*, vol. 366, no. 6470, 2019.

[23] D. Jewitt and J. Li, "Activity in Geminid parent (3200) Phaethon," *The Astronomical Journal*, vol. 140, no. 5, pp. 1519–1527, 2010.

[24] S. R. Chesley, A. S. French, A. B. Davis, R. A. Jacobson, M. Brozović, D. Farnocchia, S. Selznick, A. J. Liounis, C. W. Hergenrother, M. C. Moreau, J. Pelgrift, E. Lessac-Chenen, J. L. Molaro, R. S. Park, B. Rozitis, D. J. Scheeres, Y. Takahashi, D. Vokrouhlický, C. W. V. Wolner, C. Adam, B. J. Bos, E. J. Christensen, J. P. Emery, J. M. Leonard, J. W. McMahon, M. C. Nolan, F. C. Shelly, and D. S. Lauretta, "Trajectory estimation for particles observed in the vicinity of (101955) bennu," *Journal of Geophysical Research: Planets*, vol. 125, no. e2019JE006363, 2020.

[25] K. Walsh, E. Jawin, R.-L. Ballouz, O. Barnouin, E. Bierhaus, H. Connolly, J. Molaro, T. McCoy, M. Delbo, C. Hartzell, *et al.*, "Craters, boulders and regolith of (101955) bennu indicative of an old and dynamic surface," *Nature Geoscience*, vol. 12, no. 4, pp. 242–246, 2019.

[26] S. Tardivel, P. Michel, and D. J. Scheeres, "Deployment of a lander on the binary asteroid (175706) 1996 FG_3, potential target of the european MarcoPolo-R sample return mission," *Acta Astronautica*, vol. 89, no. August–September, pp. 60–70, 2013.

[27] O. Çelik, J. P. Sánchez, Ö. Karatekin, and B. Ritter, "A comparative reliability analysis of ballistic deployments on binary asteroids," *Acta Astronautica*, vol. 156, pp. 308–316, Mar 2019.

[28] F. Ferrari and M. Lavagna, "Ballistic landing design on binary asteroids: The AIM case study," *Advances in Space Research*, vol. 62, no. 8, pp. 2245–2260, 2018.

[29] Y. Yu and H. Baoyin, "Modeling of migrating grains on asteroid's surface," *Astrophysics and Space Science*, vol. 355, no. 1, pp. 43–56, 2014.

[30] Y. Yu and H. X. Baoyin, "Routing the asteroid surface vehicle with detailed mechanics," *Acta Mechanica Sinica/Lixue Xuebao*, vol. 30, no. 3, pp. 301–309, 2014.

[31] Y. Zhang, X. Zeng, C. Circi, and G. Vulpetti, "The motion of surface particles for the asteroid 101955 Bennu," *Acta Astronautica*, vol. 163, pp. 3–10, oct 2019.

[32] S. Van wal, R. R. Reid, and D. J. Scheeres, "Small-Body Lander Simulations Using the GPU," in *31st International Symposium on Space Technology and Science*, vol. 14, pp. 1–7, 2017.

[33] S. Tardivel, D. J. Scheeres, P. Michel, S. van Wal, and P. Sanchez, "Contact Motion on Surface of Asteroid," *Journal of Spacecraft and Rockets*, vol. 51, no. 6, pp. 1857–1871, 2014.

[34] W. J. Stronge, *Impact Mechanics*. Cambridge: Cambridge University Press, 2000.

[35] S. Van wal, R. G. Reid, and D. J. Scheeres, "Simulation of nonspherical asteroid landers: Contact modeling and shape effects on bouncing," *Journal of Spacecraft and Rockets*, vol. 57, no. 1, pp. 109–130, 2020.

[36] S. Van wal, *High-Fidelity Simulation of Small-Body Lander/Rover Spacecraft*. PhD thesis, University of Colorado Boulder, Boulder, Colorado, 2018.

[37] S. Van wal and D. Scheeres, "Effects of probe shape and surface topography in deployment to small bodies," in *15th International Planetary Probe Workshop*, (Boulder, Colorado).

[38] S. Van wal, S. Tardivel, and D. Scheeres, "Parametric Study of Ballistic Lander Deployment to Small Bodies," *Journal of Spacecraft and Rockets*, vol. 54, no. 6, pp. 1330–1355, 2017.

[39] T. Pöschel and T. Schwager, *Computational Granular Dynamics*. Berlin/Heidelberg: Springer-Verlag, 2005.

[40] S. Sawai, J. Kawaguchi, D. J. Scheeres, N. Yoshikawa, and M. Ogasawara, "Development of a Target Marker for Landing on Asteroids," *Journal of Spacecraft and Rockets*, vol. 51, no. 4, pp. 1857–1871, 2001.

[41] J. Biele, L. Kesseler, C. D. Grimm, S. Schröder, O. Mierheim, M. Lange, and T.-M. Ho, "Experimental Determination of the Structural Coefficient of Restitution of a Bouncing Asteroid Lander," may 2017. arXiv ID: 1705.00701.

[42] F. Gautier, E. Sitepu, C. Le Blay, G. Kersey, and J. Sánchez, "Drop your thesis! 2018 results: 4.74 seconds of microgravity conditions to enable future cubesat landings on asteroids," *Acta Astronautica*, 2020.

[43] A. Mehta, *Granular Physics*. New York, NY: Cambridge University Press, 2007.

[44] C. Maurel, P. Michel, J. Biele, R.-L. Ballouz, and F. Thuillet, "Numerical simulations of the contact between the lander MASCOT and a regolith-covered surface," *Advances in Space Research*, vol. 62, no. 8, pp. 2099–2124, 2018.

[45] F. Thuillet, P. Michel, C. Maurel, R.-L. Ballouz, Y. Zhang, D. C. Richardson, J. Biele, E. Tatsumi, and S. Sugita, "Numerical modeling of lander interaction with a low-gravity asteroid regolith surface-application to mascot on board hayabusa2," *Astronomy & Astrophysics*, vol. 615, p. A41, 2018.

[46] B. Cheng, Y. Yu, and H. Baoyin, "Numerical simulations of the controlled motion of a hopping asteroid lander on the regolith surface," *Monthly Notices of the Royal Astronomical Society*, vol. 485, no. 3, pp. 3097–3111, 2019.

[47] Y. Jiang, Y. Zhang, and H. Baoyin, "Surface motion relative to the irregular celestial bodies," *Planetary and Space Science*, vol. 127, no. August, pp. 33–43, 2016.

[48] H. Katsuragi and D. J. Durian, "Unified force law for granular impact cratering," *Nature Physics*, vol. 3, no. 6, pp. 420–423, 2007.

[49] D. J. Scheeres, *Orbital Motion in Strongly Perturbed Environments*. Berlin Heidelberg: Springer Praxis, 2012.

[50] K. Housen, R. Schmidt, and K. Holsapple, "Crater ejecta scaling laws: Fundamental forms based on dimensional analysis," *Journal of Geophysical Research: Solid Earth*, vol. 88, no. B3, pp. 2485–2499, 1983.

[51] R. A. Werner and D. J. Scheeres, "Exterior gravitation of a polyhedron derived and compared with harmonic and mascon gravitation representations of asteroid 4769 castalia," *Celestial Mechanics and Dynamical Astronomy*, vol. 65, no. 3, pp. 313–344, 1996.

[52] V. Szebehely, *Theory of Orbits*. Academic Press: New York, 1967.

[53] K. Holsapple and R. Schmidt, "On the scaling of crater dimensions: 2. impact processes," *Journal of Geophysical Research: Solid Earth*, vol. 87, no. B3, pp. 1849–1870, 1982.

[54] R. Schmidt, "Meteor Crater: energy of formation-implications of centrifuge scaling," in *11th Lunar and Planetary Science Conference*, pp. 2099–2128, 1980.

[55] E. Buckingham, "On physically similar systems; illustrations of the use of dimensional equations," *Physical review*, vol. 4, no. 4, p. 345, 1914.

[56] R. M. Schmidt and K. R. Housen, "Some recent advances in the scaling of impact and explosion cratering," *International Journal of Impact Engineering*, vol. 5, no. 1-4, pp. 543–560, 1987.

[57] H. J. Melosh, *Impact cratering: A geologic process*. Oxford University Press, 1989.

[58] K. A. Holsapple and K. R. Housen, "A crater and its ejecta: An interpretation of Deep Impact," *Icarus*, vol. 191, pp. 586–597, 2007.

[59] K. Kitazato, R. Milliken, T. Iwata, M. Abe, M. Ohtake, S. Matsuura, T. Arai, Y. Nakauchi, T. Nakamura, M. Matsuoka, *et al.*, "The surface composition of

asteroid 162173 ryugu from hayabusa2 near-infrared spectroscopy," *Science*, vol. 364, no. 6437, pp. 272–275, 2019.

[60] P. Sánchez and D. J. Scheeres, "The strength of regolith and rubble pile asteroids," *Meteoritics & Planetary Science*, vol. 49, no. 5, pp. 788–811, 2014.

[61] J. E. Richardson, H. J. Melosh, C. M. Lisse, and B. Carcich, "A ballistics analysis of the Deep Impact ejecta plume: Determining Comet Tempel 1's gravity, mass, and density," *Icarus*, vol. 191, pp. 176–209, 2007.

[62] D. Maxwell, "Simple z model for cratering, ejection, and the overturned flap.," in *Impact and explosion cratering: Planetary and terrestrial implications*, pp. 1003–1008, 1977.

[63] M. J. Cintala, L. Berthoud, and F. Hörz, "Ejection-velocity distributions from impacts into coarse-grained sand," *Meteoritics & Planetary Science*, vol. 34, no. 4, pp. 605–623, 1999.

[64] C. Thornton, *Granular dynamics, contact mechanics and particle system simulations*. Springer, 2015.

[65] P. A. Cundall, "A computer model for simulating progressive, large-scale movement in blocky rock system," in *Proceedings of the International Symposium on Rock Mechanics*, 1971.

[66] P. A. Cundall and O. D. Strack, "A discrete numerical model for granular assemblies," *Geotechnique*, vol. 29, no. 1, pp. 47–65, 1979.

[67] K. Walsh and D. Richardson, "Binary near-Earth asteroid formation: Rubble pile model of tidal disruptions," *Icarus*, vol. 180, no. 1, pp. 201–216, 2006.

[68] D. Richardson, P. Michel, K. Walsh, and K. Flynn, "Numerical simulations of asteroids modelled as gravitational aggregates with cohesion," *Planetary and Space Science*, vol. 57, no. 2, pp. 183–192, 2009.

[69] R.-L. Ballouz, N. Baresi, S. T. Crites, Y. Kawakatsu, and M. Fujimoto, "Surface refreshing of martian moon phobos by orbital eccentricity-driven grain motion," *Nature Geoscience*, vol. 12, no. 4, pp. 229–234, 2019.

[70] M. A. Knuth, J. Johnson, M. Hopkins, R. Sullivan, and J. Moore, "Discrete element modeling of a mars exploration rover wheel in granular material," *Journal of Terramechanics*, vol. 49, no. 1, pp. 27–36, 2012.

[71] F. Thuillet, P. Michel, S. Tachibana, R.-L. Ballouz, and S. R. Schwartz, "Numerical modelling of medium-speed impacts on a granular surface in a low-gravity environment application to hayabusa2 sampling mechanism," *Monthly Notices of the Royal Astronomical Society*, vol. 491, no. 1, pp. 153–177, 2020.

[72] E. Asphaug, J. Thangavelautham, A. Klesh, A. Chandra, R. Nallapu, L. Raura, M. Herreras-Martinez, and S. Schwartz, "A cubesat centrifuge for long duration milligravity research," *npj Microgravity*, vol. 3, no. 1, p. 16, 2017.

[73] S. R. Schwartz, J. Thangavelauthum, E. Asphaug, A. Chandra, R. teja Nallapu, and L. Vance, "Investigating asteroid surface geophysics with an ultra-low-gravity centrifuge in low-earth orbit," in *International Astronautical Congress (IAC)*, (Washington, DC), 2019.

[74] P. Michel, S. R. Schwartz, D. C. Richardson, N. Machii, and A. M. Nakamura, "Simulations of low-speed impacts into cohesive aggregates and comparison with experiments on sintered glass bead agglomerates," in *European Planetary Science Conference*, vol. 6, 2011.

[75] O. Çelik and J. P. Sanchez, "Opportunities for Ballistic Soft Landing in Binary Asteroids," *Journal of Guidance, Control, and Dynamics*, vol. 40, no. 6, 2017.

[76] J. Calsamiglia, S. W. Kennedy, A. Chatterjee, A. Ruina, and J. T. Jenkins, "Anomalous Frictional Behavior in Collisions of Thin Disks," *Journal of Applied Mechanics*, vol. 66, no. 1, pp. 146–152, 1999.

[77] D. Nishiura and H. Sakaguchi, "Microscopic measurements of planar viscoelastic body eccentric impacts on a convex corner," *International Journal of Non-Linear Mechanics*, vol. 67, pp. 133–143, 2014.

[78] S. Van wal, O. Celik, K. Yoshikawa, Y. Tsuda, and Y. Kawakatsu, "Experimental validation of hard-surface impacts using air-bearing assembly for small-body

landers," in *31st International Symposium on Space Science and Technology*, (Fukui, Japan), 2019.

[79] S. Van wal, K. Yoshikawa, and Y. Tsuda, "Deployment analysis and trajectory reconstruction of minerva-II rovers on asteroid ryugu," in *Advances in the Astronautical Sciences*, vol. 168, pp. 1891–1910, 2019.

[80] D. Dunham, "Implementation of the First Asteroid Landing," *Icarus*, vol. 159, no. 2, pp. 433–438, 2002.

[81] H. Yano, T. Kubota, H. Miyamoto, T. Okada, D. Scheeres, Y. Takagi, K. Yoshida, M. Abe, S. Abe, a. Fujiwara, S. Hasegawa, T. Hashimoto, M. Ishiguro, M. Kato, J. Kawaguchi, T. Mukai, J. Saito, S. Sasaki, and M. Yoshikawa, "Touchdown of the Hayabusa Spacecraft at the Muses Sea on Itokawa," *Science*, vol. 312, no. June, pp. 4–7, 2005.

[82] A. Savitzky and M. J. Golay, "Smoothing and differentiation of data by simplified least squares procedures.," *Analytical chemistry*, vol. 36, no. 8, pp. 1627–1639, 1964.

[83] W. Goldsmith, *Impact*. Courier Corporation, 2001.

[84] R. M. Brach, "Moments Between Impacting Rigid Bodies," *Journal of Mechanical Design*, vol. 103, pp. 812–817, 10 1981.

[85] R. M. Brach, "Rigid Body Collisions," *Journal of Applied Mechanics*, vol. 56, no. 1, pp. 133–138, 1989.

[86] R. M. Brach, *Rigid body collisions*. John Wiley & Sons, 1991.

[87] S. J. De Vet and J. R. De Bruyn, "Shape of impact craters in granular media," *Physical Review E - Statistical, Nonlinear, and Soft Matter Physics*, vol. 76, no. 4, pp. 1–6, 2007.

[88] S. Tsujido, M. Arakawa, A. I. Suzuki, and M. Yasui, "Ejecta velocity distribution of impact craters formed on quartz sand: Effect of projectile density on crater scaling law," *Icarus*, vol. 262, pp. 79–92, 2015.

[89] M. Kiuchi, A. M. Nakamura, and K. Wada, "Experimental Study on Gravitational and Atmospheric Effects on Crater Size Formed by Low-Velocity Impacts Into Granular Media," *Journal of Geophysical Research: Planets*, vol. 124, no. 5, pp. 1379–1392, 2019.

[90] S. Takizawa and H. Katsuragi, "Scaling laws for the oblique impact cratering on an inclined granular surface," *Icarus*, vol. 335, no. 113409, 2020.

[91] J. Brisset, J. Colwell, A. Dove, S. Abukhalil, C. Cox, and N. Mohammed, "Regolith behavior under asteroid-level gravity conditions: low-velocity impact experiments," *Progress in Earth and Planetary Science*, vol. 5, no. 1, p. 73, 2018.

[92] D. E. Gault and J. A. Wedekind, "Experimental hypervelocity impact into quartz sand - II, Effects of gravitational acceleration," in *Impact and Explosion Cratering*, pp. 1231–1244, New York, NY: Pergamon, 1977.

[93] S. Yamamoto, K. Wada, N. Okabe, and T. Matsui, "Transient crater growth in granular targets: An experimental study of low velocity impacts into glass sphere targets," *Icarus*, vol. 183, no. 1, pp. 215–224, 2006.

[94] K. Hayashi and I. Sumita, "Low-velocity impact cratering experiments in granular slopes," *Icarus*, vol. 291, pp. 160–175, 2017.

[95] M. J. Cintala, F. Horz, and T. H. See, "Impact Cratering in Low-Gravity Enviornments: Results of Reconnaissance Experimentation on the NASA KC-135A Reduced Gravity Aircraft," in *19th Lunar and Planetary Science Conference*, pp. 627–639, 1989.

[96] M. F. A'Hearn, M. Belton, W. Delamere, J. Kissel, K. Klaasen, L. McFadden, K. Meech, H. Melosh, P. Schultz, J. Sunshine, *et al.*, "Deep impact: excavating comet tempel 1," *Science*, vol. 310, no. 5746, pp. 258–264, 2005.

[97] H. Sawada, K. Ogawa, K. Shirai, S. Kimura, Y. Hiromori, and Y. Mimasu, "Deployable Camera (DCAM3) System for Observation of Hayabusa2 Impact Experiment," *Space Science Reviews*, vol. 208, pp. 143–164, 2017.

[98] S. Deboeuf, P. Gondret, and M. Rabaud, "Dynamics of grain ejection by sphere impact on a granular bed," *Physical Review E*, vol. 79, no. 4, pp. 1–9, 2009.

[99] J. F. Boudet, Y. Amarouchene, and H. Kellay, "Dynamics of impact cratering in shallow sand layers," *Physical Review Letters*, vol. 96, no. 15, pp. 1–4, 2006.

[100] J. E. Richardson and H. J. Melosh, "An examination of the Deep Impact collision site on Comet Tempel 1 via Stardust-NExT: Placing further constraints on cometary surface properties," *Icarus*, vol. 222, no. 2, pp. 492–501, 2013.

[101] D. C. Richardson, J. Blum, T. Weinhart, S. R. Schwartz, P. Michel, and K. J. Walsh, "Numerical Simulations of Landslides Calibrated Against Laboratory Experiments for Application to Asteroid Surface Processes," in *AAS/Division for Planetary Sciences Meeting Abstracts #44*, AAS/Division for Planetary Sciences Meeting Abstracts, Oct. 2012.

[102] Y. Yu, D. C. Richardson, P. Michel, S. R. Schwartz, and R.-L. Ballouz, "Numerical predictions of surface effects during the 2029 close approach of Asteroid 99942 Apophis," *Icarus*, vol. 242, pp. 82–96, 2014.

[103] R. Kuzmin, T. Shingareva, and E. Zabalueva, "An engineering model for the phobos surface," *Solar System Research*, vol. 37, no. 4, pp. 266–281, 2003.

[104] A. Seguin, Y. Bertho, and P. Gondret, "Influence of confinement on granular penetration by impact," *Physical Review E*, vol. 78, no. 1, 2008.

[105] Y. Zhang, D. C. Richardson, O. S. Barnouin, C. Maurel, P. Michel, S. R. Schwartz, R.-L. Ballouz, L. A. Benner, S. P. Naidu, and J. Li, "Creep stability of the proposed AIDA mission target 65803 Didymos: I. Discrete cohesionless granular physics model," *Icarus*, vol. 294, pp. 98–123, 2017.

[106] N. Murdoch, I. Avila Martinez, C. Sunday, E. Zenou, O. Cherrier, A. Cadu, and Y. Gourinat, "An experimental study of low-velocity impacts into granular material in reduced gravity," *Monthly Notices of the Royal Astronomical Society*, vol. 1272, 2017.

[107] E. Wright, A. C. Quillen, J. South, R. C. Nelson, P. Sánchez, J. Siu, H. Askari, M. Nakajima, and S. R. Schwartz, "Ricochets on asteroids: Experimental study of low velocity grazing impacts into granular media," *Icarus*, vol. 351, no. 113963, 2020.

[108] T. Bogdan, J. E. Kollmer, J. Teiser, M. Kruss, and G. Wurm, "Laboratory impact splash experiments to simulate asteroid surfaces," *Icarus*, vol. 341, no. 113646, 2020.

[109] H. Katsuragi, *Physics of soft impact and cratering*. Springer, 2016.

[110] Y. Kawakatsu, "Mission Design of Martian Moons Exploration (MMX)," in *69th International Astronautical Congress*, (Bremen, Germany), 2018.

[111] D. M. Hunten, "Capture of Phobos and Deimos by photoatmospheric drag," *Icarus*, vol. 37, no. 1, pp. 113–123, 1979.

[112] P. Rosenblatt, S. Charnoz, K. M. Dunseath, M. Terao-Dunseath, A. Trinh, R. Hyodo, H. Genda, and S. Toupin, "Accretion of Phobos and Deimos in an extended debris disc stirred by transient moons," *Nature Geoscience*, vol. 9, no. 8, pp. 581–583, 2016.

[113] W. E. Wiesel, "Stable orbits about the Martian moons," *Journal of Guidance, Control, and Dynamics*, vol. 16, no. 3, pp. 434–440, 1993.

[114] E. Canalias, L. Lorda, and J. Laurent-Varin, "Design of realistic trajectories for the exploration of Phobos," in *2018 Space Flight Mechanics Meeting*, no. January, (Reston, Virginia), American Institute of Aeronautics and Astronautics, Jan 2018.

[115] H. Ikeda, S. Mitani, Y. Mimasu, G. Ono, K. Nigo, and Y. Kawakatsu, "Orbital Operations Strategy in the Vicinity of Phobos," in *31st International Symposium on Space Technology and Science*, (Matsuyama, Japan), 2017.

[116] D. Hercik, H. Auster, D. Constantinescu, J. Blum, K. Fornaçon, M. Fujimoto, K. Gebauer, J. Grundmann, C. Güttler, O. Hillenmaier, T. Ho, A. Hördt, C. Krause, E. Kührt, L. Lorda, A. Matsuoka, U. Motschmann, A. Moussi-Soffys, I. Richter, K. Sasaki, F. Scholten, B. Stoll, B. P. Weiss, F. Wolff, and K. Glassmeier, "Magnetic Properties of Asteroid (162173) Ryugu," *Journal of Geophysical Research: Planets*, vol. 125, no. 1, 2020.

[117] H. Sawada, O. Mori, N. Okuzumi, Y. Shirasawa, Y. Miyazaki, M. Natori, S. Matsunaga, H. Furuya, H. Sakamoto, "Mission report on the solar

power sail deployment demonstration of IKAROS," in *Proceedings of 52nd AIAA/ASME/ASCE/AHS/ASC Structure, Structural Dynamics Materials Conference*, (Denver, Colorado). April 04–07, 2011. Paper no. AIAA 2011-1887.

[118] A. R. Dobrovolskis and J. A. Burns, "Life near the Roche limit: Behavior of ejecta from satellites close to planets," *Icarus*, vol. 42, no. 3, pp. 422–441, 1980.

[119] D. R. Davis, K. R. Housen, and R. Greenberg, "The unusual dynamical environment of Phobos and Deimos," *Icarus*, vol. 47, no. 2, pp. 220–233, 1981.

[120] M. Zamaro and J. D. Biggs, "Natural motion around the Martian moon Phobos: the dynamical substitutes of the Libration Point Orbits in an elliptic three-body problem with gravity harmonics," *Celestial Mechanics and Dynamical Astronomy*, vol. 122, no. 3, pp. 263–302, 2015.

[121] M. Zamaro and J. D. Biggs, "Identification of new orbits to enable future mission opportunities for the human exploration of the Martian," *Acta Astronautica*, vol. 119, no. February–March, pp. 160–182, 2016.

[122] D. Scheeres, S. Van wal, Z. Olikara, and N. Baresi, "Dynamics in the Phobos environment," *Advances in Space Research*, vol. 63, no. 1, pp. 476–495, 2019.

[123] S. L. Murchie, P. C. Thomas, A. S. Rivkin, and N. L. Chabot, "Phobos and deimos," *Asteroids IV*, vol. 4, p. 451, 2015.

[124] NASA, "Planetary satellite physical parameters." https://ssd.jpl.nasa.gov (Accessed on October 1, 2018.).

[125] R. W. Gaskell, "Gaskell phobos shape model v1.0. vo1-sa-visa/visb-5-phobosshape-v1.0," tech. rep., 2011.

[126] K. Willner, X. Shi, and J. Oberst, "Phobos' shape and topography models," *Planetary and Space Science*, vol. 102, pp. 51–59, 2014.

[127] C. M. Ernst, O. S. Barnouin, R. T. Daly, and Small Body Mapping Tool Team, "The Small Body Mapping Tool (SBMT) for Accessing, Visualizing, and Analyzing Spacecraft Data in Three Dimensions," in *Lunar and Planetary Science Conference*, Lunar and Planetary Science Conference, p. 1043, Mar 2018.

[128] S. Tardivel and D. J. Scheeres, "Ballistic Deployment of Science Packages on Binary Asteroids," *Journal of Guidance, Control, and Dynamics*, vol. 36, no. 3, pp. 700–709, 2013.

[129] S. Van wal, D. J. Scheeres, and S. Tardivel, "High-Fidelity Small Body Lander Ssimulations," in *International Conference on Astrodynamics Tools and Techniques (ICATT)*, 2016.

[130] S. Van wal, Y. Tsuda, K. Yoshikawa, A. Miura, S. Tanaka, and D. Scheeres, "Prearrival Deployment Analysis of Rovers on Hayabusa2 Asteroid Explorer," *Journal of Spacecraft and Rockets*, vol. 55, no. 4, pp. 797–817, 2018.